THESE DE DOCTORAT DE

L'ÉCOLE CENTRALE DE NANTES
COMUE UNIVERSITE BRETAGNE LOIRE

ECOLE DOCTORALE N° 602
Sciences pour l'Ingénieur
Spécialité : Génie Civil

Par

Jie YANG

Analyses numériques de la problématique multi-physique des fontis au voisinage d'une digue ou d'un ouvrage linéaire

Thèse présentée et soutenue à Nantes, le 08/07/2019
Unité de recherche : Institut de Recherche en Génie Civil et Mécanique (GeM)-UMR CNRS 6183

Rapporteurs avant soutenance :

François NICOT   Directeur de Recherche, Irstea
Dongmei ZHANG   Professeur, Tongji University, Shanghai

Composition du Jury :

Président :   Stephane BONELLI
Examinateurs : Stephane BONELLI   Directeur de Recherche, Irstea
                Amade POUYA   Directeur de Recherche, École des Ponts ParisTech
                Lucile SAUSSAYE   Ingénieur, Cerema

Directeur de thèse :   Pierre-Yves HICHER   Professeur émérite, Ecole Centrale de Nantes
Co-directeur de thèse :   Zhenyu YIN   Maître de Conférences, PolyU Hong Kong
Co-encadrant de thèse :   Farid LAOUAFA   Ingénieur - HDR, INERIS

Table of contents

List of figures

ix

List of tables

Abstract

Geo-structures such as dams and levees or dikes are subjected to seepage varying in time and space. The water flowing through these porous media can lead to the detachment and transport of part of the soil particles within the structures or their foundations. This problem is usually called internal erosion. The term suffusion, one type of internal erosions, refers to the detachment and transport of finer particles through a coarser porous soil matrix due to seepage flow. Suffusion can modify with time the hydraulic and mechanical properties of the soils and may trigger significant damage on such structures and lead eventually to their collapse.

This research attempts to contribute to the design and sustainability of geotechnical and hydraulic engineering structures, with a particular focus on embankment dams, levees, and dikes. It aims to develop a numerical model of suffusion by introducing, on the one hand, the coupling of the hydraulic and mechanical phenomena and, on the other hand, the coupling of erosion and filtration. To achieve this objective, this research has been divided into two main parts: the analysis of the laboratory scale and the development to boundary value problems at the geo-structures scale.

Based on the porous medium theory, a new numerical model has been formulated to take into account both erosion and filtration in suffusion. The model was validated by reproducing the main features observed in the laboratory erosion tests. Since the initial heterogeneity of the soil sample have been suspected to have a significant effect in the erosion-filtration process, one and two-dimensional random finite difference analyses were performed by implementing the random field theory into the numerical model of suffusion. Monte Carlo simulations were conducted to investigate the influence of the variability, the spatial correlation length, and the cross correlation of the initial porosity and initial fines content on the rate of the eroded mass and the minimum hydraulic conductivity during the test. Thereafter, the numerical model of suffusion was enhanced by including a non-linear incremental constitutive model to take into account the effects of the evolution of the fines content on the soil behavior. A numerical approach was then developed at the laboratory scale to simulate the downward erosion tests under triaxial mechanical loading with a special emphasis on the evolution of the eroded mass, the hydraulic conductivity, and the deformation of the specimen during and after erosion under triaxial condition. The influence of the stress state and the soil initial states (relative density and fines content) on the suffusion process was discussed from a numerical standpoint.

In order to perform analyses at the scale of an entire engineering structure, a more general elasto-plastic sand-silt mixture model has been coupled with the four-constituent model of suffusion. The hydro-mechanical model was first implemented into the commercial finite element code ABAQUS and used to assess how internal erosion could impact the stability of earthen structures. After having simulated some numerical examples from the literature for validating the approach, the developed model was applied to compute the suffusion induced by the leakage at the bottom of a dike-on-foundation under plane-strain assumption. The evolution of suffusion within the dike was analyzed, as well as the effects of the leakage cavity location, the erosion rate and the fines content. Then, a

unsaturated flow condition was considered and implemented into the hydro-mechanical model of internal erosion in order to describe more accurately the seepage within the dike and its foundation due to the difference in water head at the upstream and downstream sides of the dike-on-foundation. The enhanced model was applied to simulate the 3D mechanical consequences of internal erosion induced by the seepage within the dike and at the bottom of the foundation. The influences of the size of the leakage cavity and the elevation of the water head at the upstream and downstream sides were discussed. The results demonstrated that two types of damage could occur: a sliding of the downstream slope and a sinkhole above the eroded area in the vicinity of the cavity.

Keywords: internal erosion, suffusion, finite element method, fines content, hydro-mechanical coupling, erosion-filtration coupling

Résumé

Les géo-structures telles que les barrages et les digues sont soumises à des écoulements hydrauliques variant dans le temps et dans l'espace. L'eau qui traverse ces milieux poreux peut entraîner le détachement et le transport de certaines particules des sols constituant les structures et leurs fondations. Ce problème est généralement appelé "érosion interne". Le terme suffusion, un type d'érosion interne, se réfère au détachement et au transport de particules les plus fines à travers une matrice de sol poreuse plus grossière en raison d'un écoulement hydraulique. L'évolution temporelle de la suffusion peut modifier les propriétés hydrauliques et mécaniques des sols et peut entraîner des changements importants dans le comportement de telles structures pouvant aller jusqu'à leur effondrement.

Ce travail de thèse tente de contribuer à la conception et à la durabilité des ouvrages en ingénierie géotechnique et hydraulique en mettant un accent particulier sur les barrages, les levées et les digues. Il a été consacré à développer un modèle numérique de suffusion en introduisant d'une part le couplage des phénomènes hydrauliques et mécaniques et d'autre part le couplage des phénomènes d'érosion et de filtration. Pour atteindre cet objectif, ce travail a été divisé en deux parties principales : l'une à l'échelle du laboratoire et l'autre à l'échelle des problèmes aux limites concernant les géo-structures.

Basé sur la théorie des milieux poreux, un nouveau modèle numérique a été formulé pour prendre en compte à la fois l'érosion et la filtration lors de la suffusion. Le modèle a été validé en reproduisant les principales caractéristiques observées lors des tests d'érosion en laboratoire. Étant donné que l'hétérogénéité initiale des échantillons de sol ont été soupçonnés d'avoir un effet significatif dans le processus d'érosion-filtration, des analyses en différence finie aléatoire en 1D et 2D ont été effectuées en appliquant la théorie du champ aléatoire au modèle numérique de suffusion. Des simulations de Monte Carlo ont été réalisées pour étudier l'influence de la variabilité, la longueur de la corrélation spatiale et la corrélation croisée de la porosité initiale et de la teneur initiale en fines sur le taux de masse érodée et la conductivité hydraulique minimale au cours de l'essai. Par la suite, le modèle numérique de suffusion a été amélioré en incluant un modèle constitutif incrémental non linéaire afin de prendre en compte les effets des fines. Une approche numérique a ensuite été développée pour simuler à l'échelle du laboratoire les tests d'érosion sous charge mécanique triaxiale en insistant sur l'évolution de la masse érodée, de la conductivité hydraulique et de la déformation du spécimen pendant et après l'érosion, en conditions triaxiales. Les influences de l'état de contrainte et des états initiaux du sol (densité relative et teneur en fines) sur le processus de suffusion ont été discutées d'un point de vue numérique.

Afin de réaliser des analyses à l'échelle d'une structure, un modèle élastoplastique pour les mélanges sable-silt a été couplé au modèle de suffusion. Le modèle hydromécanique a d'abord été implémenté dans le code commercial aux éléments finis ABAQUS et utilisé pour évaluer l'impact de l'érosion interne sur la stabilité des structures en terre. Après avoir simulé des cas numériques issus de la littérature à des fins de validation, le modèle développé a été appliqué pour simuler la suffusion

induite par des fuites en fond d'une digue sur fondation sous l'hypothèse de déformation plane. L'évolution de la suffusion au sein de la digue a été analysée, ainsi que les effets de l'emplacement de la cavité de fuite, du taux d'érosion et de la teneur en fines. Par la suite, une condition d'écoulement non saturé a été prise en compte et intégrée dans le modèle hydromécanique d'érosion interne afin de décrire plus précisément les infiltrations dans la digue et la fondation induit par la différence de pression d'eau entre les côtés amont et aval de la digue. Le modèle amélioré a été appliqué pour simuler en 3D les conséquences mécaniques de l'érosion interne provoquée par les infiltrations dans la digue et les fuites en fond de fondation. Les influences de la taille de la cavité de fuite et de l'élévation de la hauteur d'eau en amont et en aval de la digue ont été discutées. Les résultats ont montré que deux mécanismes d'endommagement sont possibles : un glissement de la partie aval de la digue et un fontis se développant en partie supérieure de la digue à l'aplomb de la fuite.

Mots clés : érosion interne, suffusion, méthode des éléments finis, teneur en particules fines, couplage hydromécanique, couplage érosion-filtration

Résumé étendu en français

Les géo-structures telles que les barrages et les digues sont soumises à l'écoulement hydraulique variant dans le temps et dans l'espace. L'eau qui traverse ces milieux poreux peut entraîner le détachement et le transport de certaines particules des sols constituant les structures et leurs fondations. Ce problème est généralement appelé érosion interne. Le terme suffusion, un type d'érosion interne, se réfère au détachement et au transport de particules les plus fines à travers une matrice de sol poreuse plus grossière en raison d'un écoulement hydraulique. L'évolution temporelle de la suffusion peut modifier les propriétés hydrauliques et mécaniques des sols et peut entraîner des changements importants dans le comportement de telles structures pouvant aller jusqu'à leur effondrement.

Les recherches expérimentales et numériques portant sur l'érosion interne ont été examinées de manière approfondie au début de cette étude. Les essais en laboratoire et les analyses numériques à l'échelle de l'échantillon jouent sans aucun doute un rôle important dans la pratique de l'ingénierie en déterminant la susceptibilité des matériaux à l'érosion interne et dans la connaissance du mécanisme physique du phénomène d'érosion interne. Cependant, il ne permet pas de déterminer où et quand l'action de l'écoulement hydraulique va déclencher l'instabilité interne du sol granulaire et les réponses mécaniques qui en résultent à l'échelle de toute une structure de géo-ingénierie. Peu de résultats d'essais sur modèles physiques ou d'études numériques de problèmes aux limites à l'échelle des géo-structures sont disponibles dans la littérature.

Objectifs

Ce travail de thèse tente de contribuer à la conception et à la durabilité des ouvrages en ingénierie géotechnique et hydraulique en mettant un accent particulier sur les barrages, les levées et les digues. Il a été consacré à développer un modèle numérique de suffusion en introduisant d'une part le couplage des phénomènes hydrauliques et mécaniques et d'autre part le couplage des phénomènes d'érosion et de filtration. Ceci est réalisé grâce à un modèle d'érosion à quatre constituants, qui est formulé dans le cadre de la théorie du milieu poreux continu.

En implémentant le modèle à quatre constituants dans un code d'éléments finis, nous avons essayé d'améliorer la capacité de prévision de la suffusion dans le sol et de faciliter la détection et l'alerte du dysfonctionnement éventuel des ouvrages hydrauliques, des infrastructures urbaines, des ruptures de pente et des glissements de terrain.

Pour atteindre cet objectif, ce travail a été divisé en deux parties principales :

- A l'échelle du laboratoire

- Formuler un nouveau modèle numérique prenant en compte l'érosion et la filtration dans le cadre de la théorie des milieux poreux continus. Le modèle vise à reproduire les principales caractéristiques observées lors des tests d'érosion en laboratoire.

- Étudier l'influence de la variabilité spatiale du sol (la porosité initiale et la teneur en fines

initiale) sur l'érosion-filtration lors de la suffusion dans des conditions unidimensionnelles (1D) et bidimensionnelles (2D).

- Formuler un modèle numérique pour les tests d'érosion sous charges mécaniques triaxiales afin d'analyser le comportement couplé hydromécanique de sols soumis à l'érosion interne avec comme objectif son application à des fins pratiques.

- A l'échelle des géo-structures

- Implémenter le modèle hydromécanique développé dans un code d'éléments finis.

- Valider le code en simulant des études numériques issues de la littérature.

- Appliquez le modèle numérique pour effectuer des calculs 2D et 3D à l'échelle des géo-structures afin d'évaluer l'impact de l'érosion interne sur les structures en terre.

Les principales contributions et conclusions tirées de cette étude sont résumées ci-dessous, ainsi que des perspectives et des recommandations pour les travaux de recherche futurs.

Modèle numérique considérant l'érosion et la filtration lors de la suffusion dans le cadre de la théorie des milieux poreux continus

Basé sur la théorie des milieux poreux, le milieu poreux saturé est considéré comme un système composé de 4 constituants : le squelette solide, les fines érodables, les particules fluidisées et le fluide. Les fines peuvent se comporter soit comme un matériau semblable à un fluide (décrit comme des particules fluidisées), soit comme un matériau semblable à un solide (décrit comme des fines érodables). L'approche a consisté à modéliser l'érosion du squelette du sol, le transport par le flux d'eau et la filtration de particules fines par échange de masse entre les phases solide et liquide. Les termes d'échange de masse ont été introduits dans les équations du bilan de masse. Ils ont été complétés par un terme de filtration pour simuler le remplissage des vides initiaux dû à la filtration des fines transportées.

Un problème numérique unidimensionnel a été résolu par la méthode des différences finies afin de comparer les résultats numériques avec les mesures expérimentales de deux séries d'essais d'érosion effectués sur des sols sans cohésion. Il a été montré que les résultats numériques correspondent bien aux données expérimentales et que le modèle peut reproduire les principales caractéristiques de l'érosion et de la filtration pendant le processus de suffusion.

Influence de la variabilité spatiale du sol sur l'érosion-filtration pendant la suffusion

Étant donné que l'hétérogénéité initiale de l'échantillon de sol peut avoir un effet significatif dans le processus de l'érosion-filtration, des analyses en différences finies aléatoires en 1D et 2D ont été effectuées en appliquant la théorie du champ aléatoire au modèle numérique de suffusion. Des simulations de Monte Carlo ont été réalisées pour étudier l'influence de la variabilité, la longueur de corrélation spatiale et la corrélation croisée de la porosité initiale (ϕ_0) et de la teneur initiale en fines (f_{c0}) sur le taux de masse érodée et la conductivité hydraulique minimale au cours de l'essai.

Il a été constaté dans les analyses de Monte Carlo 1D qu'une augmentation de la variabilité de ϕ_0 et f_{c0} ou une diminution de la longueur de corrélation spatiale des variables diminuait généralement le taux moyen de masse érodée et la conductivité hydraulique minimale moyenne. Une plus grande variabilité conduit à des changements plus importants de la porosité du sol à l'interface des différentes couches ; les faibles longueurs de corrélation spatiale rendent les couches plus irrégulières, produisant plus d'interfaces entre les couches lâches et denses, facilitant à leur tour la capture des fines particules transportées par le flux d'eau. De plus, même si le comportement de l'échantillon est plus fortement affecté par la variabilité des sols et la corrélation spatiale et un peu moins par la corrélation croisée entre ϕ_0 et f_{c0}, les corrélations négatives entre ϕ_0 et f_{c0} sont plus susceptibles de provoquer un blocage qui peut entraîner une augmentation potentielle de la pression interstitielle et donc une dégradation de la résistance.

Les résultats obtenus lors d'analyses 2D confirment que le flux peut contourner le blocage local. Les taux moyens de masse érodée en condition 2D sont généralement inférieurs à ceux obtenus en condition 1D. De plus, une plus grande probabilité de blocage dans les champs aléatoires isotropes 2D se produit lorsque la longueur de corrélation spatiale est environ la moitié de la longueur de l'échantillon.

Modèle numérique pour les essais d'érosion sous charges mécaniques triaxiales

Le modèle à quatre composantes a été amélioré en incluant un modèle constitutif incrémental non linéaire afin de prendre en compte les effets de l'évolution de la teneur en fines sur le comportement mécanique du sol. Un modèle numérique a ensuite été construit pour simuler les essais d'érosion en laboratoire sous charges mécaniques triaxiales, en mettant l'accent sur l'évolution de la masse érodée, de la conductivité hydraulique et de la déformation de l'échantillon pendant et après l'érosion.

Le modèle numérique a été validé par des simulations du comportement de mélanges HK-CDG (Hong Kong - granite complètement décomposé) avant, pendant et après érosion au cours d'essais triaxiaux. Après une perte significative de particules fines, le comportement contrainte-déformation du sol passe de dilatant à contractant avec une diminution de la résistance au cisaillement. La comparaison entre les résultats expérimentaux et les calculs numériques a montré que le modèle peut bien reproduire l'initiation de l'érosion interne, l'augmentation soudaine du taux d'érosion, l'évolution de la conductivité hydraulique et les déformations de l'échantillon de sol. Les résultats ont confirmé que la déformation était liée au rapport de contrainte sous lequel le processus d'érosion était actif.

Le modèle numérique a ensuite été appliqué pour analyser l'influence de l'état de contrainte et de l'état initial du sol (densité relative et teneur en fines) d'un point de vue numérique. Outre le taux de contrainte, la quantité de perte de particules fines indiquant le passage d'une réponse mécanique stable à une réponse mécanique instable semble être liée à la densité initiale ainsi qu'à la teneur initiale en particules fines du mélange de sol. Ces résultats devraient fournir une inspiration pour la

conception d'expériences futures afin de mieux comprendre la physique de l'érosion interne et son impact sur le comportement du sol.

Impact de la suffusion sur la stabilité de la digue (2D)

Afin de réaliser des analyses à l'échelle des géo-structures, un modèle élastoplastique de mélange sable-silt a été couplé avec le modèle de suffusion à quatre constituants. Le modèle hydromécanique a d'abord été implémenté dans le code d'éléments finis ABAQUS et utilisé pour évaluer l'impact de l'érosion interne sur la stabilité des structures en terre.

Après avoir simulé certains cas numériques issus de la littérature pour validation de l'approche, le modèle développé a été appliqué pour simuler la suffusion induite par une fuite en fond d'une digue sur fondation sous l'hypothèse de déformation plane. Dans cet exemple, la digue a été construite sur une formation d'alluvions sable-silt sur des calcaires karstiques. Un aquifère confiné sous pression est situé sous la couche calcaire. L'eau peut s'élever à l'intérieur des cavité karstiques et atteindre la couche d'alluvions. L'érosion interne peut se produire lorsque le niveau d'eau est différent dans les alluvions et dans l'aquifère confiné. On constate que :

- L'érosion interne a entraîné une augmentation de l'indice des vides dans le sol et une diminution de la teneur en fines, entraînant à leur tour une diminution de la résistance au cisaillement de la zone érodée, évaluée par la loi de comportement du mélange sable-silt.

- Dans ce cas, les résultats numériques ont montré que la déformation de la digue se développait assez lentement lorsque la zone érodée était concentrée dans la fondation. Une déformation mesurable au sein de la digue est apparue lorsque la zone érodée s'est développée en direction de la pente. La déformation a augmenté de façon spectaculaire jusqu'à la rupture soudain de la digue en raison d'un glissement de la pente.

- Effet de la localisation de la cavité : Un tassement important de la digue est observé lorsque la cavité est située sous le sommet de la digue. Lorsque la cavité se déplace vers la surface de la pente, le glissement de la pente commence à apparaître. La simulation se termine par une rupture par glissement. Lorsque la cavité s'éloigne du pied de la pente, l'influence de l'érosion sur la stabilité de la digue diminue rapidement.

- Effet du taux d'érosion : une augmentation du taux d'érosion accélère la rupture de la digue. Pour un taux d'érosion plus élevé, l'évolution du déplacement est plus abrupte lorsqu'on se rapproche de la rupture.

- Effet de la teneur en fines : Selon les résultats d'une série de simulations avec différentes teneurs en fines initiales f_{c0}, il semble raisonnable de considérer l'existence d'un minimum f_{c0}, au-delà duquel la dégradation causée par l'érosion interne est cruciale. Dans cette analyse, la digue a atteint la rupture subitement pendant le processus d'érosion pour les cas $f_{c0} = 0.5$, 0.45, 0.4 et 0.35, alors que pour le cas $f_{c0} = 0.3$ la déformation de la digue s'est développée progressivement. Pour les cas $f_{c0} = 0.25$ et 0.2, la déformation de la digue

soumise à l'érosion est très faible.

Conséquences mécaniques de l'érosion interne de la digue pour différentes conditions aux limites en 3D

L'influence de conditions tridimensionnelles en chargements hydrauliques et mécaniques est soupçonnée d'avoir un effet significatif sur le processus d'érosion interne. Malheureusement, les outils de modélisation n'étaient pas largement disponibles pour permettre une analyse plus approfondie de ces effets 3D à l'échelle de la structure. Notre objectif était de simuler les effets 3D de l'érosion interne dans une digue linéaire sur une fondation qui retient l'eau dans des conditions initiales et aux limites plus générales et plus réalistes. Tout d'abord, une condition d'écoulement non saturé a été prise en compte et intégrée dans le modèle hydromécanique d'érosion interne afin de décrire plus précisément les infiltrations dans la digue et la fondation induites par la différence de pression d'eau entre les côtés amont et aval de la digue. Le modèle amélioré a été appliqué pour simuler les conséquences mécaniques 3D de l'érosion interne provoquée par les infiltrations dans la digue et les fuites au fond de la fondation. Les influences de la taille de la cavité de fuite et de l'élévation de la hauteur d'eau en amont et en aval de la digue ont été analysées. On constate que :

- La perte continue de particules fines en aval de la digue et de la fondation peut entraîner la rupture de la digue. Dans ce cas, la perte de fines près du pied de la digue peut stimuler le glissement global de la digue.

- L'augmentation du niveau d'eau dans la fondation en aval augmente les risques de rupture globale de la digue.

- La présence d'une cavité de fuite au-dessous de la digue peut entraîner l'apparition d'un fontis qui se forme en raison de la déformation du sol au-dessus de la zone érodée à proximité de la cavité de fuite.

- Il a été observé que l'emplacement du fontis est étroitement lié à l'emplacement de la surface phréatique.

Perspectives

Cette recherche a développé un modèle de suffusion à l'échelle des géo-structures pour faciliter la détermination de comment, où et quand l'action du flux d'infiltration peut déclencher l'instabilité interne d'un sol granulaire et les réponses mécaniques qui en résultent. Elle pourrait être appliquée pour analyser l'influence de la suffusion sur les ouvrages hydrauliques (barrages, digues, etc.), les infrastructures urbaines (pipelines, tunnels, etc.), les ruptures de pente et les glissements de terrain.

Les analyses de la suffusion dans la digue ont été données à titre d'exemple dans cette recherche. Cependant, il convient de noter que ces analyses ont été effectuées avec une charge d'eau constante. Les matériaux de la digue et de la fondation sont supposés être initialement homogènes. Dans la nature, la hauteur d'eau peut varier, lentement ou rapidement, en raison des pluies ou des activités humaines. Le trajet d'infiltration et l'emplacement de la surface de la nappe phréatique peuvent être

plus complexes et évoluer dans le temps, ce qui augmentera l'incertitude de la localisation du fontis. Ces aspects pourraient être pris en compte dans les travaux futurs pour des études de cas réels.

Dans ce qui suit, les recommandations pour les futurs travaux de recherche sont présentées, qui concerne à la fois les aspects expérimentaux et numériques.

- Des tests de laboratoire plus avancés sont nécessaires pour identifier les facteurs d'influence de la suffusion et pour saisir l'impact de l'érosion interne sur le comportement mécanique du sol. Idéalement, la conception de l'appareil d'essai d'érosion devrait prendre en compte les mesures de déformation de l'échantillon, de sa perte de masse et de l'évolution de la conductivité hydraulique le long de l'échantillon afin de faire progresser les efforts de modélisation.

- La physique du phénomène de suffusion demande à être approfondie car les résultats expérimentaux dans la littérature présentent des contradictions. D'une part, la préparation de l'échantillon pourrait introduire des perturbations significatives dans l'échantillon; d'autre part, des observations microscopiques en temps réel du sol érodé sont nécessaires pour mieux comprendre le comportement hydromécanique de ces sols.

- Prenant avantage de l'approche discrète (DEM) permettant de mieux prendre en compte et de comprendre le comportement du matériau à l'échelle du grain, une alternative aux études expérimentales peut consister à développer un outil numérique couplé hydromécanique en utilisant l'approche discrète (DEM-CFD, DEM-LBM, DEM-PFV, etc.). Il permet de visualiser la migration des particules à l'échelle du grain et de réaliser des études paramétriques à un coût relativement faible.

- Développer une approche de modélisation multi-échelle et multi-physique dans le cadre de la théorie des milieux continus, dans laquelle l'échelle multi-échelle désigne un modèle basé sur la micromécanique.

Chapter 1 Introduction

1.1. Background

Internal erosion occurs when fine particles are plucked off by hydraulic forces and transported or advected by the fluid within the porous network. The known mechanisms are either a concentration of leak erosion, or backward erosion, or soil contact erosion, or suffusion [1-3]. The term internal stability has been use to describe how a granular material manages to prevent the loss of its own fine particles when disturbing agents such as seepage forces come into play [4]. The focus of this thesis is suffusion, which corresponds to the detachment and migration of fine particles within the voids between the coarse particles due to seepage flow.

From an engineering point of view [4], the granular material is composed of a primary particle fabric and of loose particles. The primary particle fabric supports the imposed forces. These particles can be considered as fixed. Within the pores of the primary fabric there are loose and erodible fine particles which can be displaced by water flow. In a gap graded soil, usually composed of two grain sizes, the fines correspond to the smaller grains, as shown in Figure 1.1. In a broadly graded soil, the fines (f_c) can be defined according to the grain size distribution curve of the granular material, as follows [5]:

$$f_c \leq \frac{e_p\left(1-n_1\right)}{1+e_p\left(1-n_1\right)} \quad\text{...}(1.1)$$

where e_p is the void ratio of the primary fabric, n_1 is the average porosity of the loose particles within the pore space of the primary fabric.
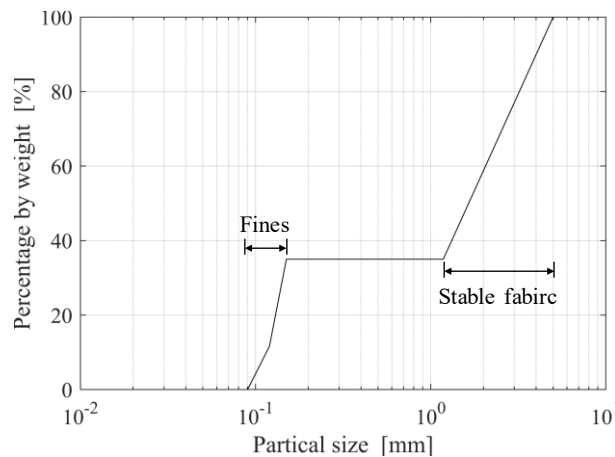
Figure 1.1 Grain size distribution of the HK-CDG soil mixture (Chang & Zhang [5])

Any change of the soil microstructure induced by the loss of fine particles may also modify the soil behavior and induce deformations at the macroscopic scale. Internal erosion can be the cause of many damages, failures or entire collapse of embankment dams [2, 6-9]. Foster & Fell [10] showed that 46% of the damages in 128 embankment dams investigated could be attributed to internal erosion. Besides, internal erosion can also trigger sinkholes and cavities as frequently observed

within dams and dikes [11, 12], as well as slope failures or instability and significant landslides [13, 14].

To evaluate the internal instability of granular materials in embankment dams, engineers have traditionally employed empirical methods [4, 15-21]. For instance, Rönnqvist et al. [9] compiled a database of 80 dams of which 23 suffered from documented internal erosion. A gradation analysis demonstrated that empirical methods could distinguish which dams were most prone of erosion from dams which did not indicate any internal erosion. Laboratory tests, by using primarily the conventional rigid-walled permeameter under self-weight condition [4, 12, 21-24], also investigated the mechanics of internal erosion and the seepage induced internal instability affecting the soils. The eroded mass, the hydraulic gradient and the flow rate were monitored to determine the likehood of seepage induced instability by incorporating the post-erosion analysis of the particle size distribution. The initial fines content and the history of the hydraulic loading appeared to play an important role in the development of internal erosion [23, 24]. Here it is important to add that the soils constituting embankment dams or levees are usually subjected to complex stress states [25]. To address this phenomenon, Moffat et al. [26, 27] developed a rigid-wall permeameter with an axial loading system so that the onset of internal instability of cohesionless soils under K_0 stress state could be verified. More recently, advanced flexible wall permeameters capable of controlling the stresses on the tested specimen have been designed so that the development of internal erosion under different stress states and the mechanical behavior of soils during and after erosion could be investigated [5, 28-31]. Most of the studies were conducted under an initial isotropic stress state. The results showed that the larger effective confining pressure led to a lesser extent of internal erosion [28, 32], even if the deformation of the specimen was limited. Chang &Zhang [5] showed that, by performing internal erosion tests under different anisotropic stress states, the maximum erosion rate, the variations in soil permeability, and the erosion induced deformation of the specimen all increased with the deviatoric stress. To investigate the influence of the loss of fine particles on the mechanical behavior of eroded soils, they performed triaxial tests on eroded specimens under different stress paths. Drained triaxial tests on eroded specimens indicated that the initially dilative behavior changed to a contractive behavior and the soil strength decreased under drained shearing [5, 30, 33, 34]. The undrained behavior of the original specimen changed from strain hardening behavior to a flow-type behavior with limited deformation after internal erosion [32, 35].

Parallel to experimental studies, numerical approaches have also described the erosion process, either within the framework of continuum mechanics with finite element or finite difference methods [36-40], or within a discrete framework by coupling the discrete element method to describe the dynamics of the granular solid phase to the fluid dynamics to solve the interstitial fluid flow [41-47]. These studies focused mainly on the hydraulic process, i.e. the evolution of the eroded mass and permeability. The mechanical part was simplified through an elastic model with damage parameters. Some attempts to model the mechanical response to internal erosion removed particles in granular materials. Muir Wood et al. [48] modeled the mechanical consequences of internal

erosion by a two-dimensional discrete element analysis and found that internal erosion changed the density state of the material from dense to loose as the current soil state was compared to the critical state line. Scholtès et al. [49] developed a three-dimensional discrete element model and an analytical micromechanical model to describe the mechanical responses induced by particle removal in granular materials. They also found that with the removal of soil particles the mechanical behavior of the soil changed from dilative to contractive. However, this removal was based on the size of the particles and the level of interlocking, and the fluid phase was not considered. Hosn et al. [50] studied the macroscopic response during internal erosion and the post-internal erosion properties of granular materials by particle removal, considering one-way coupling between the fluid and the solid phases via the discrete element and the pore scale finite volume methods. The erosion process, based on the definition of the detached and transportable particles, computed the unbalanced fluid forces and defined a controlling value of the constriction size of the connecting sections between pores. Hicher [51] presented a numerical method to predict the mechanical behavior of granular materials subjected to particle removal and concluded that the removal of soil particles may cause diffuse failure in eroded soil masses. He did not, however, consider the process of real erosion. It is therefore highly interesting to develop a numerical method that will provide the modeling of the hydro-mechanical response of soils subjected to internal erosion.

Even though the discrete element method has proved its efficiency in explaining the constitutive properties of granular materials, its prohibitive computational cost becomes an obstacle whenever real soil structures such as embankment dams are concerned. Hence, it is necessary to develop an approach that can better account for engineering boundary value problems at a real space scale.

1.2. Research objectives

The aim of this research is to contribute to the fields of geotechnical and hydraulic engineering, with a special place for sustainability in geotechnical engineering and a particular focus on embankment dams, levees, and dikes. The aim of this thesis is to develop a methodology to model the suffusion mechanism by introducing the coupling of hydraulic and mechanical phenomena, on the one hand, and the coupling of erosion and filtration, on the other hand, into a four-phase erosion model within the framework of the porous continuous medium theory. In conjunction with efficient finite element implementation and simulations, it is important to improve the predictive analysis of soil suffusion and to facilitate reliable detection and early warning of the eventual dysfunction of hydraulic structures, urban infrastructures, slope failures, and landslides.

For this purpose, the objectives of the theses are outlined below:

1) Formulating a new numerical model by considering both erosion and filtration in suffusion under the framework of the porous and continuous medium theory. The mathematical coupling formulations will be solved numerically and validated by simulating internal erosion tests to demonstrate that the model can reproduce the main features of both erosion and filtration during the

suffusion process. The influence of the coupling between erosion and filtration will be further studied.

2) Discussing the influence of the soil spatial variability of the initial porosity and fines content on clogging during suffusion. The random field theory will be implemented within the model for performing Monte Carlo analyses under one-dimensional (1D) and two-dimensional (2D) conditions to study the influence of the soil heterogeneity on suffusion and to perform a systematic probabilistic study of suffusion.

3) Analyzing the hydro-mechanical behavior of soils subjected to internal erosion. The erosion model will be coupled with an advanced constitutive model [52, 53], which has been enhanced to consider the effects of the loss of fines content. The applicability of the hydro-mechanical model to suffusion will be validated by simulating laboratory erosion tests under triaxial mechanical loadings, with a special emphasis on the evolution of the eroded mass, the hydraulic conductivity, the deformation of the specimen during the erosion tests and the stress-strain behavior under triaxial loadings of the specimen after erosion.

4) Implementing the developed hydro-mechanical model into a finite element code. The programme will be validated by simulating numerical studies collected from literature and then be applied to perform analyses at the space scale of an entire engineering structure to assess how internal erosion can impact earthen structures.

1.3. Thesis outline

The body of this thesis is divided into 8 chapters. A brief description of each chapter is provided below:

Chapter 1: Introduction

Chapter 1 consists of an introduction of the present research study. It begins with the definition of internal erosion and its consequences on earthen structures. It continues with the presentation of commonly used methods to assess the potential of internal instability, as well as a short discussion of the shortcomings of current researches, the objectives of our study, and finally, the outlines of this study.

Chapter 2: Literature Review

A critical literature review in terms of experimental and computational investigations on internal erosion is provided. It begins with a brief and not exhaustive description of different mechanisms of internal erosion. Then, the experimental process and the results of laboratory tests, physical model tests and computational analyses are reviewed. Furthermore, the key parameters controlling the onset and evolution of internal erosion and the mechanical responses of eroded soils are discussed.

Chapter 3: Modeling coupled erosion and filtration of fine particles in granular media

This chapter attempts to propose a new numerical model considering both erosion and filtration in suffusion under the framework of the porous continuous medium theory. First, a four-constituent

based mass exchange formulation is proposed to describe the detachment of finer particles and the clogging of initial voids. The coupling formulations are solved numerically using the finite difference method. Then, the model is validated by simulating 1-D internal erosion tests and demonstrating that it is able to reproduce the main features of both erosion and filtration during the suffusion process. The influence of the coupling between erosion and filtration is further studied.

Chapter 4: Analysis of suffusion in cohesionless soils with randomly distributed porosity and fines content

In this chapter, a random field theory is used with a finite difference method in order to investigate the soil suffusion with a randomly distributed initial porosity and fines content. A probabilistic study using the Monte Carlo method is conducted to analyze the effect of the variance, the spatial correlation length, and the cross correlation of the randomly distributed initial porosity and fines content on the eroded mass and on the evolution of the hydraulic conductivity under 1D and 2D conditions. All the simulations permit to quantify the probability of particles blockage during erosion.

Chapter 5: Hydro-mechanical modeling of granular soils considering internal erosion

In this chapter, we formulate a coupled hydro-mechanical model in the framework of continuum mechanics to evaluate the phenomenon of internal erosion and its consequences on the mechanical behavior of soils. The four-constituent numerical approach is extended through the stress-strain relationship of the soil mixture, represented by a non-linear incremental constitutive model. Based on experimental data, this constitutive model is enhanced by the introduction of a fines content dependent critical state, which allows us to take into account the influence of fines on soil deformation, behavior and strength. A practical simulation platform is then formulated at the scale of the representative elementary volume to simulate the downward erosion tests under triaxial mechanical loadings. It is validated by comparing numerical and experimental results of internal erosion tests on HK-CDG soil mixtures, with special emphasis on the evolution of the eroded mass, the hydraulic conductivity, the deformation of the specimen during the erosion test, and the stress-strain behavior under triaxial loading after erosion. Furthermore, the influence of the stress state, the initial soil density, and the initial fraction of fines are analyzed through numerical simulations using the proposed modeling platform.

Chapter 6: Internal erosion in dike-on-foundation modeled by a coupled hydro-mechanical approach

In this chapter, a more general elasto-plastic sand-silt mixture model is introduced into the four-constituent model of internal erosion in order to perform analyses at the space scale of an entire engineering structure. The hydro-mechanical model is solved using finite element method in order to assess how internal erosion impacts the safety of earthen structures. After having simulated some numerical cases issued from the literature, the developed program is applied to the specific case study of a dike-on-foundation subjected to internal erosion induced by the presence of a karstic

cavity beneath the alluvium layer under plain strain condition. The numerical results show the onset of erosion, the time-space evolution of the eroded zone, and the hydro-mechanical response of the soil constituting the dike. All these results highlight the effects of the cavity location, the erosion rate, and the fines content.

Chapter 7: 3D modeling of the internal erosion in dike-on-foundation

This chapter aims to simulate the 3-D effects of internal erosion within a linear dike on a foundation under more general and realistic conditions. Firstly, the unsaturated flow condition is implemented into the hydro-mechanical model of internal erosion in order to describe more accurately the seepage within the dike and the foundation due to the difference in water head at the upstream and downstream sides of the dike-on-foundation. Afterwards, the enhanced model is applied to simulate the effect of internal erosion induced by the seepage within the dike and the leakage at the bottom of the foundation under 3-dimensional condition. The influence of the size of the leakage cavity and the elevation of the water level at the upstream and downstream sides of the dike-on-foundation is discussed.

Chapter 8: Conclusion and perspectives

Chapter 8 is the summary of this research study. Achievements and findings are emphasized in this chapter in order to demonstrate the ability of the approach for engineering practices. Finally, suggestions are made for future research works.

Chapter 2   Literature review

This chapter attempts to provide a critical literature review of internal erosion in soils with a special emphasis on suffusion. It begins with a presentation of the different mechanisms of internal erosion in Section 2.1, including the concentrated leak erosion, the backward erosion, the contact erosion and the suffusion. Then, experimental and computational approaches of suffusion are reviewed in Section 2.2 and Section 2.3, respectively. From the results of these experimental and numerical studies, the key parameters of the onset and evolution of internal erosion are summarized in Section 2.4, including geometric, hydraulic, and mechanical conditions. Due to the loss of fine particles, the mechanical behavior of the soil is modified. Thus, Section 2.5 discusses the mechanical responses of eroded soils. Finally, a review of the main results is given in Section 2.6.

2.1. Internal erosion mechanisms - overview and description

Different definitions of the term internal erosion can be found in the literature [12, 54-56]. In this work the adopted definition is the one proposed by the U.S. Army Corps of Engineers (USACE) [54] for which internal erosion can be divided into four main mechanisms described below.

2.1.1. Concentrated leak erosion

Openings or cracks may exist in plastic soils, unsaturated silt, silty sand and silty sandy gravel due to differential settlement during the dam construction due to poorly compacted soil, or in operation, such as desiccation, frost action, and/or hydraulic fracture due to low stresses around conduits. The hydraulic forces induced by the water flowing through cracks and openings erode the soil along the walls of those openings (Figure 2.1). This type of erosion is known as concentrated leaks. It may also occur in a continuous zone containing coarse and/or poorly compacted materials which form an interconnected void system. The concentration of the flow can cause the erosion of the interconnected voids.

2.1.2. Backward Erosion

Backward erosion involves the detachment of soil particles when the seepage flow exits a free unfiltered surface, such as the downstream ground surface of a soil foundation or the downstream face of an embankment. The detached particles are carried away by the seepage flow and the erosion works its way towards the upstream side of the embankment or the foundation until a continuous pipe is formed, as shown in Figure 2.2. Backward erosion piping manifests itself often by the presence of sand boils. In addition to the backward erosion piping, the failure or collapse of the soil above or around the piping is defined as global backward erosion [56]. Sinkholes or near vertical cavities are formed if this collapse progresses upwards. This may result in sub-vertical sinkholes or sloughing and unravelling in the downstream face [56].

2.1.3. Contact Erosion

Contact erosion involves the selective erosion of fine particles at the contact with a coarser layer caused by the water flow through this coarse layer (e.g., the contact between silt- and gravel-sized

7

particles). It relates only to conditions where the flow in the coarse layer is parallel to the interface between the coarse and fine layers, as shown in Figure 2.3.

2.1.4. Suffusion

Suffusion involves the selective erosion of finer particles from the matrix of coarser particles within an internally unstable soil. The finer particles are transported by the seepage flow through the voids between the larger particles, leaving behind a soil skeleton formed only by the coarser particles, as shown in Figure 2.4.

In previous studies, different terms have been used to define the phenomenon of the detachment of finer particles from the matrix of coarser particles and their transport or advection within the voids of coarse particles by seepage flow. These terms include "suffusion", "suffosion"," internal segregation" and "internal instability" [4, 18, 22, 27, 28, 55, 57, 58]. Fannin and Slangen [59] made a distinction between a washed-out soil structure that remains intact and one in which some form of destruction or collapse of the structure is induced by the migration of the fine particles. With suffusion there is typically little or no volume change. The term suffosion involves the creation of an instable state whereby the transport of fine particles by seepage flow is accompanied by a volume change of the soil because the coarser particles are not in point-to-point contact.

The focus of this thesis is the analysis of the influence of the migration of fines and the induced mechanical response of the soil on the stability of the hydraulic structures. No distinction is made between suffusion and suffosion. The term suffusion is used in this work to describe the detachment and transport of fine particles with or without volume change and deformation of the solid skeleton.
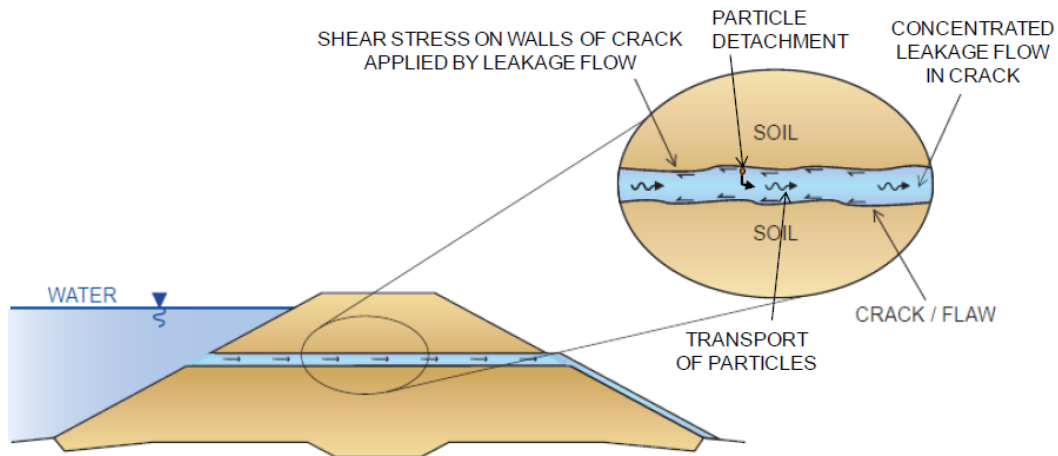
Figure 2.1 Concentrated Leak Erosion (after USACE [54])
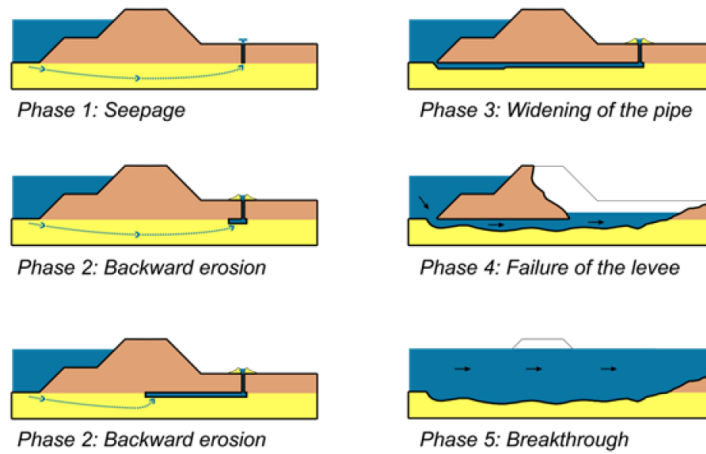
Figure 2.2 Backward Erosion Piping (after USACE [54], adapted from van Beek et al. [60])
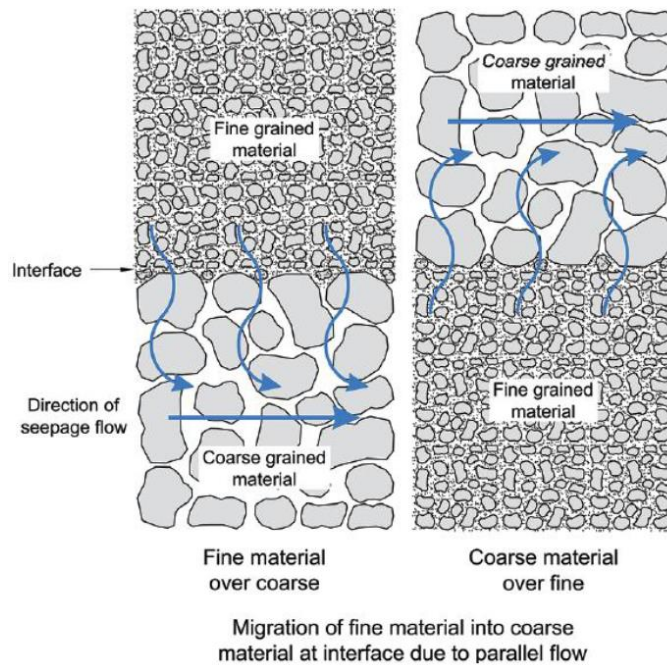
Figure 2.3 Contact Erosion Process (after USACE [54], adapted from International Levee Handbook [61])
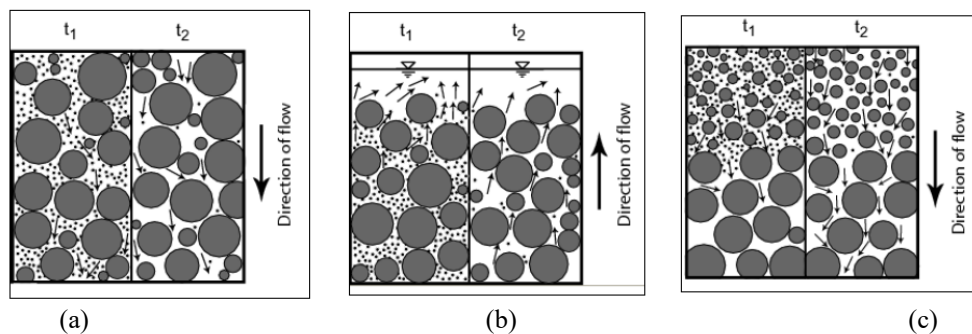
Figure 2.4 Internal Instability (Suffusion) for time steps t_1 and t_2: (a) internal suffusion; (b) external suffusion; (c) contact suffusion (after USACE [54], adapted from Ziems [62])

9

2.2. Experimental analyses of suffusion

2.2.1. Laboratory experiments

Experimental studies have been carried out during these last decades to obtain a better knowledge of the mechanisms of inception and time evolution of suffusion. The mechanism of suffusion and the susceptibility of soil to internal instability have been studied by using primarily the permeameter under self-weight (gravity load) condition. Fannin et al. [63] divided the laboratory tests on the soil susceptibility to suffusion into three generations.

(1) The first generation

The soil susceptibility to seepage-induced internal erosion was first tested in simple rigid wall permeameters with limited control of the seepage flow. The susceptibility was determined based on the loss of solid mass and on the post-erosion analysis of the particle size distribution without any measurement of the flux, the pore water pressure or the specimen deformation.

Following the basic experimental approach used by the U.S Army Corps of Engineers) [64], Kenney et al. [65] carried out dry-vibration and hydraulic filter tests under a downward seepage flow. They concluded that the controlling value of the constriction size, the narrow connecting sections between the pores through which the fine particles can be transported by the water flow, is largely independent of the shape of the filter's grain size distribution and thickness and can be related to the size of the fine particles. Kenney and Lau [4] examined the internal stability of coarse-grained cohesionless soils under a downward seepage flow using two sizes of permeameter cells (Figure 2.5). Based on the test results, they suggested that a soil can be classified as internally stable if $(H/F)_{min} \geq 1$, where F is the mass fraction of grains smaller than the particle diameter D, and H is the mass fraction of grains with a diameter in the interval D to $4D$.
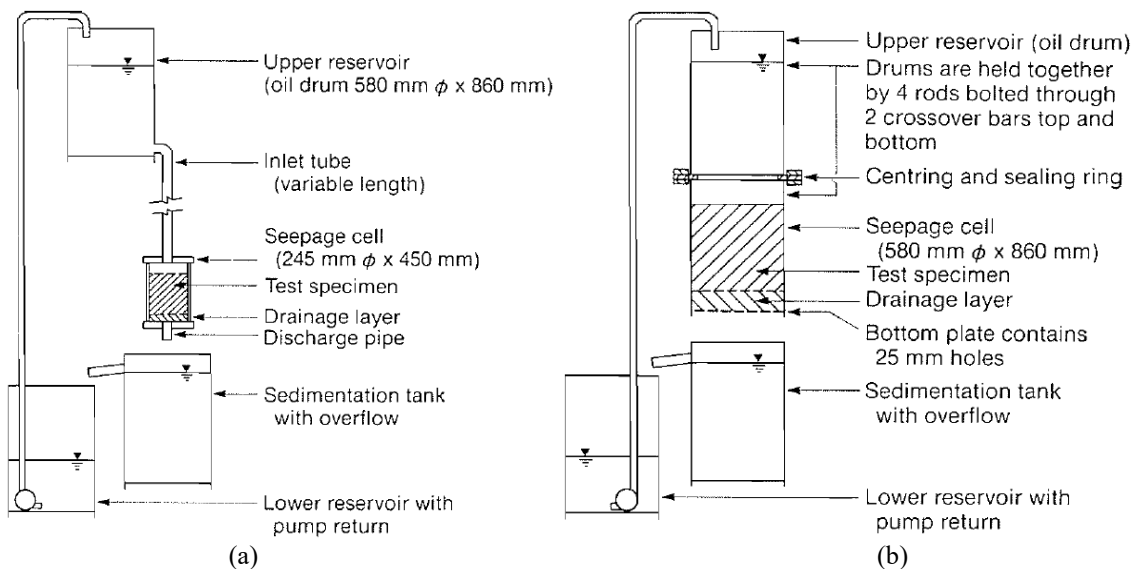
Figure 2.5 Test apparatus (Kenney and Lau, 1985): (a) 245 mm diameter seepage cell; (b) 580 mm diameter seepage cell

(2) The second generation

The second-generation of erosion tests included improved seepage control systems within the rigid wall permeameters, combined with the measurement of the mass loss, the flow rate which allowed for the determination of the hydraulic conductivity, and the post-erosion particle size distribution to determine the susceptibility of seepage-induced instability. In some tests the pore water pressure distribution was monitored by standpipes. In most of these studies, no vertical mechanical load was applied to the soil specimen.

For instance, Lafleur et al. [66] carried out filter tests on broadly graded and gap-graded spherical glass bead mixtures to study the filtration potential and the onset of suffusion in cohesionless soil. The tests were performed within a cylindrical permeameter cell subjected to a downward flow. The amount of soil lost was measured and the pore water pressure distribution was monitored by an array of piezometer tubes (Figure 2.6). They found that the self-filtration of broadly graded soils was related to the broadness coefficient and the profile of the gradation curve. Skempton and Brogan [22] carried out erosion tests on sandy gravel soils under upward seepage flow within a rigid cell. The water discharge was measured during the test, as well as the pore pressure along the specimen. Fine particles washed out of the sample were collected, dried and weighted after the tests. The objective was to determine a critical hydraulic gradient corresponding to the onset of piping.

Based on a similar experimental setup, Sterpi [12] carried out erosion tests on a reconstituted well graded silt-sand-gravel soil under an upward hydraulic loading. Changes of the soil hydraulic conductivity were evaluated by the measured water discharge and the hydraulic gradient. A relationship between the weight of the eroded fine particles, the hydraulic gradient and the time was proposed to model the erosion and transport of fine particles. This relationship was based on a single governing equation of the mass balance of the displaced particles. Following the method adopted by Sterpi [12], Cividini et al. [67] developed an experimental setup for erosion test. It consisted of four cylindrical permeameters (one of them is shown in Figure 2.7) with an internal diameter of 8 cm. Erosion tests were carried out on a reconstituted broadly graded soil under an upward seepage flow at constant water head to analyze the possible induced settlements of the buildings in the vicinity of pumping wells. Based on the experimental data, an incremental erosion law was proposed and introduced in numerical analyses.

With the second generation of permeameters, several factors influencing the soil susceptibility to internal erosion have been studied. Ke & Takahashi [68] performed a series of one-dimensional upward seepage tests on gap-graded soils at constant water head to investigate the hydraulic conditions which can trigger internal erosion, with reference to the influence of the fine particle content, the relative density and the imposed hydraulic gradient (Figure 2.8). Rochim et al. [24] carried out a series of downward seepage flow tests on four gap-graded cohesionless soils (Figure 2.9). The results demonstrated that the critical hydraulic gradient was significantly affected by the hydraulic loading history.
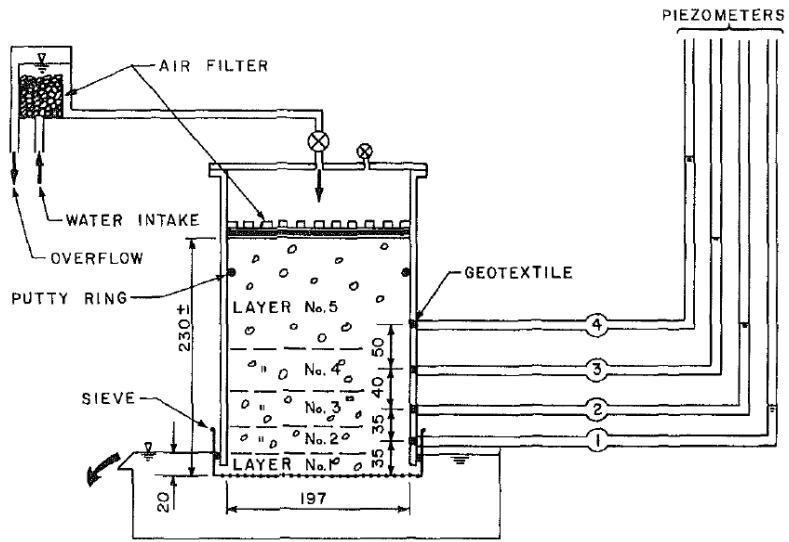
Figure 2.6 Permeameter according to Lafleur et al. [66]
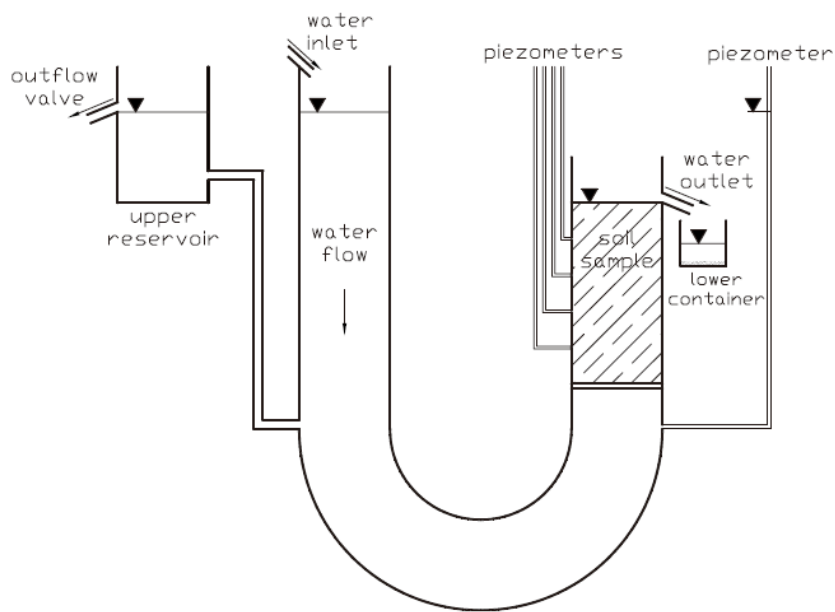
Figure 2.7 Scheme of the experimental setup for the erosion tests according to Cividini et al. [67]
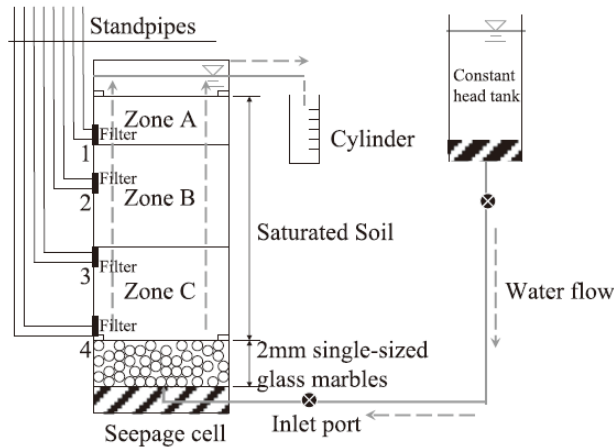
Figure 2.8 seepage test assembly according to Ke & Takahashi [68]
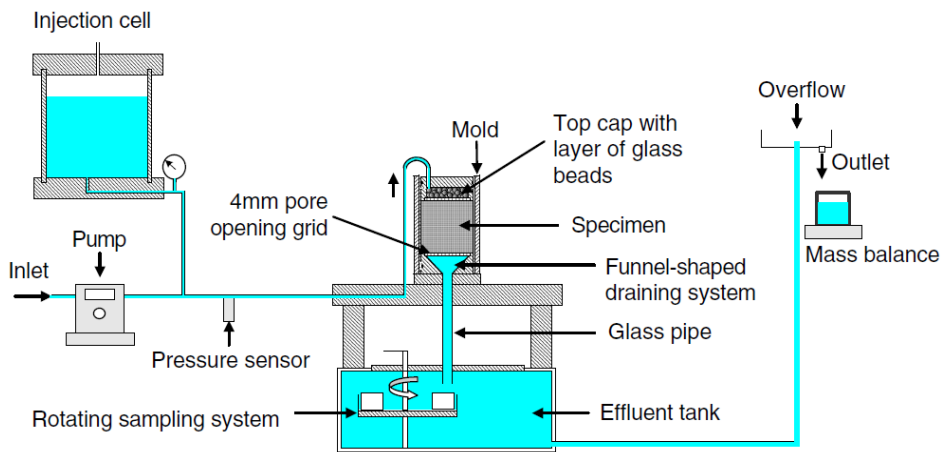
Figure 2.9 experimental bench according to Rochim et al. [24]

(3) The third generation:

The third and most recent generation of permeameters incorporated a loading system in order to control the effective stress applied on the specimens. It includes the rigid-wall permeameters with an axial loading system and the flexible-wall permeameters with a triaxial loading system. For the purpose of analyzing the conditions for the onset of instability, the hydraulic gradient, the flow rate and the eroded mass were monitored, as well as the deformation of the specimens.

Moffat & Fannin [26] modified a permeameter cell to test cohesionless granular soils subjected to a downward hydraulic flow. The device consisted of a permeameter cell, an axial loading system, a hydraulic control system, a collecting system, and a data acquisition system (Figure 2.10). It was able to measure the axial load at both the top and the bottom of the specimen. Furthermore, the measurement of the pore water pressure along the specimen with two arrays of transducers made it possible to measure the onset of failure which is mainly localized within the specimen. This apparatus was also used by Moffat & Fannin [69] and Moffat et al. [27] to analyze the development of suffusion under different vertical mechanical loads. Similarly, Sail et al. [70] developed a "large" oedo-permeameter composed of an oedo-permeameter cell with a collecting system, an axial

loading system, a hydraulic control system and a gamma densitometric system. The wall of the oedo-permeameter cell was equipped by twelve pressure ports to monitor the pore water pressure along the specimen length. The gamma densitometric system comprising a radioactive gamma-ray source and a scintillation counter on the opposite cell side made it possible to calculate the density in different parts of the specimen.

Bendahmane et al. [71] developed an experimental device based on a classical triaxial apparatus to investigate the initiation of internal erosion within a sand-kaolin mixture. The experimental device was composed of three modified triaxial cells coupled with two pressure/volume controllers (GDS). This apparatus was also used by Bendahmane et al. [28], Marot et al. [72] and Nguyen et al. [73] to investigate the influence of key parameters, such as the hydraulic load, the initial fines content, the confining pressure, the angularity of coarse particles, etc… on the mechanism of erosion. This apparatus was lately used to develop a new interpretative method by Marot et al. [29] to determine the suffusion susceptibility of cohesionless soils and clayey sand based on the eroded mass and the energy dissipated by the fluid flow.

Chang and Zhang [5] developed a stress-controlled erosion apparatus able to apply different effective stress paths during erosion and post-erosion (Figure 2.12). A series of tests was conducted on a gap-graded soil under the same confining stress but different deviatoric stresses. A similar apparatus was developed by Ke and Takahashi [30, 33, 34] who modified a triaxial chamber to conduct all the test phases, including saturation, consolidation, erosion and shearing in a triaxial cell (Figure 2.13). The developed apparatus was applied to investigate the drained and undrained behavior of a gap-graded soil with various fine contents under different confining pressures and under monotonic and cyclic loadings pre- and post-erosion.
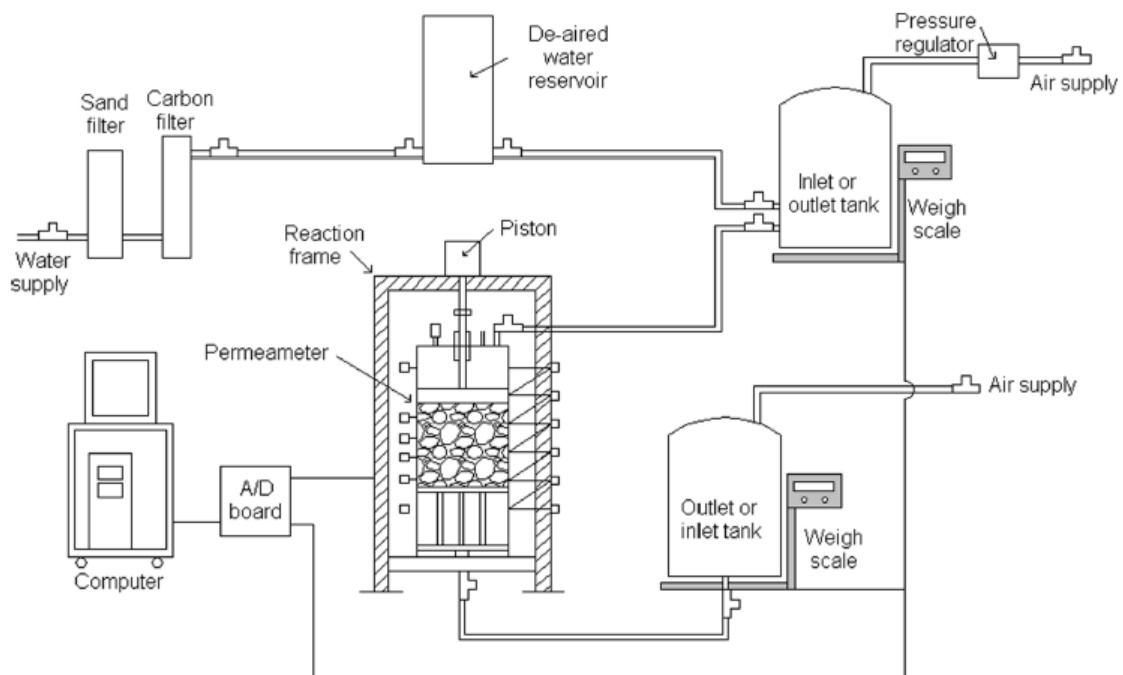
Figure 2.10 scheme of the permeameter according to Moffat & Fannin [26]
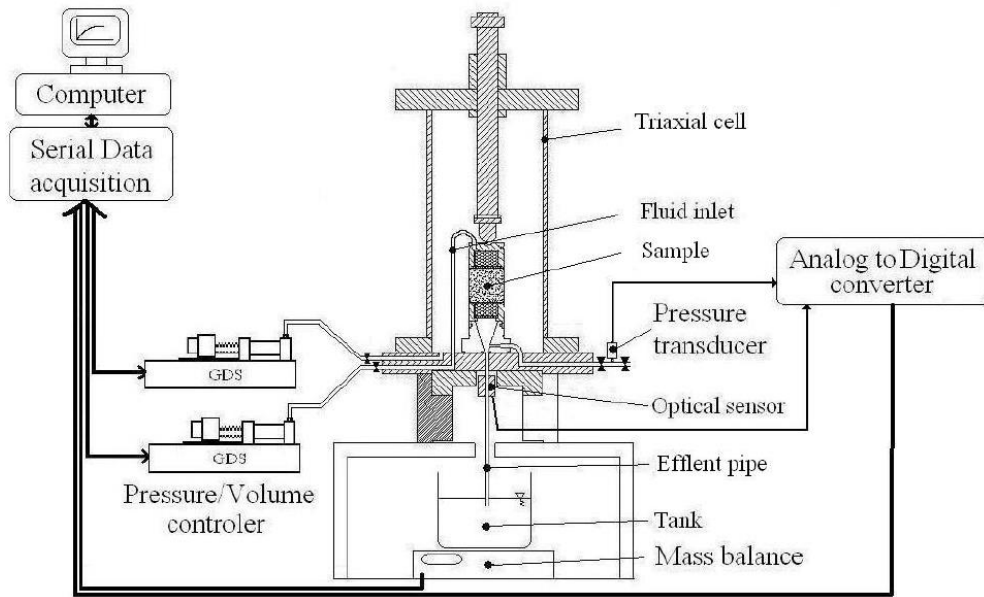
Figure 2.11 Scheme of the permeameter according to Bendahmane et al. [71]
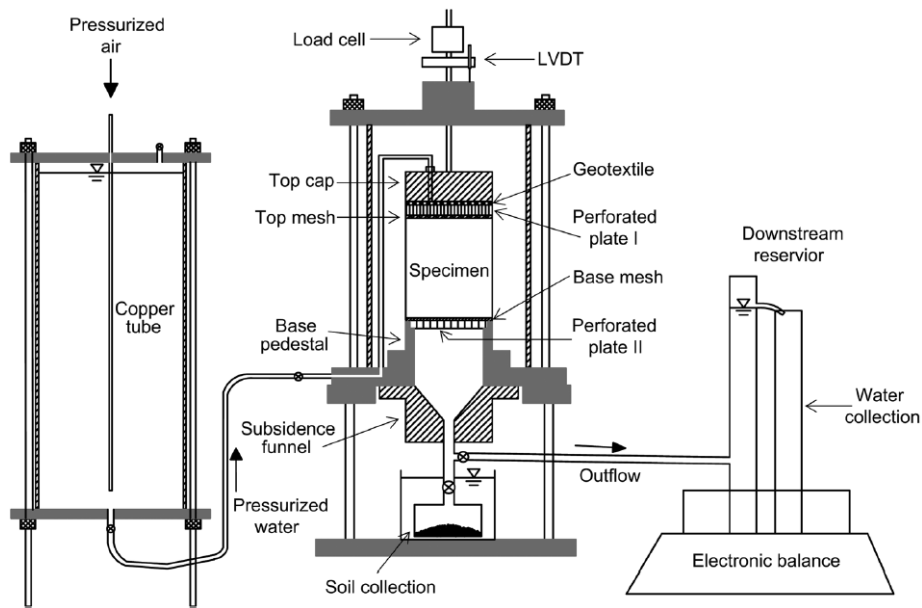
Figure 2.12 stress-controlled erosion apparatus according to Chang and Zhang [74]
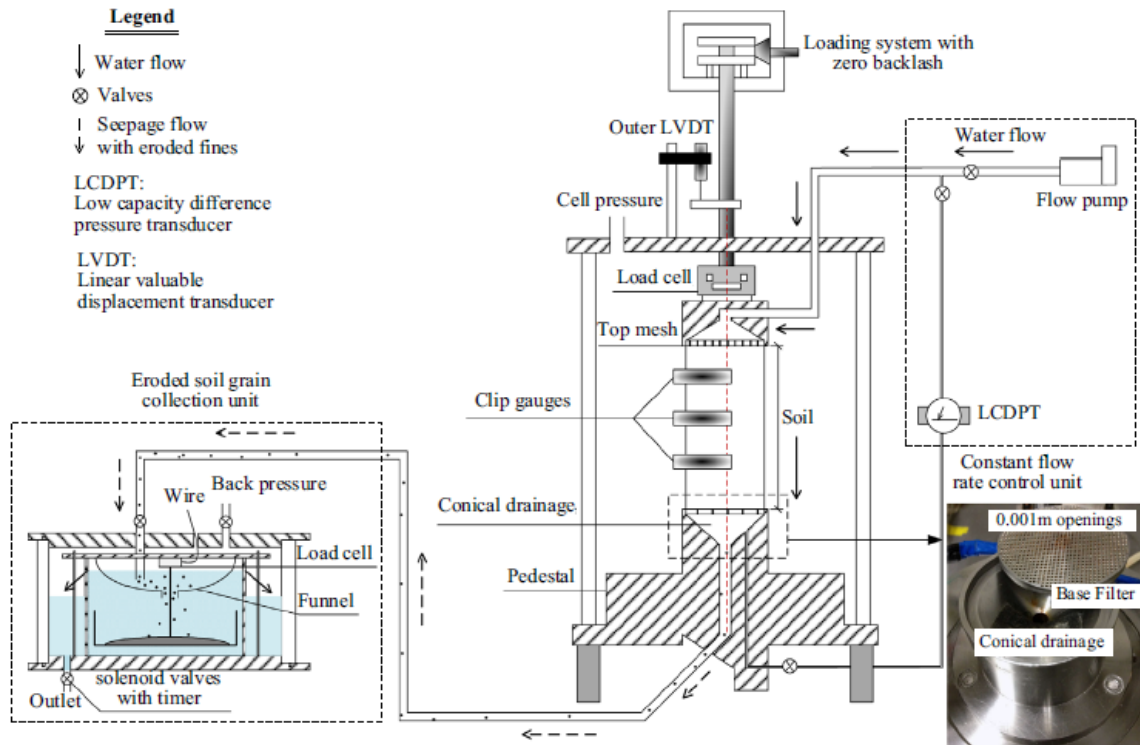
Figure 2.13 erosion apparatus according to Ke & Takahashi [33]

The impact of internal erosion on the soil strength has been investigated by comparing the mechanical behavior before and after erosion. However, the results obtained are somehow contradictory (see section 2.5 for details). An explanation of these contradictions might be attributed to the fact that the rearrangement of coarse and fine grains in the course of erosion leads to a heterogeneous soil structure which needs to be examined by monitoring the microstructural changes. Nguyen et al. [75] applied the X-ray computed tomography (X-ray CT) to study the induced microstructural changes of a granular soil during a suffusion test (Figure 2.14). The images obtained revealed indeed that the soil state during erosion was not homogeneous, with the existence of preferential flow paths that led to a more and more heterogeneous microstructure in terms of fine particles content, void ratio and inter-granular void ratio distribution.
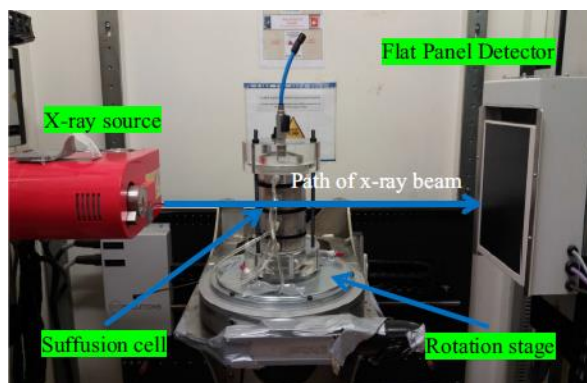
Figure 2.14 Set-up of the suffusion cell inside the X-ray chamber according to Nguyen et al. [75]

2.2.2. Physical model tests

In additions to the above-mentioned laboratory experiments which focused on the phenomenon of erosion under a uniform one-dimensional seepage flow, some studies have been carried out to study suffusion by using small models of dike or levee to directly analyze the effect of the water seepage on the mechanical stability of an earth structure. For instance, Horikoshi & Takahashi [76] performed a series of physical model tests on seepage-induced suffusion on a small-scale embankment made of a gap-graded cohesionless soil under a constant water head condition (Figure 2.15). The cumulative eroded soil mass and the discharged rate of water were monitored during the tests. The spatial extent of the variation in fines content was shown through sieve analyzes on subdivided areas of the embankment model after testing. The results revealed that a decrease in the fines content propagated along the phreatic surface from downstream. Below the phreatic surface, the eroded fines were transported not only laterally by the seepage flow, but also vertically due to the gravitational force and were deposited within the foundation. This deposition of fines resulted in a fine-rich region within the foundation, which caused a decrease in the permeability of the whole embankment.

Hu et al. [14] carried out flume tests to investigate the initiation of a fluidized landslide in a loose widely graded material collected from a coseismic landslide deposit in the 2008 Wenchuan earthquake area. The pore pressure, the internal displacement and the induced soil vibrations were monitored during the experiments. The soil mass was gradually wetted either by a uniform inflow from the ground surface at the top of the slope to simulate the infiltration of run-off water coming from upslope, or by a gradual rise of the water level at the upper boundary of the slope to simulate a rise of the groundwater table (Figure 2.16). Micro-seismicity was monitored. It was believed to be induced by local collapses of the soil structure, since the internal erosion of the finer fraction led to a more open structure characterized by more abundant macro-pores. A rapid increase of the pore water pressure was observed before the collapse of the slope, probably due to the progressive collapse of the macro-pores. The observed seismicity could, therefore, be seen as a precursor to the loss of stability and an indicator of the growing consequences of chain reactions within the soil.

With the objective of studying backward erosion piping, van Beek et al. [77] carried out a series of small-, medium-, and full-scale experiments (Figure 2.17). The observed phases in the experiments were very similar: seepage, backward erosion, widening of the channel, failure and breakthrough of the levee. Initially, a very limited almost non noticeable sand transport was obtained. An increase of the hydraulic head resulted in a backward erosion, marked by the occurrence of sand boils. The authors suggested that the transition from backward erosion to the widening of the pipe could not be observed by the amount of transported sand or by the flow rate. Failure took place afterwards within a short time.
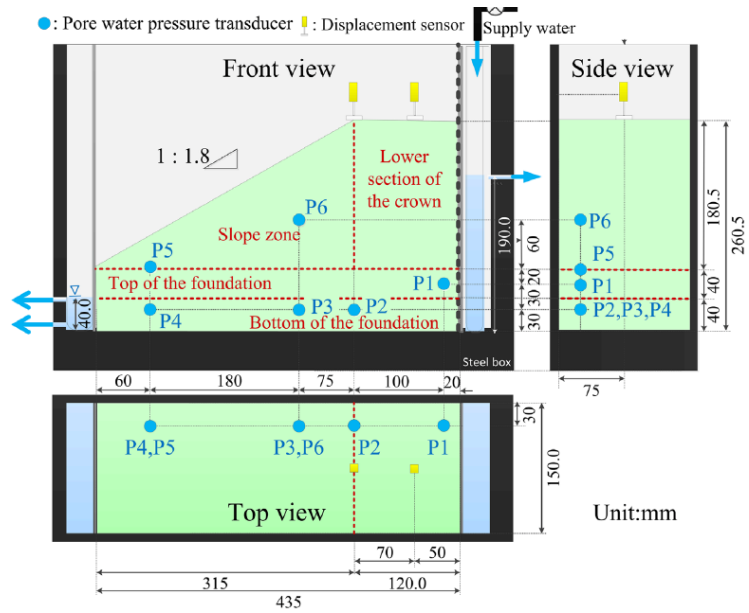
Figure 2.15 Schematic diagram of the physical model according to Horikoshi & Takahashi [76]

(a)

(b)

18
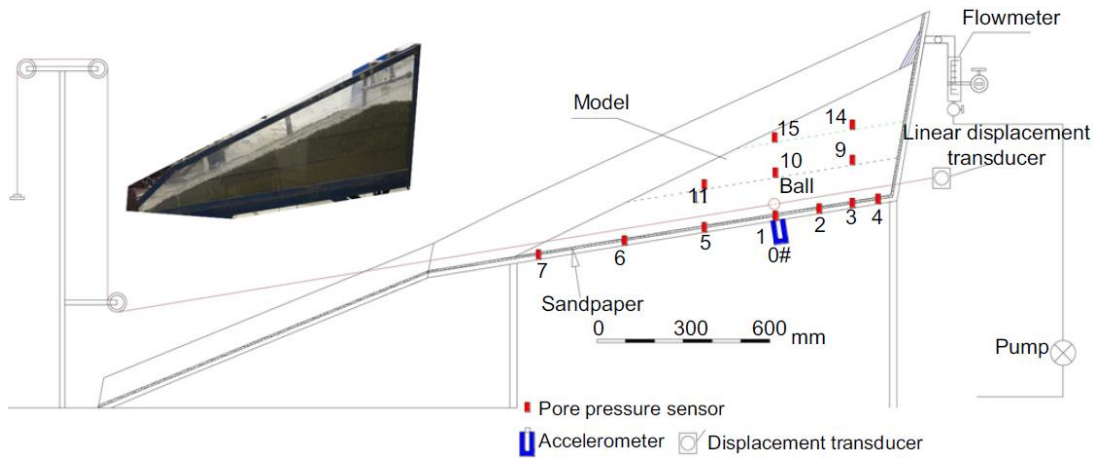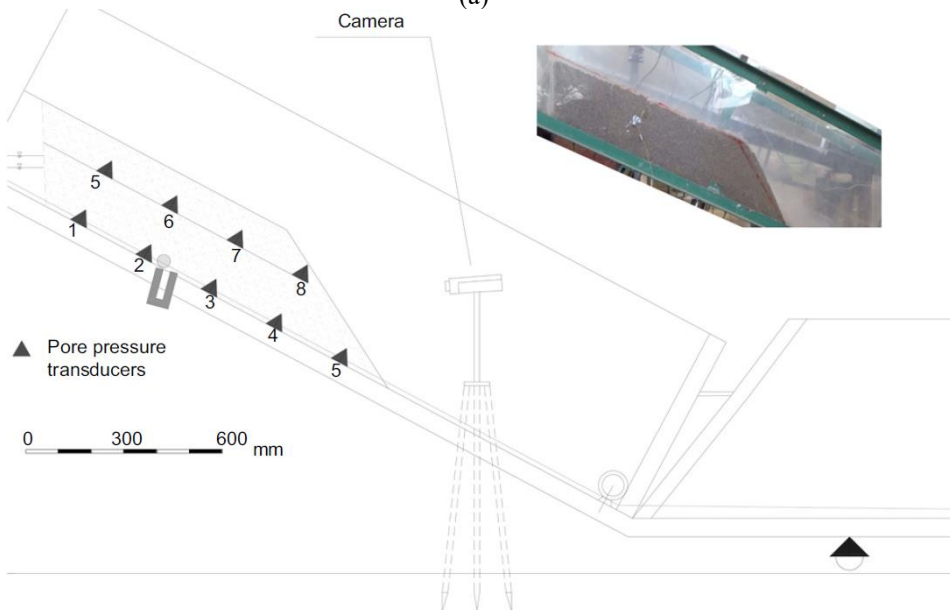
Figure 2.16 Set-up of the two flumes apparatuses according to Hu et al. [14]: (a) Water infiltration from the top of the slope; (b) Increasing water level at the upper hydraulic boundary.

(a)

(b)

(c)
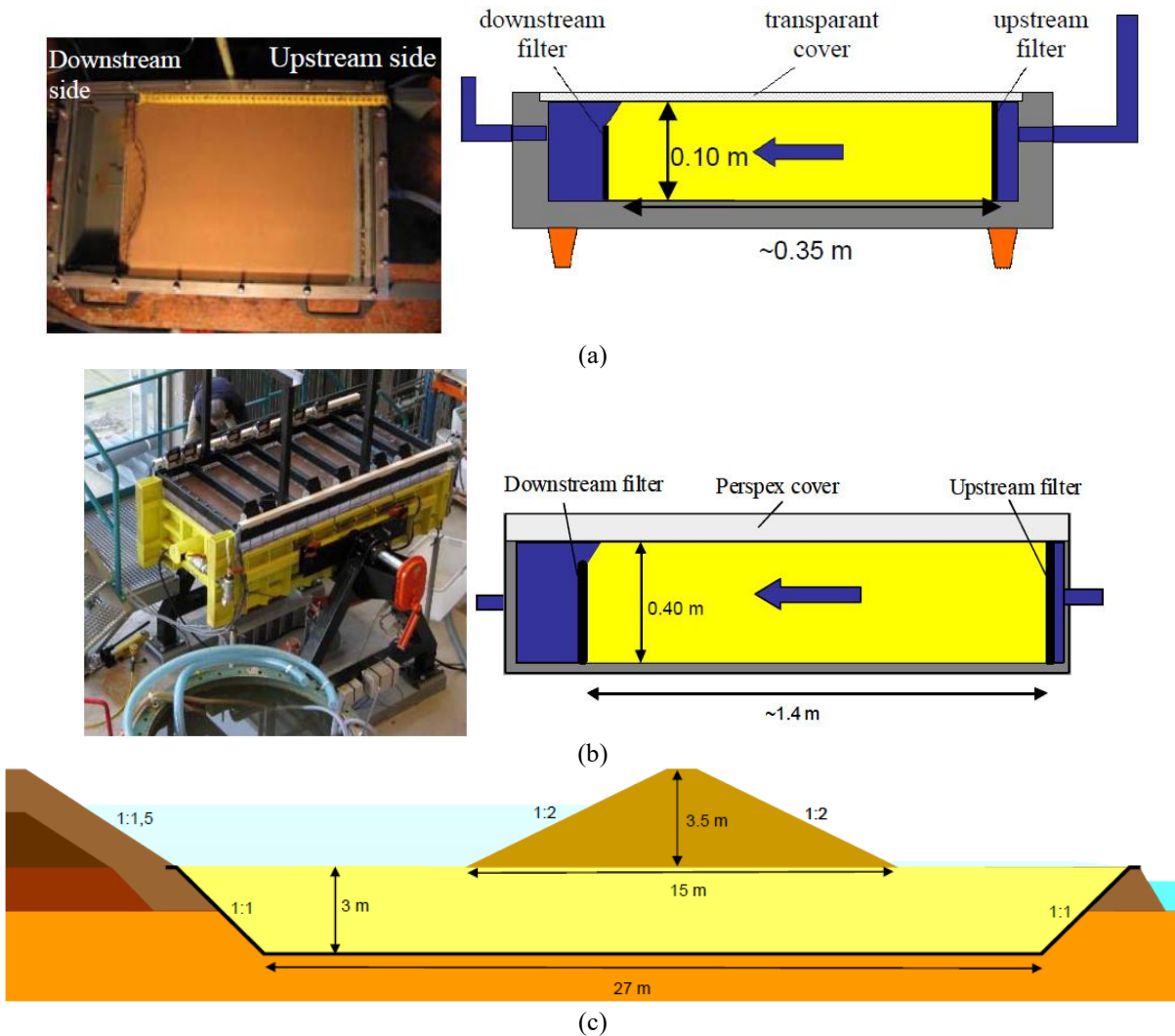
Figure 2.17 Set-up of experiments according to van Beek et al. [77]: (a) small scale; (b) medium scale; (c) full scale

2.3. Computational analyses of suffusion

In parallel to experimental studies, mathematical and numerical models have also been developed to describe the initiation and progression of particle detachment and internal erosion, either within the framework of continuum mechanics using either the finite element or the finite difference methods [36-40], or within a discrete framework by associating the discrete element method to describe the dynamics of the granular solid phase to the computational fluid dynamics to solve the interstitial fluid flow [41-47].

2.3.1. Discrete approaches

The physical and mechanical properties of granular materials such as sand can be quite different from those of continuous materials. A physics-based approach to describe the behavior of granular materials is the Discrete Element Method (DEM) proposed by Cundall & Strack [78]. Coupled with different approaches to simulate the fluid flow at the local pore scale, the discrete approach can

represent fairly well the microstructure and describe more and more accurately the physical mechanisms within granular materials. However, its computational cost limits the studies at small volume scales; most of the studies were performed at the representative elementary volume (REV) scale.

(1) DEM-CFD approach

Different numerical schemes have been presented in the literature for investigating the soil erosion at local scale, among which the DEM-CFD approach is the most widely used. Tsuji et al. [79, 80] proposed a coupling between the Computational Fluid Dynamics (CFD) model and the DEM model to describe fluid-solid systems. They demonstrated its capabilities in predicting quite well the fluid-solid interactions. The fluid flow is governed by the classical Navier-Stokes equations. The fluid velocity and pressure in the Navier-Stokes equations are regarded as continuous in space and treated as a locally averaged quantity over the fluid cell [79], which helps to increase significantly the computational efficiency. The solid phase is described by discrete elements. The particle motions are governed by Newton's Laws. The treatment of the soil-fluid interactions in CFD-DEM is achieved by assuring the continuity condition between the two phases through the semi-empirical drag force model. The DEM-CFD method has been extensively applied in geotechnical engineering. For instance, Shamy & Zeghal [81] investigated the three-dimensional response of sandy deposits subjected to critical and overcritical upward pore fluid flows; Chen et al. [82] studied the time rate of 1D consolidation problems; Zhao & Shan [47] investigated the characteristics of sand heap formed in water through hopper flow, etc.

Concerning the applications of this approach in the analysis of soil erosion, Abdoulaye Hama et al. studied the stability/instability of an initially stable material (according to the Kenney & Lau geometrical criterion, see section 2.4.1 for details) and its mechanical behavior after suffusion. In Tao & Tao [83] investigations, the mechanical solid features (contact force, contact number, etc.) and the hydraulic field features (velocity, pressure, hydraulic force and void fraction) were visualized. Li & Zhao [84] revisited the classical dam-break problem. They suggested that not only the viscous property but also the density of the liquid phase relative to the particle density played a crucial role in the early collapse and late developing stages of the dam break. Zhang et al. [85] simulated the seepage erosion in gap-graded soils around shield tunnels. The seepage erosion was simulated for loose, medium dense and dense silty sands. The evolution of the fine particles loss and the volumetric strain were investigated. Quantitative relationships between the loss of fine particles, the volumetric strain and the four influencing factors: time, hydraulic pressure, consolidated stress ratio, and void ratio were obtained through a regression analysis.

It should be noted that empirical relationships are still required to compute the drag forces in the DEM-CFD approach. Furthermore, since the fluid velocity and the pressure in the Navier-Stokes equations are treated as locally averaged quantities over the fluid cell [79], some of the microscale descriptions of the problem are lost and macroscopic assumptions are needed to account for the fluid flow: Darcy's law and Kozeny-Carman expression for the permeability, for instance [86].

Alternative approaches have been proposed to overcome these shortcomings of the DEM-CFD approach.

(2) DEM-LBM approach

Cook et al. [87] combined the discrete element method (DEM) with the lattice Boltzmann method (LBM) to simulate the coupling between the fluid flow and the particle motions. This approach demonstrated its applicability in describing reasonably well the fluid-solid interactions. Unlike in the DEM-CFD approach, the fluid-solid coupling in the DEM-LBM approach is achieved by solving directly the collision between the fluid particles and the solid nodes in the framework of the lattice Boltzmann method. Similarly, Feng et al. [88] developed a coupled DEM-LBM strategy for the simulation of particle transport in turbulent fluid flows. The coupled DEM-LBM method was then applied by Cui et al. [89] to study in 2D the soil erosion induced by a local leakage from a buried pipe and by Lominé et al. [41] and Sibille et al. [45] to study the pipe erosion. Wang et al. [90] extended the DEM-LBM method in 3D to investigate the erosion process of soil particles in granular filters placed within earth dams. The migration of individual particles within the granular filter could be visualized and the eroded particles could be traced. It should be noted, however, that LBM relies on a fixed lattice that is not changed as solid particles move.

(3) DEM-PFV approach

Wautier et al. [86, 91] attempted to combine an efficient pore-scale finite volume (PFV) method introduced by Chareyre et al. [92] with the discrete element method (DEM) to provide a microscale coupled fluid/grain modeling approach at a relatively small computational cost. The void space was discretized into connected pores. The complexity of the fluid flow was then reduced to fluid exchange laws between adjacent pores. The accuracy of this approach relies strongly on the adequate definition of how fluids are exchanged between pores in terms of the local pore geometry.

(4) Particle removal approach

Some attempts have also been made to model the mechanical response of eroded materials by removing particles. Muir Wood et al. [48] modeled the mechanical consequences of internal erosion by a two-dimensional discrete element analysis. The smallest particles in the sample were removed from the assembly with no attempt to describe any realistic erosion process. They found that this particle removal changed the relative density state of the material from dense to loose as they compared the current soil state to the critical state line. Scholtès et al. [49] developed the same approach in 3D. The smallest particles under the lowest load – corresponding to the most likely erodible particles - were identified based on the size of the particles and the degree of interlocking. They found that the mechanical behavior of the soil changed from dilative to contractive with the removal of soil particles. Aboul Hosn et al. [93] studied the macroscopic response during internal erosion and the post-erosion properties of granular materials by particle removal, considering a one-way coupling between the fluid and the solid phases. The authors simplified the erosion process by selecting the transportable particles through the calculation of the unbalance fluid forces and the

definition of a controlling value of the constriction size: the narrow connecting sections between pores through which the fine particles could be transported by the water flow. Hicher [51] proposed an analytical micromechanical model to predict the mechanical behavior of granular materials subjected to particle removal and concluded that the removal of solid particles may cause diffuse failure in eroded soil masses.

Despite the relevance of the discrete element method to shed light onto the constitutive properties of granular materials, its computational cost remains a restrictive aspect which could become an obstacle whenever real earth structures, such as embankment dams, are concerned. It is, therefore, necessary to develop approaches that can take better account of boundary value problems at the scale of engineering structures.

2.3.2. Continuous approaches

Vardoulakis et al. [39] developed a mathematical model for the sand production problem. The saturated porous medium was supposed to be composed of the solid, the fluid and the fluidized solid particles. Piping and surface erosion effects were studied based on the mass balance and particle transport equations, as well as on the fluid flow in a porous continuous medium controlled by Darcy's law. The derived governing equations were solved numerically by using the finite difference method in 1D condition to calculate the evolution of the porosity, the pore pressure and the concentration of fluidized fine particles during erosion. The model was then enhanced by Stavropoulou et al. [38] by taking account the mechanical damage induced by the sand erosion. The porosity evolving in time and space as erosion progressed was chosen as the coupling parameter. In this model, both rock stiffness and cohesion were assumed to depend on the porosity in such a way that the material became weaker when the porosity increased. The mathematical model was solved numerically by using the finite element method.

Similar mathematical models have been developed by Papamichos et al. [37], Cividini & Gioda [36], Steeb et al. [94], Uzuoka et al. [95], Zhang et al. [40]. However, no model can accurately account for the modification in the soil shear strength after internal erosion. The mechanical part consisting of an elastic model with damage is too simple for this purpose.

2.4. Governing factors of soil susceptibility to suffusion

Experimental studies based on one-directional upward or downward seepage flow (see Section 2.2 and 2.3) have demonstrated that the initiation of suffusion depends, among other factors, on the particle size ratio between the fine and the coarse fractions, the particle size distribution, the particle shape, the confining pressure, the hydraulic gradient, the flow velocity, and the seepage flow orientation. Generally speaking, the soil susceptibility to suffusion is influenced by geometric, hydraulic, and mechanical conditions.

2.4.1. Geometric criteria

To evaluate the internal instability of filters in embankment dams, early studies established the role of the particle size distribution on the material susceptibility to internal erosion. They have

suggested several useful criteria exclusively based on the particle size distribution to determine the susceptibility to seepage-induced internal instability.

(1) USACE (1953) and Istomina (1957)

The U.S. Army Corps of Engineers (USACE) [64] carried out suffusion tests on sandy gravel soils subjected to a downward flow and came out with a criterion based on the uniformity coefficient $C_u = D_{60}/D_{10}$. A soil is classified as internally stable if $C_u < 20$. Similar to the concept of USACE [64], Istomina [96] suggested that soils with $C_u < 10$ can be considered as internally stable.

(2) Kezdi (1979) and Sherard (1979)

Kezdi [18] and Sherard [20] proposed a similar method that splits the soil gradation curve into its coarse and fine components at an arbitrary grain diameter based on the classical retention criteria for granular filters suggested by Terzaghi [97]. A soil gradation is internally stable if: $D'_{15}/d'_{85} < 5$ (Sherard [20]) or, more conservatively, $D'_{15}/d'_{85} < 4$ (Kezdi [18]), where D'_{15} is the diameter of the 15% of mass passing in the coarse part; d'_{85} is the diameter of the 85% of mass passing in the fine part. However, how to decide what is the delimiting grain size remains unclear.

(3) Kenny & Lau (1985) and Li & Fannin (2008)

The Kenny & Lau method [4] was based on experimental results on 16 soil samples to evaluate the potential of internal instability in coarse grained soil. The determination of internal instability is based on the shape of the gradation curve. It requires the calculation of a stability index H/F along a prescribed length of the gradation curve, where F is the mass fraction of grains smaller than the diameter D, and H is the mass fraction of grains with a diameter in the interval D to 4D. Kenny & Lau suggested that the size of the predominant constriction within the void network of a filter is approximately one-fourth the size of the smallest particle constituting the filter, which means that particles of size D can pass through the constrictions in a filter formed by particles of size 4D and larger. A soil is classified as internally stable if $(H/F)_{\min} \geq 1$.

After confronting Kezdi's [18] and Kenny & Lau's method [4] to a database of laboratory permeameter tests on gravel and sand, Li & Fannin [19] suggested a limit value to internal stability of $(H/F)_{\min} \geq 1$ for soils with $F \leq 15\%$, or $H \geq 15\%$ for soils with $15\% \leq F \leq 30\%$.

Using the DEM-CFD method, Abdoulaye Hama et al. [98] demonstrated that even stable granular materials can lose fine particles and present a local instability. They suggested that the Kenney & Lau criterion was very conservative and should be enhanced by introducing a threshold percentage value of fine particles that granular material can lose while remaining stable.

(4) Burenkova (1993) and Wan & Fell (2008)

Based on a series of permeameter tests on gravel and sand with an unreported fines content, Burenkova [15] proposed to calculate two gradation parameters, D_{90}/D_{15} and D_{90}/D_{60} to identify the internal instability of broadly graded soils. D_{90}/D_{60} and D_{90}/D_{15} represent an upper and lower

boundary that enclose a region within which internally stable gradations can be found (Figure 2.18). Wan & Fell [21] method requires similarly the calculation of two gradation parameters, D_{20}/D_5 and D_{90}/D_{60}. They constitute the boundaries that enclose regions within which stable, unstable and "transition" gradations can be found, based on a series of laboratory permeameter tests on silt-sand-gravel or clay-silt-sand-gravel soils with a fines content up to 45%. (Figure 2.19).
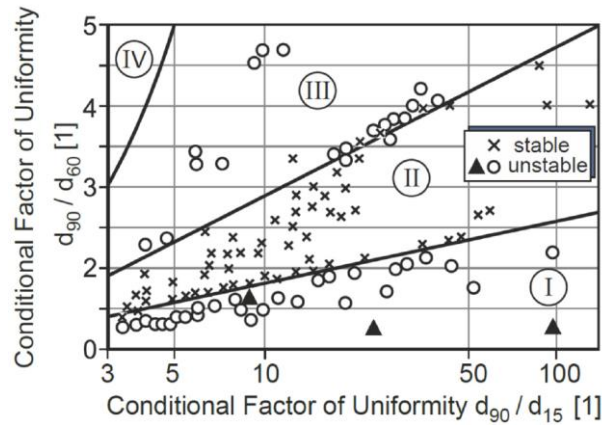
Figure 2.18 Internal instability potential according to Burenkova's Method [15]
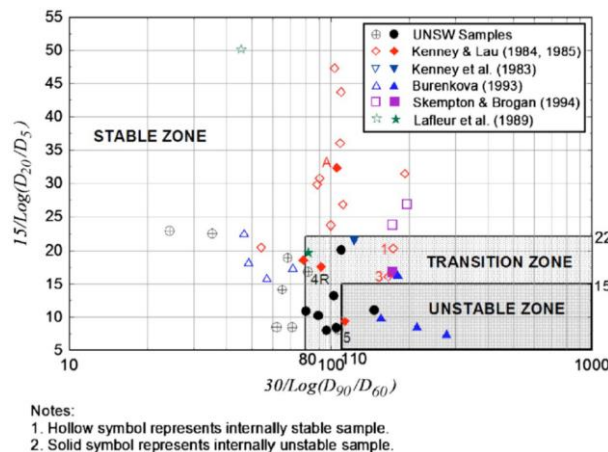
Figure 2.19 Assessing internal stability of broadly graded silt-sand-gravel soils (Wan and Fell's method [21])

(5) Chang & Zhang's method (2013)

After confronting Istomina's method [96], Kezdi's method [18], and Kenney & Lau's method [4] to a database of laboratory tests on gap-graded and well-graded soils, Chang & Zhang [99] suggested the following approach: (1) a well-graded soil with a fines content less than 5% is internally stable if it satisfies $(H/F)_{min} > 1.0$; (2) a gap-graded soil with a fines content less than 10% is internally stable if its gap ratio is smaller than 3.0. (3) a well-graded soil with a fines content of more than 20% or a gap-graded soil with a fines content of more than 35% is deemed to be internally stable.

(6) Constriction-based internal erosion criteria

According to Kenney et al. [65], the controlling void entities in the filtration process are the constrictions defined as the narrow connecting sections between pores through which the fine particles can be transported by the water flow. Accordingly, detached particles should overcome such obstacles to pass through the filter. Reboul et al. [100] and Vincens et al. [101] summarized the methods for evaluating the constriction size distributions of a numerical assembly of spheres which were generated by the Discrete Element Method. Since such an evaluation requires a high computational cost, simple probabilistic alternative methods were proposed. Indraratna et al. [102] suggested a probabilistic method to determine the controlling constriction size and subsequently a constriction-based retention criterion for granular filters. The constriction size distribution curve was obtained based on the grain size distribution and the relative density of the soil. They suggested that the ratio between the controlling constriction size of coarse particles and the fine fraction, D_{c35}/d_{85f} was the main factor to distinguish stable to unstable broadly-graded soils: (1) a soil is internally unstable if $D_{c35}/d_{85f} > 0.82$; (2) a soil is internally stable if $D_{c35}/d_{85f} < 0.73$; (3) further experiments are required if $0.73 \leq D_{c35}/d_{85f} \leq 0.82$.

(7) Influence of particle shape

Some attempts have also been made to investigate the influence of the particle shape on the susceptibility to suffusion. Marot et al. [103] carried out a series of tests on clayed sand to investigate the effect of the angularity of the coarse grains on suffusion. They noticed that the angularity of coarse grains may contribute to increase the resistance to erosion of the tested soils up to a factor of 5. Moreover, the grain shape has an effect on the decrease of the hydraulic conductivity. The angularity of the coarse grains may increase the blocking of the detached clay particles.

2.4.2. Hydraulic criteria

As mentioned in the previous section, the geometrical conditions can control the potential of internal erosion of a soil, whereas the hydraulic conditions govern the onset of internal erosion. In other words, the geometrical conditions reflect the intrinsic properties of the soils, and the hydraulic conditions express the external triggers [104]. The suffusion is triggered if the hydrodynamic forces induced by the seepage flow on the soil grains exceed a critical threshold, i.e. the critical hydraulic gradient i_c.

Terzaghi [97] proposed a critical upward hydraulic gradient $i_c (= \gamma'/\gamma_w)$ equal to 1.0 for cohesionless soils under zero effective stress. However, this criterion was initially introduced to describe the hydraulic heaving and does not apply to internal soil erosion. The laboratory tests conducted by Skempton & Brogan [22] indicated that in unstable sandy gravels piping can occur at hydraulic gradients one third to one fifth of the theoretical critical gradient suggested by Terzaghi for a homogeneous granular material of the same porosity. A stress-reduction factor α was introduced into the definition of i_c to consider the influence of the fine particles present in the soil stress matrix: $i_c = (1-\alpha)(\gamma'/\gamma_w)$. However, the definition of α remains unclear. Li [105] suggested that α was

related to d'_{85} corresponding to the fine fraction and to the actual opening size O_{50} by the following expression: $\alpha = 3.85 \left(d'_{85}/O_{50} \right) - 0.616$.

Moffat & Fannin [69] observed a trend of increase of i_{cr} with the mean vertical effective stress σ'_{vm}. Li & Fannin [106] proposed a theoretical hydro-mechanical envelope to characterize the critical hydraulic gradient of a soil under an overburden stress:

$$i_c = \frac{\alpha}{1-\alpha} \left(\bar{\sigma}'_{vm} + \frac{0.5\gamma'}{\gamma_w} \right) \quad \text{...(2.1)}$$

where α is the stress transformation coefficient, $\bar{\sigma}'_{vm}$ is the effective vertical stress in the soil.

Moffat & Herrera [107] proposed a theoretical model to determine the hydromechanical boundary of an internally unstable soil subjected to a vertical seepage flow in either the upward or downward direction. This model considers the influence of the effective stress, the porosity of the soil, the friction angle between the coarse and fine fractions, and the proportion of the effective stress that is transmitted to the finer fraction. For a downward flow:

$$i_c = \frac{G^*}{\gamma_w \Delta z} \left(\sigma'_v \tan(\phi_\mu) + \Delta\sigma'_v \right) - \frac{n^f \rho_f g}{\gamma_w} \quad \text{...(2.2)}$$

For an upward flow:

$$i_c = \frac{G^*}{\gamma_w \Delta z} \left(\sigma'_v \tan(\phi_\mu) + \Delta\sigma'_v \right) + \frac{n^f \rho_f g}{\gamma_w} \quad \text{...(2.3)}$$

where G^* is the geometric based stress reduction factor, $\Delta\sigma'_v$ is the variation of the effective stress, ϕ_μ is the friction angle, n^f is the volume fraction of fines, ρ^f is the density of the fine fraction.

Besides the effective stress, the value of the critical hydraulic gradient can also be influenced by the soil initial density, the fines content, the history of the hydraulic loading, etc. According to Ke & Takahashi [68], the lower the fines content, the bigger is the hydraulic gradient required to cause internal erosion. Specimens containing the same mass ratio of fines but a larger relative density require larger critical hydraulic gradients to initiate internal erosion. The fine particle loss increases with the imposed hydraulic gradient. Luo et al. [108] compared the results of erosion tests obtained with two test durations. They suggested that a long-term large hydraulic water head reduces the hydraulic gradient needed for the development of suffusion. Similar trends were also reported by Sibille et al. [23] and Rochim et al. [24].

2.4.3. Effect of stress state on suffusion development
Noticing the importance of the stress state within a soil specimen, Moffat & Fannin [69] carried out internal erosion tests under an upward flow at K_0 stress state and then established a hydro-mechanical relation between the effective stress and the local critical hydraulic gradient in four soils. An increase of the critical hydraulic gradient with the increase of the effective stress was found.

However, the impact of the isotropic confining pressure on the erodibility of fine particles remains unclear, since the results in the literature present certain contradictions. Bendahmane et al. [28] and

Ke & Takahashi [30] reported that a larger effective confining pressure would lead to a less extent of suffusion. However, Chang [104] showed that, as the confining stress decreased, the maximum cumulative fine loss also decreased. It is, therefore, quite difficult to understand clearly the effects of the effective stress level on suffusion. According to Ke & Takahashi [30], the fines are expected to be densely packed among coarse grains at larger confining pressures and the interstitial spaces are expected to be narrower. For soil specimens under high confining pressures, a seepage flow may well dislodge fewer fines. However, the force transfer mechanism within a granular material is much more complex: force-arching may develop at the intersection with the boundary, which may hold the fines from erosion. At larger confining pressures, force-arches could fail, which, in turn, might cause a further erosion of fines.

The numerical studies performed by Zhang et al. [85] confirmed the explanation given by Ke & Takahashi [30]. Zhang et al. simulated the erosion process for loose, medium dense and dense silty sand under different stress states by the DEM-CFD method. They suggested that the fine particles were eroded in two patterns. The first pattern was induced by the axial pressure extruding fine particles through seams without hydraulic pressure. The second pattern was induced by the fluid drag force transporting fine particles under hydraulic pressure. The results showed that dense sand is more prone to particle erosion in the first pattern because of the breaking of force-arching, whereas loose sand is more prone to particle erosion in the second pattern.

Few studies can be found in the literature dealing with the analyses of the influence of an anisotropic stress state on suffusion. Chang & Zhang [5] carried out a series of tests on a gap-graded soil under the same confining stress but under different deviatoric stresses. The results showed that the maximum erosion rate, the variations in soil permeability, and the deformation of the soil specimens increased with the increase of the deviatoric stress. A multi-scale approach including a discrete element model and an analytical micromechanical model was proposed by Scholtès et al. [49] and Hicher [51] to assess the impact of internal erosion on the induced deformations and the changes of soil properties during and after erosion. The erosion process was modeled by a random removal of particle (for the DEM modeling) or by a progressive increase of the granular assembly void ratio (for the analytical micromechanical modeling), at different shear stress ratios $\eta(=q/p')$.

The simulations demonstrated that, under elevated stress ratios, large deformations could develop and lead to soil failure, as shown in Figure 2.20.
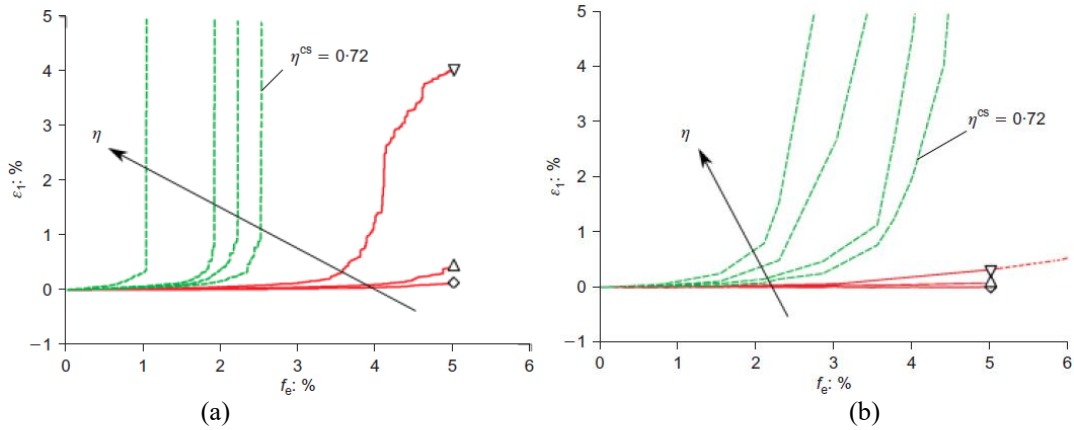
Figure 2.20 Evolution of vertical deformation during erosion at different stress levels: (a) DEM and (b) micromechanical model simulations according to Hicher [51]

2.4.4. Interpretation of soil erodibility

Erodibility represents the erosion resistance of a soil subjected to water flow: a high erodibility corresponds to a low resistance. According to Wan & Fell [3], the susceptibility of a soil can be described in two aspects: (1) the rate of erosion, and (2) the ease of initiating erosion within the soil. Based on a series of erosion tests on reconstituted well graded silt-sand-gravel soils under an upward hydraulic flow, Sterpi [12] proposed a relationship between the percentage by weight of eroded fine particles μ_e, the hydraulic gradient i and the time t as follows:

$$\mu_e = \mu_0 \left[1 - \exp\left(-\left(\frac{t}{t_0}\right)^b \frac{i^c}{a} \right) \right] \quad ....(2.4)$$

where μ_0 is the initial fines content by weight, $t_0 = 1h$, a, b and c are non-dimensional parameters.

Following the same approach, Cividini et al. [67] proposed an incremental form to describe the erosion rate as follows:

$$\frac{\partial \rho_f}{\partial t} = d\sqrt{i}\left(\rho_f - \rho_{f\infty} \right) \quad ....(2.5)$$

$$\rho_{f\infty} = \rho_{f0} \left[(1 - c_\infty)\exp\left(-ai^b\right) + c_\infty \right] \quad ....(2.6)$$

where ρ_f is the weight fraction of the fine particles within the sample at a given time and ρ_{f0} its initial value; $\rho_{f\infty}$ is the long term value of ρ_f which depends on the hydraulic gradient i and on three non-dimensional parameters a, b and c_∞.

Based on laboratory erosion tests [12, 67], Uzuoka et al. [95] suggested that the material time derivative of the fines content is assumed to be a function of the absolute value of the Darcy's flow velocity q_w:

$$\frac{\partial f_c}{\partial t} = -\lambda_e \left(f_c - f_{c\infty} \right)|q_w| \quad ....(2.7)$$

$$f_{c\infty} = f_{c0} \left\{ (1 - c_e)\exp\left(-a_e |q_w|^{b_e}\right) + c_e \right\} \quad ....(2.8)$$

28

where $f_{c\infty}$ is the ultimate fines content after a long seepage period; a_e, b_e and c_e are non-dimensional parameters.

Based on the forces acting on a fine particle within the pore channels, Wan & Fell [3] and Bonelli & Marot [109] proposed to describe soil erosion by using the hydraulic shear stress:

$$\dot{m} = k_d \left(\tau - \tau_c \right)$$ ....(2.9)

where $\dot{m}$ is the soil erosion rate, k_d is the erodibility coefficient, τ is the hydraulic shear stress at the soil-water interface, and τ_c is the critical hydraulic shear stress at the initiation of erosion. According to Reddi et al. [110], the hydraulic shear stress for a horizontal flow between upstream section A and downstream section B of the system can be given by:

$$\tau = \frac{\Delta h \gamma_w}{\Delta z} \sqrt{\frac{2k\mu}{\gamma_w n}}$$ ....(2.10)

where Δh is the hydraulic head drop, Δz is the altitude change for an one-dimensional flow between an inlet section A and an outlet section B, k is the hydraulic conductivity, μ is the dynamic viscosity, and n is the porosity.

Some attempts have also been made to assess the initiation of erosion by using an energy-based approach. With the objective to take into account the whole history of the hydraulic loading, Sibille et al. [23, 24, 108] proposed an expression of the erosion rate function of the fluid expended power:

$$\dot{m} = \alpha_{ref} \left(\frac{1}{\frac{\Delta E_v}{P_v t^*} + 1} \right) P_v^b$$ ....(2.11)

where α_{ref} and b are intrinsic parameters of the tested material controlling its erodibility; t^* is a characteristic time relative to the tested material; ΔE_v is the flow energy per unit volume cumulated from the initiation of the hydraulic loading, expressed as :

$$\Delta E_v = \int_{t_{ini}}^{t > t_{ini}} P_v \mathrm{d}t$$ ....(2.12)

P_v is the flow power per unit volume expressed as :

$$P_v = k_0 \left(\frac{\Delta p^2}{\gamma_w \Delta z_0^2} + \frac{2\Delta p}{\Delta z_0} + \gamma_w \right)$$ ....(2.13)

where Δp describes the hydraulic loading applied on the specimen along the length Δz_0, k_0 is the hydraulic conductivity which is assumed to be constant.

By considering experimental and theoretical studies in relation to the filtration of non-colloidal solid particles in porous media [111, 112], Vardoulakis et al. [39] proposed an expression of the rate of the eroded mass based on the discharge of fluidized particles cq_w:

$$\dot{m} = \rho_s \lambda q_0 \frac{1-\varphi}{k}\left(c - \frac{c^2}{c_r}\right)\left|\frac{q_w}{q_0}\right|^n \quad \text{...(2.14)}$$

where ρ_s is the density of the solid particles, φ is the porosity, k is the permeability, c is the concentration of fluidized particles, q_w is the volumetric discharge rate, c_r is a critical value of c which takes into account the deposition of fluidized particles.

2.5. Mechanical responses of soils subjected to suffusion

The migration of fine particles through the voids between the larger particles can change the porosity and the fines content, which in turn can induce changes in the mechanical behavior of soils. Before addressing the experimental and numerical studies on the mechanical behavior of eroded soils, it is necessary to introduce the effects of non-plastic fine particles on the soil behavior.

Many experimental studies have been carried out to analyze the effects of both the fines in silty sand and the coarse grains in sandy silt on the physical properties (e.g., void ratio, relative density, etc.) and on the mechanical behavior (e.g., critical state, strength, stress-dilatancy, etc.) [113-117]. Thevanayagam et al. [118] proposed different packing arrangements function of the relative amount of coarse and fine grains in the mixture (Figure 2.21). The equivalent inter-granular contact index e_{eq} was introduced to evaluate the active grain contacts in a soil mixture. In the case of a coarse grain skeleton, the coarse grain contacts play a primary role in the mechanical response of the soil and the fines offer a secondary contribution. With an increase in the fines content, the contacts between the fine grains increase, the coarse grains start to disperse in the mixture and provide a secondary reinforcement effect. Based on experimental results, Yin et al. [52] proposed a unified formulation for the inter-grain contact index and the void ratio of sand-silt mixtures from pure sand to pure silt:

$$e_{eq} = \frac{e - af_c}{1 - f_c}\frac{1 - \tanh\left[\xi(f_c - f_{th})\right]}{2} + \frac{e}{f_c + \frac{1-f_c}{(R_d)^m}}\frac{1 + \tanh\left[\xi(f_c - f_{th})\right]}{2} \quad \text{...(2.15)}$$

where a is a material constant depending on the structure of the soil mixture; R_d is the ratio of the mean size of coarse grains D_{50} to the mean size of fine grains d_{50}; m is a coefficient depending on the grain characteristics and the fine grain packing; ξ is a material constant controlling the evolution rate of the transition zone, f_{th} is the threshold fines content from a coarse grain skeleton to a fine grain skeleton. The formulation, as a function of the fines content, was then applied to determine the position of the critical state line of sand-silt mixtures from pure sand to pure silt.
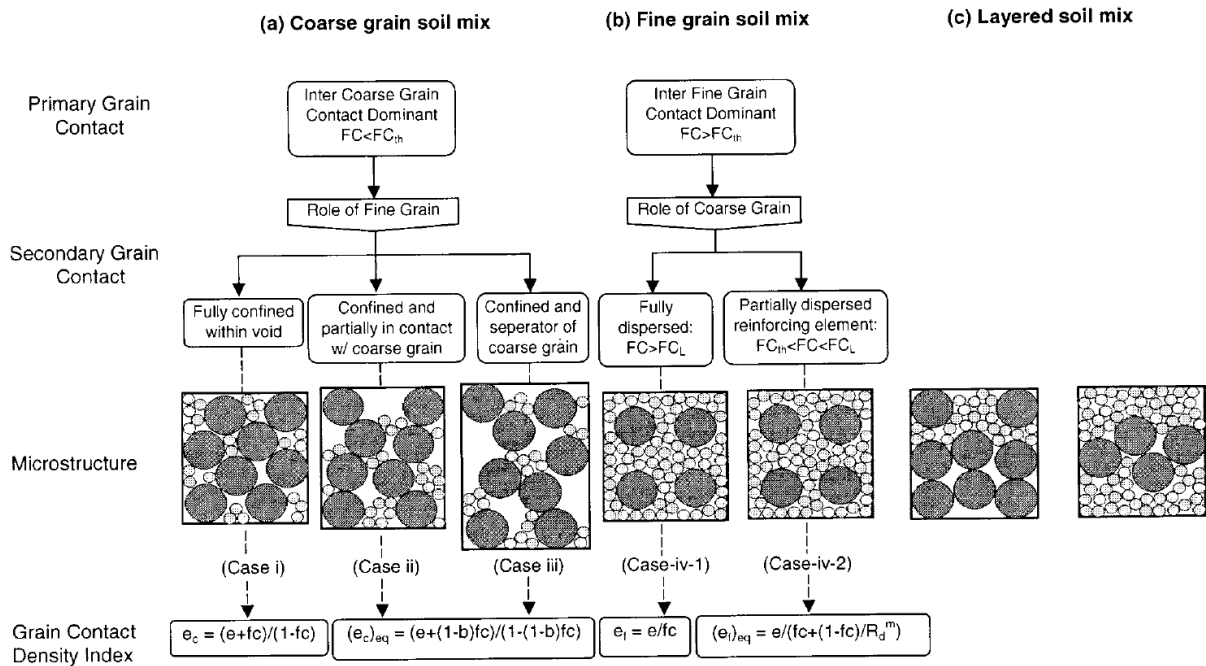
Figure 2.21 Intergranular soil mix classification according to Thevanayagam et al. [118]

Moreover, triaxial tests have been carried out on eroded specimen under different stress paths to investigate the influence of the loss of fine particles on the mechanical behavior of eroded soils. Chang & Zhang [5] carried out a series of drained triaxial compression tests on eroded gap-graded soils. They suggested that, after the loss of a significant amount of fine particles, the stress-strain relation of the soil changed from a dilative to a contractive behavior and the peak shear strength decreased, as shown in Figure 2.22. They attributed this phenomenon to the increase of the void ratio when the fine particles were washed out. The mechanical behavior which depends on the void ratio then changed.
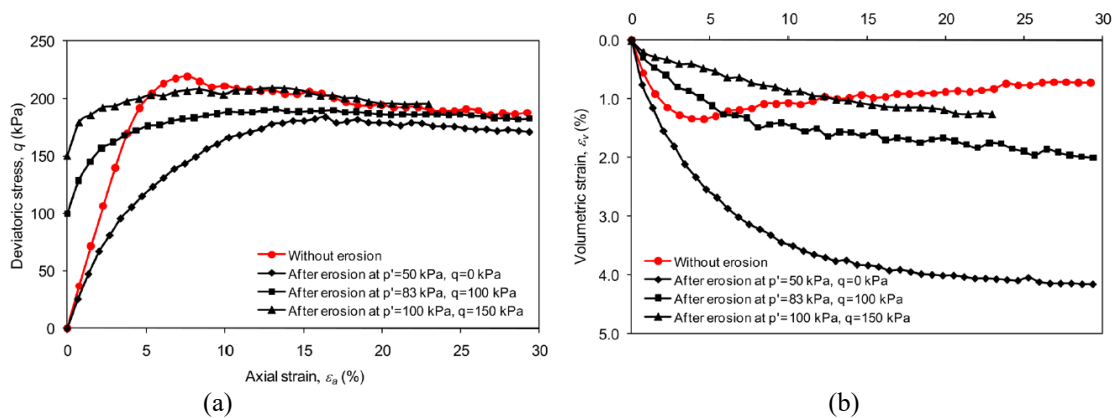
Figure 2.22 Stress-strain relationships without and with internal erosion under different initial stress conditions according to Chang and Zhang [5]: (a) deviatoric stress versus axial strain and (b) volumetric strain versus axial strain

However, some contradictory observations in the comparison of the mechanical behavior of soil before and after erosion have also been reported. Ke & Takahashi [33] conducted drained triaxial compression tests on eroded gap-graded soils and found that suffusion caused the reduction of the

soil strength at large strains, whereas, at small strain levels, the deviatoric stress of the eroded specimens was larger compared to that of intact specimens (Figure 2.23). Similarly, Ke & Takahashi [30] performed undrained compression triaxial tests and showed also that the eroded specimens might gain shear strength after erosion, as shown for example in Figure 2.24. An explanation for such soil behavior is given by Ke & Takahashi [33] by considerations at the grain level. The movement of fines was impeded due to the restriction of the constriction sizes and accumulated at the contact points among coarse grains. The coarse grains were then reinforced at those spots where fines have accumulated. Therefore, the eroded soil specimens showed larger strength and stiffness at the small strain level. The reinforcement might be damaged for subsequent compression at larger strains.
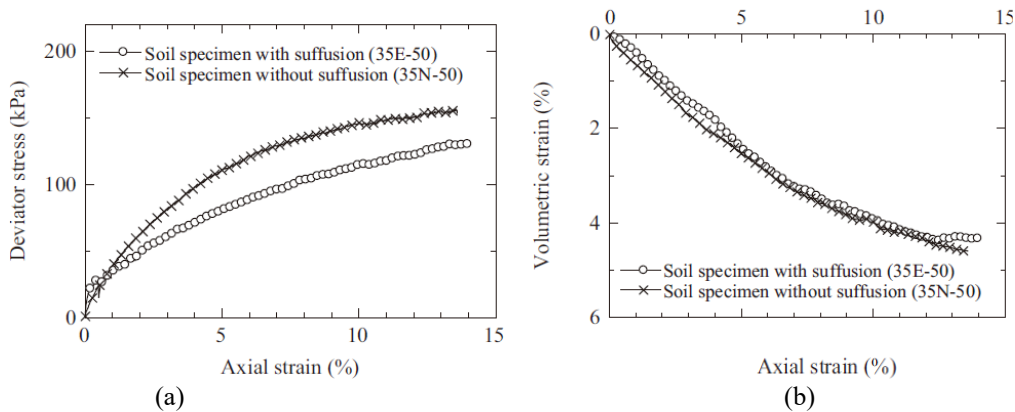
Figure 2.23 Comparison of drained response of the soil specimen with and without suffusion according to Ke & Takahashi [33]: (a) Axial strain versus drained deviator stress, (b) axial strain versus volumetric strain.
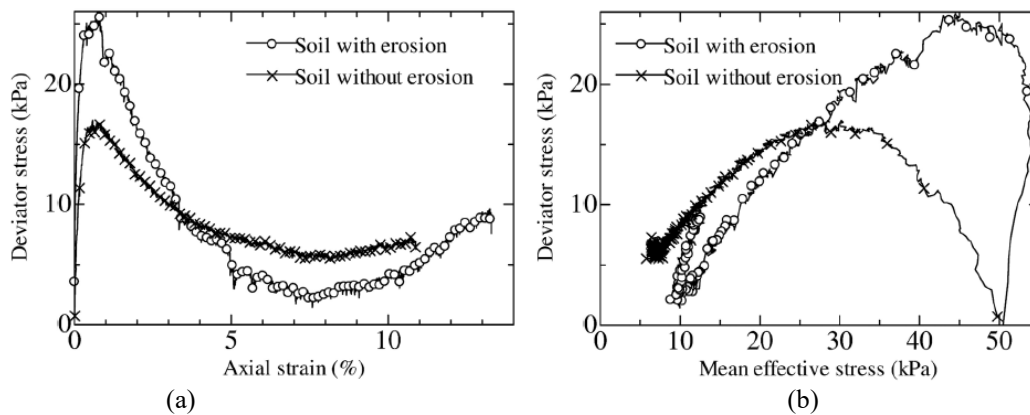
Figure 2.24 Comparison of undrained response of the soil specimen with and without suffusion according to Ke & Takahashi [30]: (a) Axial strain versus drained deviator stress, (b) mean effective stress versus drained deviator stress.

In reality, the eroded soil becomes usually heterogeneous, as shown by the variations in the grain-size distributions in different layers of the soil specimen [5, 33] and by the images obtained by the X-ray computed tomography [75].The accumulation of fine particles within specific zones might provide local reinforcements to the granular skeleton.

More recently, Mehdizadeh et al. [32] investigated the post-erosion undrained behavior of a gap-graded internally unstable soil within a range of erosion durations and inflow velocities in a triaxial apparatus. They found that the strain hardening behavior of non-eroded specimens changed to a flow type with limited deformation after internal erosion and that the dilation tendency was postponed. However, the initial undrained peak shear strength showed a significant increase. This mechanical improvement disappeared once the residual fines content passed a critical point. They suggested that the initial increase in the peak shear strength should be linked to a better interlocking of the angular coarse particles due to absence of the fine particles.

In addition to these experimental studies, some attempts have also been made to investigate the mechanical behavior of eroded soils by using a computational approach. Scholtès et al. [49] developed a three-dimensional discrete element model and investigated the post particle extraction response under compression. They observed that the specimen behavior changed from dilative to contractive and obtained a drop in the shear strength. By adopting a similar approach, Maeda & Kondo [119] and Wang & Li found that the peak strength and dilation tendency decreased after the removal of fine particles. The residual friction angle was found to be unchanged regardless of the percentage of particle erosion. More recently, Aboul Hosn et al. [93] mimicked the suffusion process by using an extraction procedure considering a one-way fluid-solid coupling. The results showed that, if mainly inactive particles were removed, the specimen might suffer sudden collapse during shearing, revealing its hidden loose character induced by the voids left by the eroded particles; when more active particles were eroded, the specimen presented a contracting behavior under shearing with a reduced shear strength with respect to the non-eroded soil. The comparison with a granular assembly generated in an initially loose state showed that the post-erosion mechanical behavior could not be described only by an increase in porosity.

2.6. Summary

In granular soils, fine particles may migrate within the pore spaces between coarse particles under a critical hydraulic gradient. This phenomenon is known as suffusion, which is a type of internal erosion occurring in internally unstable soils.

The main results of experimental and computational investigations of internal erosion have been reviewed in this chapter. It was found that the detachment of fine particles requires a sufficiently high hydraulic loading able to pluck off the fine grains. Numerous researches [3, 21, 22, 68, 105] showed that the critical hydraulic gradient for internally unstable soils is much lower than the theoretical value suggested by Terzaghi [97] for internally unstable soil. In fact, existing studies [23, 24, 68, 69, 106-108] revealed that the critical hydraulic loading parameter depends on the density of the soil, the seepage direction, the fines content, the particle shape and the stress state.

Once a particle is detached, the migration of this particle is controlled by the geometrical properties of the soil, i.e. the constriction sizes and the void network. Several empirical methods have been suggested to assess the potential of erosion in internally unstable soils [4, 15, 18, 19, 21, 100]. Initially, these methods were based on the particle size distribution of the granular soil [4, 15, 18-

21, 64, 96]; more recently the constriction size distribution of the granular assembly has been used to evaluate the suffusion potential [100-102]. Once suffusion takes place, different factors [5, 24, 28, 30, 51, 85] may influence its development and the induced soil deformations, including the change in density of the soil, the stress state, the hydraulic loading history, etc.

The laboratory experimental tests and the numerical analyses at the scale of the representative elementary volume play undoubtedly an important role in the understanding of the physical mechanisms behind the internal erosion phenomena. However, these studies did not provide a clear understanding of where and when the action of the seepage flow could trigger the internal instability in a granular soil mixture at larger scales for boundary value problems. Several physical model tests have been carried out for this purpose [14, 76, 77]. However, few numerical studies at the scale of an entire engineering structure are available in the literature [36, 38-40, 95]. Furthermore, the mechanical responses of an eroded soil were often neglected or simplified by using an elastic model with induced damage parameters.

Hence, with the aim of improving the prediction of soil suffusion and facilitating reliable detection and early warning of the eventual dysfunction of hydraulic structures, urban infrastructures, slope failures and landslides, it is necessary to develop an approach that can take better account of the hydro-mechanical coupled suffusion phenomena in engineering problems at real space scales.

Chapter 3 Modeling erosion and filtration coupling process

3.1. Introduction

As presented in the literature review (see chapter 2.4), several models based on experimental findings [36, 38, 39, 120-124] have been proposed. Many of these models are built in the framework of the porous continuous medium theory based on finite element or finite difference methods to enhance the design of hydraulic earth structures. Most of these models can describe quite well the detachment and transport of finer soil particles within the pores of the solid matrix. Even so, recent studies [36, 75, 125, 126] have shown that erosion is usually followed by self-filtration and clogging. Self-filtration and clogging are similar in that each phenomenon consists of the filling of the initial voids of the soil due to the migration of the fluidized fine solid particles. Induced within the soil specimen or close to the outlet, it decreases the hydraulic conductivity. Therefore, this chapter is devoted to the presentation of a new numerical modeling approach to describe the detachment, the transport, and the clogging of fine particles during suffusion. This new approach treats the material as a continuous medium. The model is built assuming four constituents. The detachment and transport of the fine particles are described via a model of mass exchange between the solid and the fluid phases. Filtration has been incorporated to simulate the filling of the inter-grain voids created by the migration of the fluidized fine particles with the seepage flow; thus, the self-filtration is coupled with the erosion process. A 1-D flow normal to the free surface is solved with a finite difference method. The aim of such a "simple problem" is to see if the model can capture the main features of both erosion and filtration during the suffusion process. The way to do so is to compare the numerical results with the experimental measurements. Furthermore, the influence of the coupling process between erosion and filtration has been highlighted, including the introduction of material heterogeneity induced by the combination of erosion and filtration.

3.2. Model formulations

3.2.1. Mass balances and transported particles

The balance equations are derived based on the porous medium theory [127-129]. According to [123], it is possible to consider the saturated porous medium as a material system composed of 4 constituents: the stable fabric of the solid skeleton (*ss*), the erodible fines (*se*), the fluidized particles (*fp*) and the pure fluid phase (*ff*), as shown in Figure 3.1. The fines can behave either as a fluid-like (described as fluidized particles) or as a solid-like (described as erodible fines) material. Thus, a liquid-solid phase transition process has been accounted for in the present model by the introduction of a mass and volume production term into the corresponding mass and volume balances for erodible fines (*se*) and fluidized particles (*fp*).
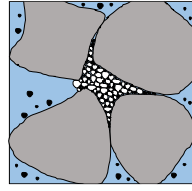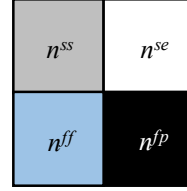
(a) Micro-scale   (b) 4 constituents

Figure 3.1 REV of a fully-saturated soil mixture and the four-constituent continuum model

In a given Representative Elementary Volume (REV), dV, constituted by the four constituents, the volume fraction of a single constituent i is expressed as follows:

$$n^i(x,t) = \frac{dV^i(x,t)}{dV}$$ ....(3.1)

with $i = \{ss, se, ff, fp\}$ denoting the 4 constituents, V^i denoting the volume of the corresponding constituent.

At a material point level, the mass balance for the i phase is given, neglecting the hydro-mechanical dispersion tensor, by Schaufler et al. [123]:

$$\frac{\partial(\rho^i)}{\partial t} + \operatorname{div}(\rho^i \mathbf{v}^i) = \rho^{ex,i}$$ ....(3.2)

where $\rho^{ex,i}$ and $\mathbf{v}^i$ denote, respectively, the mass exchange term and the velocity of the corresponding constituent. The partial density ρ^i is defined as the ratio between the mass dm^i of the constituent i with respect to the total volume dV of the REV, leading to a relation between partial densities ρ^i and effective densities ρ^{iR}, which corresponds to the bulk density of the corresponding constituents:

$$\rho^i = \frac{dm^i}{dV} = \frac{dm^i}{dV^i}\frac{dV^i}{dV} = \rho^{iR} n^i$$ ....(3.3)

The mass balances for the four constituents are then reduced to the corresponding volume fraction balance:

$$\frac{\partial(n^i)}{\partial t} + \operatorname{div}(n^i \mathbf{v}^i) = n^{ex,i}$$ ....(3.4)

$n^{ex,i}$ is the term of the volume of mass exchange to be discussed in the following section.

Moreover, it is assumed that fluid and fluidized particles have at any time and at a given point the same velocity. The solid skeleton is assumed to be deformable but non-erodible. The porosity field $\phi(x,t)$, the amount of erodible fines $f_c(x,t)$ and the concentration of the fluidized particles $c(x,t)$ are defined as follows:

$$\phi = \frac{dV_v}{dV} = \frac{dV^{ff} + dV^{fp}}{dV} = n^{ff} + n^{fp}$$ ....(3.5)

$$f_c = \frac{n^{se}}{n^{ss} + n^{se}} = \frac{n^{se}}{1 - \phi}$$ ....(3.6)

$$c = \frac{n^{fp}}{n^{ff} + n^{fp}} = \frac{n^{fp}}{\phi} \quad \text{...(3.7)}$$

The phase transition of the fine particles from solid to fluidized particles leads to:

$$-n^{ex,fp} = n^{ex,se} = \hat{n}, \ n^{ex,ss} = 0, \ n^{ex,ff} = 0 \quad \text{...(3.8)}$$

The mass balance equations are then given by the following expressions:

$$-\frac{\partial \phi}{\partial t} + \operatorname{div}(\mathbf{v}_s) - \operatorname{div}(\phi \mathbf{v}_s) = \hat{n} \quad \text{...(3.9)}$$

$$\frac{\partial(f_c)}{\partial t} - \frac{\partial(f_c \phi)}{\partial t} + \operatorname{div}(f_c \mathbf{v}_s) - \operatorname{div}(f_c \phi \mathbf{v}_s) = \hat{n} \quad \text{......................................(3.10)}$$

$$\frac{\partial(c\phi)}{\partial t} + \operatorname{div}(c\mathbf{q}_w) + \frac{\partial(c\phi \mathbf{v}_s)}{\partial t} = -\hat{n} \quad \text{..(3.11)}$$

$$\operatorname{div}(\mathbf{q}_w) + \operatorname{div}(\mathbf{v}_s) = 0 \quad \text{..(3.12)}$$

where $\mathbf{q}_w$ denotes the volume discharge rate (the volume of flow through the unit cross-sectional area in unit time):

$$\mathbf{q}_w = \phi(\mathbf{v}_f - \mathbf{v}_s) \quad \text{...(3.13)}$$

$$\mathbf{v}_s = \frac{\partial \mathbf{u}(x,t)}{\partial t} \quad \text{...(3.14)}$$

with $\mathbf{u}(x.t)$ indicating the displacement field of the soil skeleton. The strain ε_{ij} and volumetric strain ε_v are then given by the following expressions under small strain assumption:

$$\varepsilon_{ij} = -\frac{1}{2}(u_{i,j} + u_{j,i}) \quad \text{...(3.15)}$$

$$\frac{\partial(\varepsilon_v)}{\partial t} = -\operatorname{div}(\mathbf{v}_s) \quad \text{...(3.16)}$$

The study in this chapter focuses on the erosion-filtration process. A simple elastic model has been used to describe the skeleton behavior and, thus, to compute the displacement field evolution according to the change of effective stresses due to the pore pressure evolution. In the selected experimental tests, the loading is purely hydraulic. Note that the irreversible coupling between mechanics and hydraulics, *i.e.* the influence of the volume deformation on the evolution of the porosity and, in turn, on the permeability has been implicitly considered by introducing the volume change in the mass balance equations: Eq. (9)-(12). The complete hydro-mechanical coupling can be easily enhanced by considering an accurate non-linear elastoplastic model. In the cases of external mechanical loadings applied on the boundaries, the strength changes induced by the evolution of the porosity and the fines content are then considered. This aspect will be discussed in Chapter 5.

Eq.(3.9) describes the behavior of the solid phase (solid skeleton and erodible fines). Eq.(3.10) represents the balance of volume of the erodible fines, whereas Eq.(3.11) is the balance of volume of the fluidized particles. The balance of the mass of the mixture, *i.e.*, the continuity equation, is given by Eq.(3.12).

Note that the amount of erodible fines f_c can be obtained explicitly from the current porosity ϕ and the volumetric strain ε_v, which indicates that Eq.(3.10) can be replaced by :

$$f_c = 1 - \frac{(1+\varepsilon_v)(1-\phi_0)(1-f_{c0})}{1-\phi}$$ ....(3.17)

where $\phi_0(x)$ and $f_{c0}(x)$ denote the initial value of $\phi(x,t)$ and $f_c(x,t)$, respectively.

3.2.2. Erosion law: coupling of erosion and filtration

The variable $\hat{n}$ in Eqs.(3.9)-(3.12) is the volume of mass exchange, which corresponds to the rate of eroded mass volume ($\hat{n}_e$) and filtrated mass volume ($\hat{n}_f$) at any time and any point.

$$\hat{n} = \hat{n}_e + \hat{n}_f$$ ....(3.18)

A model for the rate of the eroded mass is given by the relation [95]:

$$\hat{n}_e = -\lambda_e(1-\phi)(f_c - f_{c\infty})|\mathbf{q_w}|$$ ....(3.19)

where $f_{c\infty}$ is the ultimate fine content fraction after a long seepage period, λ_e is a material parameter. The ultimate fine content fraction $f_{c\infty}$ is assumed to be decreasing with the increase of the hydraulic gradient [67] as

$$f_{c\infty} = f_{c0}\left[(1-\alpha_1)\exp\left(-|\mathbf{q_w}|\times10^{\alpha_2}\right)+\alpha_1\right]$$ ....(3.20)

where f_{c0} is the initial fine content fraction, α_1 and α_2 are material parameters. The term $(f_c - f_{c\infty})$ in Eq.(3.19) corresponds to the residual fine content fraction. The erosion rate depends not only on the total discharge of liquid $\mathbf{q_w}$ but also on the residual fine content fraction as shown by Eq.(3.19).

It is assumed that, with an increasing concentration of transported fine particles, the probability of the existence of the filtration phenomenon in the system of pore canals will also increase. The following model for the rate of the filtrated mass is suggested:

$$\hat{n}_f = \lambda_f \frac{\phi - \phi_{min}}{\phi^\beta}c|\mathbf{q_w}|$$ ....(3.21)

where λ_f and β are material parameters, ϕ_{min} is the minimum porosity of the soil mixture. The probability of filtration increases with an increasing discharge of the fluidized particles ($c|\mathbf{q_w}|$). Moreover, the filtration process is expected to be more intense in intact regions, which are characterized by smaller pore canals, i.e. smaller porosity. β is related to the heterogeneity of the soil mixture, which is discussed in the following section.

Note that the erosion and filtration laws were selected so that the necessary features of soil behavior would be introduced as simply as possible. For more precise predictive ability, these two laws may need to be revised as more documented experimental data becomes available.

3.2.3. Porous fluid flow

In this study, it is assumed that the flow in the porous medium is governed by Darcy's law which states that the flow rate is driven by the gradient of the pore fluid pressure $p_w(x,t)$:

$$q_w = -\frac{k(f_c, \phi)}{\eta_k \bar{\rho}(c)} \frac{\partial(p_w)}{\partial x} \quad\text{...(3.22)}$$

where $k(f_c, \phi)$ denotes the intrinsic permeability of the medium, η_k is the kinematic viscosity of the fluid, p_w is the pore fluid pressure, and $\bar{\rho}(c)$ is the density of the mixture defined as:

$$\bar{\rho} = c\rho_s + (1-c)\rho_f \quad\text{..(3.23)}$$

with ρ_s the density of the solid and ρ_f the density of the fluid. For a mixture, the intrinsic permeability $k(x,t)$ of the porous medium depends on the current porosity $\phi(x,t)$ and on the fine content fraction as [130]:

$$k = k_0 \left(1 - \varphi_v\right)^{3m} \quad\text{...(3.24)}$$

where m is the so-called "cementation exponent" and varies with the pore geometry. A high value of the cementation exponent indicates a strong decoupling between the total interconnected porosity and the effective porosity that controls the flow. $\varphi_v(x,t)$ is the volume fraction of the fine content:

$$\varphi_v = f_c (1 - \phi) \quad\text{...(3.25)}$$

3.3. Finite difference based numerical solution

This chapter focuses on one-dimensional suffusion problems along the x axis, chosen normal to the free surface and pointing downward into the interior of the specific finite domain (see Figure 3.2).

By combining Eqs. (3.9)-(3.25), the governing equations for the pore pressure $p_w(x,t)$, the porosity $\phi(x,t)$ and the concentration of fluidized particles $c(x,t)$ can be expressed as follows under one-dimensional condition:

$$\frac{\partial(p_w)}{\partial t} - \frac{Ek(f_c, \phi)}{\eta \bar{\rho}(c)} \frac{\partial^2(p_w)}{\partial x^2} = 0 \quad\text{...(3.26)}$$

$$\frac{\partial \phi}{\partial t} + \frac{\partial u}{\partial t} \frac{\partial \phi}{\partial x} - \frac{\partial \varepsilon_v}{\partial t} \phi + \frac{\partial \varepsilon_v}{\partial t} + \left(-\lambda_e (1-\phi)(f_c - f_{c\infty}) + \lambda_f \frac{\phi - \phi_{min}}{\phi^\beta} c\right)|q_w| = 0 \quad\text{...............................(3.27)}$$

$$\frac{\partial c}{\partial t} + \left(\frac{q_w}{\phi} + \frac{\partial u}{\partial t}\right) \frac{\partial c}{\partial x} + \frac{1}{\phi}\left[\frac{\partial \phi}{\partial t} + \mathrm{div}(q_w) + \frac{\partial \phi}{\partial x} \frac{\partial u}{\partial t} - \phi \frac{\partial \varepsilon_v}{\partial t}\right] c$$
$$+ \frac{1}{\phi}\left(-\lambda_e (1-\phi)(f_c - f_{c\infty}) + \lambda_f \frac{\phi - \phi_{min}}{\phi^\beta} c\right)|q_w| = 0 \quad\text{..................................(3.28)}$$

The coupled non-linear problem is supplemented by the following boundary and initial conditions:

$$p_w(x_0, t) = p_0, \; p_w(x_L, t) = p_L, \; c(x_0, t) = c_0, \; \frac{\partial c(x_L, t)}{\partial t} = 0 \quad\text{...(3.29)}$$

$$p_w(x,0) = 0, \; c(x,0) = 0, \; \phi(x,0) = \phi_0(x), \; f_c(x,0) = f_{c0}(x) \quad\text{..(3.30)}$$

The initial porosity and the initial fine content depend on the homogeneity of the soil, which can vary along the space.
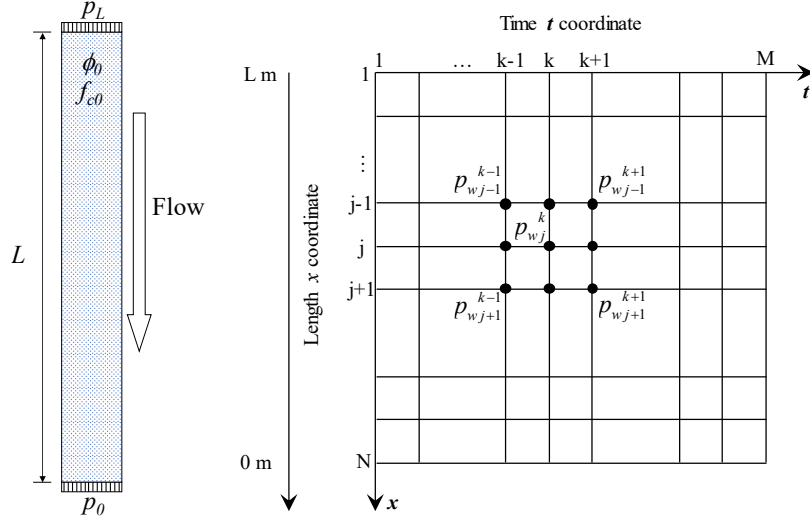
Figure 3.2 Geometry and finite difference grid in space-time of analyzed 1-D internal erosion

Eqs. (3.26)-(3.28) make up an unsteady, coupled non-linear system of partial differential equations. The current state of the system depends on its previous state. The primary unknowns are the pore pressure $p_w(x,t)$, the porosity $\phi(x,t)$, and the transport concentration $c(x,t)$. Other unknowns such as displacement $u(x,t)$, attached fine content $f_c(x,t)$ and flow rate $q_w(x,t)$ can be determined explicitly by Eqs. (3.15), (3.17) and (3.22).

This system of partially differential equations has been solved through an explicit finite difference procedure. With the terminology shown in Figure 3.2, Eqs. (3.26)-(3.28) become

$$\frac{p_{wj}^{k+1}-p_{wj}^{k}}{\Delta t}-\frac{\left[A_{p_w}\right]_{j+1/2}^{k}\left(p_{wj+1}^{k+1}-p_{wj}^{k+1}\right)+\left[A_{p_w}\right]_{j-1/2}^{k}\left(p_{wj}^{k+1}-p_{wj-1}^{k+1}\right)}{\left(\Delta x\right)^2}=0 \quad \text{.................................(3.31)}$$

$$\frac{\phi_j^{k+1}-\phi_j^{k}}{\Delta t}+\left[A_\phi\right]_j^{k}\frac{\phi_j^{k+1}-\phi_{j-1}^{k+1}}{\Delta x}+\left[B_\phi\right]_j^{k}\phi_j^{k}+\left[C_\phi\right]_j^{k}=0 \quad \text{..(3.32)}$$

$$\frac{c_j^{k+1}-c_j^{k}}{\Delta t}+\left[A_c\right]_j^{k}\frac{c_j^{k+1}-c_{j-1}^{k+1}}{\Delta x}+\left[B_c\right]_j^{k}c_j^{k}+\left[C_c\right]_j^{k}=0 \quad \text{...(3.33)}$$

with

$$\left[A_{p_w}\right]_{j-1/2}^{k}=\left(\frac{0.5}{\left[A_{p_w}\right]_{j-1}^{k}}+\frac{0.5}{\left[A_{p_w}\right]_{j}^{k}}\right)^{-1},\quad \left[A_{p_w}\right]_{j+1/2}^{k}=\left(\frac{0.5}{\left[A_{p_w}\right]_{j}^{k}}+\frac{0.5}{\left[A_{p_w}\right]_{j+1}^{k}}\right)^{-1},\quad \left[A_{p_w}\right]_{j}^{k}=\left[\frac{Ek\left(f_c,\phi\right)}{\eta\bar{\rho}(c)}\right]_j^{k}$$

$$A_\phi=\frac{u_j^{k+1}-u_j^{k}}{\Delta t},\quad B_\phi=-\frac{\varepsilon_{vj}^{k+1}-\varepsilon_{vj}^{k}}{\Delta t},\quad C_\phi=\frac{\varepsilon_{vj}^{k+1}-\varepsilon_{vj}^{k}}{\Delta t}+\left[\left(-\lambda_e\left(1-\phi\right)\left(f_c-f_{c\infty}\right)+\lambda_f\frac{\phi-\phi_{\min}}{\phi^\beta}c\right)|q_w|\right]_j^{k}$$

$$A_c=\left(\left[\frac{q_w}{\phi}\right]_j^{k}+\frac{u_j^{k+1}-u_j^{k}}{\Delta t}\right),\quad B_c=\frac{1}{\phi_j^{k}}\left(\frac{\phi_j^{k+1}-\phi_j^{k}}{\Delta t}+\left[\operatorname{div}\left(q_w\right)\right]_j^{k}+\frac{\phi_{j+1}^{k}-\phi_{j-1}^{k}}{2\Delta x}\frac{u_j^{k+1}-u_j^{k}}{\Delta t}-\phi_j^{k}\frac{\varepsilon_{vj}^{k+1}-\varepsilon_{vj}^{k}}{\Delta t}\right),$$

$$C_c = \left[\left(-\lambda_e (1-\phi)(f_c - f_{c\infty}) + \lambda_f \frac{\phi - \phi_{\min}}{\phi^\beta} c \right) |q_w| / \phi \right]_j^k$$

where the subscripts $j(0,1...,N)$ represent the variation in length, described by the x co-ordinate, and the subscripts $k(0,1...,M)$ represent the variation in the time t co-ordinate. $k(f_c, \phi)$, $\bar{p}(c)$ and $q_w(x,t)$ vary with depth and time. As a simple approximation, their values at (j, k) are used.

Defining $r_1 = \Delta t / (\Delta x)^2$ and $r_2 = \Delta t / \Delta x$ allows the Eqs. (3.31) - (3.33) to be rewritten

$$-r_1 \left[A_{p_w} \right]_{j-1/2}^k p_{wj-1}^{k+1} + \left\{ 1 + r_1 \left(\left[A_{p_w} \right]_{j-1/2}^k + \left[A_{p_w} \right]_{j+1/2}^k \right) \right\} p_{wj}^{k+1} - r_1 \left[A_{p_w} \right]_{j+1/2}^k p_{wj+1}^{k+1} = p_{wj}^k \quad ....(3.34)$$

$$-r_2 A_\phi \phi_{j-1}^{k+1} + (1 + r_2 A_\phi) \phi_j^{k+1} = (1 - \Delta t B_\phi) \phi_j^k - \Delta t C_\phi \quad ....(3.35)$$

$$-r_2 A_c c_{j-1}^{k+1} + (1 + r_2 A_c) c_j^{k+1} = (1 - \Delta t B_c) c_j^k - \Delta t C_c \quad ....(3.36)$$

Eqs. (3.34)-(3.36) can then be solved with initial and boundary conditions for $p_w(x,t)$, $\phi(x,t)$, $c(x,t)$ given in Eqs. (3.29)-(3.30). The model has been coded with MATLAB software [131]. To obtain accuracy and run-time efficiency, the sensitivity of the results to space and time increments was examined. The computations of the following sections were carried out with $\Delta x = 5 \times 10^{-4}$ m (100 nodes) and 2000 increments in time. The above finite difference scheme can be easily extended to analyze a two-dimensional or three-dimensional seepage flow, as it will be presented in the next chapter.

3.4. Numerical simulations of laboratory tests

Two series of erosion tests on cohesionless soils were selected to examine the model performances: (1) Series A: Rochim et al. [24] performed hydraulic-gradient controlled downward erosion tests on gap-graded sand and gravel mixtures to evaluate the effects of the hydraulic loading history on the suffusion susceptibility of cohesionless soils, and (2) Series B: Aboul Hosn [132] performed flow-rate controlled downward erosion tests on gap-graded mixtures of coarse and fine silica Hostun sand in order to investigate the effects of the soil density on suffusion.

3.4.1. Series A

The experimental set-up consisted of a modified triaxial cell surrounded by a steel mold to ensure the oedometric condition, a pressurized water supply system, and a water/soil collecting system. The specimens of 50 mm in diameter and 50 mm in height were prepared by using a single layer semi-static compaction technique, and then placed on a 4 mm pore opening grid to allow the migration of all sand particles. Two values of the initial dry density were targeted: 90% and 97% of the optimum Proctor density. After saturating the sample with an upward interstitial flow, the fluid was forced through the sample in the downward direction during the erosion test. Three gap-graded sand-gravel mixtures with different initial fine contents (20% for soil A, 25% for soil B and 29% for soil C) under two different hydraulic loadings were simulated. Figure 3.3 shows the time evolution of the applied hydraulic gradients. The first multi-stage hydraulic gradient condition (named a) consisted of increasing the hydraulic gradient by steps of 0.1, 0.15, 0.2 and 0.25 up to 0.5, 0.8, 1 and 2, respectively, then by steps of 0.5 between 2 and 4 and by steps of 1 beyond 4. For the second

kind of hydraulic loading named (b), the hydraulic gradient increment was directly imposed equal to 1. For both hydraulic loadings, each stage of the hydraulic gradient was kept constant for 10 min. Table 2 summarizes the initial dry density and initial permeability of the tested specimens, the values of the applied hydraulic gradient, and the duration of each test.

Table 3.1 properties of simulated test specimens

Soil reference	Specimen reference	Initial dry density γ_d (kN/m³)	Initial permeability k (m/s)	Applied hydraulic gradient, i	Test duration (min)
A	A90-a	17.39	1.2×10^{-5}	Type a, from 0.1 to 15	270
	A90-b	17.39	2.0×10^{-5}	Type b, from 1 to 13	130
B	B97-a	18.74	1.3×10^{-5}	Type a, from 0.1 to 12	240
	B97-b	18.74	2.0×10^{-5}	Type b, from 1 to 9	90
C	C97-a	18.74	1.2×10^{-5}	Type a, from 0.1 to 9	210
	C97-b	18.74	2.0×10^{-5}	Type b, from 1 to 7	70
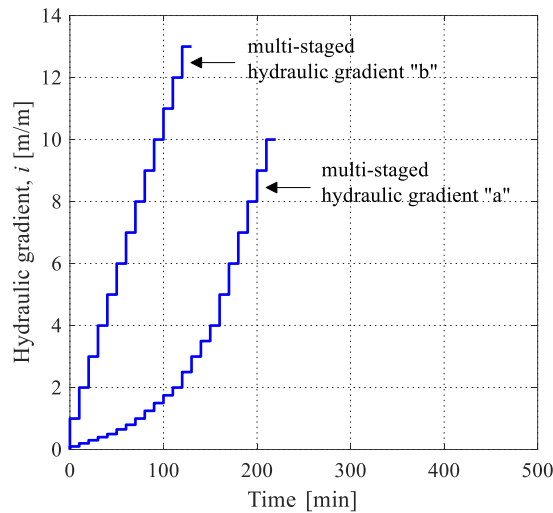
Figure 3.3 Time evolution of multi-staged hydraulic gradients

The physical properties of the soil mixtures are summarized in Table 3.2, taken directly from the referred laboratory tests [24]. The erosion parameters (λ_e , α_1 and α_2), filtration parameters (λ_f and β) and permeability parameter (m) were calibrated by fitting the evolution of the hydraulic conductivity and the cumulative loss of dry mass in the soil mixture C (shown by the blue lines in Figure 3.4) by a trial-error procedure for the hydraulic loadings (a) and (b). An alternative way would be to use optimization techniques [133, 134]. All the values of the model parameters, summarized in

Table 3.3, were used to predict the other tests.

Table 3.2 Physical properties of the soil mixtures

Density of fluid	ρ_f	1.0 g/cm³
Density of solids	ρ_s	2.65 g/cm³
Kinematic viscosity of fluid	η_k	5.0×10^{-6} m²s⁻¹

Minimum porosity	$\phi_{\min}$	0.22

Table 3.3 Values of model parameters for tested soil mixtures A, B and C

Tests	Erosion parameters				Filtration parameters			Permeability parameter
	λ_e	α_1	α_2		λ_f	β		m
Series A	151.6	0.89	3.42		170.6	1.0		16
Series B	3.1	0.74	2.68		13.4	1.0		16

Figure 3.4 presents the comparison between experimental and numerical results of erosion tests on three types of soil mixtures in the case of hydraulic loadings (a) and (b). It shows that the history of the hydraulic loading and the initial fine content affect significantly the hydraulic behavior of the tested soil mixtures. Two phases can be distinguished from the time evolution of the hydraulic conductivity. At first, the hydraulic conductivity slowly increased or decreased, depending on the hydraulic loading type. The duration of this first phase was much longer under less severe hydraulic loading. For a given hydraulic loading, the decreasing phase was longer for a specimen with a smaller initial fine content. These results illustrate a positive correlation between the erosion rate and the initial fine content. The second phase of the hydraulic conductivity evolution was characterized by its rapid increase. Finally, the hydraulic conductivity reached a constant value.

The proposed model was able to reproduce the two phases of the erosion until a stable stage was reached. However, in some cases, discrepancies between experimental and numerical hydraulic conductivity evolution could be found, especially during the first phase. Only few data are available in the literature concerning the self-filtration phenomenon during an erosion test. Ke and Takahashi [30, 33] attributed the deviation of the hydraulic conductivity to the difference in homogeneity along the reconstituted soil specimens. Another aspect which has not been taken into account is the unknown influence of the saturation stage, which may also lead to the heterogeneity of the soil sample before erosion. The influence of the soil heterogeneity is discussed in the following section.

The predicted eroded mass can be calculated by [39]:

$$\Delta M = \rho_s \int_0^L \left[\phi(1-c) - \phi_0(1-c_0) \right] dx \quad\dots\dots\dots\dots\dots\dots\dots\dots\dots\dots\dots\dots\dots\dots\dots\dots\dots\dots\dots\dots\dots(3.37)$$

Marot et al. [29] proposed an energy-based method to characterize the erosion susceptibility. The authors suggested characterizing the fluid loading by the total flow power P_{flow}, expressed as

$$P_{\text{flow}} = q_w \gamma_w \Delta h \quad\dots\dots\dots\dots\dots\dots\dots\dots\dots\dots\dots\dots\dots\dots\dots\dots\dots\dots\dots\dots\dots\dots\dots\dots\dots\dots\dots(3.38)$$

where q_w is the flow rate; γ_w is the unit weight of water; Δh is the drop of hydraulic head. In series A, Rochim et al. [24] characterized the evolution of the cumulative eroded mass with the variation of the cumulative expended energy E_{flow}, computed by the time integration of the instantaneous flow power P_{flow}.

Experimental and numerical values of the eroded mass are in good agreement for the calibration tests C97-a and C97-b, but also for other validation tests differing from the initial fine content and

the hydraulic loading history. However, the prediction of the eroded mass is not totally in agreement with the experimental data for tests A90-a and A90-b. The eroded masses represent only 0.4% (test A90-a) and 1.2% (test A90-b) of their initial fine content, whereas the hydraulic conductivity increased by a factor of 9 (test A90-a) and 4 (test A90-b) in the second phase of the hydraulic conductivity evolution. Obviously, such small loss mass should not in itself result in such a rapid increase of the hydraulic conductivity. This discrepancy could be explained by the early presence of preferential flows created by particle rearrangements in the case of a lower initial fine content of the soil.
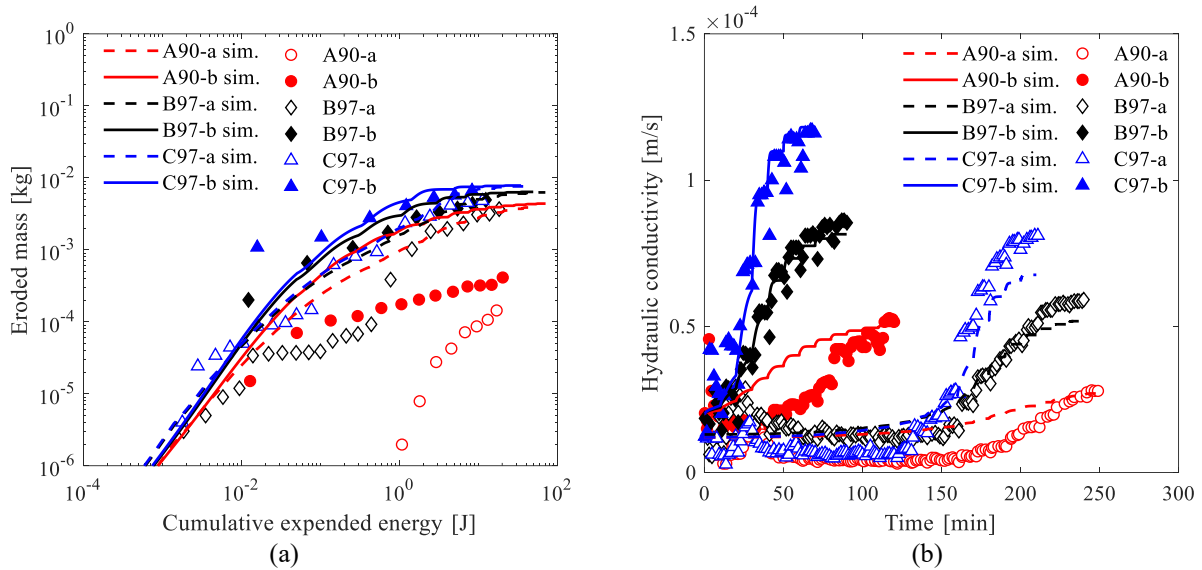
Figure 3.4 Comparison between laboratory tests (symbols) and simulated data (continuous lines): (a) cumulative eroded masses versus cumulative expended energy; (b) time evolution of hydraulic conductivity

3.4.2. Series B

Similar erosion tests on gap-graded mixtures of coarse and fine silica Hostun sand were performed by Aboul Hosn [132] to investigate the effects of the soil density on suffusion. The suffusion tests were carried out using a newly developed permeameter made up of a cylindrical Plexiglass cell (140 mm in height and 70 mm in internal diameter), a pressurized water supply system and a fine collector. Three soil samples with the same initial fine content ($f_c = 25\%$) and three different relative densities (0.2, 0.4, 0.6) were subjected to erosion tests by flushing water in the downward direction under a controlled multi-stage flow rate. The model parameters summarized in

Table 3.3 were calibrated by fitting simultaneously the evolution of the hydraulic conductivity and the cumulative loss of dry mass in test ES-0.2-CD (shown by the red lines in Figure 3.5) by a trial-error procedure. They were then used to predict the other tests of Series B.
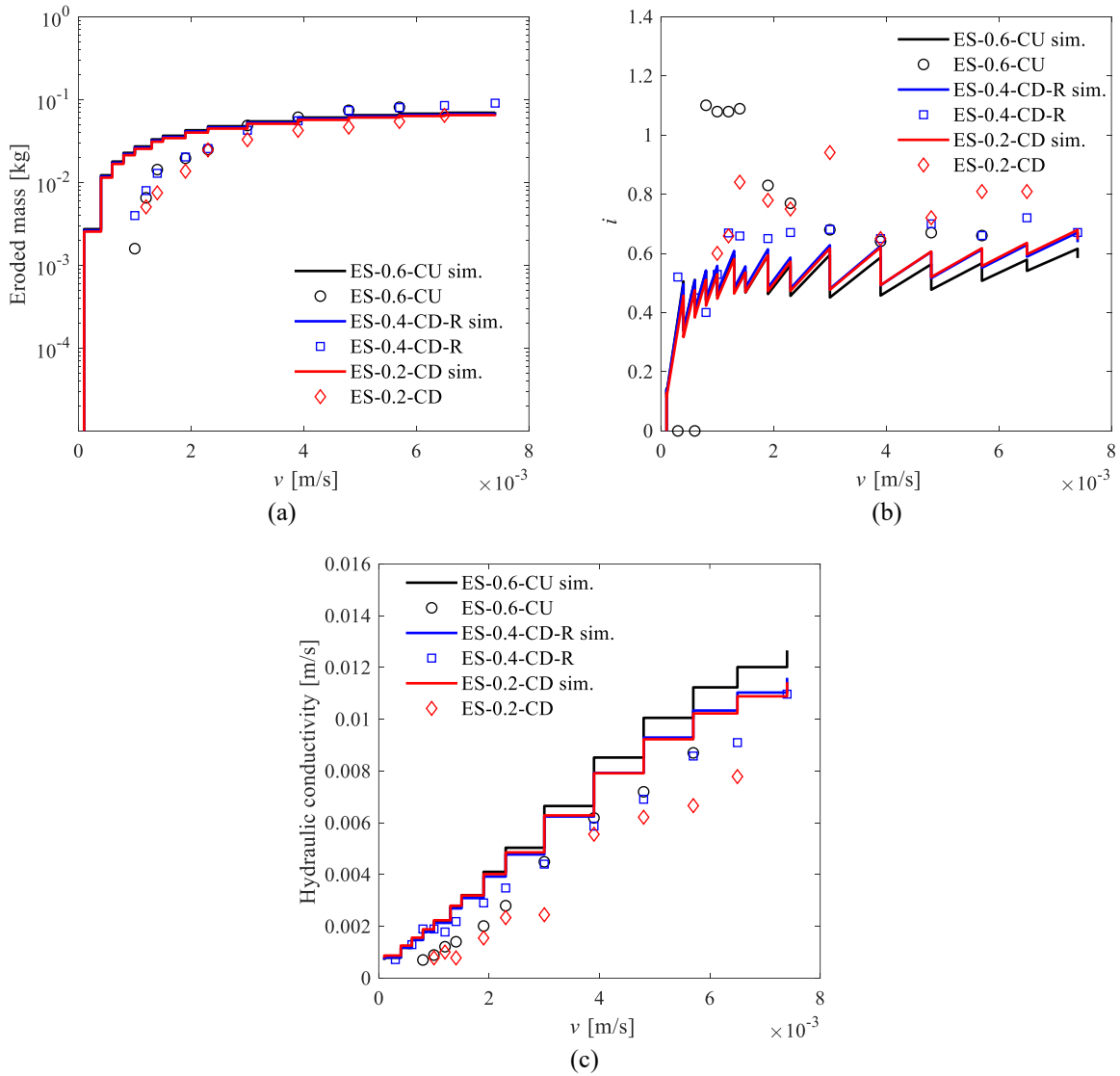
Figure 3.5 Comparison between laboratory tests (symbols) and simulated data (continuous lines) for three different initial densities: (a) the variation of cumulative eroded masses with the increasing flow rate; (b) the variation of hydraulic gradient, i, with the increasing flow rate; (c) the variation of hydraulic conductivity with the increasing flow rate

The comparison between experimental and numerical results of the erosion tests with three different relative densities (Id=0.2, 0.4, 0.6) is presented in Figure 3.5. The curves show similar tendencies. With the increase in Darcy's flow velocity, the eroded mass increased with time at a gradual decrease rate. The deviations of the experimental results appear to be very small, possibly due to the minor differences of their initial porosity (0.36, 0.34, 0.32 for Id=0.2, 0.4, 0.6, respectively). The proposed model was able to capture the main features of the flow-rate controlled erosion tests.

3.5. Discussion

Comparing the time evolution of the hydraulic conductivity with the measured eroded mass constitutes a way to improve the understanding of the suffusion process. Figure 3.6 shows how the numerical results depend on the choice of the parameter β which controls the filtration rate (Eq.

22). The complex phenomenon of suffusion appears to be a combination of three processes: detachment, transport, and filtration of the finer fraction. This combination results in the development of heterogeneities in the soil grading. Experimental results [24, 68] showed that the loss of fine particles is higher in the upstream part. The transport of detached particles from upstream to downstream can partly offset the loss of particles in the downstream region. The spatial profiles of porosity at different time steps for different values of β are compared in Figure 3.7. A larger value of β leads to a more severe soil heterogeneity at the early stage of the suffusion, which suggests that more detached particles are filtered in the downstream part of the soil. However, to calibrate the value of β, it is necessary to measure the concentration of fluidized particle within the outlet flow at discrete times during an experiment. Under a given hydraulic gradient condition, a strong increase of the concentration of fluidized particle in the outlet flow occurs simultaneously to the rapid increase of the hydraulic conductivity, as shown in Figure 3.8. For a given density, a lower fine content is accompanied by a larger amount of coarse particles and a smaller constriction size within the porous network, which facilitates the filtration process.
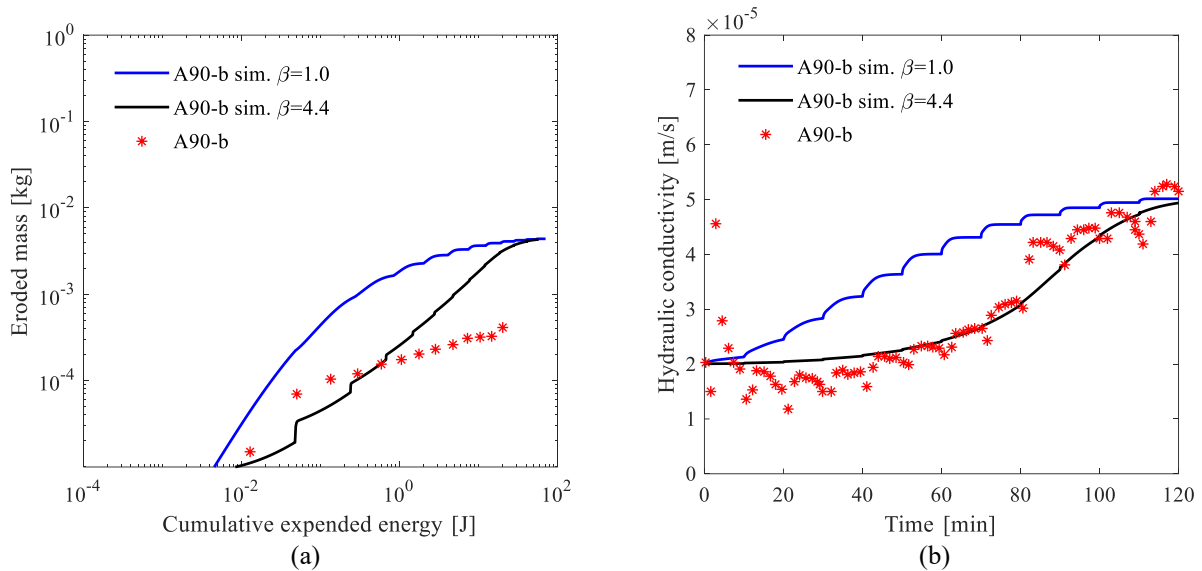
Figure 3.6 Comparison between laboratory tests (symbols) and simulated data (continuous lines) for different values of β: (a) cumulative eroded masses versus cumulative expended energy; (b) time series of hydraulic conductivity

46
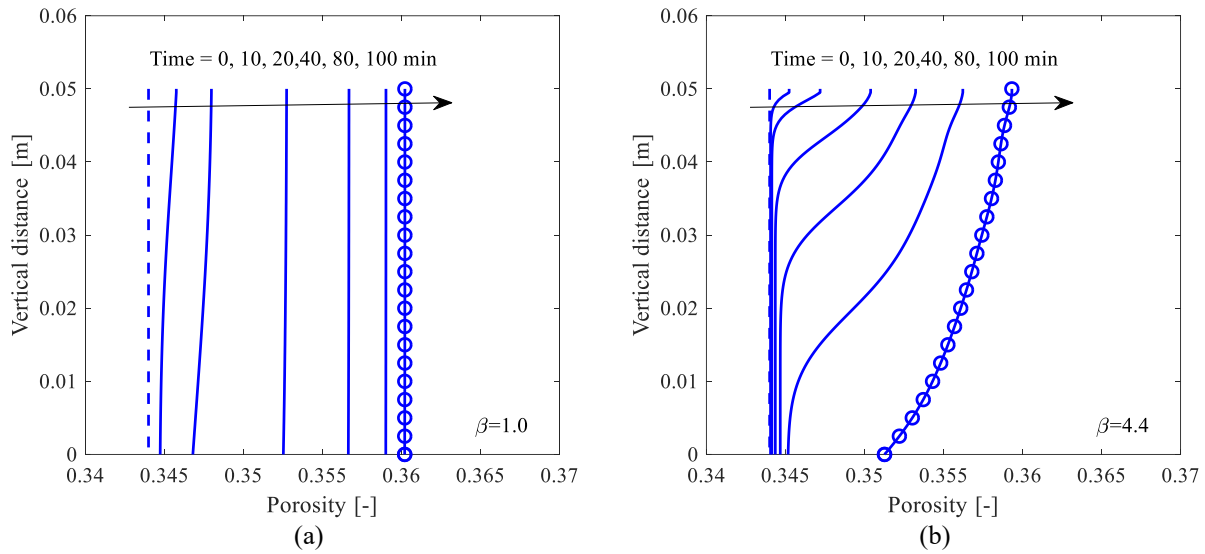
Figure 3.7 Spatial profiles of porosity at various time steps: (a) $\beta = 1.0$; (b) $\beta = 4.4$
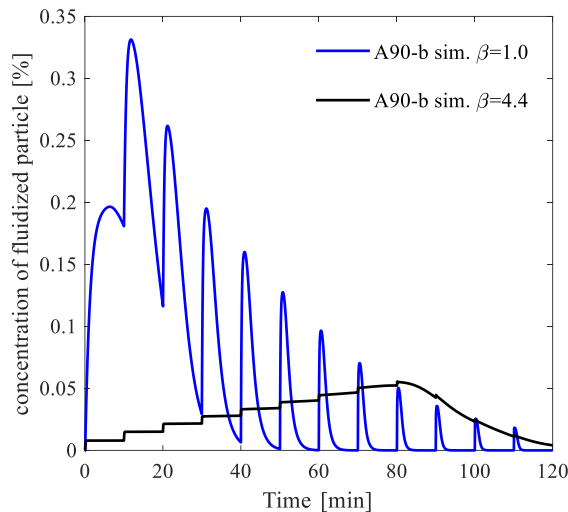
Figure 3.8 Comparison of the concentration of fluidized particle of the outlet flow for different values of β

The rapid decrease of the hydraulic conductivity is systematically accompanied by a clogging of the pores. The compaction of the reconstituted soil specimens and the disturbance during the saturation stage may lead to initially heterogeneous soil samples. Fine particles that are displaced can fill certain pores during compaction and saturation. Figure 3.10 compares experimental and numerical results for different soil homogeneities. The initial fine content and the corresponding porosity are presented in Figure 3.9.
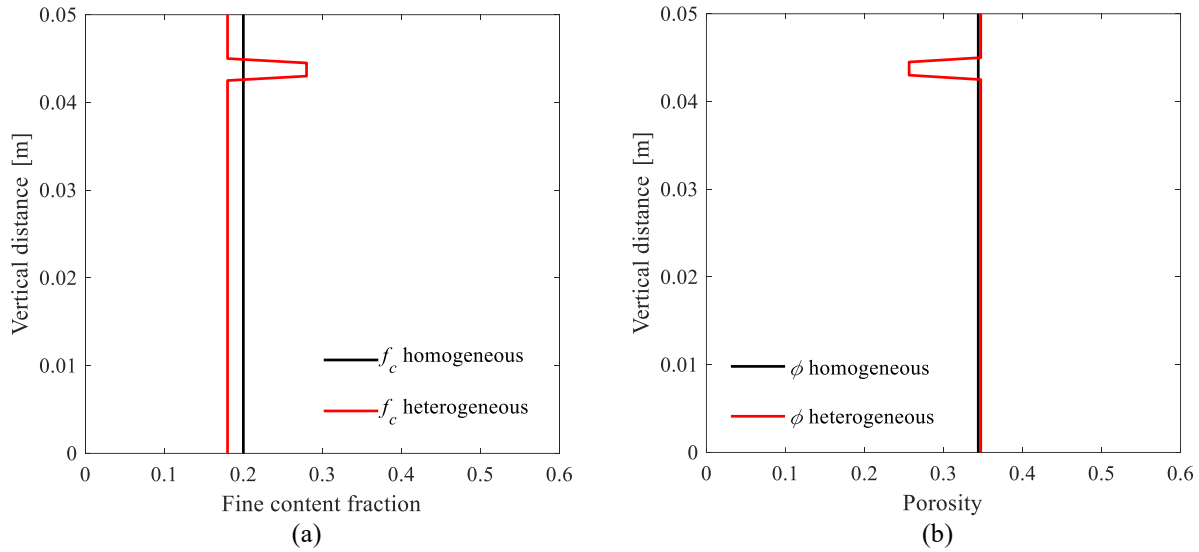
Figure 3.9 Initial soil state before erosion for different soil homogeneity: (a) initial fine content fraction; (b) initial porosity

A clogging, at first restricting the water flow, can then be blown away, accompanied by a significant increase of the hydraulic conductivity. Thus, the predominant process during the second phase is the detachment and transport of fine particles. Finally, the hydraulic conductivity tends to stabilize when the hydraulic drag force can no longer transport any more fine particles through the soil skeleton.
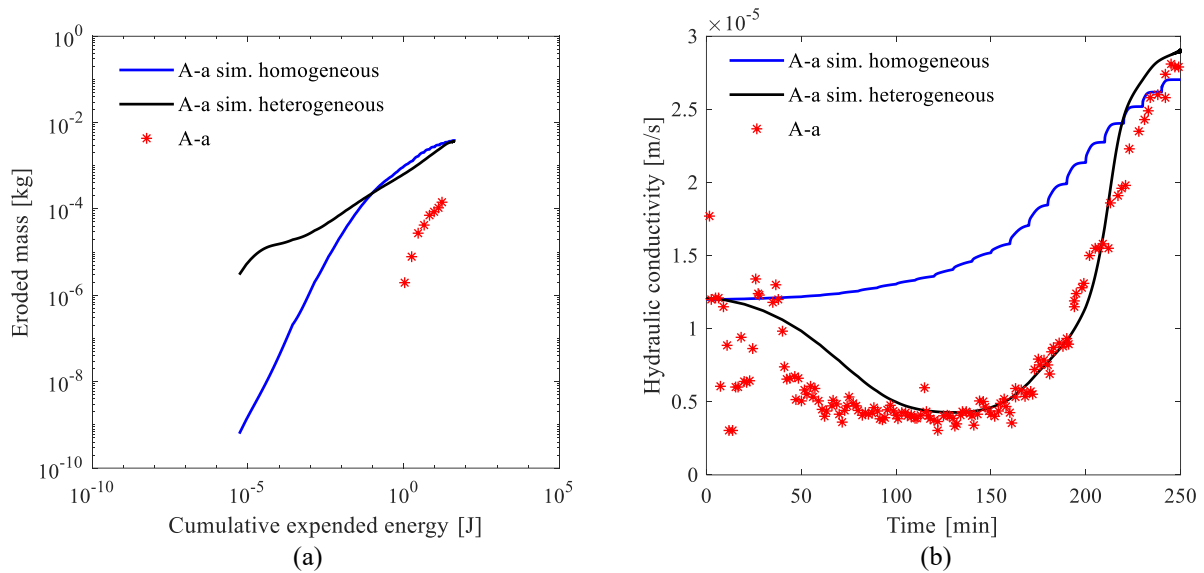
Figure 3.10 Comparison between laboratory tests (symbols) and simulated data (continuous lines) for different soil homogeneity: (a) cumulative eroded masses versus cumulative expended energy; (b) time series of hydraulic conductivity

3.6. Conclusion

This chapter provided a novel contribution to the numerical approach in modeling the internal erosion of soils. The approach consisted of modeling the erosion of the soil skeleton, the transport by the water flow and the filtration of fine particles through the mass exchange between the solid

and fluid phases. The governing differential equations were formulated based on the mass balance of four assumed constituents: the stable fabric of the solid skeleton, the erodible fines, the fluidized particles, and the pure fluid. The terms of mass exchange were introduced into the mass balance equations. It was complemented by a filtration term to simulate the filling of initial voids due to the filtration of transported fines from the suspension to the solid fraction. The model was solved numerically by a finite difference method restricted to 1-D flows normal to the free surface and, accordingly, the hydrodynamic dispersion was disregarded.

Two series of erosion tests on cohesionless soils were selected in order to examine the model performance. Two phases of the suffusion process up to a stable stage could be distinguished from the time evolution of the hydraulic conductivity and both were well reproduced by the model. The hydraulic conductivity first slowly increased, or even decreased, depending on the hydraulic loading history. The second phase of the hydraulic conductivity evolution was characterized by a rapid increase. Finally, the hydraulic conductivity reached a constant value. The results showed that the numerical model is able to describe both erosion and filtration during the tests.

A complementary study on the coupling between erosion and filtration indicated that a larger value of the parameter β controlling the amplitude of filtration leads to a more severe soil heterogeneity at the early stage of the erosion, which suggests that more detached particles are filtered in the downstream part of the soil. Thus, the hydraulic conductivity of the whole specimen could slowly increase or decrease. The second phase of the hydraulic conductivity evolution characterized by a rapid increase occurs simultaneously with the unblocking of the clogged pores. Finally, the hydraulic conductivity reaches a constant value when the hydraulic force is no longer able to drag fine particles through the soil skeleton.

Let us emphasize that the decrease of the hydraulic conductivity at the beginning of erosion is followed by the clogging of the pores. This process is significantly influenced by the initial degree of the heterogeneity of the soils. Note that natural soils are highly heterogeneous. This is why it should be important to perform a stochastic analysis to evaluate the influence of the randomly distributed porosity and fines content on suffusion, as will be discussed in the next chapter.

Chapter 4　Random finite difference analysis of suffusion in cohesionless soils

4.1. Introduction

The analyses performed in the previous chapter have shown that the clogging of the pores is significantly influenced by the initial degree of homogeneity of the soils. Natural or human made soils are seldom homogeneous, which makes suffusion analysis more complex to perform but also more accurate.

Soil characteristics are highly variable in space [135-137] and evolve with time. Such variations could be introduced by its history of formation and further deformations due to natural forces or human activities. In recent years, many researches have attempted to quantify the soil variability and to assess the resulting uncertainty in hydro-mechanical problems by using stochastic approaches. For instance, Freeze [138] performed 1D consolidation by introducing a cross correlation between the coefficient of volumetric compressibility and the soil permeability; Badious et al. [139] investigated 1D consolidation with the thin layer method combined with Monte Carlo simulations; Huang et al. [140] performed systematic 1D and 2D random consolidation analyses over a range of parametric variations using the random field theory [141]. Related works on foundation and slope problems using stochastic approaches can also be found in the literature [142-145].

However, the problem of suffusion has not yet been deeply studied through a systematic probabilistic approach under the framework of the porous continuous medium theory. The aim of this chapter is to contribute to this domain by covering the following points:

(1) to implement within the four-constituent model described previously the random field theory for a Monte Carlo analysis under one-dimensional (1D) and two-dimensional (2D) conditions;

(2) to analyze the influence of the soil heterogeneity on suffusion and to perform a systematic probabilistic study of suffusion. Both the initial porosity and fines content have been considered as random fields, for which the spatial correlation has been taken into account through the random field theory.

The influence of the soil spatial variability on clogging during suffusion will then be discussed.

4.2. Random finite difference analysis

4.2.1. Numerical modeling

According to chapter 3, the four-constituent erosion kinetic equations (3.9)-(3.12), coupled with the erosion-filtration constitutive law equations (3.18)-(3.21), make up an unsteady, coupled non-linear system of partial differential equations. The primary unknowns are the pore pressure $p_w(\underset{\sim}{x},t)$, the porosity $\phi(\underset{\sim}{x},t)$, the fraction of fine content $f_c(\underset{\sim}{x},t)$, and the transport concentration $c(\underset{\sim}{x},t)$. $\underset{\sim}{x}$ denotes the current spatial position, t denotes the current time. In this chapter, this system of partially differential equations are solved through an explicit finite difference procedure under a

one-dimensional (1D) and a two-dimensional (2D) condition for a hydraulic-gradient controlled downward erosion tests on gap-graded sand and gravel mixtures performed by Zhong [146], shown in Figure 4.1. The oedo-permeameter consisted of a 285 mm inner diameter rigid wall cylinder cell, a pressurized water supply system and a water/soil collecting system. A stainless-steel mesh screen was placed on the specimen support. The cell wall was equipped with twelve pressure ports (two arrays of six pressure ports, with a vertical spacing of 100 mm, face to face on opposite cell sides). The specimen of 430 mm in height was placed in the oedo-permeameter. A downward interstitial flow was forced through the specimen to investigate the susceptibility to suffusion after the saturation of the soil specimen.
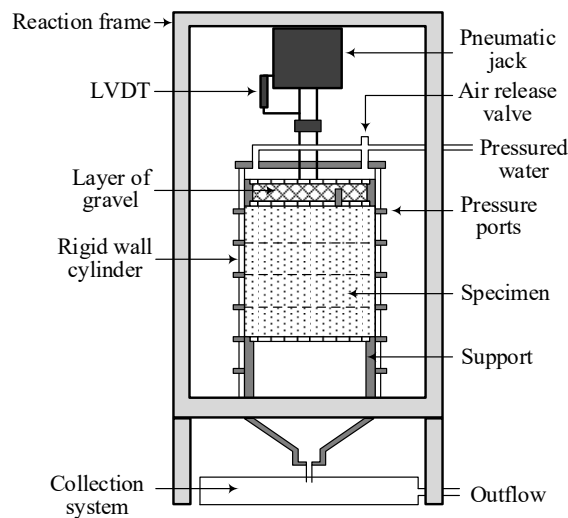
Figure 4.1 Schema of analyzed internal erosion test

Because of the non-linear nature of the analysis, computing the Monte Carlo simulations is labor and time intensive. In this study, the system of partially differential equations was first solved in 1D condition in order to obtain the main influences of the randomly distributed initial porosity and fines content and then, complemented by a set of 2D simulations, to evaluate the effects of dimensionality.
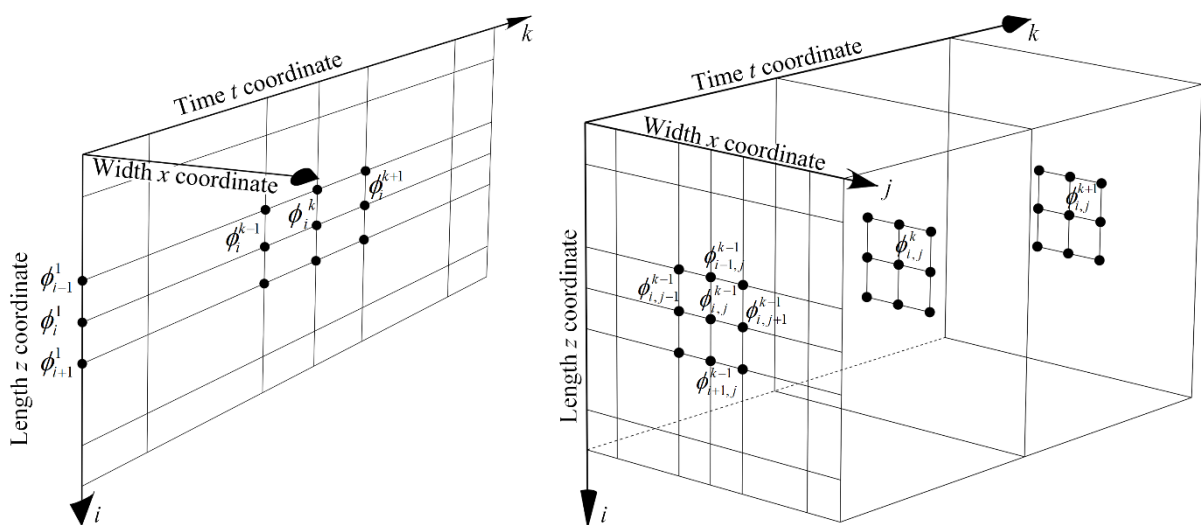
Figure 4.2 Finite difference grid of the primary unknowns (p_w, ϕ, f_c and c) in space-time of analyzed 1D and 2D internal erosion tests

With the terminology shown in Figure 4.2a in 1D condition, Eqs.(3.9), (3.11) and (3.12) become

$$\frac{\phi_i^{k+1} - \phi_i^k}{\Delta t} + \left[A_\phi\right]_i^k \frac{\phi_i^{k+1} - \phi_{i-1}^{k+1}}{\Delta z} + \left[B_\phi\right]_i^k \phi_i^{k+1} + \left[C_\phi\right]_i^k = 0 \quad \dots\dots\dots\dots(4.1)$$

$$\frac{c_i^{k+1} - c_i^k}{\Delta t} + \left[A_c\right]_i^k \frac{c_i^{k+1} - c_{i-1}^{k+1}}{\Delta z} + \left[B_c\right]_i^k c_i^{k+1} + \left[C_c\right]_i^k = 0 \quad \dots\dots\dots\dots(4.2)$$

$$\frac{p_{wi}^{k+1} - p_{wi}^k}{\Delta t} - \frac{\left[A_{p_w}\right]_{i+1/2}^k \left(p_{wi+1}^{k+1} - p_{wi}^{k+1}\right) + \left[A_{p_w}\right]_{i-1/2}^k \left(p_{wi}^{k+1} - p_{wi-1}^{k+1}\right)}{\left(\Delta z\right)^2} = 0 \quad \dots\dots\dots\dots(4.3)$$

where the subscripts $i(1,...,N_1)$ represent the variation in length, described by the z coordinate, and the subscripts $k(1,...,M)$ represent the variation in the time t coordinate. A, B and C are equation coefficients given in chapter 3 for 1D condition.

Similarly, this system of partially differential equations can be extended to 2D condition by (shown in Figure 4.2b):

$$\frac{\phi_{i,j}^{k+1} - \phi_{i,j}^k}{\Delta t} + \left[A_\phi\right]_i^k \frac{\phi_{i,j}^{k+1} - \phi_{i-1,j}^{k+1}}{\Delta z} + \left[A_\phi\right]_j^k \frac{\phi_{i,j}^{k+1} - \phi_{i,j-1}^{k+1}}{\Delta x} + \left[B_\phi\right]_{i,j}^k \phi_{i,j}^{k+1} + \left[C_\phi\right]_{i,j}^k = 0 \quad \dots\dots(4.4)$$

$$\frac{c_{i,j}^{k+1} - c_{i,j}^k}{\Delta t} + \left[A_c\right]_i^k \frac{c_{i,j}^{k+1} - c_{i-1,j}^{k+1}}{\Delta z} + \left[A_c\right]_j^k \frac{c_{i,j}^{k+1} - c_{i,j-1}^{k+1}}{\Delta x} + \left[B_c\right]_{i,j}^k c_{i,j}^{k+1} + \left[C_c\right]_{i,j}^k = 0 \quad \dots\dots(4.5)$$

$$\frac{p_{wi,j}^{k+1} - p_{wi,j}^k}{\Delta t} - \frac{\left[A_{p_w}\right]_{i+1/2}^k \left(p_{wi+1,j}^{k+1} - p_{wi,j}^{k+1}\right) + \left[A_{p_w}\right]_{i-1/2}^k \left(p_{wi,j}^{k+1} - p_{wi-1,j}^{k+1}\right)}{\left(\Delta z\right)^2}$$

$$\dots\dots\dots\dots(4.6)$$

$$- \frac{\left[A_{p_w}\right]_{j+1/2}^k \left(p_{wi,j+1}^{k+1} - p_{wi,j}^{k+1}\right) + \left[A_{p_w}\right]_{j-1/2}^k \left(p_{wi,j}^{k+1} - p_{wi,j-1}^{k+1}\right)}{\left(\Delta x\right)^2} = 0$$

with

$$\left[A_\phi\right]_i^k = \frac{u_{xi,j}^{k+1} - u_{xi,j}^k}{\Delta t}, \quad \left[A_\phi\right]_j^k = \frac{u_{zi,j}^{k+1} - u_{zi,j}^k}{\Delta t}, \left[B_\phi\right]_{i,j}^k = -\frac{\varepsilon_{vi,j}^{k+1} - \varepsilon_{vi,j}^k}{\Delta t}, \quad \left[C_\phi\right]_{i,j}^k = \frac{\varepsilon_{vi,j}^{k+1} - \varepsilon_{vi,j}^k}{\Delta t} + \left[\hat{n}\right]_{i,j}^k$$

$$\left[A_c\right]_i^k = \left(\left[\frac{q_{w,x}}{\phi}\right]_{i,j}^k + \frac{u_{xi,j}^{k+1} - u_{xi,j}^k}{\Delta t}\right), \quad \left[A_c\right]_j^k = \left(\left[\frac{q_{w,y}}{\phi}\right]_{i,j}^k + \frac{u_{yi,j}^{k+1} - u_{yi,j}^k}{\Delta t}\right),$$

$$\left[B_c\right]_{i,j}^k = \frac{1}{\phi_{i,j}^k}\left(\frac{\phi_{i,j}^{k+1} - \phi_{i,j}^k}{\Delta t} + \left[\text{div}(\mathbf{q_w})\right]_{i,j}^k + \frac{\phi_{i,j+1}^k - \phi_{i,j-1}^k}{2\Delta x}\frac{u_{xi,j}^{k+1} - u_{xi,j}^k}{\Delta t} + \frac{\phi_{i+1,j}^k - \phi_{i-1,j}^k}{2\Delta z}\frac{u_{zi,j}^{k+1} - u_{zi,j}^k}{\Delta t} - \phi_{i,j}^k\frac{\varepsilon_{vi,j}^{k+1} - \varepsilon_{vi,j}^k}{\Delta t}\right),$$

$$\left[C_c\right]_{i,j}^k = \left[\hat{n}/\phi\right]_{i,j}^k$$

$$\left[A_{p_w}\right]_{i-1/2}^k = \left(\frac{0.5}{\left[A_{p_w}\right]_{i-1,j}^k} + \frac{0.5}{\left[A_{p_w}\right]_{i,j}^k}\right)^{-1}, \quad \left[A_{p_w}\right]_{i+1/2}^k = \left(\frac{0.5}{\left[A_{p_w}\right]_{i,j}^k} + \frac{0.5}{\left[A_{p_w}\right]_{i+1,j}^k}\right)^{-1}$$

$$\left[A_{p_w}\right]^k_{j-1/2} = \left(\frac{0.5}{\left[A_{p_w}\right]^k_{i,j-1}} + \frac{0.5}{\left[A_{p_w}\right]^k_{i,j}}\right)^{-1}, \quad \left[A_{p_w}\right]^k_{j+1/2} = \left(\frac{0.5}{\left[A_{p_w}\right]^k_{i,j}} + \frac{0.5}{\left[A_{p_w}\right]^k_{i,j+1}}\right)^{-1}$$

$$\left[A_{p_w}\right]^k_{i,j} = \left[\frac{K_{\text{MOD}} k(f_c,\phi)}{\eta \bar{\rho}(c)}\right]^k_{i,j}$$

where the subscripts $j(1,...,N_2)$ represent the variation in width, described by the x coordinate. $\mathbf{u}(u_x,u_z)$ indicates the displacement field of the soil skeleton. The volumetric strain ε_v are then calculated under small strain assumption using an elastic model with bulk modulus K_{MOD}. The strength degradation induced by the evolution of the porosity and the fines content are discussed in chapter 5.

Note that the amount of erodible fines f_c can be obtained explicitly from the current porosity ϕ and the volumetric strain ε_v according to Eq. (3.17). Eqs. (4.1) - (4.6) can then be coded and solved with the MATLAB software [131] with the given boundary conditions and initial values for p_w, ϕ, c:

$$\left(p_w\right)^k_{i=1,j} = p_0, \quad \left(p_w\right)^k_{i=N_1,j} = p_L, \quad c^k_{i=1,j} = c_0, \quad c^k_{i=N_1,j} = c^k_{i=N_1-1,j} \quad \text{................................}(4.7)$$

$$\left(p_w\right)^1_{i,j} = 0, \quad c^1_{i,j} = 0, \quad \phi^1_{i,j} = \phi_0(\underset{\sim}{x}), \quad \left(f_c\right)^1_{i,j} = f_{c0}(\underset{\sim}{x}) \quad \text{................................}(4.8)$$

4.2.2. Random field modeling of initial porosity and fines content

In this study, the initial porosity ϕ_0 and the initial fines content fraction f_{c0} within the soil mass are spatially varied. The initial fines content fraction f_{c0} is assumed to be lognormally distributed with the mean value $\mu_{f_{c0}}$, standard variation $\sigma_{f_{c0}}$ and spatial correlation length $\theta_{\ln f_{c0}}$. The lognormal distribution is one of many possible choices, which will guarantee non-negative soil properties. The lognormal distribution of f_{c0} means that $\ln f_{c0}$ is normally distributed and the standard variation $\sigma_{f_{c0}}$ and mean $\mu_{f_{c0}}$ of the normal distribution of $\ln f_{c0}$ are given by:

$$\sigma_{\ln f_{c0}} = \sqrt{\ln\left[1+\left(\sigma_{f_{c0}}/\mu_{f_{c0}}\right)^2\right]} \quad \text{................................}(4.9)$$

$$\mu_{\ln f_{c0}} = \ln \mu_{f_{c0}} - \frac{1}{2}\sigma^2_{\ln f_{c0}} \quad \text{................................}(4.10)$$

In this study, the random fields were generated with the local average subdivision (LAS) method [147]. Each discrete local average given by a realization becomes the average property within each discrete element. The lognormal random field $f_{c0}(\underset{\sim}{x})$ has been obtained by first simulating a normally distributed random field $G_{\ln f_{c0}}(\underset{\sim}{x})$, having zero mean, unit variance and an autocorrelation function $\rho_{\ln f_{c0}}(\underset{\sim}{x})$. An anisotropic exponential autocorrelation function has been adopted, which is expressed in 2D condition as:

$$\rho_{\ln f_{c0}}(x,z) = \exp\left(\frac{-2|x|}{\theta_{\ln f_{c0},x}}\right)\exp\left(\frac{-2|z|}{\theta_{\ln f_{c0},z}}\right) \quad\text{...}(4.11)$$

where $\theta_{\ln f_{c0},x}$ and $\theta_{\ln f_{c0},z}$ denote the horizontal and vertical correlation length of f_{c0}, respectively; $|x|$ and $|z|$ denote the absolute coordinate differences of any two points of concern, in the horizontal and the vertical direction, respectively. After establishing the normally distributed random field, the required lognormally distributed random field is subsequently obtained as:

$$f_{c0}(\underset{\sim}{x}) = \exp\left[\mu_{\ln f_{c0}} + \sigma_{\ln f_{c0}}G_{\ln f_{c0}}(\underset{\sim}{x})\right] \quad\text{...}(4.12)$$

The initial porosity ϕ_0 is assumed to be higher than $\phi_{\min} > 0$. A beta distribution is often used for bounded random variables. Unfortunately, a beta distributed random field has a very complex joint distribution, and the simulation is difficult to perform. To simplify the procedure, we selected a shifted lognormal distribution, i.e. $\phi_n = (\phi_0 - \phi_{\min})$ is assumed to follow a lognormal distribution. The normally distributed random field $G_{\ln\phi_0}(\underset{\sim}{x})$ has zero mean and unit variance as $G_{\ln f_{c0}}(\underset{\sim}{x})$. Conceivably, $\theta_{\ln\phi_0}$ is taken to be equal to $\theta_{\ln f_{c0}}$, since it seems reasonable to assume that, if the spatial correlation structure is caused by changes in the constitutive nature of the soil over space, both ϕ_0 and f_{c0} would have similar correlation lengths. Both lengths will be referred to simply as $\theta(\theta_x, \theta_z)$. A dimensionless correlation length is defined as

$$\Theta(\Theta_x, \Theta_y) = \frac{\theta(\theta_x, \theta_y)}{L}, \quad\text{...}(4.13)$$

where L denotes the height of the specimen.

Since the cross correlation between ϕ_0 and f_{c0} is unclear, the cross correlation extremes ρ have been investigated from -1 to 1 in order to determine if its chosen value is significant. The cross correlation between ϕ_0 and f_{c0} has been implemented via the covariance matrix decomposition proposed by Fenton [148].

4.3. Deterministic simulation

In the internal erosion test performed by Zhong [146], the soil specimen was supposed to be initially homogeneous. However, the initial pore pressure along the specimen after the saturation stage, shown in Figure 4.3, confirmed the initial heterogeneity along the specimen. This initial heterogeneity may have been caused, on one hand, by the compaction of the reconstituted soil specimen and, on the other hand, by the impact of the saturation stage. The initial profiles of porosity ϕ and fines content f_c were, therefore, calibrated by fitting the initial pore pressure along the specimen, summarized in Table 4.1, named "Case 0". The thickness of the ith layer is h_i.
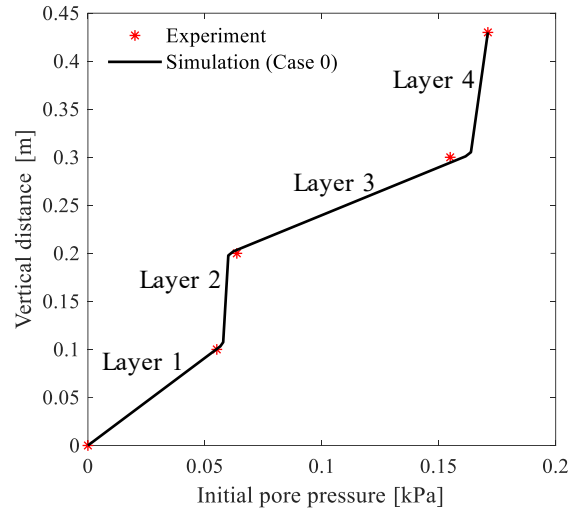
Figure 4.3 The initial pore pressure at the beginning of the erosion stage

Table 4.1 Initial profiles of porosity and fine content

Case 0				Case 1				Case 2			
i layer	h_i [149]	ϕ_0	f_{c0}	i layer	h_i [149]	ϕ_0	f_{c0}	i layer	h_i [149]	ϕ_0	f_{c0}
1	100	0.30	0.28	1	224	0.29	0.30	1	100	0.31	0.27
2	100	0.38	0.19	2	206	0.38	0.19	2	100	0.35	0.24
3	100	0.29	0.30					3	100	0.31	0.27
4	130	0.36	0.22					4	130	0.36	0.22

After the soil became saturated, the fluid was forced to flow downwards through the specimen during the erosion test. A multi-stage hydraulic gradient condition consisted of increasing by steps the hydraulic gradient from 0.04 to 0.5. Each stage of the hydraulic gradient was kept constant for about 30 min. The physical properties of the soil mixture are summarized in Table 4.2. The model parameters were calibrated by fitting the time evolution of the hydraulic conductivity and the cumulative loss of the dry mass of the soil mixture, using an optimization technique [133, 134]. All the values determined for the model parameters, summarized in Table 4.3, were used in the following analyses.

Table 4.2 Physical properties of the soil mixtures according to [146]

Density of fluid	ρ_f	1.0 g/cm³
Density of solids	ρ_s	2.65 g/cm³
Kinematic viscosity of fluid	η_k	5.0×10^{-6} m²s⁻¹
Minimum porosity	ϕ_{min}	0.2
Initial permeability	k	3.6×10^{-3} m/s

Table 4.3 Values of model parameters for tested soil mixtures

Erosion parameters				Filtration parameters			Permeability parameters
λ_e	α_1	α_2		λ_f	β		m
14.0	0.88	4.0		0.6	7.2		10.7

In Figure 4.4, the experimental and numerical results of the erosion test are compared. The hydraulic conductivity of the specimen is shown in Figure 4.4a. It can be seen that the numerical model was able to reproduce the two phases of the erosion up to a stable stage. The decrease of the hydraulic conductivity in the first phase was accompanied by a clogging of the pores. A clogging, which at first restricted the water flow, could then be blown away, leading to a significant increase of the hydraulic conductivity. Therefore, the second phase of the hydraulic conductivity evolution could be characterized by its rapid increase. The hydraulic conductivity reached at last a constant value and tended to stabilize when the hydraulic drag force could no longer transport any more fine particles through the soil skeleton. Figure 4.4b plots the time evolution of the cumulative eroded masses. The two-phase process of the erosion can be clearly identified. Experimental and numerical values of the eroded mass agree well with each other.
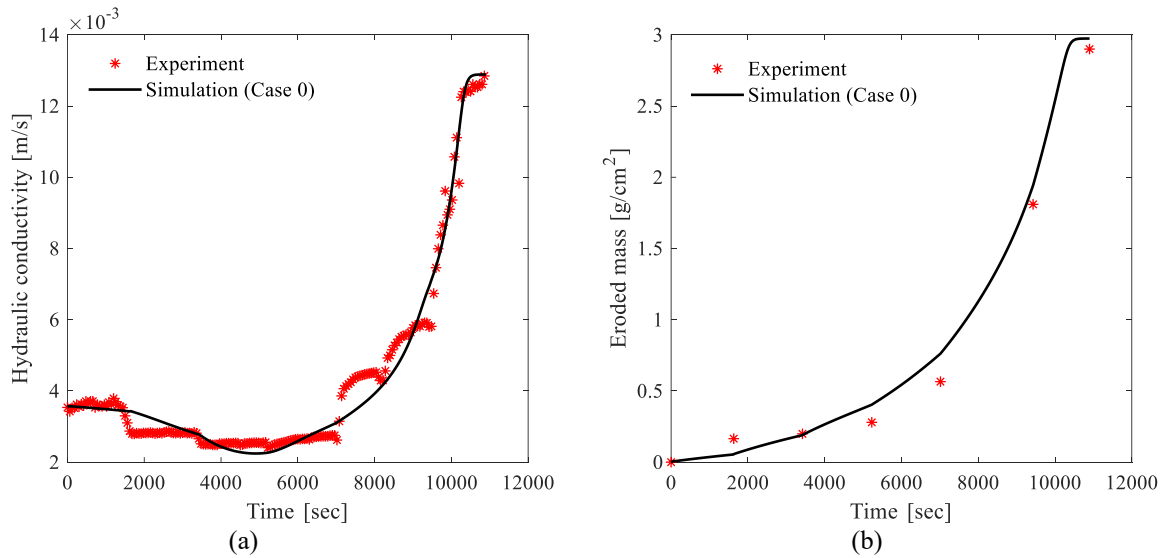
Figure 4.4 Comparison between laboratory test (symbols) and simulated data (continuous lines): (a) time evolution of hydraulic conductivity; (b) time evolution of cumulative eroded masses

The spatial profiles at different time steps of the porosity and the concentration of the fluidized fine particles are shown in Figure 4.5. Corresponding to the decrease of the hydraulic conductivity in the first phase shown in Figure 4.4a, the clogging of the pores was observed at the interface where the porosity dropped at t = 2180s and 4360s in Figure 4.5a. This indicates that the fluidized fine particles were filtrated at the interfaces. It is more clearly shown in Figure 4.5b by the drop of the transport concentration at the interfaces. As a consequence of the actual boundary conditions, a front of concentration (steep gradient of concentration) was observed passing through the domain from the inlet to the outlet. The clogging began to be unblocked when the front of concentration reached the clogging, accompanied by the increase of the hydraulic conductivity. The erosion-filtration process stopped when the ultimate fines content fraction $f_{c\infty}$ was attained, determined by Eq.(3.20).
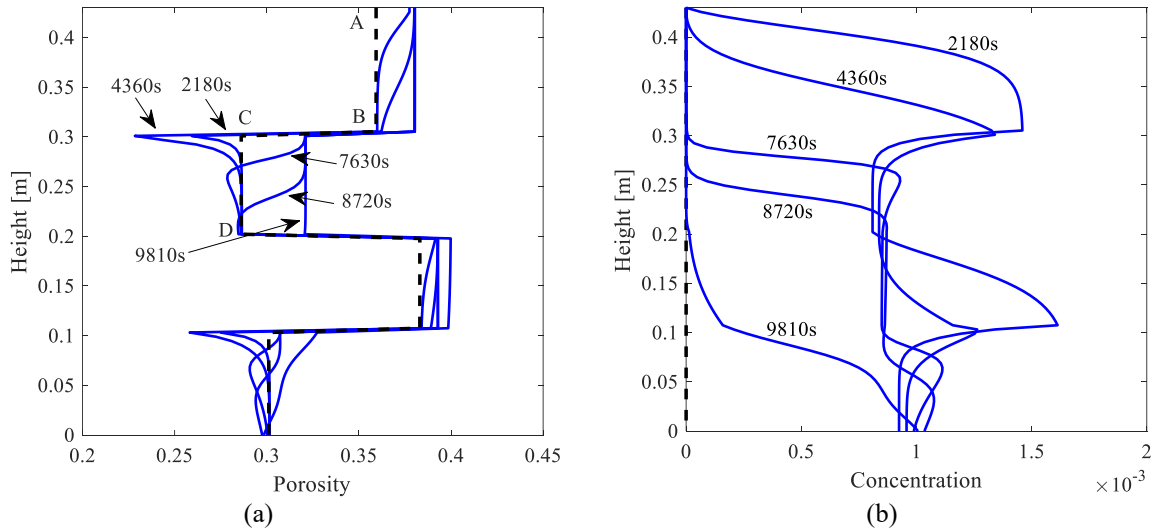
Figure 4.5 Spatial profiles of (a) porosity and (b) concentration of fluidized fine particles, respectively at various time steps (the dashed black lines indicate the initial profiles)

Note that the proposed model is well-suited for simulating a filter cake formation caused by clogging. A filter cake is a localized layer of highly reduced permeability. In a 1D domain, it is divided into two parts (Figure 4.6). Two different types of filter cakes might occur [123, 150, 151]. First, it is possible for an external filter cake to form at the interface where the constriction sizes of the pore channels are smaller than the average diameter of the fluidized fines. Hence, the fines are unable to penetrate significantly into the downstream part of the domain. Rather, the fines are deposited at the border between the layers. On the other hand, an internal filter cake is formed if the fines do penetrate into the second part of the domain. As more particles accumulate, a layer with reduced permeability will develop. In 2D condition, as the influx can bypass the local blockage, the permeability of the specimen will not decrease until a continuous clogged layer is formed. It has to be pointed out, however, that the proposed model can apply to cases of internal filter cakes only. To capture the occurrence of an external filter cake, it is necessary to consider a geometrical analysis of the constriction size distribution.
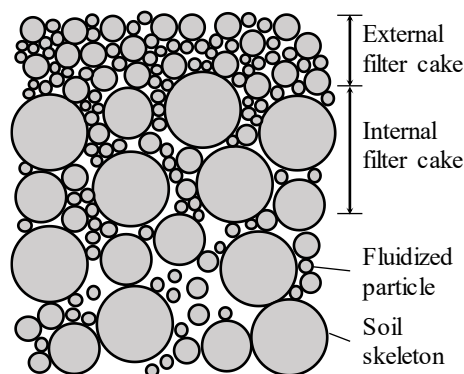
Figure 4.6 Schematic of filter cake (external and internal) in porous media

To analyze how the soil heterogeneity influences the suffusion, it was decided to simulate 3 additional presumed cases with different initial profiles of porosity and fines content. The mean ϕ_0

and f_{c0} for each case were kept at 0.33 and 0.25, respectively, while the variations of ϕ_0 and f_{c0}, and the thickness of the layers were varied according to Table 4.1. Compared to Case 0, Case 1 has the same variation of ϕ_0 and f_{c0} but only 2 layers; Case 2 has 4 layers, but a smaller variation. For Case 3, ϕ_0 and f_{c0} are uniformly distributed.

Figure 4.7 clearly demonstrates that assuming a homogeneous soil condition is insufficient in predicting the decrease of the hydraulic conductivity. By comparing the rate of eroded mass and the minimum value of the hydraulic conductivity of the specimen during the test period, it could be seen that the more heterogeneous the specimen, the slower the eroded mass increased and the more severe the clogging became. In the following sections, the influence of the initial profiles of porosity ϕ_0 and fine content f_{c0} will be systematically discussed through an analysis of the sensitivity of the rate of eroded mass and the minimum hydraulic conductivity during the test period to the randomly generated ϕ_0 and f_{c0}.
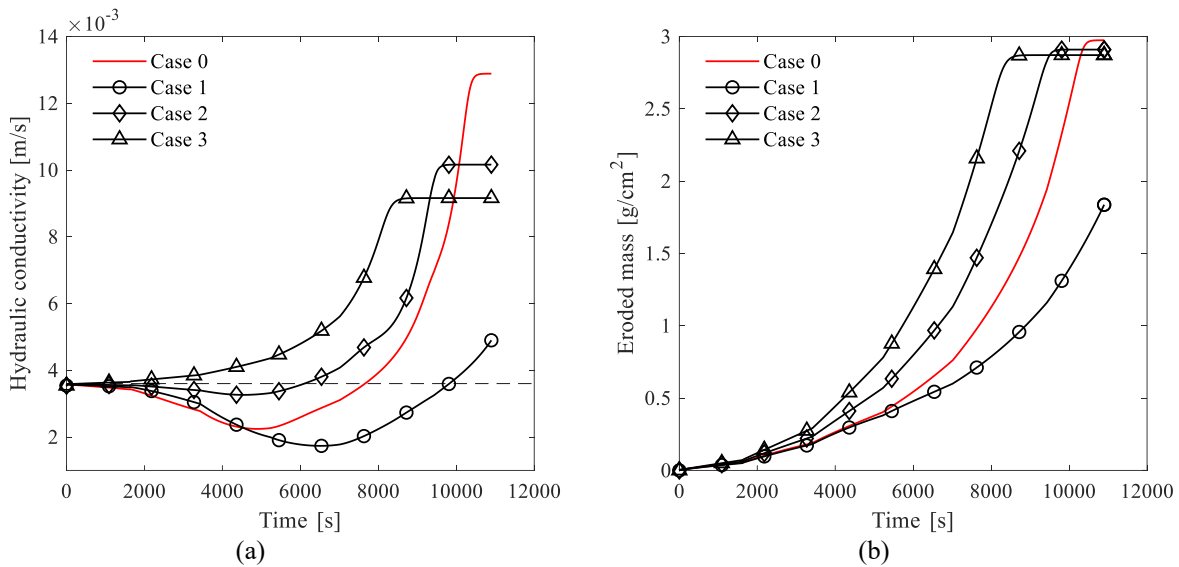
Figure 4.7 Time variation of (a) hydraulic conductivities and (b) cumulative eroded masses for the layered soils

4.4. Monte Carlo simulations in 1D condition

1D Monte Carlo simulations were firstly performed on the above configuration (with length $L = 0.43\text{m}$) to investigate the sensitivity of the eroded mass and the hydraulic conductivity of the specimen to the randomly generated ϕ_0 and f_{c0}. The mean ϕ_0 and f_{c0}, referred to as μ_{ϕ_0} and $\mu_{f_{c0}}$, respectively, were kept at 0.33 and 0.25, while the coefficient of variation COV ($= \sigma/\mu$), the normalized spatial correlation length Θ ($= \theta/L$), for both ϕ_0 and f_{c0}, and the cross-correlation coefficient ρ were changed systematically, according to Table 4.4.

Table 4.4 Random field parameters used in the study

COV	0.05	0.1	0.15	0.2	
Θ	0.25	0.5	1.0	2.0	4.0

| ρ | -1.0 | 0.0 | 1.0 | | |

In fact, the coefficient of variance of ϕ_0 and f_{c0} may be different. The reason for using the same value of COV for both ϕ_0 and f_{c0} in this paper is only for the purpose of comparison. Not much data is available to indicate the level of correlation between ϕ_0 and f_c. Strong negative or positive correlation between the porosity and the fines content fraction for sand-silt mixtures has been shown by Yin et al. [52] for different conditions. For the purpose of this paper's probabilistic study, the cross-correlation coefficient between ϕ_0 and f_c was set to -1.0, 0.0 and 1.0.

4.4.1. Determination of the number of MCS runs

When using the Monte Carlo simulations (MCS), the number of runs should be first determined to obtain converged results. For the sake of accuracy and run-time efficiency, the sensitivity of the results to the number of Monte Carlo simulations was examined. The "worst" cases with the highest $COV = 0.2$ and $\Theta = 0.25$ were chosen to investigate the effect of the number of simulations on the output quantities. Figure 4.8 shows the convergence of the ultimate eroded mass and the ultimate hydraulic conductivity of the specimen as the number of simulations increases. It can be seen that 2000 simulations were enough to provide reliable and reproducible estimates. Hence, for each parametric combination in the following studies, 2000 Monte Carlo simulations were performed.
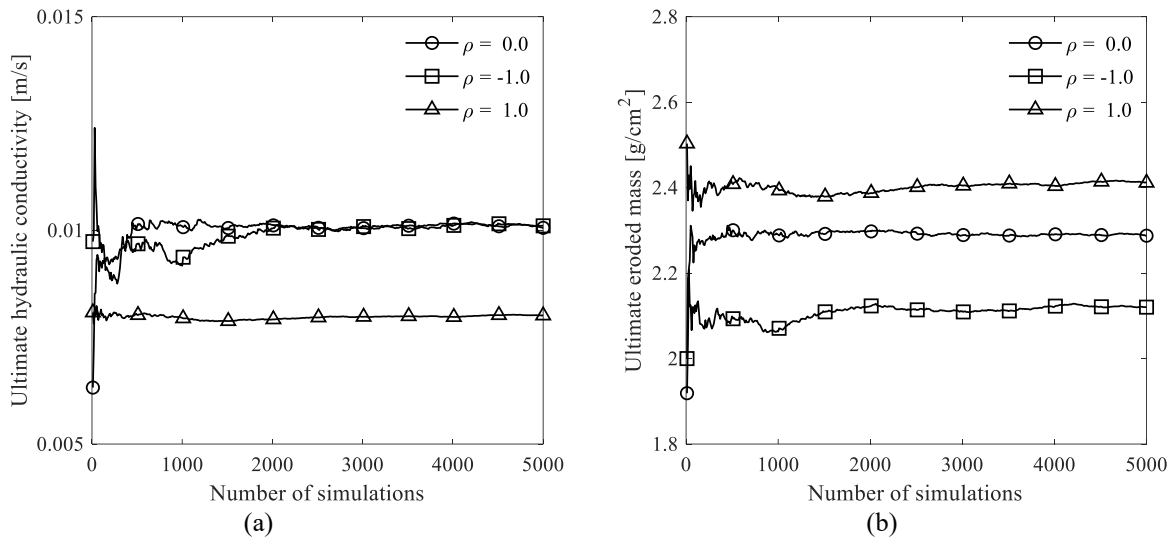
Figure 4.8 Influence of the number of Monte Carlo simulations on (a) ultimate eroded mass and (b) ultimate hydraulic conductivity ($COV = 0.2$ and $\Theta = 0.25$)

4.4.2. Simulation results

Figure 4.9 shows how the sample mean rate of eroded mass $\dot{m}$ and minimum hydraulic conductivity during the test period $k_{\min}$, taken as the average over the 2000 realizations and referred to as $\mu_{\dot{m}}$ and $\mu_{k_{\min}}$, respectively, vary with correlation length, soil variability, and cross-correlation between ϕ_0 and f_{c0}. In 1D analyses, an increase of soil variability generally decreased the mean rate of the eroded mass and the mean minimum hydraulic conductivity during the test period. These

results illustrate that the higher the soil variability, the greater the number of transported fine particles are captured and re-deposited within the soil skeleton. This may be explained by the fact that a higher variability is accompanied by severer transitions between dense and loose layers in the specific domain, which facilitates the filtration process. The greatest reduction of μ_m and $\mu_{k_{\min}}$ induced by the clogging are observed for negatively correlated ϕ_0 and f_{c0} ($\rho = -1$), the least reduction when ϕ_0 and f_{c0} are perfectly correlated ($\rho = 1$), and the independent case ($\rho = 0$) lies between these two extremes. The sample mean is more strongly affected by the soil variability and somewhat less so by the cross-correlation between ϕ_0 and f_{c0}.

(a)   (b)
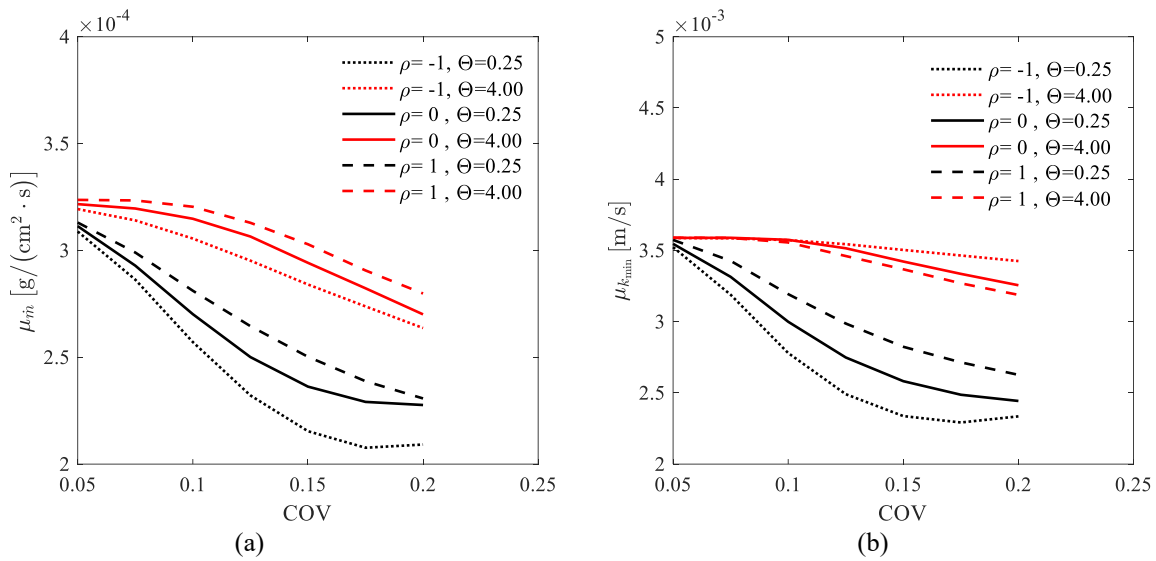
Figure 4.9 Sample mean of (a) rate of eroded mass μ_m, and (b) minimum hydraulic conductivity during the test period $\mu_{k_{\min}}$

(a)   (b)
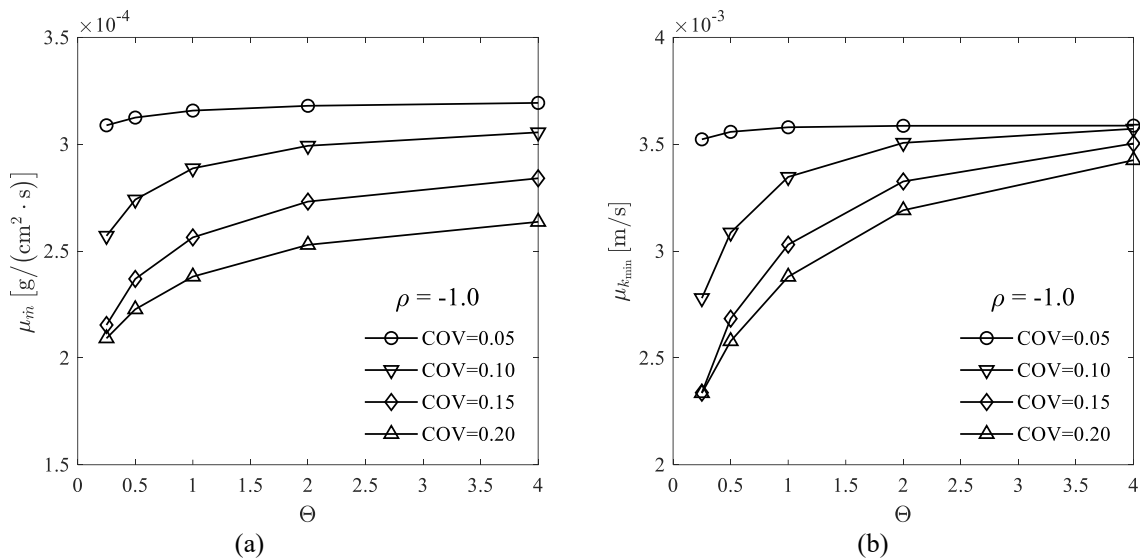
Figure 4.10 $\rho = -1.0$, comparison of: (a) the mean final cumulative eroded mass; (b) the mean minimum hydraulic conductivity during suffusion process

60

Figure 4.9 also shows that the dimensionless correlation length, Θ, has a significant influence. The variations of μ_m and $\mu_{k_{\min}}$ with respect to Θ are more clearly seen in Figure 4.10. In a 1D analysis, an increase of Θ generally increased μ_m and $\mu_{k_{\min}}$. A higher Θ makes the layered system more uniform, thus leading to a smoother transition between the dense and loose layers. As a consequence, the filtration process is reduced and, in turn, the sample mean rate of eroded mass and minimum hydraulic conductivity during the test period will increase.

The usual simulation practice for suffusion is based on the sole mean values in homogeneous soil. The above results confirm that the erosion rate and the evolution of the hydraulic conductivity are different in heterogeneous soil with consideration to the soil variability and the spatial correlation length. What this implies from a design standpoint is that the susceptibility of soil to internal erosion may be different with that obtained in deterministic analysis in homogeneous soil.

4.4.3. Probabilistic interpretation
The plucking-off of the fine particles and the transport of these fines may cause the soil structure to become looser. At the same time clogging may occur which could reduce permeability and lead to an increase of excess pore pressure. The combination of these two phenomena will result in the strength degradation of the soil [14].
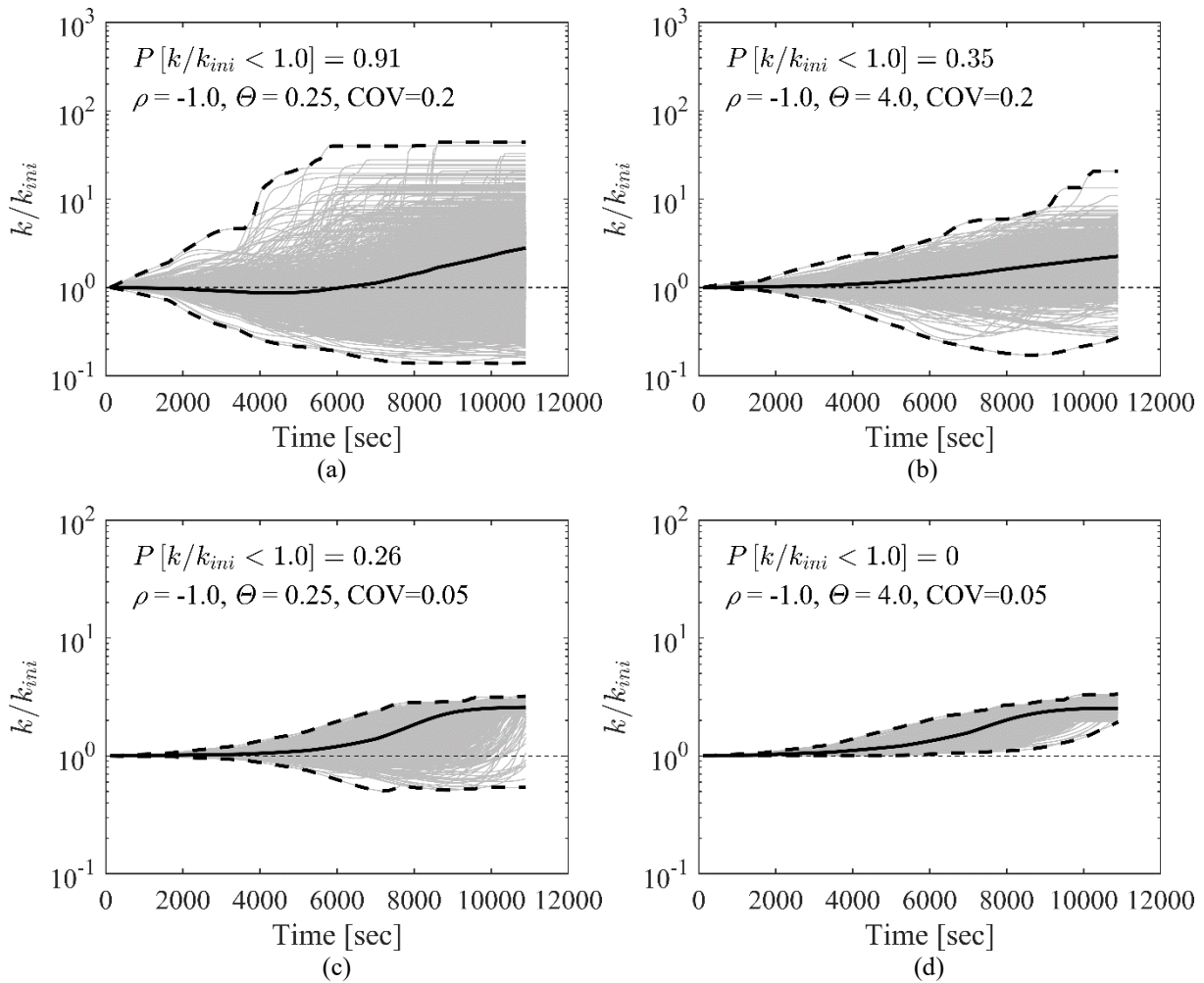
Figure 4.11 Time histories of normalized hydraulic conductivity of the specimen with different soil uncertainties, $\rho = -1.0$: (a) $\Theta = 0.25$, $\upsilon = 0.2$; (b) $\Theta = 4.0$, $\upsilon = 0.2$; (c) $\Theta = 0.25$, $\upsilon = 0.05$; (d) $\Theta = 4.0$, $\upsilon = 0.05$

Figure 4.11 shows the time histories of the normalized hydraulic conductivity of the specimen with different input statistics. The probability of blockage during suffusion can be defined by counting the number of simulations in which the hydraulic conductivity during the erosion simulation is smaller than its initial value, *i.e.,* counting the number of simulations in which $[k/k_{ini} < 1.0]$ and dividing it by the total number of simulations. Figure 4.12 compares the probability of blockage during the suffusion simulations with different coefficients of cross correlation, different lengths of correlation, and different coefficients of variation of ϕ_0 and f_{c0}.

The results indicate that an increase of the variability in ϕ_0 and f_{c0} values will generally increase the probability of blockage during suffusion. This can be explained by the fact that a greater variability will lead to more dramatic changes of soil porosity and permeability at the interface of the different layers, which in turn facilitates the capture of the fine particles transported within the water flow. Moreover, the random fields of ϕ_0 and f_{c0} values with lower spatial correlation lengths make the layered system more uneven, therefore accelerating the formation of filter cakes at the interface. Moreover, negatively correlated ϕ_0 and f_{c0} are likelier to cause blockage.

(a)

(b)

(c)
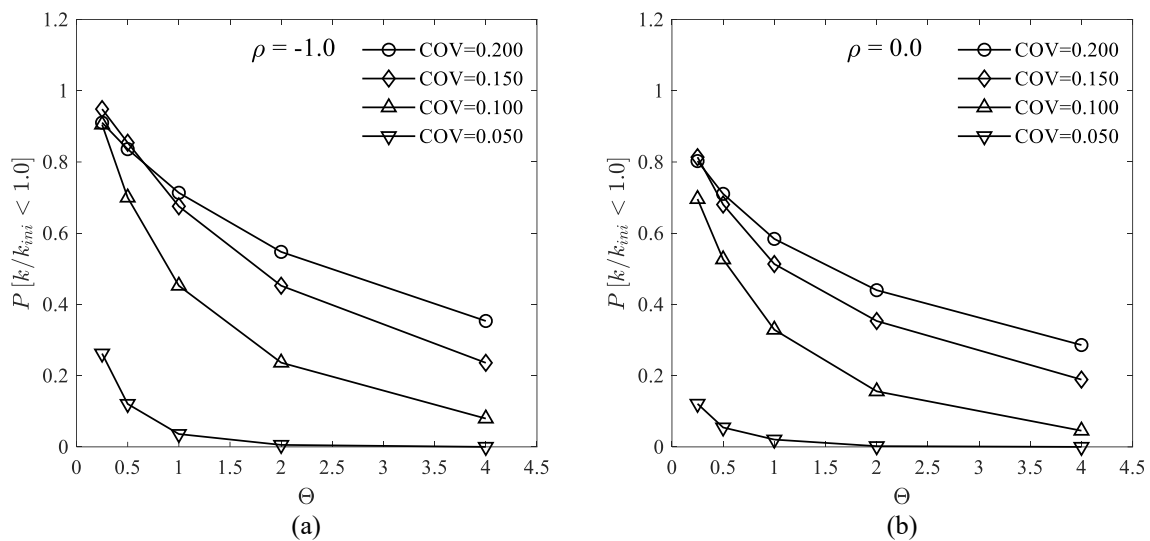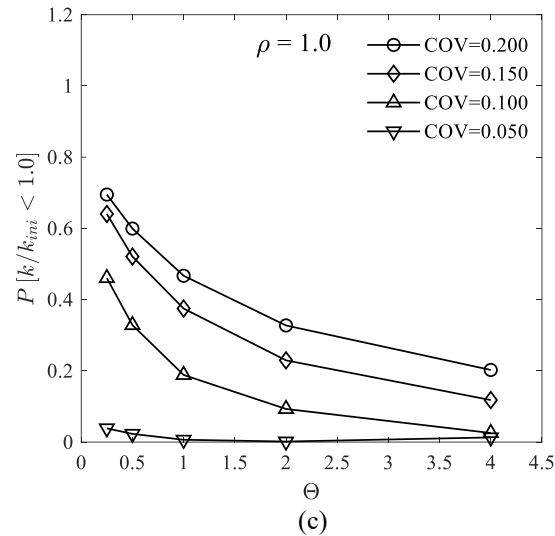
Figure 4.12 Comparison of probability of blockage during suffusion process: (a) $\rho = -1.0$; (b) $\rho = 0.0$; (c) $\rho = 1.0$

The susceptibility of soil to internal erosion when its spatial variability is considered may be different from that which is obtained by a deterministic analysis in a homogeneous soil. The probability of blockage increases significantly when the soil variability increases and when the spatial correlation length decreases, resulting in the increase of the risk of damage of linear earthen structures such as levees, dikes, etc., induced by the pore pressure increase.

4.5. Monte Carlo simulations in 2D condition

In 2D condition, the influx can bypass the local blockage, which leads to the decrease of the permeability at blockage. The part below investigates how the spatial correlation lengths of ϕ_0 and f_{c0} influence suffusion in both isotropic and layered anisotropic 2D random fields. 7 cases with different magnitudes of the spatial correlation length in isotropic fields and 5 cases with different horizontal and vertical correlation lengths in an anisotropic field are shown in Table 4.5. Because the horizontal correlation length is often larger than the vertical correlation length, the anisotropic ratio $r_{xy} = \Theta_x/\Theta_y$ is set >1 with a constant $\Theta_y = 0.25$ in the following anisotropic cases.

Table 4.5 Spatial correlation length in 2D random fields

Case	Correlation length Θ_x	Correlation length Θ_y
ISO-1	0.05	0.05
ISO-2	0.1	0.1
ISO-3	0.25	0.25
ISO-4	0.5	0.5
ISO-5	1.0	1.0
ISO-6	2.0	2.0
ISO-7	4.0	4.0
ANI-1	0.5	0.25
ANI-2	1.0	0.25
ANI-3	2.0	0.25
ANI-4	4.0	0.25
ANI-5	250.0	0.25

Figure 4.13 shows six realizations of the generated random fields of initial porosity with different spatial correlation lengths. It appears evident that in isotropic random fields, when Θ decreases, any point at which the porosity is lower is surrounded by points where the porosity is higher. The diffused loose area or dense area tends to be connected into blocks as the correlation length increases in both horizontal and vertical directions. In anisotropic random fields, the soil domain tends to be horizontally stratified, as the horizontal correlation length becomes increasingly larger than the vertical correlation length. It should be noted that the COV and the cross-correlation of ϕ_0 and f_{c0} are fixed at 0.1 and -1 for all the cases shown in Table 4.5.
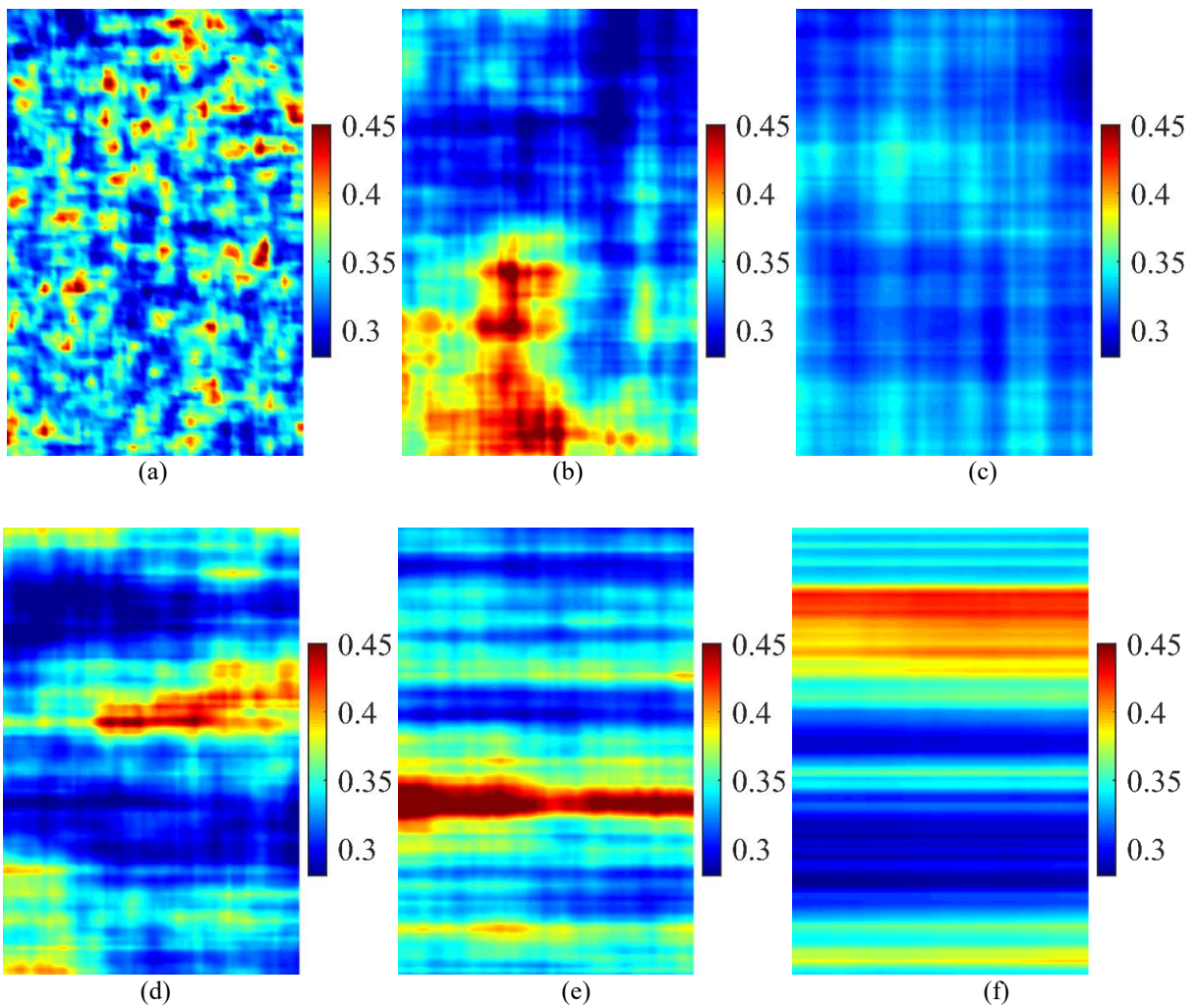
Figure 4.13 Generated random fields of initial porosity according to different spatial correlation length: (a) Case ISO-1: $\Theta_x = \Theta_y = 0.05$; (b) Case ISO-4: $\Theta_x = \Theta_y = 0.5$; (C) Case ISO-6: $\Theta_x = \Theta_y = 2.0$; (d) Case ANI-2: $\Theta_x = 1.0$, $\Theta_y = 0.25$; (e) Case ANI-4: $\Theta_x = 4.0$, $\Theta_y = 0.25$; (f) Case ANI-5: $\Theta_x = 250.0$, $\Theta_y = 0.25$

4.5.1. Single realization

A simulation example of a 2D suffusion in a non-homogeneous field for a single realization is shown in Figure 4.14 to Figure 4.17. Figure 4.14 shows the randomly generated initial porosity and

fines content for statistics inputs $\mu_{\phi_0} = 0.33$ and $\mu_{f_{c0}} = 0.25$, $\text{COV} = 0.1$, $\Theta_x = \Theta_y = 0.25$ and $\rho = -1$. In Figure 4.14a, the blue areas correspond to low porosity where the transported fine particles can be filtered more easily, and the red areas correspond to high porosity.

<center>(a)   (b)</center>
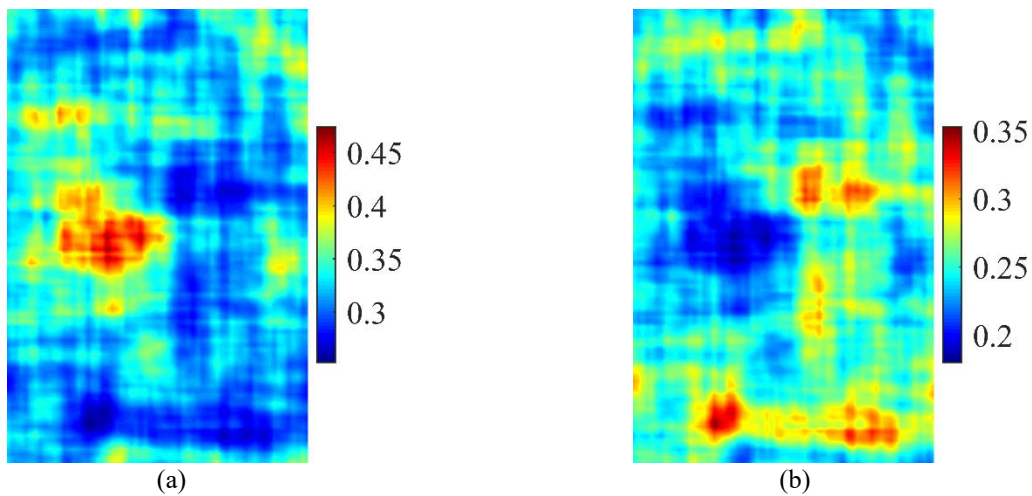
Figure 4.14 2D stochastic simulation for a single realization (a) initial porosity; (b) initial fraction of fine content

The time evolution of the hydraulic conductivity of the specimen and the cumulative eroded masses are shown in Figure 4.15. Figure 4.16 and Figure 4.17 illustrate the evolution of the fines content and the porosity with respect to its initial state at 5 different time steps corresponding to points A to E shown in Figure 4.15. The fine particles were firstly detached in the vicinity of the inlet, transported downwards and partially captured within the denser area. From the start to time step A, erosion and filtration proceeded simultaneously in a rather diffused manner. No area was continuously clogged; no preferential flow channel was formed, all of which contributed to the initial stable stage of hydraulic conductivity. From time step A, the diffused clogged areas began to unite. The clogged area can be seen more clearly in Figure 4.17. A clogged layer can be observed at the lower part of the specimen, which explains the decrease of the hydraulic conductivity. Furthermore, from Figure 4.16b and Figure 4.16c, it seems that the influx has bypassed the denser area at the top of the specimen. From time step C, the clogged area begins to be unblocked. A preferential channel can be observed at the bottom left of the specimen in Figure 4.16d and Figure 4.17d, which explains the significant increase of the hydraulic conductivity. The clogging, restricting at first the water flow, was then blown away. This stage is characterized by a rapid increase of hydraulic conductivity.
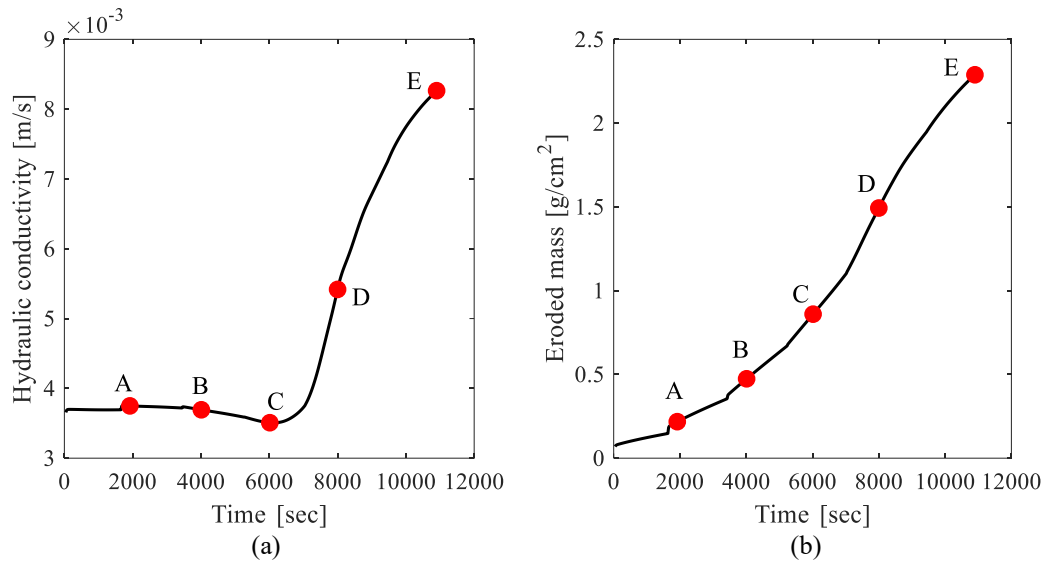
Figure 4.15 2D stochastic simulation for a single realization (a) time evolution of hydraulic conductivity; (b) time evolution of cumulative eroded masses

(a) Time step A

(b) Time step B

(c) Time step C

(d) Time step D
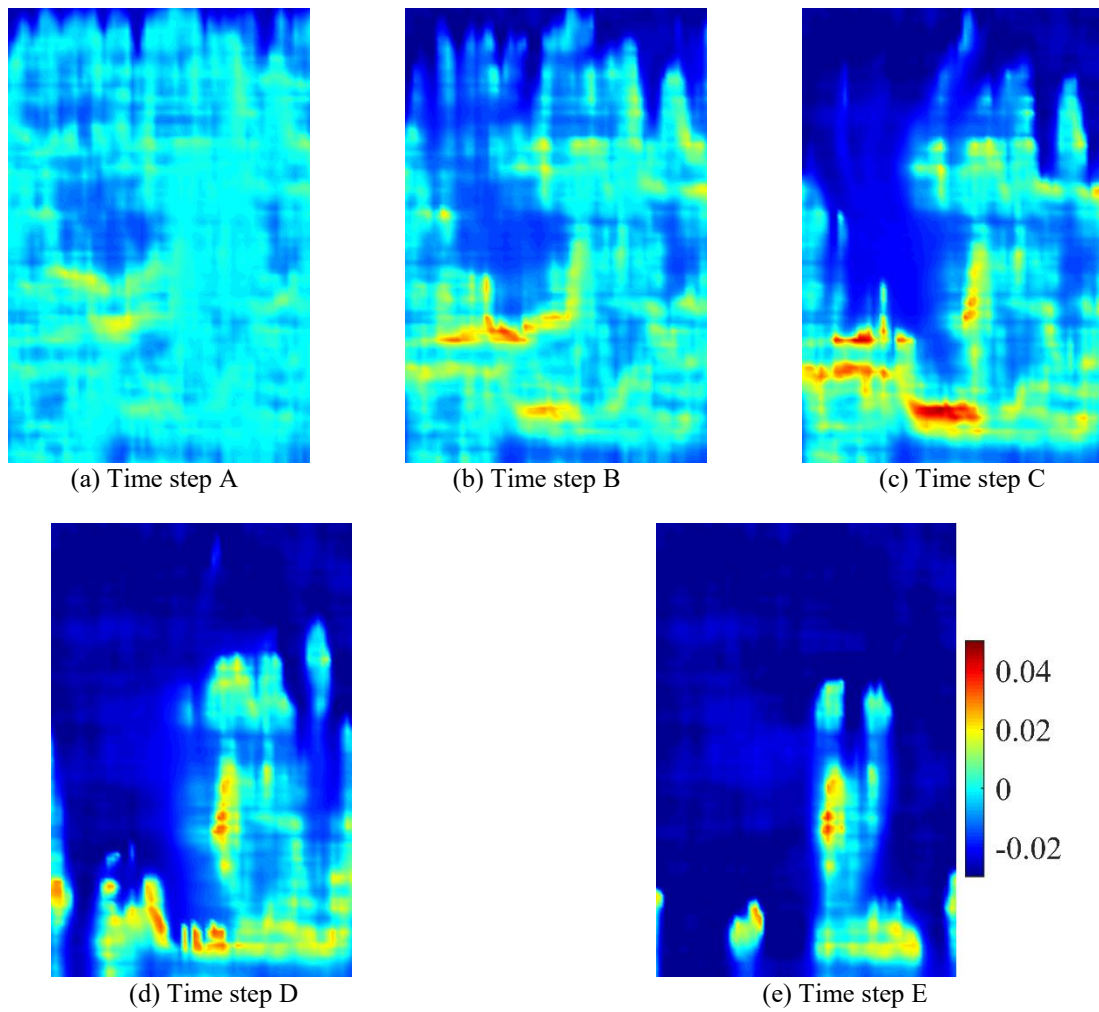
(e) Time step E

Figure 4.16 The evolution of fine content at different time steps with respect to its initial state for the single realization

|(a) Time step A|(b) Time step B|(c) Time step C|
|(d) Time step D|(e) Time step E|
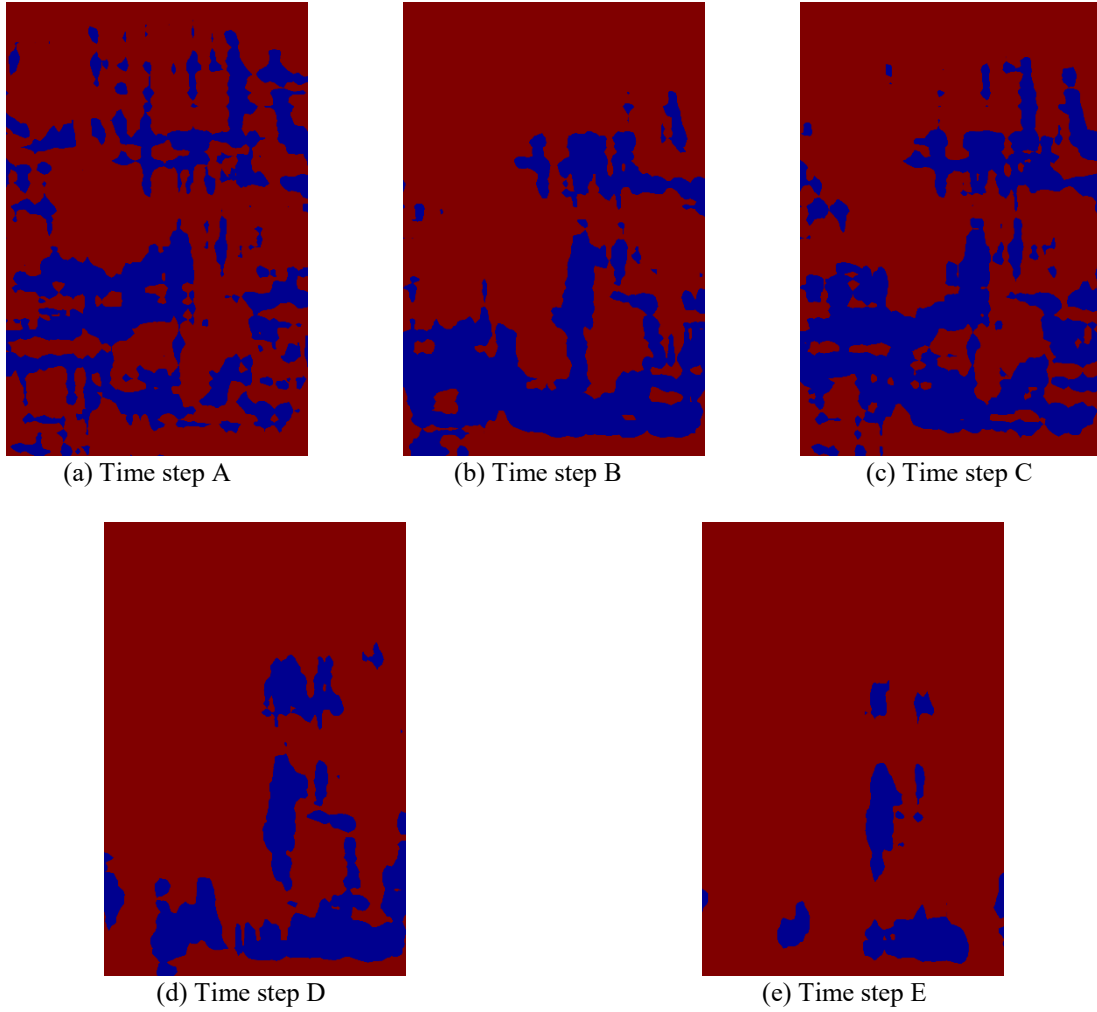
Figure 4.17 The evolution of porosity at different time steps with respect to its initial state for the single realization (the blue area indicates the clogged area, the red area indicates the eroded area)

4.5.2. Influence of spatial correlation in 2D random fields

The comparison between 1D and 2D isotropic analyses is shown in Figure 4.18. The mean rates of the eroded mass $\mu_{\dot{m}}$ in 2D condition are generally smaller than that in 1D condition. Interestingly, the greatest reduction in $\mu_{\dot{m}}$ in 2D condition occurs when the spatial correlation length θ is about half of the specimen length L, while in 1D condition, $\mu_{\dot{m}}$ increases monotonically with θ. The same trend was found in the evolution of the probability of blockage, as shown in Figure 4.18c. The highest probability of blockage in 2D condition occurs when θ is between $0.3L$ and $0.5L$, while the probability of blockage in 1D condition keeps decreasing from 1 when θ is extremely small ($\theta = 0.05L$ in this case). This can be explained by the fact that, as the correlation length drops down to zero, the random field becomes infinitely rough with all points in the field becoming independent of each other. Therefore, in 1D condition, more filter cakes will form at the interface of different layers, which leads to the decrease of $\mu_{k_{\min}}$ and $P[k/k_{ini} < 1.0] \rightarrow 1.0$ as $\theta \rightarrow 0$. However, in 2D condition, the locally denser areas are scattered throughout the whole region, as shown in Figure 4.13a, which hinders the formation of the continuous clogged layer, leading to $\mu_{k_{\min}} \rightarrow k_{ini}$ and

67

$P[k/k_{ini} < 1.0] \rightarrow 0$ as $\theta \rightarrow 0$. When the correlation length increases to infinity, the random field becomes spatially constant, albeit still random, from realization to realization. In this case, fewer transported fine particles can be filtrated, which leads, on the one hand, to the increase of $\mu_{k_{min}}$ and, on the other hand, to the decrease of $P[k/k_{ini} < 1.0]$.
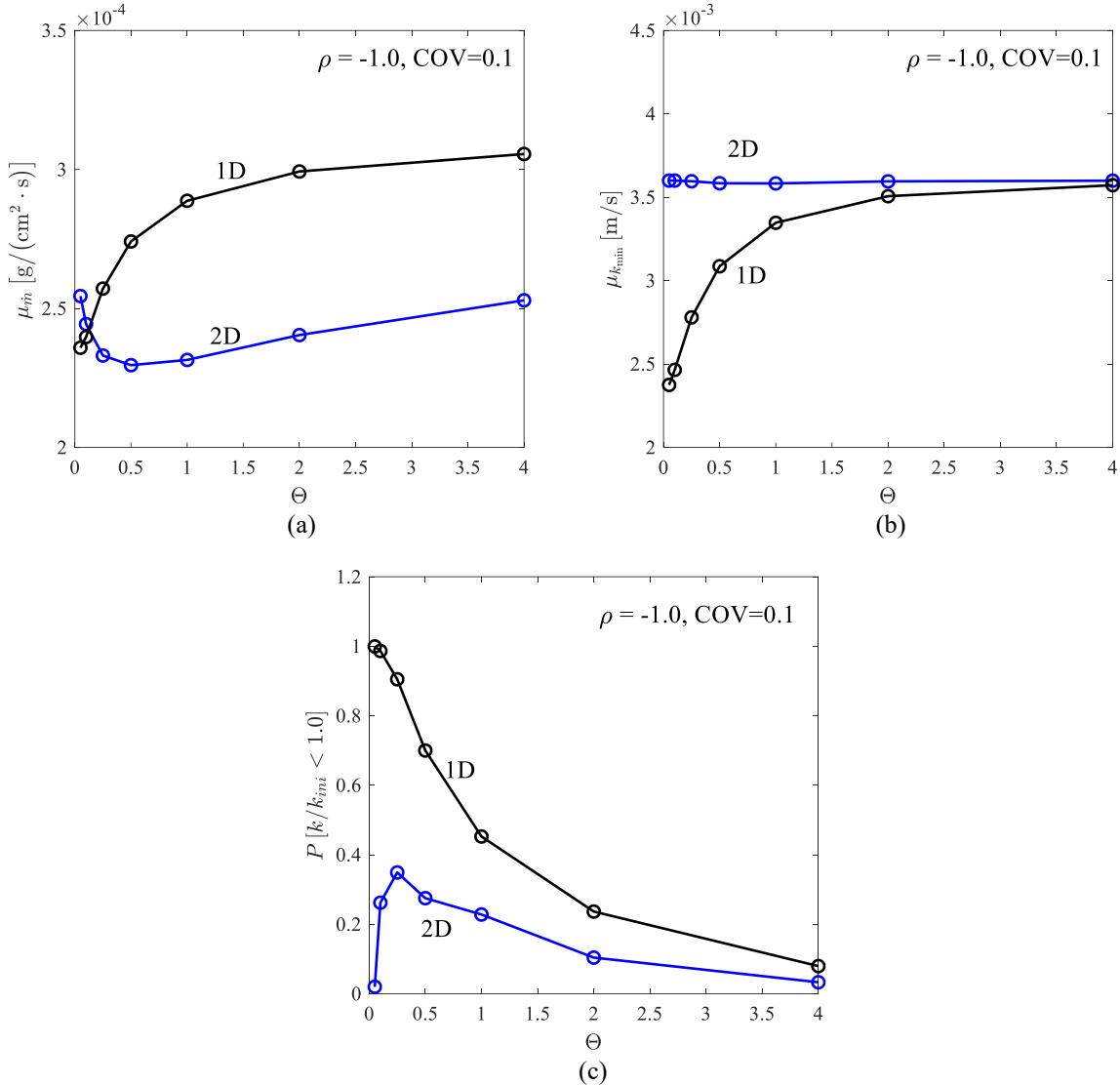
Figure 4.18 Comparison between 1D and 2D isotropic analyses (a) mean rate of eroded mass $\mu_{\dot{m}}$, (b) mean minimum hydraulic conductivity during the test period $\mu_{k_{min}}$ and (c) probability of blockage

From Case ISO-3 and cases ANI-1 to ANI-5, the anisotropic ratio $r_{xy} = \Theta_x/\Theta_y$ increases from 1 to 1000, as Θ_x increases from 0.25 to 250 with a constant Θ_y at 0.25. Figure 4.19 shows the variation of the mean values of the eroded mass rate and the minimum hydraulic conductivity during the test period, as well as the probability of blockage when r_{xy} is increased. Obviously $\mu_{\dot{m}}$ and $P[k/k_{ini} < 1.0]$ are always lower and $\mu_{k_{min}}$ is always higher in 2D rather than in 1D. One can anticipate the three-dimensional (3D) values of $\mu_{\dot{m}}$ and $P[k/k_{ini} < 1.0]$ to be also lower.
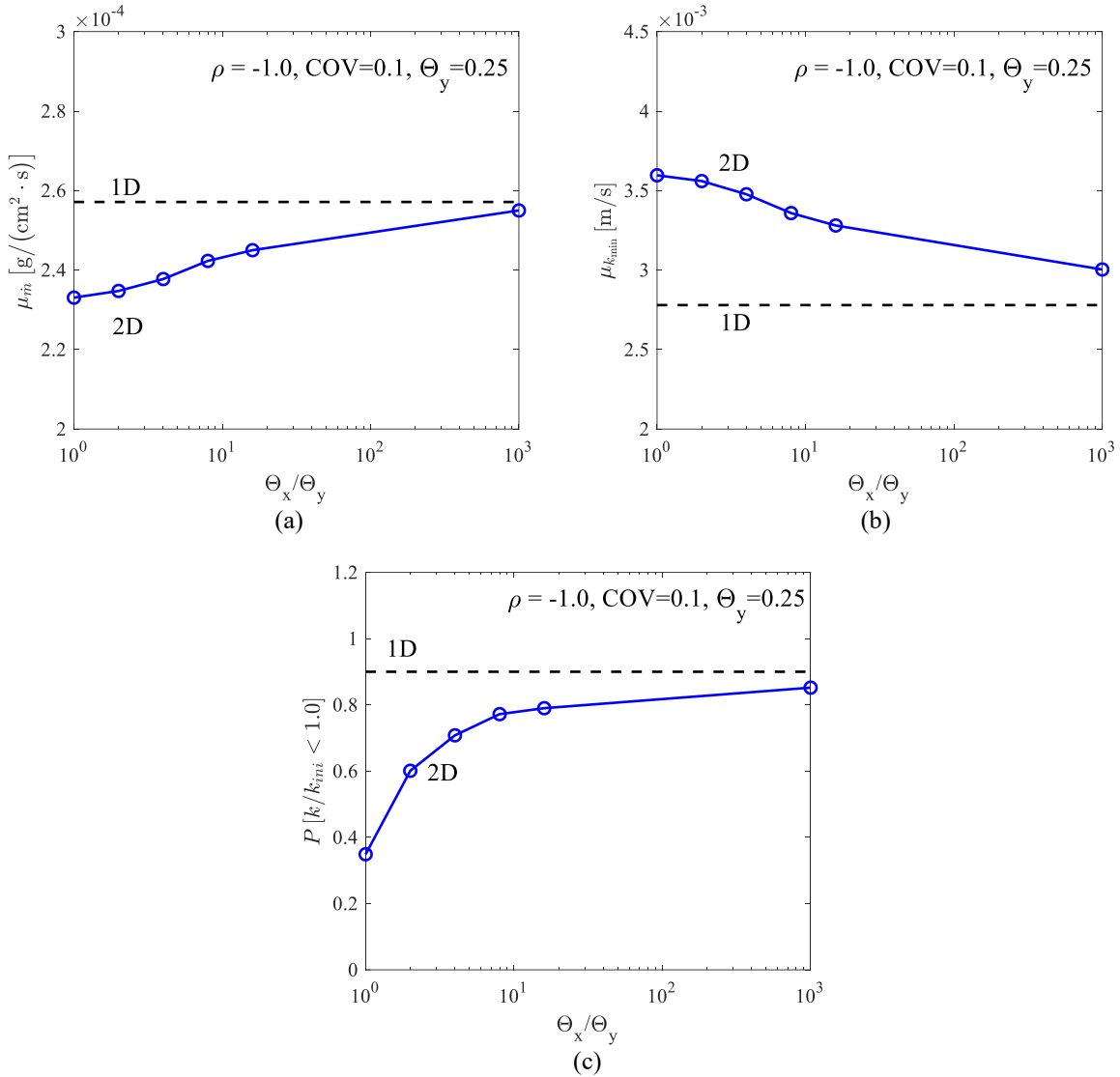
Figure 4.19 Comparison between 1D and 2D anisotropic analyses (a) mean of rate of eroded mass $\mu_{\dot{m}}$, (b) mean of minimum hydraulic conductivity during the test period $\mu_{k_{\min}}$ and (c) probability of blockage

4.6. Conclusion

In this chapter, the random finite difference method was first established by applying the random field theory to the finite difference code for one- and two-dimensional analyses. The influence of the soil heterogeneity on suffusion was discussed by considering the initial porosity ϕ_0 and the fines content fraction f_{c0} as random fields. A four-constituent model was implemented into the code. Monte Carlo simulations of suffusion were conducted to investigate the influence of the variability, the spatial correlation length, and the cross correlation of ϕ_0 and f_{c0} on the rate of the eroded mass and the minimum hydraulic conductivity during the test period. The most significant findings drawn from the results of this study are summarized as follows.

First, the four-constituent continuum model is used to describe the temporal behavior with regard to both eroded soil and permeability change as observed in laboratory experiments. The deterministic

simulations clearly show that the assumption of soil homogeneity is insufficient in predicting for instance the decrease of the hydraulic conductivity.

Secondly, in 1D Monte Carlo analyses, an increase of the variability in ϕ_0 and f_{c0}, or a decrease of the spatial correlation length of the variables generally decreases the mean rate of the eroded mass and the mean minimum hydraulic conductivity. Greater variability leads to more significant changes of soil porosity at the interface of different layers; the lower spatial correlation lengths cause the layers to become more uneven, producing more interfaces between loose and dense layers, both of them in turn facilitate the capture of the fine particles transported by the water flow. The susceptibility of soil to internal erosion based on the evaluation of the rate of erosion may be different to that obtained in a deterministic analysis of a homogeneous soil. Furthermore, even if the sample behavior is more strongly affected by the soil variability and spatial correlation, and somewhat less so by the cross-correlation between ϕ_0 and f_{c0}, negatively correlated ϕ_0 and f_{c0} are more likely to cause blockage leading to the potential increase of excess pore pressure and, thus, a strength degradation.

The results of 2D analyses confirm that the influx can bypass the local blockage. The mean rates of the eroded mass in 2D condition are generally smaller than in 1D condition. Interestingly, the greatest probability of blockage in 2D isotropic random fields occurs when the spatial correlation length is about half of the specimen length.

It should be noted that an enhanced constitutive model, considering the influence of the porosity and the fines content on the mechanical behavior of soils, is still needed to account for the hydro-mechanical coupling of suffusion problems.

Chapter 5   A hydro-mechanical model for granular soils considering internal erosion

5.1. Introduction

The previous chapters mainly focused on the hydraulic process, i.e. the evolution of the eroded mass and permeability while the mechanical part was neglected. It is important to add that the soils constituting embankment dams or levees are usually subjected to complex stress states [25]. Some attempts have been made to model the mechanical response to internal erosion by removing particles in granular materials. Muir Wood et al. (2010) [48] modeled the mechanical consequences of internal erosion by a two-dimensional discrete element analysis and found that internal erosion changes the density state of the material from dense to loose as they compared the current soil state to the critical state line. Scholtès et al. (2010) [49] developed a three-dimensional discrete element model and an analytical micromechanical model to describe the mechanical responses induced by particle removal in granular materials. They found that the mechanical behavior of the soil changes from dilative to contractive with the removal of soil particles. However, this removal was based on the size of the particles and their degree of interlocking, and the fluid phase was not considered. Hosn et al. (2018) [50] studied the macroscopic response during internal erosion and the post-internal erosion properties of granular materials by particle removal, considering a one-way coupling between the fluid and the solid phases via the discrete element and the pore scale finite volume methods. The erosion process was simplified into the definition of the detached and transportable particles by calculating the unbalanced fluid force and by defining a controlling constriction size. Hicher (2013) [51] presented a numerical method to predict the mechanical behavior of granular materials subjected to particle removal and concluded that the removal of soil particles may cause diffuse failure in eroded soil masses. However, the process of real erosion was not considered. It is, therefore, of interest to develop a numerical method that will provide the modeling of the hydro-mechanical response of soils subjected to internal erosion.

Although the discrete element method could better explain (with some assumptions and simplifications) the behavior of granular materials at the micro-scale (particle scale level), the computational time still remains too long when we address real soil structure problems such as embankment dams. This chapter proposes a relevant numerical model built within the framework of continuum mechanics in order to investigate the coupled hydro-mechanical behavior of soils subjected to internal erosion for practical purpose. The four-constituent model has been enhanced to describe the detachment and transport of fine particles induced by the fluid with more realistic consideration of the effects of the fines content and the shear stress. This process has been coupled with an advanced critical state-based constitutive model, which has been improved by taking into account the effects of the evolution of the fines content inside the soil. Assuming a homogenous soil sample, a practical simulation platform for the triaxial erosion tests under mechanical loadings has also been proposed. The predictive ability of the approach has also been examined by simulating

internal erosion tests on HK-CDG mixtures (sand and completely decomposed granite) under mechanical loadings. Finally, the influence of the stress state, the initial density, and the initial fines content of the soil have been investigated by the new model.

5.2. Coupled hydro-mechanical model

5.2.1. Mass balances and transported particles

According to chapter 3, the hydraulic process of suffusion can be described by a system of non-linear partial differential equations deduced from the mass balance of the mixture system:

$$\text{div}\left(\mathbf{q}_w\right)+\text{div}\left(\mathbf{v}_s\right)=0 \quad \dotfill (5.1)$$

$$-\frac{\partial\phi}{\partial t}+\text{div}\left(\mathbf{v}_s\right)-\text{div}\left(\phi\mathbf{v}_s\right)=\hat{n} \quad \dotfill (5.2)$$

$$\frac{\partial\left(f_c\right)}{\partial t}-\frac{\partial\left(f_c\phi\right)}{\partial t}+\text{div}\left(f_c\mathbf{v}_s\right)-\text{div}\left(f_c\phi\mathbf{v}_s\right)=\hat{n} \quad \dotfill (5.3)$$

$$\frac{\partial\left(c\phi\right)}{\partial t}+\text{div}\left(c\mathbf{q_w}\right)+\frac{\partial\left(c\phi\mathbf{v}_s\right)}{\partial t}=-\hat{n} \quad \dotfill (5.4)$$

where $\phi(x,t)$, $f_c(x,t)$ and $c(x,t)$ are the porosity, the amount of erodible fines and the concentration of the fluidized particles, respectively; $\hat{n}$ is the source term describing the exchange between the erodible fines and the fluidized particles; $\mathbf{v}_s$ is the velocity of the soil skeleton; $\mathbf{q}_w(x,t)$ is the total discharge of the pore fluid assumed to be governed by Darcy's law:

$$\mathbf{q_w}=-\frac{k\left(f_c,\phi\right)}{\eta_k\bar{\rho}\left(c\right)}\mathbf{grad}\left(p_w\right) \quad \dotfill (5.5)$$

with the intrinsic permeability of the medium $k(f_c,\phi)$ and the density of the mixture $\bar{\rho}(c)$ defined as:

$$k=k_0\left[1-f_c\left(1-\phi\right)\right]^{3m_k} \quad \dotfill (5.6)$$

$$\bar{\rho}=c\rho_s+\left(1-c\right)\rho_f \quad \dotfill (5.7)$$

where η_k is the kinematic viscosity of the fluid; p_w is the pore fluid pressure; ρ_s and ρ_f are the density of the solid and the fluid respectively; m_k is a power index which varies with the pore geometry [130]. More details can be found in chapter 3.

5.2.2. Balance of linear momentum

The model has been developed for geotechnical applications and it is not the aim of the present paper to present the thermodynamical setting of the erosion model. Therefore, the linear momentum balance equation of a constituent is given as follows under isothermal and quasi-static conditions:

$$\text{div}\left(\boldsymbol{\sigma}_i\right)+\hat{\mathbf{p}}_i=0,\ \sum_i\hat{\mathbf{p}}_i=0 \quad \dotfill (5.8)$$

where $\boldsymbol{\sigma}_i$ is the total Cauchy stress tensor of the solid or liquid phase; $\hat{\mathbf{p}}_i$ is the interaction force between solid and liquid phases. In this configuration, further density driven momentum production (see Steeb and Diebels 2003 [128]) and body forces are not taken into account. Nevertheless, we

assume that the process is slow, i.e. the inertia forces can be neglected. This equilibrium equation allows prescribing the total force $\mathbf{t} = \boldsymbol{\sigma} \cdot \mathbf{n}$ and the solid displacement $\mathbf{u}_s$ at the boundary of the body.

The partial Cauchy stresses $\boldsymbol{\sigma}_i$ for the two phases are derived as follows for a fluid saturated medium [152]:

$$\boldsymbol{\sigma}_s = \boldsymbol{\sigma}' - (1-\phi) p_w \mathbf{I}, \ \boldsymbol{\sigma}_l = -\phi p_w \mathbf{I} \quad ....(5.9)$$

where $\boldsymbol{\sigma}'$ is the effective stress tensor, calculated by the non-linear incremental constitutive model presented in the next section; p_w is the pore fluid pressure. Thus the set of equations (5.1)-(5.4) can be closed by:

$$\operatorname{div}(\boldsymbol{\sigma}' - p_w \mathbf{I}) = 0 \quad ....(5.10)$$

5.2.3. Erosion law

The variable $\hat{n}$ in Eqs. (5.2)-(5.4) is the volumetric mass exchange at any point in time, given by the following relation [95]:

$$\hat{n} = -\lambda_e (1-\phi)(f_c - f_{c\infty}) |\mathbf{q_w}| \quad ....(5.11)$$

where $f_{c\infty}$ is the ultimate fines content after a long seepage period; λ_e is a material parameter. The erosion rate depends not only on the total discharge of fluid $\mathbf{q_w}$, but also on the residual fines content $(f_c - f_{c\infty})$. $f_{c\infty}$ is assumed to decrease when the hydraulic gradient increases as follows [67]:

$$f_{c\infty} = f_{c0} \left[\left(1 - \frac{\alpha_1}{\exp(\eta/M_p)}\right) \exp\left(-|\mathbf{q_w}|^{\alpha_3} \times 10^{\alpha_2}\right) + \frac{\alpha_1}{\exp(\eta/M_p)} \right] \quad ....(5.12)$$

where f_{c0} is the initial fines content, α_1, α_2 and α_3 are material parameters. A mechanical component "η" defined later on is introduced into the definition of $f_{c\infty}$, in order to take into account the influence of the stress state on the erosion rate.

Note that the mass exchange term $\hat{n}$ is defined as a function of the porosity, the initial fines content, the flow rate and the stress state. There isn't any explicit expression to define the critical hydraulic gradient required to initiate the erosion or the soil skeleton deformation. All the unknown variables are coupled implicitly and solved by the system of the partial differential equations.

This chapter focuses on the hydro-mechanical coupling during suffusion, while on the one hand the strength evolution induced by the decrease of the fines content has been addressed, but the clogging during suffusion on the other hand has not been considered.

5.2.4. Critical state based soil model considering fines content effect

A non-linear incremental constitutive model including the critical state concept has been adopted [53]. The non-linear frictional behavior of the granular materials can be described by an asymptotic relation between the stress ratio η and the shear strain ε_d as follows:

$$\eta = M_p\left(1 - e^{-\frac{G_\eta}{M_p}\varepsilon_d}\right) \quad\text{...(5.13)}$$

where M_p is the maximum strength ratio; $G_\eta = 3G/p'$ is the initial stiffness; p' is the effective pressure; G is the shear modulus. The model has been enhanced by introducing a non-linear elasticity, a non-linear stress dilatancy, and the critical state concept [133, 153, 154]. More details of the model can be found in [53].

The constitutive equations under axisymmetric triaxial condition are briefly summarized as follows:

$$\delta p' = K\left\{\delta\varepsilon_v - A_d\left(M_{pt} - \frac{q}{p'}\right)\delta\varepsilon_d\left[1 - \exp(-d\eta)\right]\right\} \quad\text{...........................(5.14)}$$

$$\delta q = 3G\delta\varepsilon_d\left(1 - \frac{q}{p'M_p}\right) + \frac{q}{p'}\delta p' \quad\text{...(5.15)}$$

with

$$G = G_0\frac{(2.97-e)^2}{(1+e)}\left(\frac{p'}{p_{at}}\right)^n, \quad K = K_0\frac{(2.97-e)^2}{(1+e)}\left(\frac{p'}{p_{at}}\right)^n \quad\text{...............(5.16)}$$

$$M_p = \frac{6\sin\phi_p}{3-\sin\phi_p}, \quad M_{pt} = \frac{6\sin\phi_{pt}}{3-\sin\phi_{pt}} \quad\text{................................(5.17)}$$

where ϕ_p and ϕ_{pt} are determined by

$$\tan\phi_p = \left(\frac{e_c}{e}\right)^{n_p}\tan\phi_c, \quad \tan\phi_{pt} = \left(\frac{e_c}{e}\right)^{-n_d}\tan\phi_c \quad\text{...................(5.18)}$$

with the critical state void ratio e_c given by

$$e_c = e_{cr0} - \lambda\left(\frac{p'}{p_{at}}\right)^\xi \quad\text{...(5.19)}$$

where the stress ratio $\eta = q/p'$ under axisymmetric triaxial condition is defined by the deviatoric stress q ($q = \sigma_a - \sigma_r$) and the mean effective stress p' ($p' = (\sigma_a' + 2\sigma_r')/3$), with σ_a and σ_r the axial and radial stress, respectively; the deviatoric strain increment $\delta\varepsilon_d = 2(\delta\varepsilon_a - \delta\varepsilon_r)/3$ is a function of the axial and radial strain increments; $\delta\varepsilon_v = \delta\varepsilon_a + 2\delta\varepsilon_r$ is the volumetric strain increment; K and G are the bulk and shear moduli with the reference bulk and shear moduli K_0 and G_0; Poisson's ratio $\upsilon = (3K_0 - 2G_0)/(6K_0 + 2G_0)$; the non-linear elastic constant n (typically 0.5-0.7); $p_{at} = 101.325\ kPa$ is the atmospheric pressure chosen as the reference stress; A_d and d are the stress-dilatancy parameters; e_{cr0} is the reference critical void ratio at extremely low confining pressure; λ and ξ are material constants controlling the non-linearity of the critical state line; ϕ_c is the critical friction angle.

Since the fines content evolves during internal erosion, the constitutive model needs to consider such internal soil mass evolution. According to [52, 155], e_{cr0} is a function of the evolutive fines

content f_c, in order to unify the mechanical behavior of a sand-silt mixture for different fines contents:

$$e_{cr0} = \left[e_{hc,cr0} \left(1 - f_c \right) + a f_c \right] \frac{1 - \tanh \left[\zeta \left(f_c - f_{th} \right) \right]}{2} + e_{hf,cr0} \left(f_c + \frac{1 - f_c}{\left(R_d \right)^m} \right) \frac{1 + \tanh \left[\zeta \left(f_c - f_{th} \right) \right]}{2} \quad \text{................................(5.20)}$$

where $e_{hc,cr0}$ and $e_{hf,cr0}$ are the reference critical void ratios for the pure sand and the pure silt, respectively. a, ζ, R_d, m and f_{th} are material constants: a controls the slope of the curve $e_{cr0} - f_c$ for the silty sand varying from -1.0 to 1.0. m controls the slope of the curve $e_{cr0} - f_c$ for the sandy silt varying from 0.0 to 1.0, f_{th} and ζ control the transition zone between the silty sand and the sandy silt. ζ controls the evolution rate of the transition zone ($\zeta = 20$ after Yin et al. 2014; 2016), f_{th} is the threshold fines content from a coarse grain skeleton to a fine grain skeleton, varying usually from 0.2 to 0.35 on the basis of existing experimental data; R_d is the ratio of the mean size of the coarse grains D_{50} to the mean size of the fine grains d_{50}. The material constants a, m and f_{th} can be determined by measuring the evolution of the minimum void ratio $e_{\min}$ versus f_c, which is obtainable at low experimental cost, as suggested by [52, 155]. It should be pointed out that Eq. (5.20) is mathematically structured based on the hyperbolic tangent function to ensure a continuous and smooth transition domain; more validation and discussion can be found in [52, 155].

5.2.5. Hydro-mechanical responses of soils during internal erosion

Two main influences can be noted concerning the mechanical impact of the decrease of the fines content induced by internal erosion. First, according to Eq.(5.16), the increase of the void ratio can reduce the elastic moduli G and K, leading to increasing deformation of the granular assembly. The second consequence is linked to the interlocking features. The sliding resistance between particles has two origins: one is the friction between two particles, the other is related to the geometrical (topological) effect of the neighboring particles which will resist the sliding displacement of two particles in contact, i.e. the interlocking effect. From a macroscopic standpoint, the first aspect is characterized by the internal friction angle ϕ_c, corresponding to the critical state; the second aspect is related to the density state, which will in turn influence the peak strength and the dilative/contractive behavior of the soil. In the model, this interlocking influence is taken into account by Eqs. (5.18)-(5.20), which relate the sliding resistance, controlled by the mobilized peak friction angle ϕ_p to the density state (e_c/e) of the assembly. Therefore, the loss of fine particles affects the interlocking, i.e. the density state, by changing simultaneously the void ratio e and the critical void ratio e_c. When a part of the fine particles is detached from the soil skeleton, the void ratio e increases, the critical void ratio e_c evolves according to the fines content f_c evaluated by Eqs. (5.19)-(5.20). According to [52, 155], in the case of a fine grain skeleton, the loss of fine particles will decrease the critical void ratio e_c. From a microscopic standpoint, the loss of fine particles makes it easier for the force chains which control the soil stability to buckle. As observed by [5], the dilative behavior of the non-eroded specimen changed to a contractive behavior after

erosion. In the case of a coarse grain skeleton, the loss of fine particles will make the critical state line move upwards in the *e-logp'* plane. The interlocking effect could, therefore, be enhanced when e_c/e increases. This might explain the observed increase of the initial peak strength of the eroded specimen in some cases [32]. Thus, when a part of the fine particles is detached from the soil skeleton, the void ratio e increases, and the critical void ratio e_c evolves according to the fines content f_c, creating a disequilibrium of internal and external forces and, consequently, a deformation of the granular assembly.

During an internal erosion experimental test, the soil specimen is subjected to constant boundary stresses, whereas the amount of eroded fine particles increases progressively. Therefore, the stress ratio η is kept constant while the peak strength ratio M_p and the initial stiffness G_η evolve as a function of the density state of the soil. The shear strain can be written in an incremental form from Eq. (5.13):

$$\delta\varepsilon_d = -\frac{M_p^{(i)}}{G_\eta^{(i)}}\ln\left(1-\frac{\eta^{(i)}}{M_p^{(i)}}\right) + \frac{M_p^{(i-1)}}{G_\eta^{(i-1)}}\ln\left(1-\frac{\eta^{(i-1)}}{M_p^{(i-1)}}\right) \quad\text{...(5.21)}$$

with the superscript (i) representing the current loading step and $(i-1)$ the previous loading step. The volumetric strain increment can then be computed as:

$$\delta\varepsilon_v = -\frac{p'}{K^2}\delta K + A_d\left(M_{pt}-\frac{q}{p'}\right)\delta\varepsilon_d\left[1-\exp(-d\eta)\right] \quad\text{...(5.22)}$$

The incremental modification of the void ratio induced by the body deformation is added to the void ratio change caused by erosion:

$$(\delta e)_{total} = (\delta e)_{er} + \delta\varepsilon_v(1+e) \quad\text{...(5.23)}$$

Under triaxial condition, the axial and radial strain increments ($\delta\varepsilon_a$ and $\delta\varepsilon_r$) are functions of the shear and volumetric strain increments:

$$\delta\varepsilon_a = \delta\varepsilon_d + \frac{1}{3}\delta\varepsilon_v, \quad \delta\varepsilon_r = \frac{1}{3}\delta\varepsilon_v - \frac{1}{2}\delta\varepsilon_d \quad\text{...(5.24)}$$

Thus, $\delta\varepsilon_a$ and $\delta\varepsilon_r$ can be used alternatively instead of $\delta\varepsilon_d$ and $\delta\varepsilon_v$.

The influence of the effective stress on the erosion of fine particles is considered in two parts. First, the volume change induced by the effective stress ($\text{div}(\mathbf{v}_s) = \partial(\varepsilon_v)/\partial t$) has been used in the mass balance equations (5.1)-(5.4). Thus, the impact of the effective stress is implied in the volume change, which will further induce changes in the permeability as well as in the flow rate and the erosion rate, according to Eqs. (5.5)-(5.7) and (5.11)-(5.12). Secondly, the mass exchange term $\hat{n}$ for the mass balance equations (5.1)-(5.4) is formulated to be dependent directly on the shear stress ratio η/M_p, according to Eqs. (5.11)-(5.12), as shown by experimental results [5]. However, the impact of the confining pressure on the erodibility of fine particles still remains unclear since the results in the literature [5, 28, 33, 69, 108] present contradictions. More advanced experimental tests

with visualization of particles are needed to calibrate more precisely the relationship between the erosion rate and the stress state.

5.3. Simulations of tests

5.3.1. Description of laboratory tests

Chang & Zhang (2011) [5] performed several hydraulic-gradient controlled downward erosion tests on gap-graded HK-CDG mixtures with a newly developed stress-controlled erosion apparatus. These experiments were performed in order to investigate the initiation and the development of internal erosion in soils subjected to multi-step fluid flow under complex stress states, as well as the stress-strain behavior of soils subjected to internal erosion. The experimental set-up consisted of a triaxial apparatus, a pressurized water supply system, a particle collection system, and a water collection system (See Figure 2.12). A hollow base pedestal was designed for the eroded soil and the seepage water to pass through in the downward direction. The tested soil was obtained by mixing the commercial washed Leighton Buzzard sand (fraction E), and the completely decomposed granite (CDG) extracted from a construction site on Beacon Hill, Hong Kong, following the grain size distribution shown in Figure 5.1.
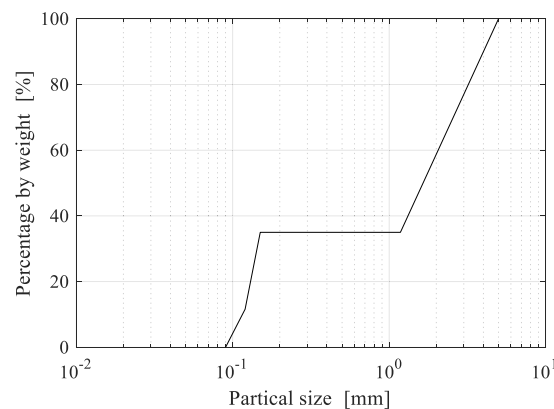
Figure 5.1 Grain size distribution of the tested HK-CDG mixture

Each triaxial specimen, 100 mm in diameter and 100 mm in high, was prepared by moist tamping to prevent soil segregation. The erosion tests were carried out under initial isotropic and anisotropic stresses with the major principal stress being parallel to the seepage direction. After a saturation stage, the consolidation of the specimen was realized by increasing gradually the confining stress. For the tests under an anisotropic stress condition, the vertical stress was gradually increased up to the target value after the specimen had been isotropically consolidated to a given stress state. After the stress state being applied to the specimen, the pressurized water supply and the water collection system were connected to the triaxial system. The hydraulic gradient, i, was increased in stages to the final value (i.e., 0.15 per 10 min for $i \leq 1.0$, 0.25 per 10 min for $1.0 < i < 2.0$, and 0.50 per 10 min for $i \geq 2.0$). For 10 min, the hydraulic gradient was increased within the first 2 min and then kept constant for the following 8 min. Once the soil erosion was initiated, the hydraulic gradient was kept constant until no further soil loss was observed (i.e. $< 25.0 \text{g/m}^2$ per 10 min). Then, the hydraulic gradient was increased to another level. A typical increase of the hydraulic gradient is

77

illustrated in Figure 5.2. During the internal erosion testing, the applied hydraulic gradient, the vertical displacement, the outflow rate, and the eroded soil mass were continuously measured. The radial deformation was deduced from planar deformation observed on digital photographs. Conventional drained triaxial compression tests were then carried out to study the stress-strain behavior of the soil having been subjected to internal erosion. Note that the samples of gap-graded or broadly graded granular soils are normally more or less heterogeneous with non-uniform distribution of initial void ratio and fines content in spatial space. During the erosion process, fluidized fine particles may be blocked when passing the interface between the local "loose" area and the local "dense" area, which results in heterogeneous particle size distributions. However, not enough detail (i.e. the evolution of pore pressure along the height of the specimen) was given by [5] to be able to consider the initial heterogeneity of the soil specimen; as a consequence, the specimens in the following simulations were assumed to be initially homogeneous.
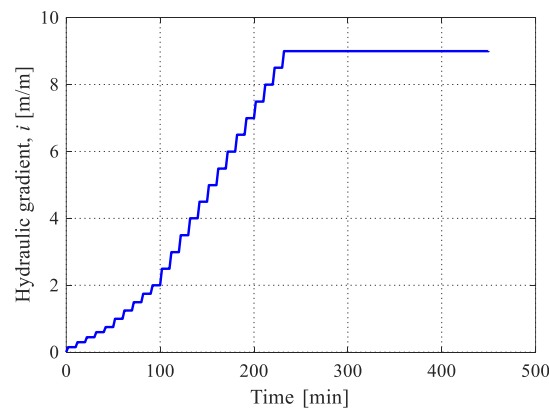
Figure 5.2 Illustration of increasing hydraulic gradient applied during internal erosion test

A series of tests on the gap-graded HK-CDG mixtures samples [5, 104] were selected for simulations. BM-C-1, BM-C-2, and BM-C-3 were conventional drained triaxial tests on isotropically consolidated samples without erosion, under confining stresses of 50, 100, and 200 kPa, respectively. GS-C-1, GS-C-2, and GS-C-3 were erosion tests under isotropic stress states with confining stress of 50, 100 and 200 kPa, respectively. GS-C-4, GS-C-5 and GS-C-6 were erosion tests under anisotropic stress states with confining stress of 50 kPa and deviatoric stress of 50, 100 kPa and 150 kPa, respectively. For the eroded samples, drained triaxial tests were carried out starting at the stress state applied during the erosion tests. More details about the laboratory test soil can be found in Chang (2012) [104].

5.3.2. Simulation schemes

The numerical modeling scheme can be summarized in Figure 5.3 for granular media under constant stresses considering internal erosion. (i) represents the current step and $(i-1)$ the previous step. The set of partial differential equations were solved explicitly in time and by the finite difference method in space, the primary unknowns being the soil skeleton displacement ($\mathbf{u}_s(x,t)$), the pore pressure ($p_w(x,t)$), the porosity ($\phi(x,t)$), the fines content ($f_c(x,t)$) and the concentration

of fluidized particles ($c(x,t)$). Other unknowns, such as the total discharge rate $\mathbf{q}_w(x,t)$, the density of the mixture $\bar{\rho}(x,t)$, and the intrinsic permeability $k(x,t)$ could be explicitly determined by Eqs. (5.5)-(5.7). For clarity, time t and space x variables are omitted in the equations.

$$[\mathbf{u}_s, p_w, \phi, f_c, c]^{(i-1)}$$

$$\Downarrow$$

$$\text{div}(\mathbf{q}_w) + \text{div}(\mathbf{v}_s) = 0$$

$$-\frac{\partial \phi}{\partial t} + \text{div}(\mathbf{v}_s) - \text{div}(\phi \mathbf{v}_s) = \hat{n}$$

$$\frac{\partial(f_c)}{\partial t} - \frac{\partial(f_c \phi)}{\partial t} + \text{div}(f_c \mathbf{v}_s) - \text{div}(f_c \phi \mathbf{v}_s) = \hat{n}$$

$$\frac{\partial(c\phi)}{\partial t} + \text{div}(c\mathbf{q}_w) + \frac{\partial(c\phi \mathbf{v}_s)}{\partial t} = -\hat{n}$$

$$\Downarrow$$

$$[p_w, \phi, f_c, c]^{(i)}$$

$$\Downarrow$$

$$\delta\varepsilon_d = -\frac{M_p^{(i)}}{G_\eta^{(i)}} \ln\left(1 - \frac{\eta^{(i)}}{M_p^{(i)}}\right) + \frac{M_p^{(i-1)}}{G_\eta^{(i-1)}} \ln\left(1 - \frac{\eta^{(i-1)}}{M_p^{(i-1)}}\right)$$

$$\delta\varepsilon_v = -\frac{p'}{K^2}\delta K + A_d\left(M_{pt} - \frac{q}{p'}\right)\delta\varepsilon_d\left[1 - \exp(-d\eta)\right]$$

$$\Downarrow$$

$$[\mathbf{u}_s]^{(i)}, (\delta e)_{\text{total}}^{(i)} = (\delta e)_{\text{er}}^{(i)} + \delta\varepsilon_v^{(i)}(1+e)$$
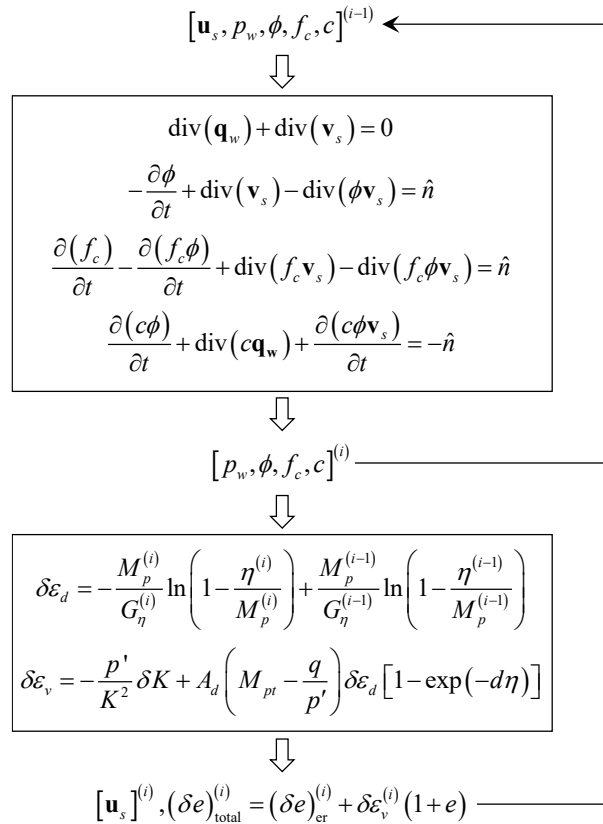
Figure 5.3 Computation flowchart for internal erosion under constant stresses

Based on the above numerical scheme, the simulation could be conducted with the real dimensions of the tests by using the finite element method to investigate the temporal and spatial variations of the fines content and hydraulic conductivity during internal erosion. However, under the framework of continuum mechanics, the erosion process is uniform under the assumption of an initially uniform homogeneous specimen. In this study, the example of a well-controlled erosion coupled with the mechanical loading triaxial tests on reconstructed specimens can be seen as a case of a representative elementary volume with the hydraulic gradient across the specimen as input boundary condition. Hence, a very interesting simplified erosion and mechanics coupled simulation model can be formulated, which should be useful in evaluating the eroded mass as well as the induced deformation of the soil element. In conventional drained triaxial test simulations before and after erosion, the confining stress was maintained constant. Thus, the ratio between the incremental deviatoric stress and the incremental mean effective stress was equal to 3. From Eqs. (5.14) and (5.15), the deviatoric stress and the volumetric strain could be obtained by imposing an incremental deviatoric strain as follows:

$$\delta q = 3G\delta\varepsilon_d\left(1 - \frac{q}{p'M_p}\right) \Bigg/ \left(1 - \frac{q}{3p'}\right) \quad\text{...(5.25)}$$

$$\delta p' = \frac{\delta q}{3} \quad \text{..(5.26)}$$

$$\delta \varepsilon_v = \frac{\delta p'}{K} + A_d \left(M_{pt} - \frac{q}{p'} \right) \delta \varepsilon_d \left[1 - \exp(-d\eta) \right] \quad \text{..(5.27)}$$

Note that the above conventional drained triaxial test simulations were performed on a representative elementary volume, thus the time t and the space $_x$ were not considered in the simulations.

5.3.3. Calibration of parameters

The physical properties of the soil mixtures are summarized in Table 5.1. The initial void ratio e_0 before the external stress being applied is 0.53. The mechanical parameters were calibrated as follows (see Figure 5.4): (a) the elastic parameters (K_0, G_0 and n) were determined from an isotropic compression test with an assumed value of Poisson's ratio $\upsilon = 0.35$; (b) the friction angle ϕ_c was determined from the stress paths of the triaxial tests; (c) the CSL related parameters (λ, ξ) were measured from drained triaxial tests. It was difficult to determine these two parameters because strain localizations appeared systematically at the end of the tests [104]; due to a lack of experimental data, the assumption of parallel critical state lines was made, and the values suggested by [155] were adopted. (d) due to the lack of data concerning Chang's tests, the values of the other parameters ($e_{hc,cr0}$, $e_{hf,cr0}$, a, m and f_{th}) were assumed based on published data on other similar materials (Yin et al., 2014, 2016) [52, 155]; e_{cr0} was measured from experiments (Figure 5.4b); (e) finally, the dilatancy parameters (d and A_d) were determined by fitting the stress-strain relations obtained in the triaxial tests BM-C-1, BM-C-2, and BM-C-3. The erosion parameters were calibrated by fitting the time evolution of the hydraulic conductivity and the cumulative loss of dry mass in tests GS-C-1 and GS-C-5. All determined parameters summarized in Table 5.2 and Table 5.3 were used to predict the hydro-mechanical behavior during the erosion tests and the following drained triaxial tests after erosion. Note that the parameters can also be identified by using optimization methods [134, 156, 157].

Table 5.1 Physical properties of the tested soil mixtures

Density of fluid	ρ_f	1.00 g/cm3
Density of solids	ρ_s	2.65 g/cm3
Kinematic viscosity of fluid	η_k	5.0×10-6 m2·s-1
Initial void ratio	e_0	0.53
Initial permeability	k	7.5×10-5 m·s-1
Initial fines content	f_{c0}	0.35

Table 5.2 Mechanical constants of HK-CDG mixture

Elastic parameters			Dilatancy parameters		CSL-related parameters				
K_0/MPa	G_0/MPa	n	d	A_d	$e_{hc,cr0}$	$e_{fc,cr0}$	ξ	λ	ϕ_c
50	16.7	0.95	18	0.35	0.8	0.86	0.45	0.03	40.5

Table 5.3 Erosion constants of HK-CDG mixture

Fines parameters			Erosion parameters				
a	m	f_{th}	λ_e	α_1	α_2	α_3	m_k
0.79	0.46	0.28	40	0.85	11	3	4
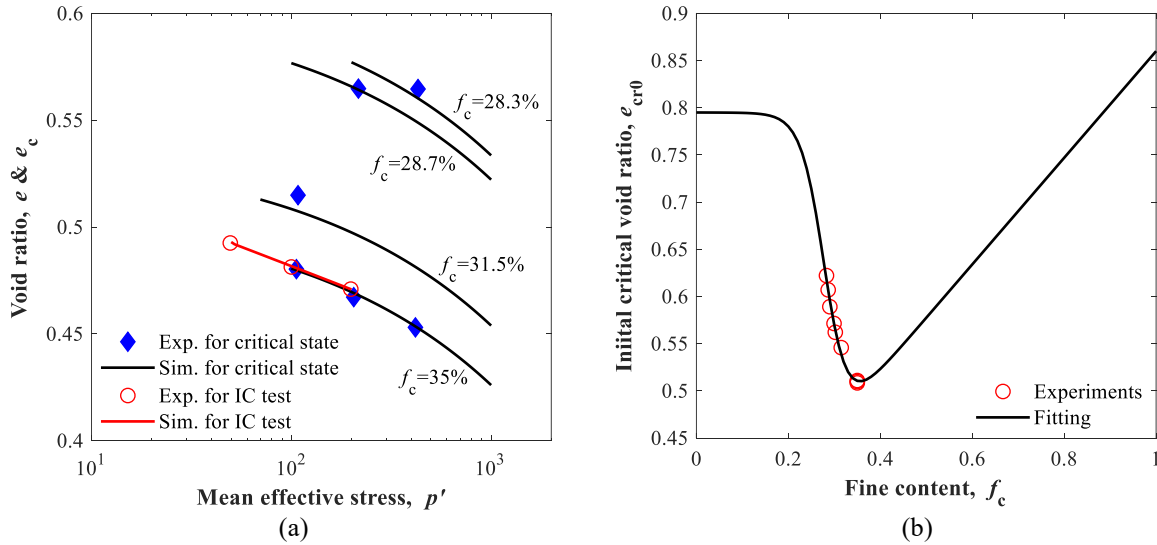
Figure 5.4 (a) Isotropic compression test simulation and critical state; (b) fitted reference critical void ratio versus fines content for HK CDG mixture

5.3.4. Hydro-mechanical modeling during erosion

Figure 5.5 shows the cumulative eroded soil mass and the variations in hydraulic conductivity during the internal erosion tests under different stress states. The experimental results show that the stress state during internal erosion affects significantly the hydraulic behavior of the soil. Specimens GS-C-1, GS-C-5, and GS-C-6 were tested under the same confining pressure (50 kPa), but with different deviatoric stresses: 0 kPa, 100 kPa and 150 kPa, respectively. Figure 5.5a shows the cumulative weights of the eroded soil in the three tests. It was found that the average erosion rate within the testing period increased with the increase of the deviatoric stress. [5] attributed this observation to the fact that the primary structure formed by the coarse particles became more unstable with the increase of the applied stress ratio. Combined with the effect of the loss of fine particles that provided lateral "support" for the primary soil skeleton structure, the erosion rate in the highest stress ratio case (specimen GS-C-6) was much larger than that in the isotropic stress case (specimen GS-C-1). Moreover, due to the loss of fine particles, the permeability increased significantly in the three tests as shown in Figure 5.5b. The more the fine particles were lost, the larger the permeability became. Finally, the permeability reached a relatively constant value.

The proposed model was able to reproduce the general trend of the erosion evolution until a stable step was reached. However, some differences between experimental and numerical results could be found, especially for the evolution of the hydraulic conductivity. After the loss of a significant number of fine particles, the soil specimen reached a new equilibrium state, where the increment of

81

the eroded mass was generally limited. During this period, the soil permeability slightly decreased because part of the transported fine particles was assumed to be captured within the soil skeleton during the erosion process, which induced a clogging of the constrictions among the coarse particles, i.e. a self-filtration phenomenon. The decreased diameters of the effective pore throats resulted in a reduction of permeability. Only few data are available in the literature concerning the self-filtration phenomenon during an erosion test. [30, 33] attributed the deviation of the hydraulic conductivity to the difference in homogeneity along the reconstituted soil specimens, induced probably by the segregation during preparation and placement of the specimen. Another aspect which was not considered was the unknown influence of the saturation stage, which might also lead to the heterogeneity of the soil sample before erosion. Not enough detail on this particular aspect was given by [104] to calibrate the filtration term in the mass exchange equations.
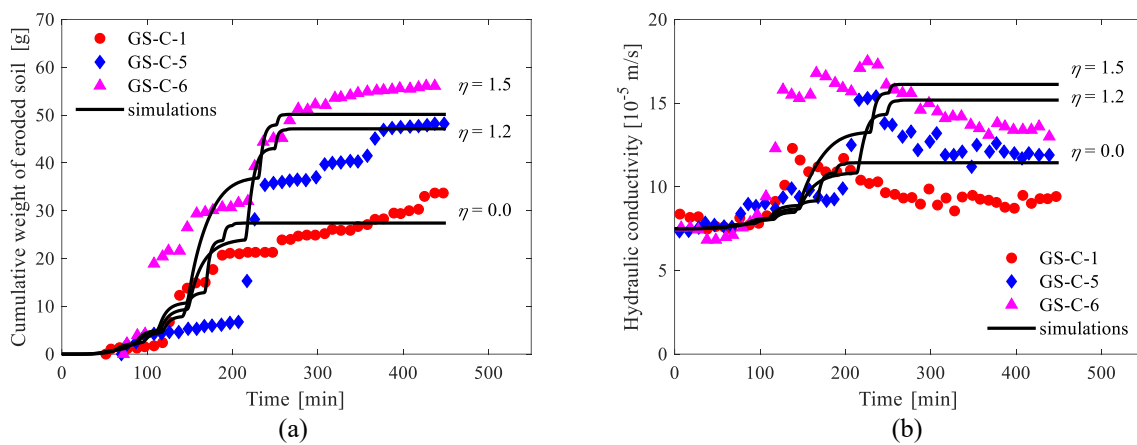
Figure 5.5 Comparison between experimental results and simulations for HK CDG mixture during erosion tests under different stress states: (a) Cumulative eroded soil mass and (b) variations of the coefficient of permeability

Figure 5.6 presents the applied increasing hydraulic gradients for the three internal erosion simulations under different stress states. When the hydraulic gradient is increased to 0.6, i.e. the initiating hydraulic gradient i_{start}, the fine particles will start to be eroded, as shown in Figure 5.5. According to the above cited experimental tests of [5], once the rate of the eroded weight became smaller than 0.02g/min, the hydraulic gradient was increased to another level. Sudden increases in the erosion rate, hydraulic conductivity and deformations of the specimen were observed at a gradient of 1.5, i.e. the soil skeleton deformation hydraulic gradient i_{sd}, as shown in Figure 5.5and Figure 5.7. In the numerical simulations, the final equilibrium states were reached at a gradient around 2.2 at 200 min for GS-C-1 and at 280 min for GS-C-5 and GS-C-6. Once the self-filtration mechanism is added into the simulations, the critical hydraulic gradients could be expected to increase, and the appearance of the final equilibrium state to be delayed. With the increase of the hydraulic gradient, the pore channels previously clogged could be unblocked. This aspect will be discussed in future work based on better documented experimental data that will consider the spatial variation of the fine particles during internal erosion.
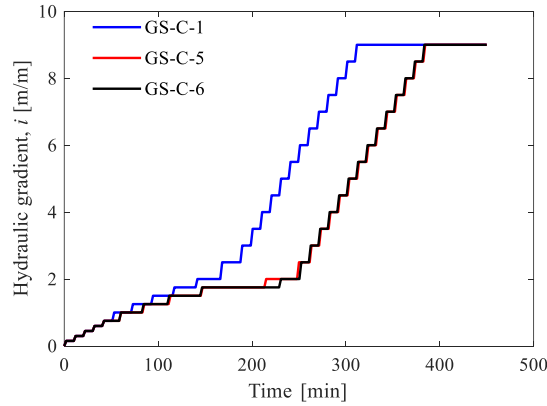
Figure 5.6 Increasing hydraulic gradients applied during internal erosion in the simulations

Figure 5.7 shows the axial and radial strains of the soil specimens caused by internal erosion. Here, the negative values mean that the sample diameter increased. Larger axial and radial strains were associated with higher stress ratios during the erosion process. The model was able to reproduce the initial small deformation stage, the skeleton deformation stage and the final equilibrium stage. A higher stress ratio was associated with larger axial and radial strains during the erosion process. Moreover, from a macroscopic point of view, the jumps in the evolution of the specimen deformation should be attributed to the changes in the hydraulic gradient. The results of the simulations under the applied increasing hydraulic gradients during internal erosion shown in Figure 5.6 and Figure 5.7 demonstrate that the numerical approach is also able to reproduce the temporary equilibrium state reached under the applied stresses with a relatively low hydraulic gradient.
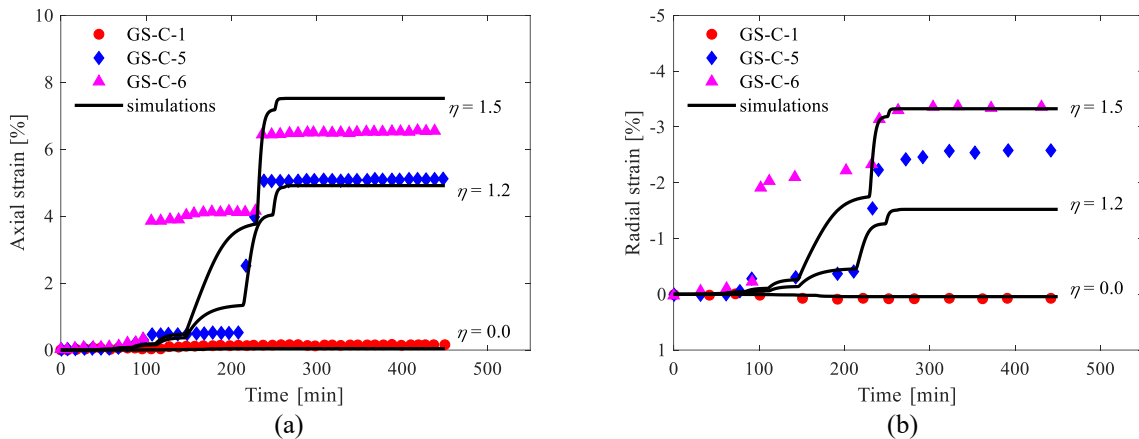
Figure 5.7 Comparison of the deformation of the specimen between experimental results and simulations for HK CDG mixture during erosion tests under different stress states: (a) axial strain and (b) radial strain.

5.3.5. Mechanical responses after erosion

Figure 5.8 illustrates a comparison between the experimental and the numerical results of drained triaxial tests on samples before and after erosion. Both experimental and numerical results show that the loss of fine particles during internal erosion affects significantly the mechanical behavior of the soil. When the soil loses a significant number of fine particles, its stress-strain behavior changes

from dilative to contractive. When a part of the solid fraction is eroded, the density state (e_c/e) decreases and, consequently, the shear resistance decreases, creating additional deformation of the granular assembly.

The proposed numerical approach was able to reproduce the general trend of the soil behavior up to the peak strength which corresponded in the experiments to the development of strain localization within the specimens. In some cases, discrepancies between experimental and numerical results could be seen, possibly due to the difficulty of measuring accurately certain material properties, such as the elastic stiffness or the friction angle, as a function of the fines content. Another aspect which was not considered in the simulations was that heterogeneity within the specimen could be produced by the combined effects of transport and filtration of the fine particles. Not enough detail of this particular aspect was given by [104].
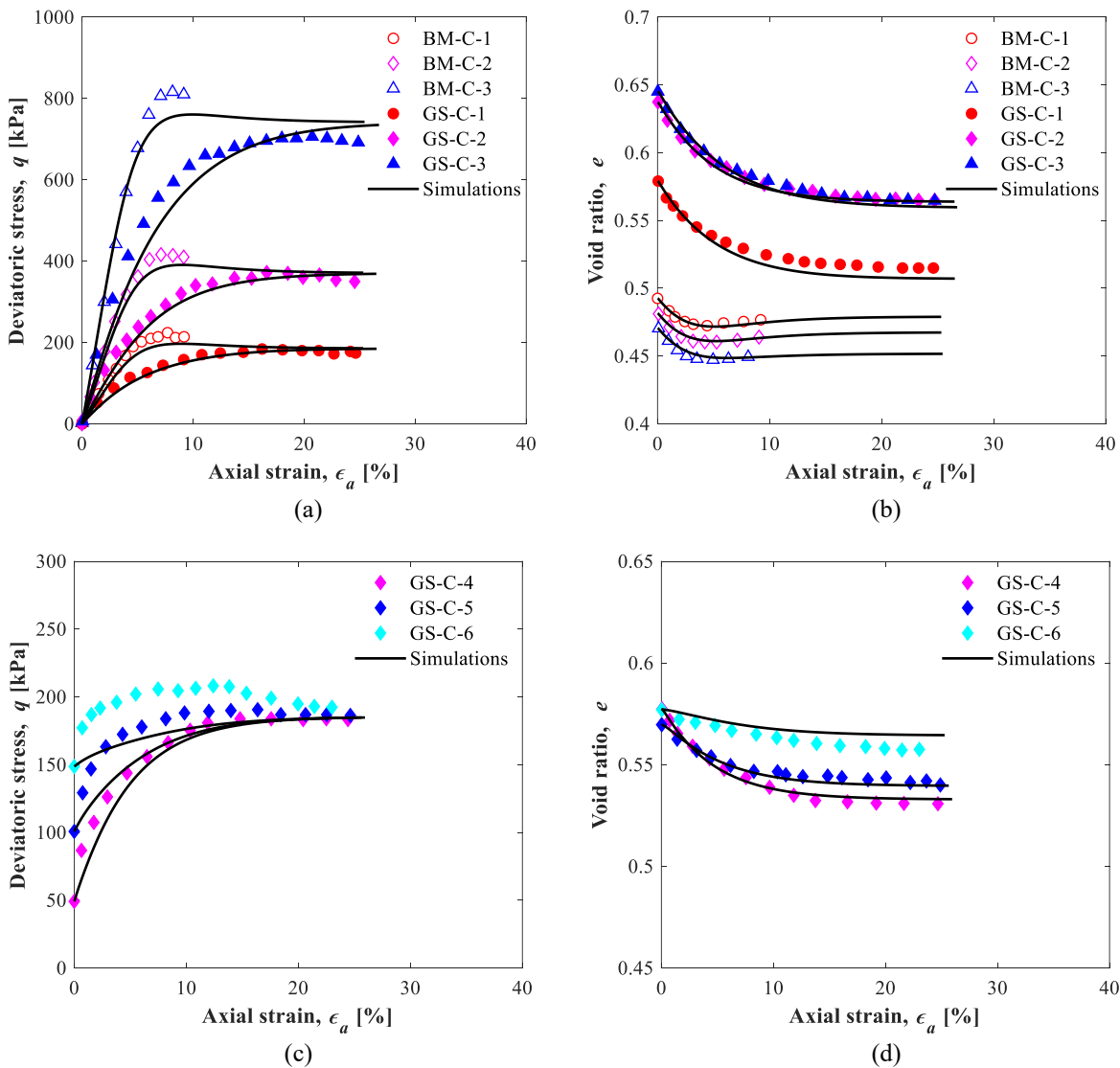
Figure 5.8 Comparison between experimental results and simulations for HK-CDG mixture before and after erosion: (a,c) deviatoric stress versus axial strain; (b,d) void ratio versus axial strain

5.4. Discussion

Several numerical tests were performed on the HK-CDG samples to investigate systematically the soil behavior which lost fines content during the erosion process, as well as the influences of soil's initial density and initial fines content. After applying the external stresses, each specimen was subjected to a hydraulic gradient at constant external stresses, as shown in Figure 5.2.

5.4.1. Influence of the soil's initial state on the initiation of erosion

According to Figure 5.5 and Figure 5.6, the proposed model is able to distinguish the initiating hydraulic gradient i_{start} and the soil skeleton deformation hydraulic gradient i_{sd} of the erosion process. Numerical tests were performed on the HK-CDG samples to further study the influence of the soil's initial state on the initiation of erosion. Figure 5.9 presents the cumulative weight of the eroded soil as a function of hydraulic gradient for (a) different initial fines contents and (b) different initial void ratios. It is obvious that the increase of the initial fines content or the decrease of the initial void ratio increases the hydraulic gradient required to cause erosion, which appears reasonable in view of the experimental phenomenon.
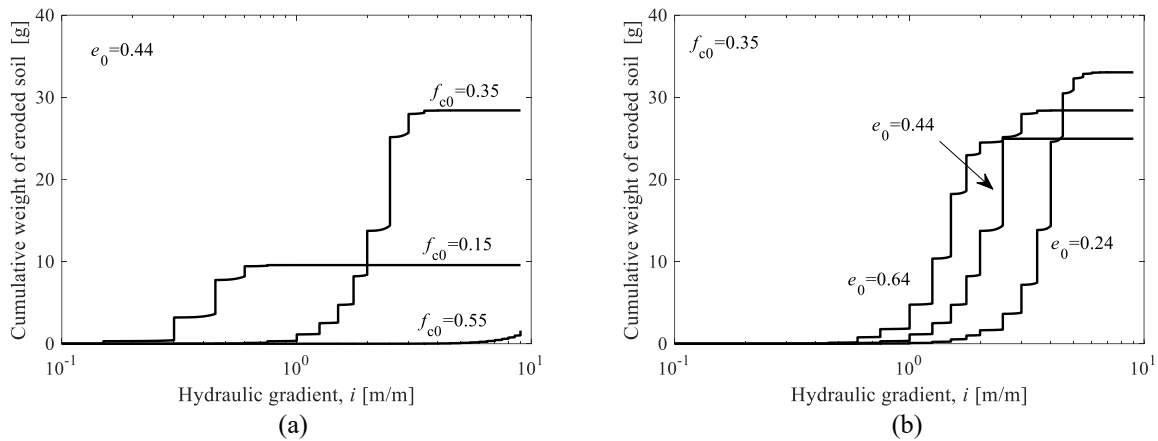
Figure 5.9 Cumulative weight of eroded soil as a function of hydraulic gradient for (a) different initial fines contents; and (b) different initial void ratios

5.4.2. Effect of internal erosion on the hydro-mechanical response

Numerical tests were performed on the HK-CDG samples, with $e_0 = 0.45$ and $f_{c0} = 0.35$. All the specimens were isotropically consolidated up to $p' = 100$ kPa and then sheared at different stress levels. Afterwards, each specimen was subjected to a hydraulic gradient while the external stresses were kept constant. Figure 5.10 presents the axial and the volumetric strains versus the eroded fraction of fine particles. For small stress ratios ($\eta = q/p' < 1$), a slight contraction occurred with the increase of the eroded fraction and the samples reached a final equilibrium state with an axial strain smaller than 5% after the entire erosion process. For intermediate η values ($\eta = 1.0$; 1.25), two stages could be identified. Slight contractions occur firstly, and the axial strain developed slowly. After 20% and 16.5% of the total mass being eroded for the samples under $\eta = 1.0$ and 1.25, the deformation increased much faster and the samples exhibited a large contraction. This result indicates that, at this stage, important grain rearrangements occurred in the microstructure so as to reach a new stable

mechanical state. However, for $\eta \geq 1.5$, no new equilibrium state could be reached; more details can be found in the next section for similar numerical tests on denser samples. Obviously, given Δf_c (or the fines loss in terms of percentage of the total fines $\Delta f_c / f_{c0} \times 100\%$), values can be identified as the triggering factor for the development of large macroscopic deformations. Furthermore, the higher the stress ratio is during erosion, the smaller an eroded fraction will be needed in order to lead the sample to failure. The predicted axial strains of GS-C-1 ($\eta = 0$), GS-C-5 ($\eta = 1.2$) and GS-C-6 ($\eta = 1.5$) with large fines content loss are compared in Figure 5.11 (the solid lines correspond to loss of fines content observed in experiments, and the dashed lines predict the erosion evolution in case the loss of fines content continues). It is shown that for the specimen GS-C-1 ($\eta = 0$), even if all the fines are eroded, the deformation remains below 1%; for specimens GS-C-5 ($\eta = 1.2$) and GS-C-6 ($\eta = 1.5$), a temporary equilibrium state is reached at $\Delta f_c = 5\%$, and then remains stable up to 15% (for GS-C-6) and 18% (for GS-C-5) of eroded fines. The axial strain then develops very rapidly with a small loss of fines.
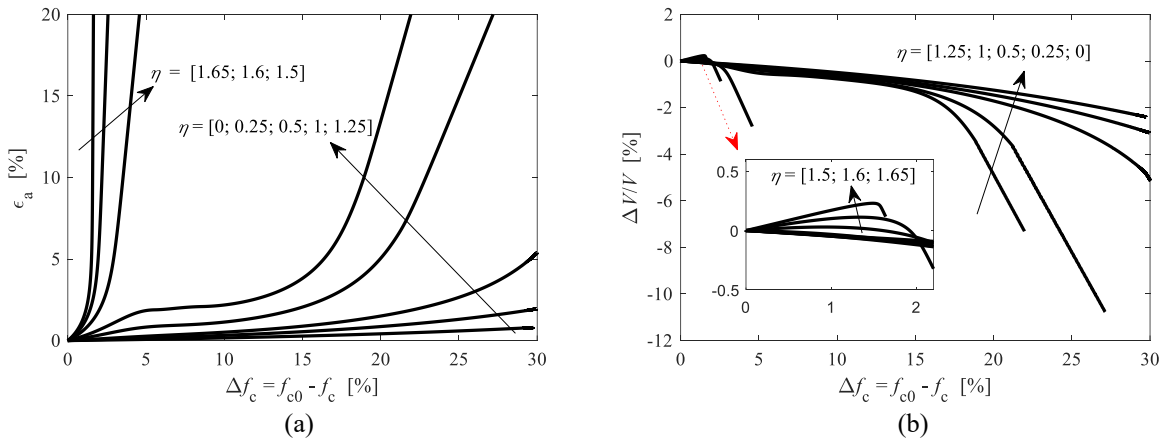
Figure 5.10 Specimen deformations as a function of the eroded fraction of fine particles in the simulations of erosion for different stress ratios $\eta = q/p'$: (a) axial strains; (b) volumetric strains
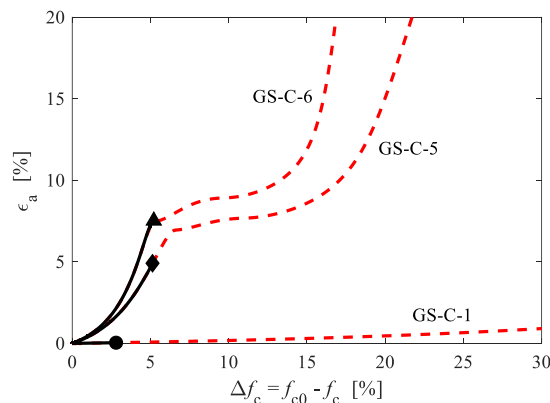
Figure 5.11 Simulated results of the calibrated erosion tests with continuing fines loss

As presented in Figure 5.12(c) and Figure 5.12(f), the erosion process tends to increase the sample porosity without producing significant macroscopic deformation, especially for low and medium η

values. As shown by the DEM simulations in [49, 158, 159], a certain amount of fine particles can be removed without significant consequence at the macroscopic scale due to the presence of floating grains not involved in the force chain network. Furthermore, the creation of a more open microstructure due to the loss of fines content dominates the effect of sample compression induced by local destabilizations.

In order to bring all the specimens to failure, triaxial compression was performed on the samples which stabilized after a certain fraction of the eroded mass. Figure 5.12 presents the simulations of the erosion for different stress ratios $\eta=q/p'$ and the following triaxial compression of the samples which stabilized at $\Delta f_c = 0.15$ and $\Delta f_c = 0.25$, respectively. These results demonstrate that the increase of the porosity produced a change in the specimen behavior from dilative to contractive. As shown also in Figure 5.10, the strain path was linked to the stress ratio. It is remarkable that the limiting threshold of η under which the sample failed during erosion was generally smaller than the value of q/p' at critical state (η_{cs}) obtained from the drained triaxial tests and dependent on the amount of the loss of fines. For a high degree of erosion (i.e. $\Delta f_c = 0.25$ as shown in Figure 5.12d-f), the specimen developed large compaction during erosion, even though the stress ratio $\eta=1.0$ was far from its value at the critical state ($\eta_{cs} = 1.68$). Even if the soil became denser and, therefore, somewhat stronger, large deformations might occur, leading to heavy damages to the earth structures. As stated in [51], granular assemblies can develop instability at a shear stress level much lower than the critical state failure line; the so-called diffuse failure can occur in highly eroded soils. Besides, the results demonstrate that the proposed model was able to take into account the evolution of the critical state which was different for the degraded specimens in comparison to the intact ones.

(a)

(d)
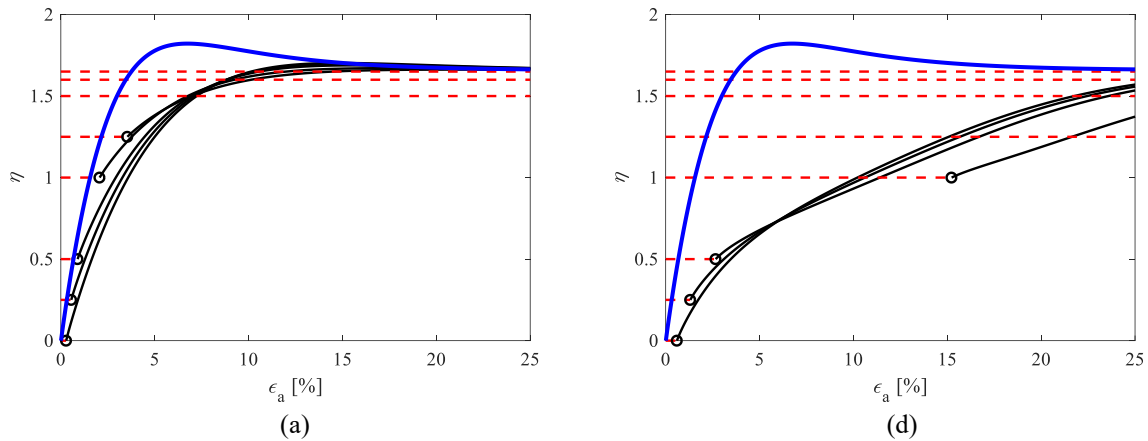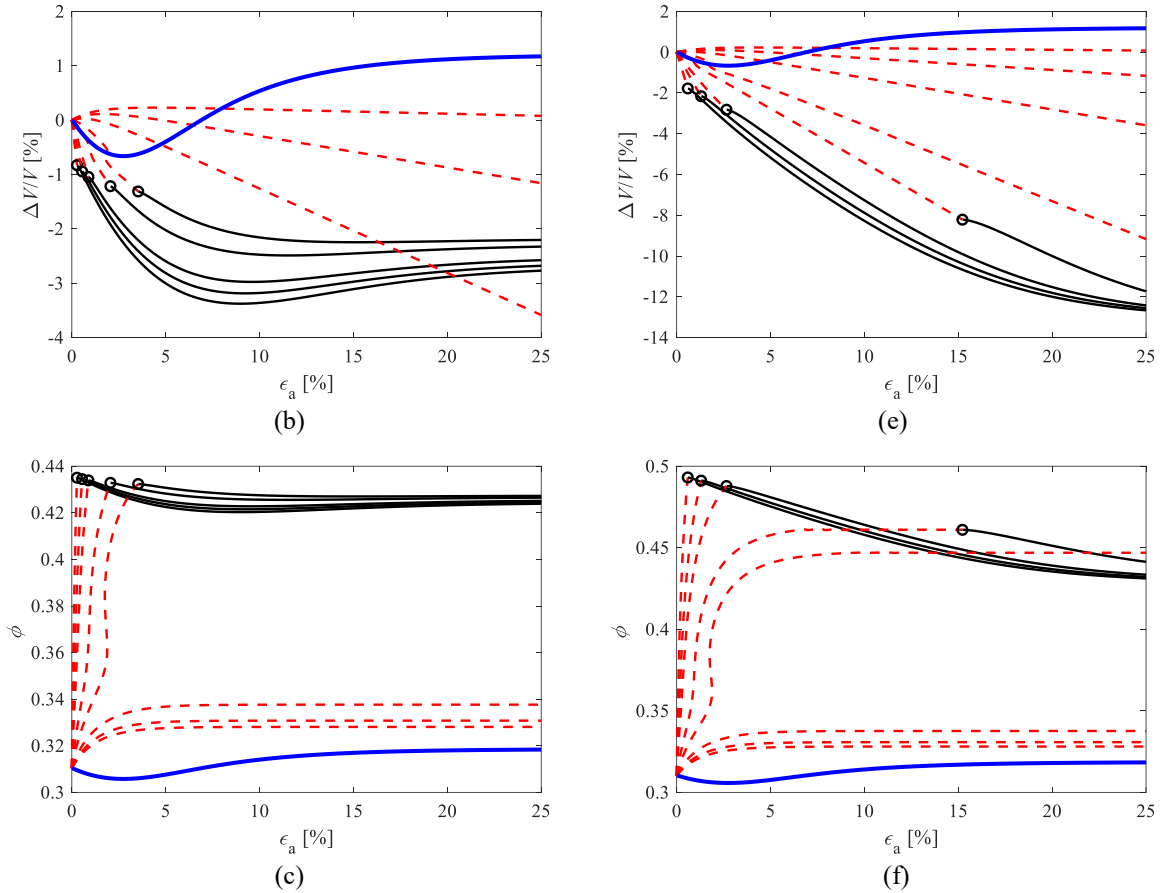
Figure 5.12 Simulations of erosion for different stress ratio $\eta=q/p'$ and the following triaxial compression which stabilized at $\Delta f_c = 0.15$ for (a - c), and $\Delta f_c = 0.25$ for (d - f), respectively: the thick blue lines indicate the triaxial compression of the initial specimen, the dashed thin lines indicate the erosion process, the solid lines indicate the following triaxial compression of the eroded samples

5.4.3. Influence of the soil's initial density on the hydro-mechanical response

Numerical tests were performed on dense samples of HK-CDG mixture, with $e_0 = 0.35$ and $f_{c0} = 0.35$, in order to evaluate the influence of the initial density of the soil on the mechanical response during internal erosion. By comparing Figure 5.13 with Figure 5.10, it can be concluded that, at a given stress ratio, a denser sample is more resistant and less inclined to deform when fine particles are progressively eroded. A larger Δf_c value is, therefore, necessary to trigger the development of large macroscopic deformations. For high stress ratios ($\eta \geq 1.5$), the specimens dilated with the loss of fines. Let us consider the specimen with $\eta = 1.6$ as an example. The volumetric and axial strains of the specimen increased slowly to 0.2% and 1.4%, respectively, until $\Delta f_c = 12.5\%$. Afterwards, the volume of the specimen increased rapidly, indicating that the mechanical state of the soil changed from stable to unstable, leading to the transition of the development of the axial strain from a slow to a large increase. At $\Delta f_c = 18.9\%$, a sudden decrease of the volume indicated the failure of the specimen, resulting in a high increase of the axial strain from

$\varepsilon_a = 5.9\%$ to an unlimited value. The final failure of the specimen was linked to the collapse of the initial microstructure, leading to the rapid decrease of the specimen volume.
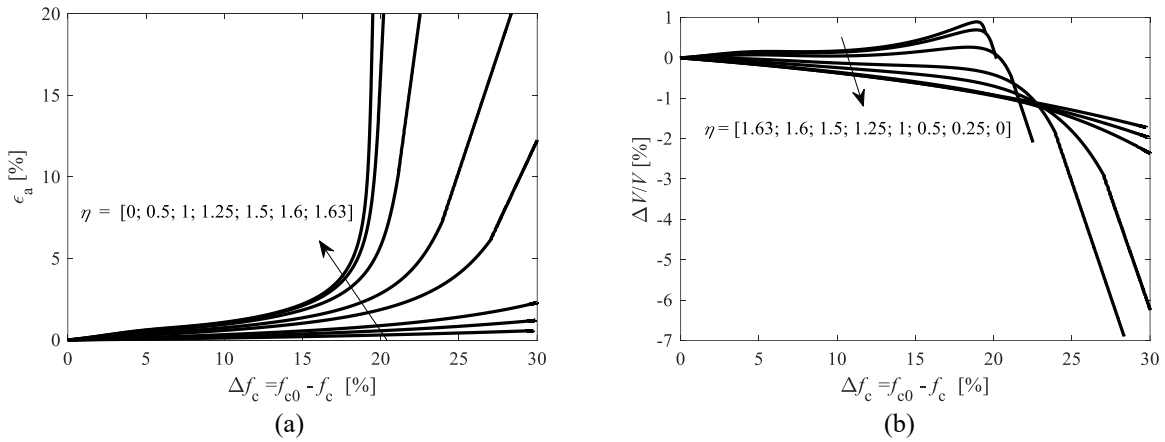
Figure 5.13 Specimen deformations in the simulations of erosion for different stress ratio $\eta = q/p'$ on dense HK-CDG mixture with $e_0 = 0.35$: (a) axial strains and (b) volumetric strains as a function of eroded fraction of fine particles.

Figure 5.14 presents the simulations of erosion for different stress ratios $\eta = q/p'$ and the following triaxial compression of the samples which stabilized at $\Delta f_c = 0.15$ for (a-c) and $\Delta f_c = 0.25$ for (d-f), respectively. Compared to Figure 5.12, the results confirmed that, for initially denser specimens, the initial microstructure supported more loss of fine particles with limited macroscopic deformation.

(b)   (e)

(c)   (f)
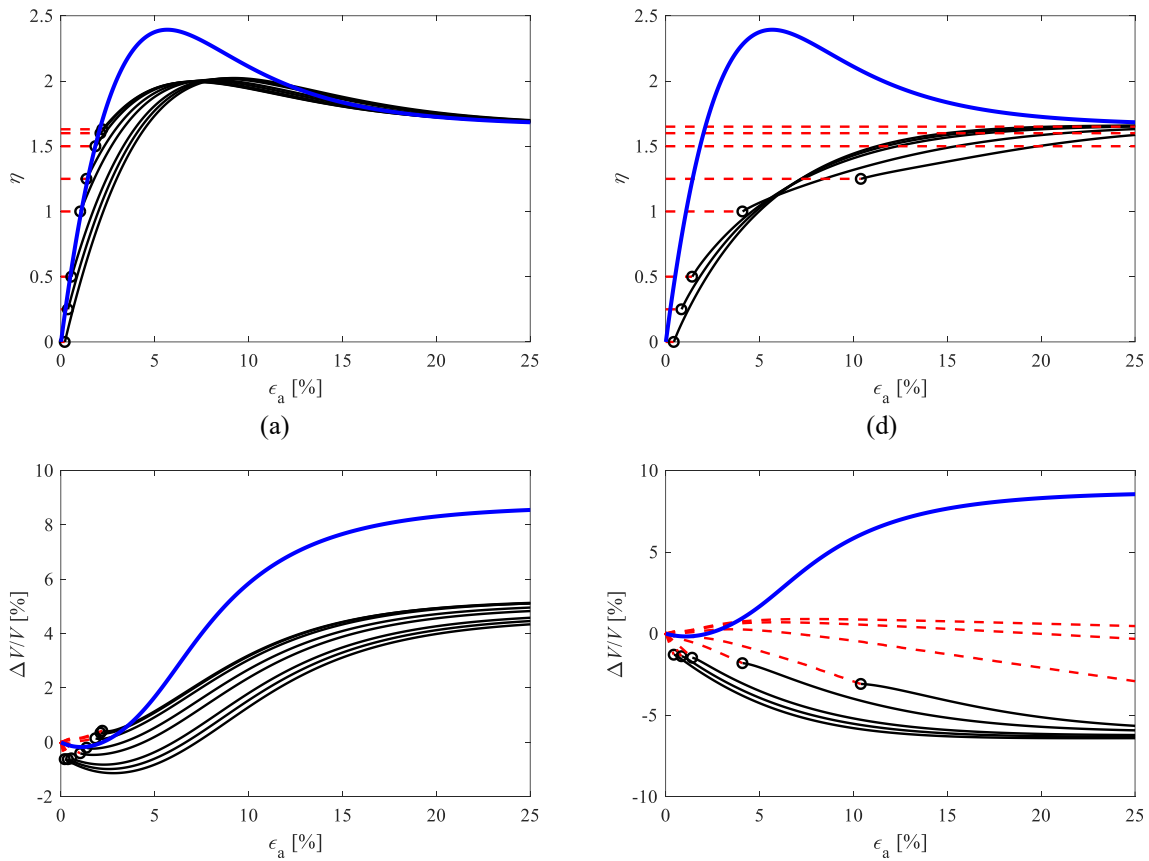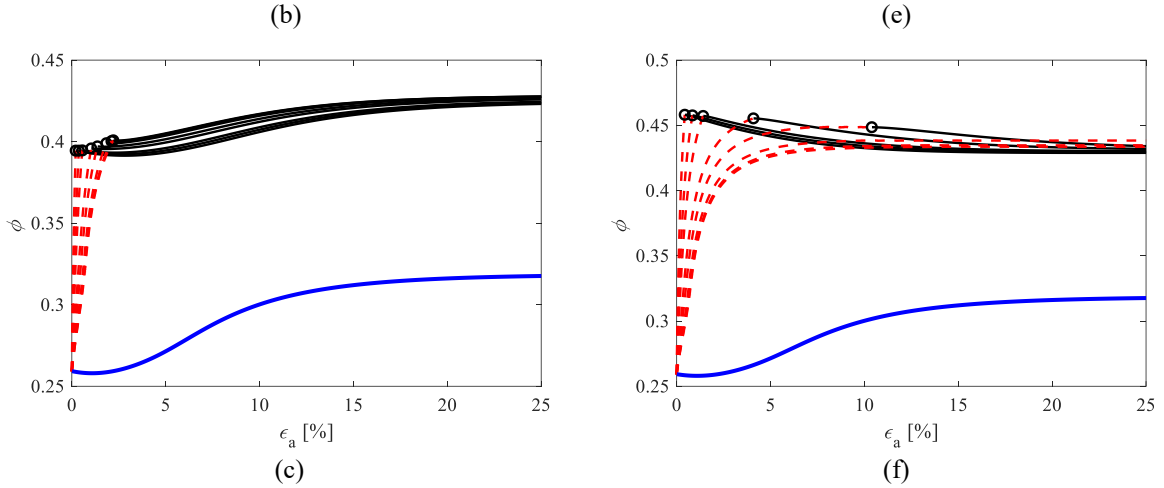
Figure 5.14 Simulations of erosion on initially dense HK-CDG mixture with $e_0 = 0.35$ for different stress ratio $\eta = q/p'$ and the following triaxial compression which stabilized at $\Delta f_c = 0.15$ for (a-c), and $\Delta f_c = 0.25$ for (d-f) respectively: thick blue lines indicate the triaxial compression of the initial specimen, dashed thin lines indicate the erosion process, solid lines indicate the triaxial compression of the eroded samples

5.4.4. Influence of the initial fines content on the hydro-mechanical response

Natural soils can contain different proportions of fine particles. The influence of the initial fines content on the mechanical behavior during erosion was evaluated by a series of numerical tests on HK-CDG mixture with $e_0 = 0.45$, $f_{c0} = 0.2$. Figure 5.15 presents the specimen deformations in the simulations of erosion for different stress ratios $\eta = q/p'$ on HK-CDG mixture with $f_{c0} = 0.2$. By comparing Figure 5.10 and Figure 5.15, it can be concluded that, for a low initial fines content, more loss of fine particles is necessary to trigger large deformations. Let us consider the specimen with $\eta = 1.65$ as an example. In the cases $f_{c0} = 0.35$ and 0.2, respectively, the critical Δf_c necessary to trigger the failure are 1.5% and 15.5% respectively. This can be understood from the phenomenological constitutive relation $f_c - e_{cr0}$. The reference critical void ratio e_{cr0} corresponding to the initial fines content f_{c0} is shown in Figure 5.4(b). It can be seen that the value of e_{cr0} at $f_{c0} = 0.2$ is larger than that at $f_{c0} = 0.35$, leading to a higher initial position of the critical state line in the $e - p'$ plane. Therefore, the specimen with $f_{c0} = 0.2$ is in a denser state than the specimen with $f_{c0} = 0.35$, evaluated by the value of e_0/e_c. This specimen remains stable until a large number of fine particles are eroded. Nevertheless, the specimen under a large stress ratio exhibited a dilatant behavior during the erosion process.
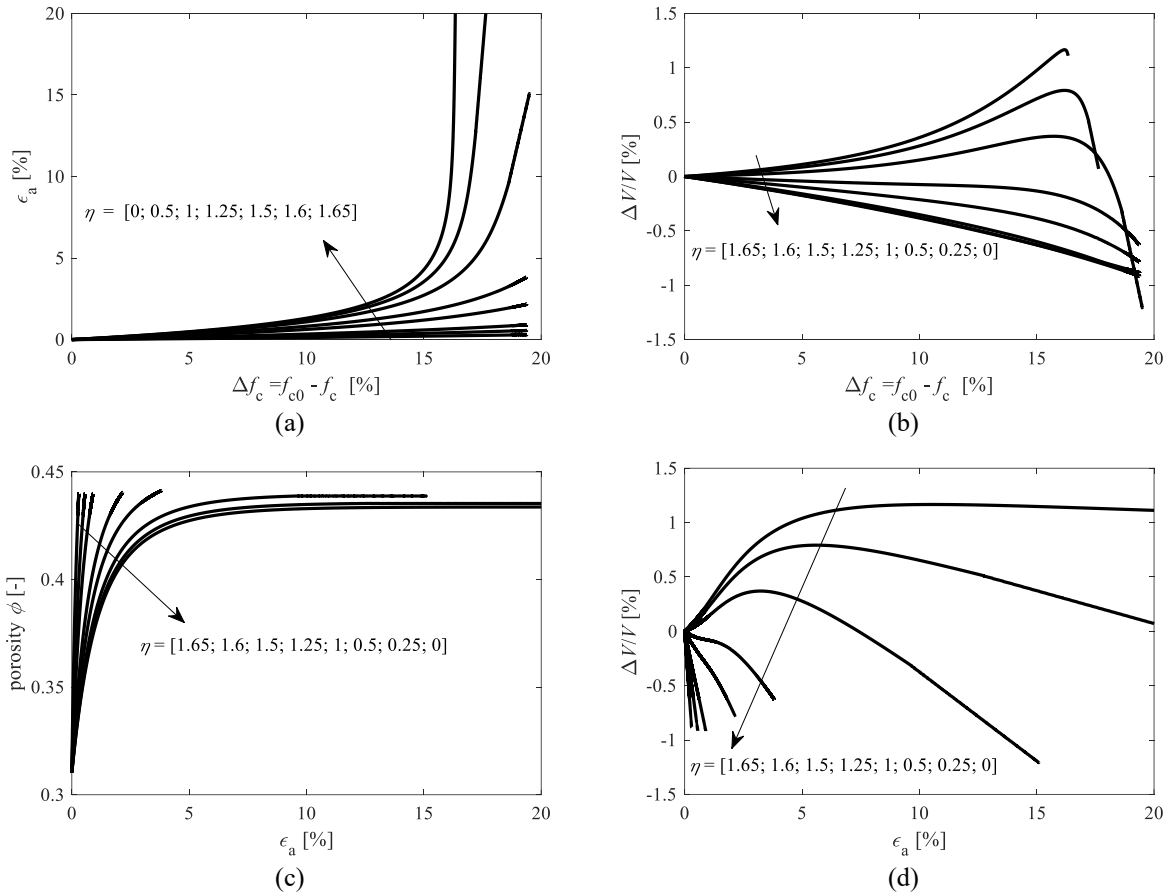
Figure 5.15 Specimen deformations in the simulations of erosion for different stress ratios $\eta = q/p'$ on sand mixture with $f_{c0} = 0.2$: (a,b) axial and volumetric strains as a function of the eroded fraction of fine particles; (c,d) porosity and volumetric strain as a function of axial strain.

5.5. Conclusion

This chapter provides a novel contribution to the numerical approach of quantifying the impact of internal erosion on the mechanical behavior of granular soils. The detachment and transport of fine particles induced by internal erosion has been modeled by a mass exchange between the solid and the fluid phases. The governing equations were formulated based on the mass balance of four assumed constituents: the stable fabric of the solid skeleton, the erodible fines, the fluidized particles, and the fluid. A non-linear incremental model was adopted in order to obtain a non-linear stress-strain relationship for the soil mixture. The model was enhanced by the introduction of the critical state concept and by formulating the influence of the fines content on the critical state line in the *e-p'* plane based on experimental results in order to take into account the impact of the amount of eroded fines on soil deformability and strength.

An erosion and mechanics coupled model has been formulated which is able to evaluate the eroded mass as well as the deformation of a soil specimen during internal erosion. This model was validated by simulating the behavior of HK-CDG mixtures before, during, and after erosion during triaxial tests. After a significant amount of fine particle loss, the stress-strain behavior of the soil changed from dilative to contractive with the shear resistance decreasing. The comparison between

91

experimental results and simulations demonstrated that the model can reproduce with a reasonable success the initiation of internal erosion, the sudden increases in erosion rate, the change in hydraulic conductivity and the deformations of the specimen. The results confirmed that the deformation was linked to the stress ratio under which the erosion process was active. Note that it is in our interest to understand better the development of internal erosion. The experimental analysis on erosion induced deformations under controlled stress states is still in its infancy, not to mention the systematic analysis of the influence of the soil's initial states (initial relative density and fines content) under different stress states. Therefore, the influence of the stress state and the soil's initial states (relative density and fines content) were investigated from a numerical standpoint. Interestingly, besides the stress ratio, the amount of loss of fines indicating the yielding from a stable to an unstable mechanical response appeared to be related to the initial density as well as to the initial fines content of the soil mixture. These results should provide some inspiration for the design of future experiments in order to better understand the physics of internal erosion and its impact on the soil behavior.

Chapter 6   Development of a hydro-mechanical finite element approach via ABAQUS-UEL and application to the analysis of internal erosion in dike-on-foundation

6.1. Introduction

In the previous chapter, the four-constituent model of internal erosion was enhanced by implementing a non-linear incremental model to consider the effects of the evolution of the fines content of the soil mixture on its mechanical behavior. A practical simulation platform was then formulated at the scale of the representative elementary volume to simulate the downward erosion tests under triaxial mechanical loading with special emphasis on the evolution of the eroded mass, the hydraulic conductivity and the deformation of the specimen during and after erosion, under triaxial condition. In this chapter, a more general elasto-plastic sand-silt mixture model has been introduced into the four-constituent model of internal erosion in order to perform analyses at the space scale of an entire engineering structure. The hydro-mechanical model was implemented into the commercial finite element code ABAQUS via UEL (User defined ELement) to assess how internal erosion can impact the stability of earthen structures. After having simulated some numerical cases issued from the literature, the developed program was applied to model the internal erosion within a dike under plane-strain condition. The effects of the cavity location, the erosion rate, and the fines content are discussed.

6.2. Formulating a time dependent physical problem

6.2.1. Mass balance and particle transport

The mass balance equations are given by the following expressions according to chapter 3:

$$-\frac{\partial \phi}{\partial t} + \mathrm{div}(v_s) - \mathrm{div}(\phi v_s) = \hat{n} \quad \text{...(6.1)}$$

$$\frac{\partial(f_c)}{\partial t} - \frac{\partial(f_c\phi)}{\partial t} + \mathrm{div}(f_c v_s) - \mathrm{div}(f_c \phi v_s) = \hat{n} \quad \text{...................................(6.2)}$$

$$\frac{\partial(c\phi)}{\partial t} + \mathrm{div}(cq_w) + \frac{\partial(c\phi v_s)}{\partial t} = -\hat{n} \quad \text{..(6.3)}$$

$$\mathrm{div}(q_w) + \mathrm{div}(v_s) = 0 \quad \text{..(6.4)}$$

where $\phi(x,t)$, $f_c(x,t)$ and $c(x,t)$ are the porosity, the amount of erodible fines and the concentration of the fluidized particles, respectively; $\hat{n}$ is the source term describing the exchange between the erodible fines and the fluidized particles; $\mathbf{v}_s$ is the velocity of the soil skeleton; $\mathbf{q}_w(x,t)$ is the total discharge of the pore fluid assumed to be governed by Darcy's law:

$$v_s = \frac{\partial u(x,t)}{\partial t} \quad \text{...(6.5)}$$

$$\mathbf{q}_w = -\frac{k(f_c,\phi)}{\eta_k \bar{\rho}(c)} \mathbf{grad}(p_w) \quad \text{...(6.6)}$$

with $u(x.t)$ indicating the displacement field of the soil skeleton. The strain ε_{ij} and volumetric strain ε_v, assuming small strains, are then given by the following expressions:

$$\varepsilon_{ij} = -\frac{1}{2}\left(u_{i,j} + u_{j,i}\right)$$ ....(6.7)

$$\frac{\partial(\varepsilon_v)}{\partial t} = -\mathrm{div}(v_s)$$ ....(6.8)

The intrinsic permeability of the medium $k(f_c,\phi)$ is considered to be dependent on the porosity $\phi(x,t)$ via the Kozeny-Carman relationship [130]:

$$k = k_0 \frac{\phi^{k_1}}{(1-\phi)^{k_2}}$$ ....(6.9)

and the density of the mixture $\bar{\rho}(c)$ is defined as:

$$\bar{\rho} = c\rho_s + (1-c)\rho_f$$ ....(6.10)

where η_k is the kinematic viscosity of the fluid; p_w is the pore fluid pressure; ρ_s and ρ_f are the density of the solid and the fluid respectively; k_1 and k_2 are permeability parameters.

Note that the amount of erodible fines $f_c(x,t)$ can be obtained explicitly from the current porosity $\phi(x,t)$ and the volumetric deformation ε_v, which indicates that Eq. (3.10) can be replaced by :

$$f_c = 1 - \frac{(1+\varepsilon_v)(1-\phi_0)(1-f_{c0})}{1-\phi}$$ ....(6.11)

where $\phi_0(x)$ and $f_{c0}(x)$ denote the initial value of $\phi(x,t)$ and $f_c(x,t)$, respectively.

6.2.2. Erosion law

Eqs. (3.9)-(3.17) do not suffice for solving a boundary value problem, as the mass exchange term needs also to be formulated. A model for the rate of the eroded mass, suggesting that erosion is mainly driven by the discharge of the fluidized particles $c|q_w|$, is given by the following relation [39]

$$\hat{n} = \beta c |q_w|$$ ....(6.12)

where β is a material parameter determined experimentally.

It should be noted, however, that with the presented mass exchange model, the erosion process will not stop until all the fine particles are washed away. Over the years, the expression for the mass exchange coefficient of internal erosion problems has evolved [36, 95, 109] to be able to consider the residual proportion of fines content under a given hydraulic gradient, which in turn limits the increasing of the porosity. The present paper does not focus upon the comparison of different mass exchange coefficients, since the numerical approach suggested here is modular; it is possible to choose the most appropriate governing equation of the mass exchange coefficient for different numerical analyses. Therefore, in the following analysis, a residual fines content is artificially given

for the sake of simplicity. Furthermore, by the mechanical model, the void ratio is strictly limited since the critical state concept is used, which will be explained in the following sections.

6.2.3. Balance of linear momentum

The mechanical behavior of the porous solid is controlled by the following equations:

$$\sigma_{ij,i} = w_i \quad \dots\dots\dots\dots\dots\dots\dots\dots\dots\dots\dots\dots\dots\dots\dots\dots\dots\dots\dots\dots\dots\dots\dots\dots\dots\dots\dots\dots\dots\dots(6.13)$$

$$d\sigma_{ij} = d\sigma'_{ij} + Bdp_w\delta_{ij} = D^{ep}_{ijkl}d\varepsilon_{ij} + Bdp_w\delta_{ij} \quad \dots\dots\dots\dots\dots\dots\dots\dots\dots\dots\dots\dots\dots\dots\dots\dots\dots\dots(6.14)$$

where σ_{ij} denotes the component of the total stress tensor, σ'_{ij} denotes the component of the effective stress tensor, p_w the pore pressure, D^{ep}_{ijkl} the component of the elastoplastic stiffness matrix, B the Biot effective stress coefficient ($B=1$ in our study), δ_{ij} the Kronecker Delta, w_i the body force per unit volume.

Eq. (6.14) can also be obtained from the linear balance of momentum of the mixture, as presented in chapter 5.2.2, neglecting the inertial forces [128]. Since the model has been developed for geotechnical applications and it is not the aim of the present paper to present the thermodynamical setting of the erosion model, in this configuration further density driven momentum production (see Steeb et al [128].) is not taken into account.

6.3. Development of Abaqus/UEL for hydro-mechanical modeling

6.3.1. User-defined element (UEL) in Abaqus

Abaqus [160] provides a user subroutine option (UEL) that allows users to implement non-linear finite elements with user's defined degrees of freedom (DOFs). The interface makes it possible to define any (proprietary) element of arbitrary complexity along with the powerful pre- and post-processing and highly efficient matrix solvers. In general, Abaqus/UEL solves the overall system of non-linear equations by Newton's method:

$$\mathbf{AMATRX}\cdot\mathbf{d}_N = \mathbf{RHS} \quad \dots\dots\dots\dots\dots\dots\dots\dots\dots\dots\dots\dots\dots\dots\dots\dots\dots\dots\dots\dots\dots\dots\dots\dots\dots\dots\dots\dots\dots(6.15)$$

where $\mathbf{AMATRX}$ and $\mathbf{RHS}$ are the Jacobian (stiffness) matrix and the residual nodal fluxes or forces needed to be defined in the subroutine; $\mathbf{d}_N$ is the nodal vector of the DOFs.

In procedures involving the time integration of the rates of change of the nodal degrees of freedom, the backward difference method is used:

$$\dot{u}_{t+\Delta t} = \frac{1}{\Delta t}\left(u_{t+\Delta t} - u_t\right) \quad \dots\dots\dots\dots\dots\dots\dots\dots\dots\dots\dots\dots\dots\dots\dots\dots\dots\dots\dots\dots\dots\dots\dots\dots\dots\dots(6.16)$$

where t and Δt indicate the current time and the incremental time; u is a nodal degree of freedom, such as the nodal displacement.

6.3.2. Implementation of the user-element

The following governing equations were obtained by combining the balance and constitutive equations in order to formulate the Initial Boundary Value Problem (IBVP) of internal erosion:

95

$$\sigma'_{ij,j} + \left(p_w \right)_{,j} - w_j = 0 \quad \dotfill (6.17)$$

$$\operatorname{div}\left(v_s \right) + \operatorname{div}\left(q_w \right) = 0 \quad \dotfill (6.18)$$

$$-\frac{\partial(\phi)}{\partial t} + \operatorname{div}\left(v_s \right) - \operatorname{div}\left(\phi v_s \right) + \beta c \left| q_w \right| = 0 \quad \dotfill (6.19)$$

$$\frac{\partial(c\phi)}{\partial t} + \operatorname{div}\left(c q_w \right) + \operatorname{div}\left(c\phi v_s \right) - \beta c \left| q_w \right| = 0 \quad \dotfill (6.20)$$

$$q_w + \frac{k(\phi)}{\eta_k \bar{\rho}(c)} \operatorname{grad}\left(p_w \right) = 0 \quad \dotfill (6.21)$$

where the primary unknowns are the soil skeleton displacement ($u(x,t)$), the pore pressure ($p_w(x,t)$), the porosity ($\phi(x,t)$), the concentration of fluidized particle ($c(x,t)$) and the flow rate $q_w(x,t)$. Other unknowns, such as the kinematic velocity of the soil skeleton $v_s(x,t)$, the erodible fines $f_c(x,t)$, the density of the mixture $\bar{\rho}(x,t)$ and the intrinsic permeability $k(x,t)$ can be determined explicitly by Eqs. (5.5) to (3.17). For the sake of simplicity, the time t and the space x variables have been omitted in the equations.

This coupled mechanical-erosion process is a non-linear transient problem. Weak forms of the governing partial differential equations have been implemented into the finite element code Abaqus [160]. A new isoparametric 8-node quadrilateral plane strain element has been developed for this purpose. The soil skeleton displacement (u) discretization is based on a quadratic Serendip element with an 8 nodes element, whereas the other 4 variables (p_w, ϕ, c, q_w) are discretized with a linear interpolation (4 nodes located at the corners) to fulfil the Inf-Sup or LBB condition [161-163].

The variables have been discretized in space and expressed in terms of their nodal values as follows

$$u = \mathbf{N}_2 \mathbf{u}, \ p_w = \mathbf{N}_1 \mathbf{p}_w, \ \phi = \mathbf{N}_1 \boldsymbol{\phi}, \ c = \mathbf{N}_1 \mathbf{c}, \ q_w = \mathbf{N}_1 \mathbf{q}_w \quad \dotfill (6.22)$$

where $\mathbf{N}_1$ and $\mathbf{N}_2$ are the shape functions over the element, of order 1 and of order 2, respectively.

The Galerkin-weighted residuals of the governing equations have been formed by their multiplication by each shape function and, then, by their integration over the element, which gives

$$R_1 = \int_V \mathbf{B}_2^t \boldsymbol{\sigma} dV - \int_V \mathbf{N}_2^t w dV - \oint_S \mathbf{N}_2^t \tau dS \quad \dotfill (6.23)$$

$$R_2 = -\frac{k}{\eta_k \bar{\rho}} \int_V \left[-\mathbf{B}_1^t \mathbf{B}_1 \mathbf{p}_w + \frac{k_1 + \left(k_2 - k_1 \right) \phi}{\phi(1-\phi)} \mathbf{N}_1^t \mathbf{p}_w^t \mathbf{B}_1^t \mathbf{B}_1 \boldsymbol{\phi} - \frac{\rho_s - \rho_f}{\bar{\rho}} \mathbf{N}_1^t \mathbf{p}_w^t \mathbf{B}_1^t \mathbf{B}_1 \mathbf{c} \right] dV$$
$$+ \int_V \mathbf{N}_1^t \mathbf{m}^t \mathbf{B}_2 \frac{\Delta u}{\Delta t} dV + \oint_S \mathbf{N}_1^t v_n dS \quad \dotfill (6.24)$$

$$R_3 = \int_V \left[\mathbf{N}_1^t \left(\frac{\Delta \phi}{\Delta t} - \beta \left| q_w \right| c \right) + (\phi - 1) \mathbf{N}_1^t \mathbf{m}^t \mathbf{B}_2 \frac{\Delta u}{\Delta t} + \mathbf{N}_1^t \operatorname{grad}(\phi) \mathbf{N}_2 \frac{\Delta u}{\Delta t} \right] dV \quad \dotfill (6.25)$$

$$R_4 = \int_V \left[\mathbf{N}_1^t \left(\frac{\Delta(c\phi)}{\Delta t} - \beta \left| \mathbf{q}_w \right| c \right) + \mathbf{N}_1^t \operatorname{grad}(c) \mathbf{q}_w + (c\phi - c) \mathbf{N}_1^t \mathbf{m}^t \mathbf{B}_2 \frac{\Delta u}{\Delta t} \right] dV$$
$$+ \int_V \left[\mathbf{N}_1^t \operatorname{grad}(\phi) \mathbf{N}_2 c \frac{\Delta u}{\Delta t} + \mathbf{N}_1^t \operatorname{grad}(c) \mathbf{N}_2 \phi \frac{\Delta u}{\Delta t} \right] dV \quad \dotfill (6.26)$$

$$R_5 = \int_V \left[\mathbf{N}_1^t \mathbf{q}_w \frac{\eta_k \overline{\rho}}{k} + \mathbf{N}_1^t \mathbf{B}_1 \mathbf{p}_w \right] dV \quad \dots\dots\dots\dots\dots\dots\dots\dots\dots\dots\dots(6.27)$$

where the superscript "t" means the matrix transpose; $\mathbf{B}_1$ and $\mathbf{B}_2$ are the spatial derivatives of the shape functions $\mathbf{N}_1$ and $\mathbf{N}_2$, respectively.

The non-linear system to be solved by using the Newton method can be written in a compact form

$$R(u, p_w, \phi, c, q_w) = 0 \quad \dots\dots\dots\dots\dots\dots\dots\dots\dots\dots\dots\dots\dots\dots\dots\dots\dots(6.28)$$

The linearized form of the weak forms, which need to be defined in the Abaqus/UEL subroutine (Eq. (6.15)), are then derived as:

$$
\begin{vmatrix}
\dfrac{\partial R_1}{\partial u} & \dfrac{\partial R_1}{\partial p_w} & 0 & 0 & 0 \\[2mm]
\dfrac{\partial R_2}{\partial u} & \dfrac{\partial R_2}{\partial p_w} & \dfrac{\partial R_2}{\partial \phi} & \dfrac{\partial R_2}{\partial c} & 0 \\[2mm]
\dfrac{\partial R_3}{\partial u} & 0 & \dfrac{\partial R_3}{\partial \phi} & \dfrac{\partial R_3}{\partial c} & \dfrac{\partial R_3}{\partial q_w} \\[2mm]
\dfrac{\partial R_4}{\partial u} & 0 & \dfrac{\partial R_4}{\partial \phi} & \dfrac{\partial R_4}{\partial c} & \dfrac{\partial R_4}{\partial q_w} \\[2mm]
0 & \dfrac{\partial R_5}{\partial p_w} & \dfrac{\partial R_5}{\partial \phi} & \dfrac{\partial R_5}{\partial c} & \dfrac{\partial R_5}{\partial q_w}
\end{vmatrix}_{(m)}
\begin{vmatrix}
\delta u \\ \delta p_w \\ \delta \phi \\ \delta c \\ \delta q_w
\end{vmatrix}_{(m+1)}
= -
\begin{vmatrix}
R_1 \\ R_2 \\ R_3 \\ R_4 \\ R_5
\end{vmatrix}_{(m)}
\quad \dots\dots\dots\dots(6.29)
$$

The integer m is the iteration counter. The partial derivatives of the Galerkin-weighted residuals which form the elements of the Jacobian matrix are given as follow.

$$\frac{\partial R_1}{\partial u} = \int_V \mathbf{B}_2^t \mathbf{D} \mathbf{B}_2 dV \quad \dots\dots\dots\dots\dots\dots\dots\dots\dots\dots\dots\dots\dots\dots\dots\dots\dots(6.30)$$

$$\frac{\partial R_1}{\partial p_w} = -\int_V \mathbf{B}_2^t \mathbf{m} \mathbf{N}_1 dV \quad \dots\dots\dots\dots\dots\dots\dots\dots\dots\dots\dots\dots\dots\dots\dots\dots(6.31)$$

$$\frac{\partial R_2}{\partial u} = \frac{1}{\Delta t} \int_V \mathbf{N}_1^t \mathbf{m}^t \mathbf{B}_1 dV \quad \dots\dots\dots\dots\dots\dots\dots\dots\dots\dots\dots\dots\dots\dots\dots(6.32)$$

$$\frac{\partial R_2}{\partial p_w} = -\frac{k}{\eta_k \overline{\rho}} \int_V \left[-\mathbf{B}_1^t \mathbf{B}_1 + \frac{k_1 + (k_2 - k_1)\phi}{\phi(1-\phi)} \mathbf{N}_1^t \phi^t \mathbf{B}_1^t \mathbf{B}_1 - \frac{\rho_s - \rho_f}{\overline{\rho}} \mathbf{N}_1^t \mathbf{c}^t \mathbf{B}_1^t \mathbf{B}_1 \right] dV \quad \dots\dots\dots\dots(6.33)$$

$$\frac{\partial R_2}{\partial \phi} = -\frac{k}{\eta_k \overline{\rho}} \int_V \left[\frac{k_1 + (k_2 - k_1)\phi}{\phi(1-\phi)} \mathbf{N}_1^t \mathbf{p}_w^t \mathbf{B}_1^t \mathbf{B}_1 + \frac{(k_2 - k_1)\phi^2 + 2k_1 \phi - k_1}{\phi^2 (1-\phi)^2} \mathbf{N}_1^t \mathbf{p}_w^t \mathbf{B}_1^t \mathbf{B}_1 \phi \mathbf{N}_1 \right] dV$$
$$-\frac{k}{\eta_k \overline{\rho}} \frac{k_1 + (k_2 - k_1)\phi}{\phi(1-\phi)} \int_V \left[-\mathbf{B}_1^t \mathbf{B}_1 \mathbf{p}_w + \frac{k_1 + (k_2 - k_1)\phi}{\phi(1-\phi)} \mathbf{N}_1^t \mathbf{p}_w^t \mathbf{B}_1^t \mathbf{B}_1 \phi - \frac{\rho_s - \rho_f}{\overline{\rho}} \mathbf{N}_1^t \mathbf{p}_w^t \mathbf{B}_1^t \mathbf{B}_1 \mathbf{c} \right] \mathbf{N}_1 dV$$
$$\dots\dots\dots\dots(6.34)$$

$$\frac{\partial R_2}{\partial c} = -\frac{k}{\eta_k \overline{\rho}} \int_V \left[-\frac{\rho_s - \rho_f}{\overline{\rho}} \mathbf{N}_1^t \mathbf{p}_w^t \mathbf{B}_1^t \mathbf{B}_1 + \left(\frac{\rho_s - \rho_f}{\overline{\rho}} \right)^2 \mathbf{N}_1^t \mathbf{p}_w^t \mathbf{B}_1^t \mathbf{B}_1 \mathbf{c} \mathbf{N}_1 \right] dV$$
$$+\frac{k}{\eta_k \overline{\rho}^2} (\rho_s - \rho_f) \int_V \left[-\mathbf{B}_1^t \mathbf{B}_1 \mathbf{p}_w + \frac{k_1 + (k_2 - k_1)\phi}{\phi(1-\phi)} \mathbf{N}_1^t \mathbf{p}_w^t \mathbf{B}_1^t \mathbf{B}_1 \phi - \frac{\rho_s - \rho_f}{\overline{\rho}} \mathbf{N}_1^t \mathbf{p}_w^t \mathbf{B}_1^t \mathbf{B}_1 \mathbf{c} \right] \mathbf{N}_1 dV$$
$$\dots\dots\dots\dots(6.35)$$

$$\frac{\partial R_3}{\partial u} = \int_V \left[\frac{(\phi-1)}{\Delta t} \mathbf{N}_1^t \mathbf{m}^t \mathbf{B}_2 + \frac{1}{\Delta t} \mathbf{N}_1^t \mathrm{grad}(\phi) \mathbf{N}_2 \right] dV \quad \dots\dots\dots\dots\dots\dots\dots\dots(6.36)$$

$$\frac{\partial R_3}{\partial \phi} = \int_V \left[\frac{1}{\Delta t} \mathbf{N}_1^t \mathbf{N}_1 + \mathbf{N}_1^t \mathbf{m}^t \mathbf{B}_2 \frac{\Delta u}{\Delta t} \mathbf{N}_1 + \mathbf{N}_1^t \frac{\Delta u^t}{\Delta t} \mathbf{N}_2^t \mathbf{B}_1 \right] dV \quad \dots\dots(6.37)$$

$$\frac{\partial R_3}{\partial c} = -\int_V \mathbf{N}_1^t \mathbf{N}_1 \beta |q_w| dV \quad \dots\dots(6.38)$$

$$\frac{\partial R_3}{\partial q_w} = -\int_V \mathbf{N}_1^t \beta c \frac{q_w^t}{|q_w|} \mathbf{N}_1 dV \quad \dots\dots(6.39)$$

$$\frac{\partial R_4}{\partial u} = \int_V \left[\frac{c\phi - c}{\Delta t} \mathbf{N}_1^t \mathbf{m}^t \mathbf{B}_2 + \frac{c}{\Delta t} \mathbf{N}_1^t \text{grad}(\phi) \mathbf{N}_2 + \frac{\phi}{\Delta t} \mathbf{N}_1^t \text{grad}(c) \mathbf{N}_2 \right] dV \quad \dots\dots(6.40)$$

$$\frac{\partial R_4}{\partial \phi} = \int_V \left[\frac{c}{\Delta t} \mathbf{N}_1^t \mathbf{N}_1 + \mathbf{N}_1^t \text{grad}(\phi) \mathbf{q}_w + \frac{c}{\Delta t} \mathbf{N}_1^t \mathbf{m}^t \mathbf{B}_2 \Delta u \mathbf{N}_1 \right] dV$$
$$+ \int_V \left[\frac{c}{\Delta t} \mathbf{N}_1^t \Delta u^t \mathbf{N}_2^t \mathbf{B}_1 + \mathbf{N}_1^t \text{grad}(c) \mathbf{N}_2 \frac{\Delta u}{\Delta t} \mathbf{N}_1 \right] dV \quad \dots\dots(6.41)$$

$$\frac{\partial R_4}{\partial c} = \int_V \left[\left(\frac{\phi}{\Delta t} - \beta |q_w| \right) \mathbf{N}_1^t \mathbf{N}_1 + \mathbf{N}_1^t \mathbf{q}_w^t \mathbf{B}_1 + (\phi - 1) \mathbf{N}_1^t \mathbf{m}^t \mathbf{B}_2 \frac{\Delta u}{\Delta t} \mathbf{N}_1 \right] dV$$
$$+ \int_V \left[\mathbf{N}_1^t \text{grad}(\phi) \mathbf{N}_2 \frac{\Delta u}{\Delta t} \mathbf{N}_1 + \frac{\phi}{\Delta t} \mathbf{N}_1^t \Delta u^t \mathbf{N}_2^t \mathbf{B}_1 \right] dV \quad \dots\dots(6.42)$$

$$\frac{\partial R_4}{\partial q_w} = \int_V \left[-\mathbf{N}_1^t \beta c \frac{q_w^t}{|q_w|} \mathbf{N}_1 + \mathbf{N}_1^t \text{grad}(c) \mathbf{N}_1 \right] dV \quad \dots\dots(6.43)$$

$$\frac{\partial R_5}{\partial p_w} = \int_V \mathbf{N}_1^t \mathbf{B}_1 dV \quad \dots\dots(6.44)$$

$$\frac{\partial R_5}{\partial \phi} = \int_V \left[\mathbf{N}_1^t \mathbf{q}_w \mathbf{N}_1 \frac{\eta_k \bar{\rho}}{k} \frac{(k_1 - k_2)\phi - k_1}{\phi(1-\phi)} \right] dV \quad \dots\dots(6.45)$$

$$\frac{\partial R_5}{\partial c} = \int_V \left[\mathbf{N}_1^t \mathbf{q}_w \mathbf{N}_1 \frac{\eta_k}{k} (\rho_s - \rho_f) \right] dV \quad \dots\dots(6.46)$$

$$\frac{\partial R_5}{\partial q_w} = \int_V \left[\mathbf{N}_1^t \mathbf{N}_1 \frac{\eta_k \bar{\rho}}{k} \right] dV \quad \dots\dots(6.47)$$

All the integrals are evaluated numerically using the Gaussian integration method.

6.4. Numerical verification

6.4.1. Wellbore erosion simulation

The developed numerical approach was firstly applied to simulate the wellbore erosion problem defined by Stavropoulou et al. [38]. An erosion law which considers the plugging as a higher-order effect was used:

$$\hat{n} = \beta(1-\phi)\left(c - \frac{c^2}{c_{cr}}\right)|\mathbf{q_w}| \quad \dots\dots(6.48)$$

where c_{cr} denotes the critical value of c for which the two competing phenomena, erosion and plugging, balance each other. The obtained results were then compared to the results of Stavropoulou et al. [38] in order to validate our approach.
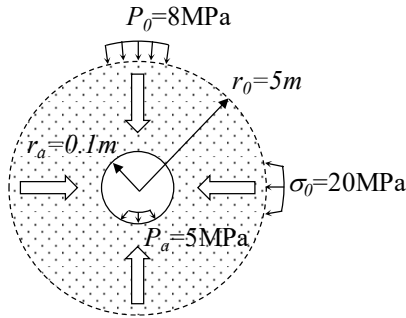
Figure 6.1 Geometric and boundary conditions for the wellbore erosion problem (Stavropoulou et al. [38])

Figure 6.1 illustrates the horizontal section of a wellbore in deep rock [38], which is assumed to be a porous permeable material. A water pressure gradient initiated a fluid flow towards the inner free surface of the wellbore. This process led to internal erosion. The mechanical behavior of the soil skeleton was assumed to be elastic. The initial porosity was $\phi_0 = 0.25$, the initial concentration of fluidized particles $c_0 = 0.001$, the erosion coefficient $\beta = 5m^{-1}$.

In this example, the material was assumed to be non-linear elastic, whereas the rock elasticity parameters depended on the porosity in such a way that the material became weaker with the increase of porosity:

$$E = \bar{E}(1-\phi)$$ ....(6.49)

where $\bar{E}$ is the Young's modulus, and the porosity ϕ is a damage parameter. More details can be found in Stavropoulou, Papanastasiou [38].

Figure 6.2 andFigure 6.3 show the spatial profiles of porosity and pore pressure at various time steps, respectively. Figure 6.4 and 6.5 show the spatial profiles of the computed effective stresses. Our 2D plane strain simulation results are in good agreement with the results of the axisymmetric analysis results carried out by Stavropoulou et al. [38]. The slight differences may be related to the time increment and the mesh size, which were not given by Stavropoulou et al. [38].
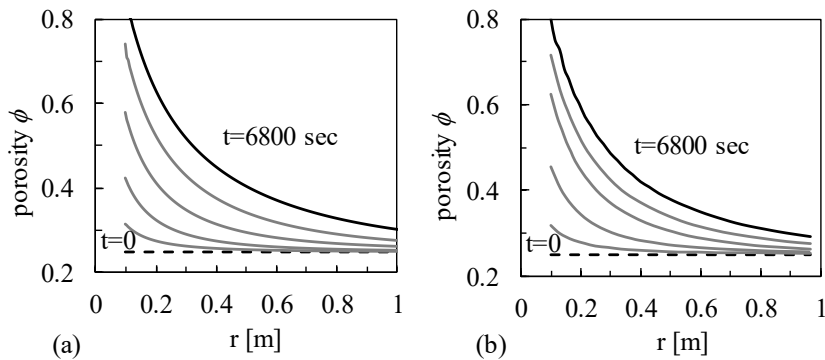
Figure 6.2 Spatial profiles of porosity at various times: (a) Results of Stavropoulou et al. 1998; (b) Results of Stavropoulou et al. [38]
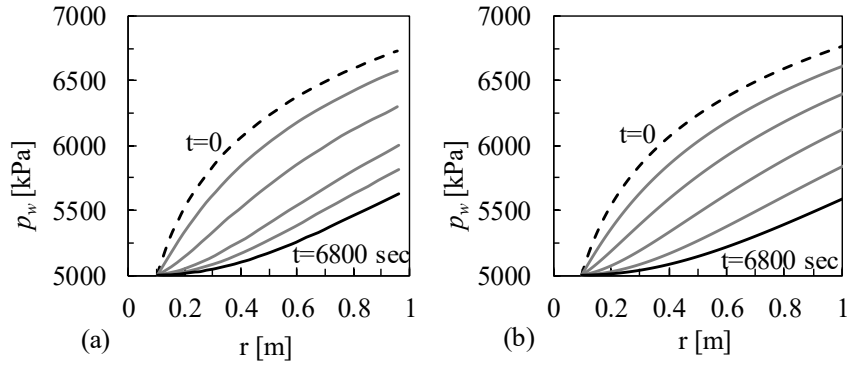
Figure 6.3 Spatial profiles of pore pressure at various times: (a) Results of Stavropoulou et al. [38]; (b) Simulation results
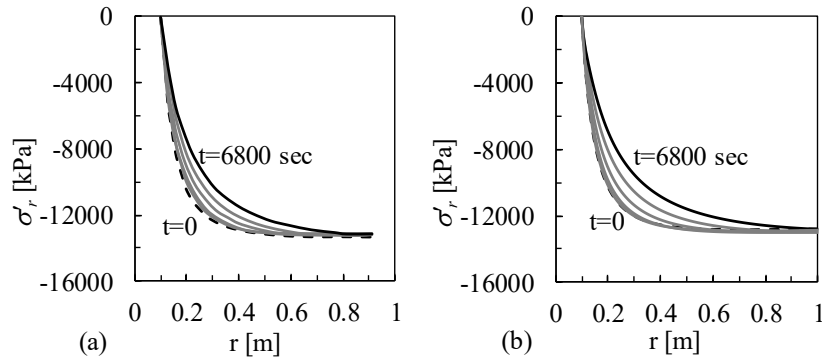
Figure 6.4 Distribution of radial effective stress at various times: (a) Results of Stavropoulou et al. [38]; (b) Simulation results
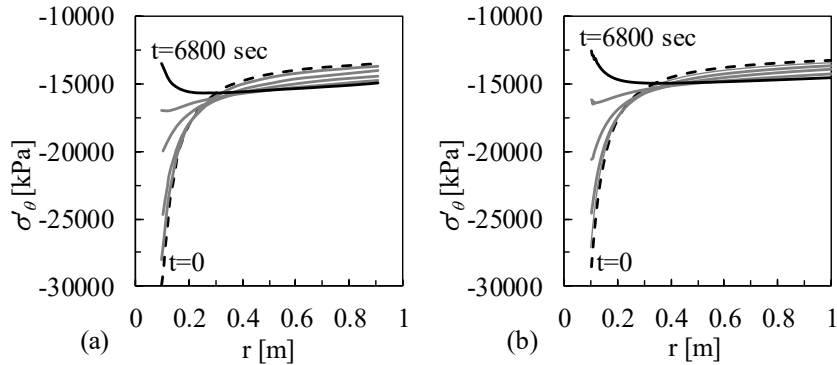
Figure 6.5 Distribution of tangential effective stress at various times: (a) Results of Stavropoulou et al. [38]; (b) Simulation results

6.4.2. 1D infiltration simulation

The developed approach is also able to model an infiltration problem with an opposite mass exchange process. Finer particles pass from the fluidized phase to the solid phase. In this section, a 1D infiltration simulation studied by Schaufler, Becker [123] was reproduced to check the validity of our approach. The constitutive equation for the mass exchange in this example is the following:

$$\hat{n} = -\beta c |\mathbf{q}_w| \quad \text{..(6.50)}$$

The investigated volume depicted in Figure 6.6 is fully saturated with the 4 previously described constituents. The boundary conditions for the water pressure p are applied at boundaries $x = 0$ and $x = L$, which initiates a fluid flow from left to right. In addition, a given constant concentration $c(x = 0) = 0.1$ was applied. Within the domain, an initial condition was used for c, setting $c_0(x) = 0.001$. For more details, the reader can refer to Schaufler, Becker [123].
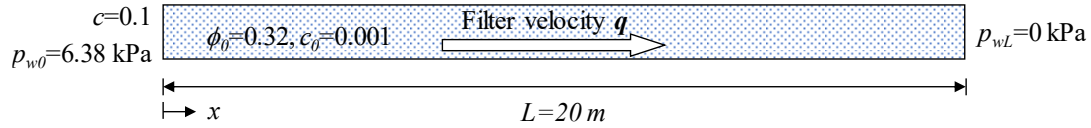
Figure 6.6 Geometric and boundary conditions for the 1D infiltration problem

Figure 6.7 compares the evolution of porosity in space and time between the simulation results and the published results by Schaufler, Becker [123]. An infiltration process takes place leading to an increase of porosity. A good agreement was obtained between the two approaches.
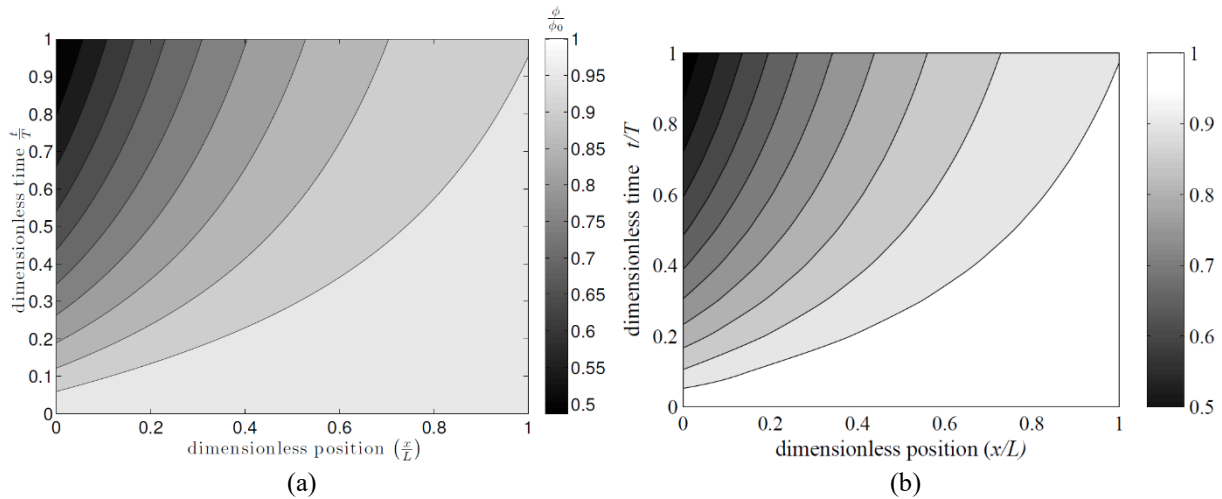
Figure 6.7 Contour plot describing the evolution of the porosity in space and time in the domain: (a) Results of Schaufler et al. [123]; (b) Simulation results

In Figure 6.8, the distribution of the concentration of particles in the suspension for different values of the erosion coefficient λ_e is illustrated. The results with the presently proposed numerical approach are identical to those obtained by Schaufler, Becker [123].
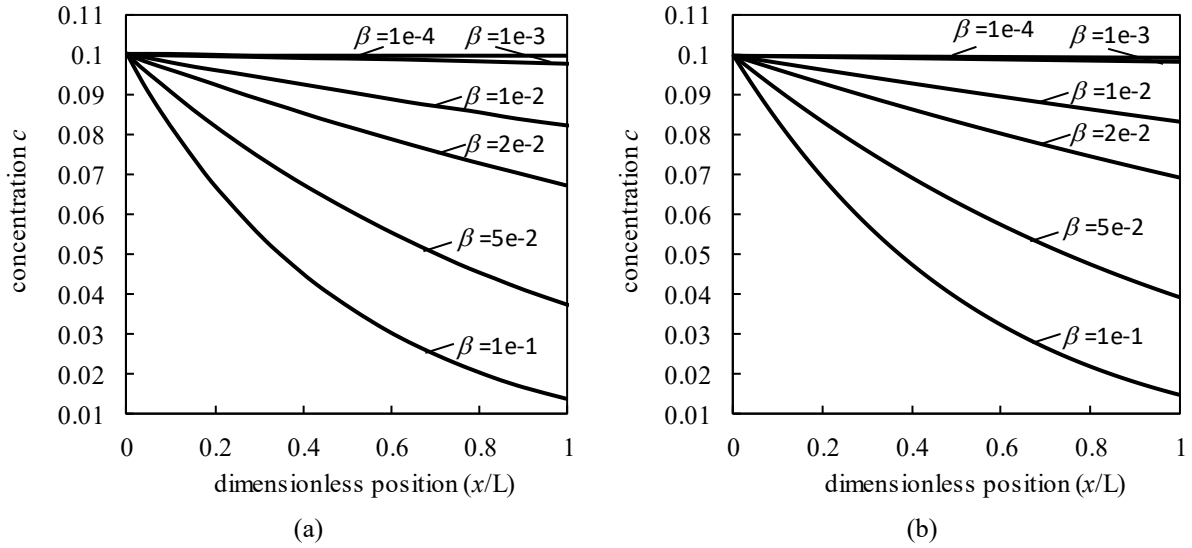
Figure 6.8 Distribution of concentration: (a) Results of Schaufler et al. 2013 [123]; (b) Simulation results

6.5. A sand-silt mixture model for the solid phase

To assessing the mechanical responses of the loss of fines content induced by the internal erosion in an earthen structure, a non-associated elastoplastic constitutive model for sand-silt mixture is adopted for the solid skeleton [52]. This model has been extended from the basic SIMSAND model [133, 164, 165] under the framework of the critical state concept and elastoplasticity theory (illustrated in Figure 6.9 and summarized in Table 6.1 and Table 6.2), by the incorporation of the position of the critical state line as a function of the fines content in order to unify the mechanical behavior of a sand-silt mixture from silt to sand or sand to silt (see (6.51) and (6.52), and illustration in Figure 6.9). Therefore, this model can take into account the influence of the change of porosity and the fines content on the mechanical behavior of the soil during the erosion process.
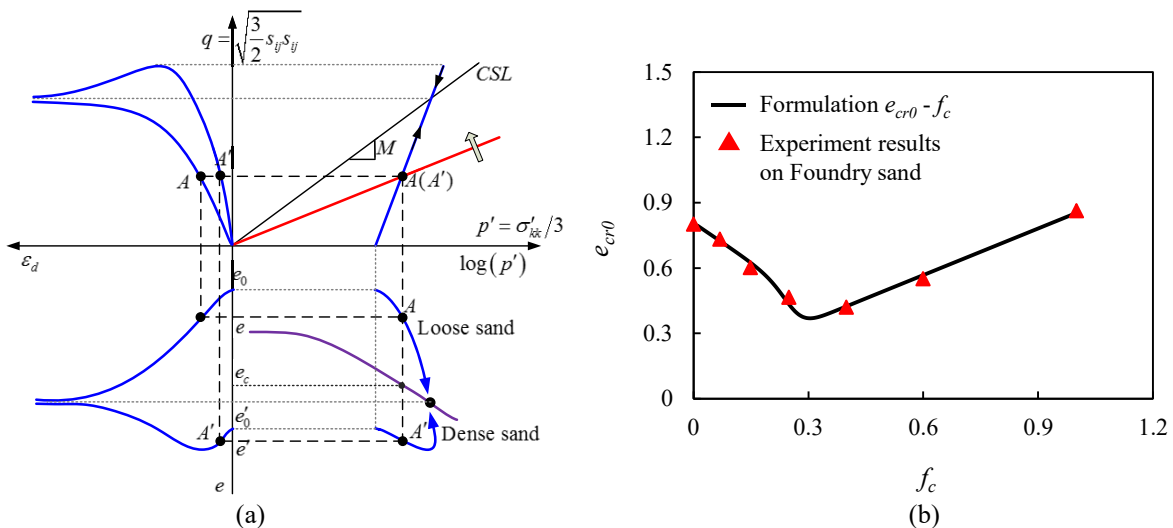
Figure 6.9 Principle of critical-state-based nonlinear hardening soil model for sand-silt mixtures: (a) SIMSAND model; (b) Reference critical void ratio versus fine content for Foundry sand–silt mixtures

Table 6.1 Basic constitutive equations of SIMSAND

Components	Constitutive equations
Elasticity	$\delta\varepsilon_{ij}^{e} = \dfrac{1}{2G}\delta\sigma_{ij}' - \dfrac{\upsilon}{2G(1+\upsilon)}\delta\sigma_{kk}'\delta_{ij}$ $G = G_0 p_{at} \dfrac{(2.97-e)^2}{(1+e)}\left(\dfrac{p'}{p_{at}}\right)^{n}$
Yield surface in shear	$f_s = \dfrac{q}{p'} - H$
Potential surface in shear	$\dfrac{\partial g_s}{\partial p'} = A_d\left(M_{pt} - \dfrac{q}{p'}\right); \quad \dfrac{\partial g_s}{\partial s_{ij}} = \{1 \ \ 1 \ \ 1 \ \ 1 \ \ 1 \ \ 1\}$
Hardening rule for shear	$H = \dfrac{M_p \varepsilon_d^p}{k_p + \varepsilon_d^p}$
Critical state line and inter-locking effect	$e_c = e_{cr0} - \lambda\left(\dfrac{p'}{p_{at}}\right)^{\xi}$ $\tan\varphi_p = \left(\dfrac{e_c}{e}\right)\tan\varphi_\mu \quad \tan\varphi_{pt} = \left(\dfrac{e}{e_c}\right)\tan\varphi_\mu$

Table 6.2 Parameters of SIMSAND

Parameters	Definitions
e_0	Initial void ratio
υ	Poisson's ratio
G_0	Referential shear modulus (dimensionless)
n	Elastic constant controlling nonlinear stiffness
φ_μ	Critical friction angle
e_{cr0}	Reference critical state void ratio
λ	Constant controlling the slope of CSL
ξ	Constant controlling the nonlinearity of CSL
A_d	Constant controlling the magnitude of the stress-dilatancy (0.5~1.5)
k_p	Plastic modulus (0.01~0.0001)

Similar to the critical state based non-linear incremental constitutive model presented in chapter 5.2.4, the same non-linear expression of the critical state line was adopted here, as follows

$$e_c = e_{cr0} - \lambda\left(\frac{p'}{p_{at}}\right)^{\xi} \quad\text{...(6.51)}$$

where e_{cr0} is the reference critical void ratio corresponding to the void ratio e at the mean effective stress $p' = 0$. It determines the position of the CSL in the $e - p'$ plane. λ and ξ are material constants controlling the non-linear expression of the CSL.

According to Yin et al. [52, 155], e_{cr0} is considered as a function of the fines content in order to unify the mechanical behavior of a sand-silt mixture for different fines contents (see Figure 6.9 (b)):

$$e_{cr0} = \left[e_{hc,cr0} \left(1 - f_c \right) + af_c \right] \frac{1 - \tanh\left[\zeta \left(f_c - f_{th} \right) \right]}{2} + e_{hf,cr0} \left(f_c + \frac{1 - f_c}{\left(R_d \right)^m} \right) \frac{1 + \tanh\left[\zeta \left(f_c - f_{th} \right) \right]}{2} \quad \dots\dots\dots\dots\dots\dots\dots(6.52)$$

where $e_{hc,cr0}$ and $e_{hf,cr0}$ are the reference critical void ratios for the pure sand and pure silt, respectively. a, ζ, R_d, m and f_{th} are material constants; more details can be found in chapter 5.2.4.

6.6. Hydro-mechanical coupling

The hydro-mechanical coupling of internal erosion is assured by the relationship between the decrease of the fines content and the change of the shear strength evaluated by the constitutive model of the sand-silt mixture. The internal friction angle (ϕ_μ) is assumed to be constant during the erosion process because the mineralogy and the shape of the coarse and small grains are assumed to be identical.

Therefore, the hydro-mechanical coupling effect has been treated as a two steps process. In the first step, the internal erosion leads to an evolution of the porosity, which in turn leads to the change of the permeability (defined by Eq.(6.9)). As a consequence, the pore pressure and the effective stresses will change. In the second step, the loss of fine particles due to the seepage flow affects (1) the void ratio and (2) the location of the critical state line, obtained by combining Eqs. (6.51) and (6.52) for a sand-silt mixture.

Figure 6.10 shows the influence of the loss of fines content on the silty sand behavior: (a) when $f_c > f_{th}$; (b) when $f_c < f_{th}$, if we take an initially dense soil mixture as an example. With the loss of fine particles, the void ratio e will increase. At the same time, Eq. (6.52) determines dynamically the location of the critical state line, *i.e.,* e_{cr0} increases with f_c when $f_c > f_{th}$, or decreases with f_c when $f_c < f_{th}$. Therefore, the mechanical response corresponding to the loss of the fines content induced by internal erosion will be discussed for two initial soil conditions as follows: (1) for a soil mixture with an initial fines content $f_c > f_{th}$, the loss of fine particles induced by internal erosion leads to an increase of the void ratio e_0 and a decrease of the reference critical void ratio e_{cr0}, which both result in the decrease of the undrained shear strength together with the increase of the contractive behavior, as shown in Figure 6.10(a), taking initially a dense soil mixture as an example. (2) For a soil mixture with an initial fines content $f_c < f_{th}$, the loss of fine particles induced by internal erosion leads to an increase of the void ratio e_0 and an increase of the reference critical void ratio e_{cr0}, which are two opposing processes in terms of their influence on the undrained shear strength. The increase of the void ratio leads to the decrease of the undrained shear strength together with the increase of the contraction, whereas the increase of the reference critical void ratio leads to the increase of the undrained shear strength together with the decrease of the contraction. In most cases the undrained shear strength will decrease with the loss of fine particles in both cases. This can be explained by the fact that the increase of the void ratio is usually larger than the increase of the reference critical void ratio. This aspect is also implied through the derivation of the equivalent void ratio in Chang and Yin [166].
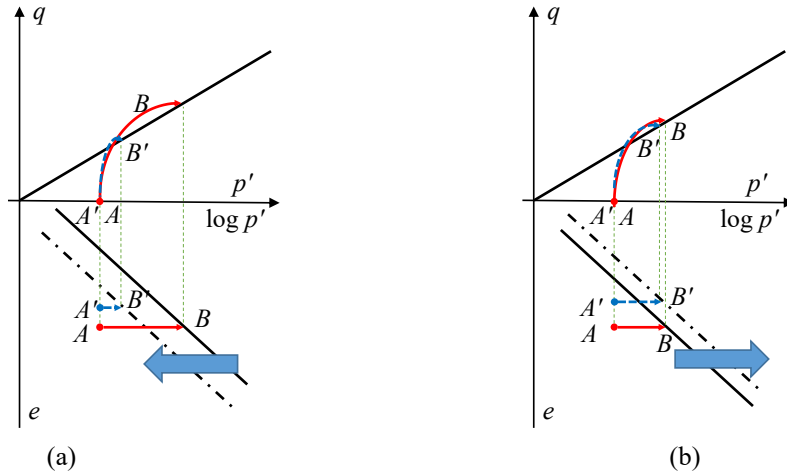
Figure 6.10 The influence of loss of fine content on silty sand: (a) when $f_c > f_{th}$; (b) when $f_c < f_{th}$

The change of void ratio, either increase or decrease, induced by the volume deformation of soil skeleton may affect the permeability and hydraulic process inversely. In this study, the irreversible coupling from mechanics to hydraulics is considered implicitly by introducing the volume deformation in the mass balance equations Eqs. (3.9)-(3.12) and (6.8). Only few data are available in the literature concerning the influence of stress state on the erosion process during an erosion test. Chang & Zhang[5] found that the average erosion rate within the testing period increased with the increase of the deviatoric stress. However not enough detail on this particular aspect was given to calibrate the stress term in the model for the rate of the eroded mass.

6.7. Numerical modeling of internal erosion within a dike

6.7.1. Description of the problem

To illustrate the capacity of the numerical model to treat real scale engineering problems, it was decided to analyze an example of the dike-on-foundation problem, where erosion took place due to high local hydraulic gradients. The characteristics of the studied configuration are presented in Figure 6.11 according to the typical cross section of the dike of Val d'Orléans [167]. The dike was built on sandy-silt alluvium formation over karstic limestones. A confined aquifer under pressure is located underneath the limestone layer. It can rise inside the karstic caves and even reach the alluvium layer. Internal erosion due to seepage flow can take place when the water level is different in the alluvium and in the confined aquifer. The computations aim to show how the internal erosion may weaken the foundation and the dike, which will eventually lead to subsidence or collapse of the dike. However, since this numerical approach is based on continuum mechanics, the passage from a continuous medium to a discontinuous medium cannot be accounted for, and the model ceases to apply when macroscopic discontinuities appear. In this simulation, it is supposed that only fine particles are transported within the water flow; the eventual formation of a piping channel cannot, therefore, be reproduced. It should be pointed out that the erosion takes place due to high local hydraulic gradients. In this example, the formation of a karstic cavity is assumed to create the high local hydraulic gradients in the vicinity of the cavity and therefore trigger the erosion. Meanwhile, other raisons can trigger the internal erosion as well. For example, the seepage due to the drop of

hydraulic head within a dam can lead the detached fine particles move from the up-stream side to the down-stream side.

The problem is analyzed under the assumption of a plane strain condition. The dimension and the finite element mesh of the physical domain are shown in Figure 6.12. The water level is located at the top of the dike, *i.e.,* 10.5 m, as the extreme configuration of a flooding condition is considered. The dike is assumed to be initially stable under gravity and the water head of the confined aquifer is assumed to be 11.0m. Presumably, a karst collapse underneath the alluvium layer leads to a cavity connecting the alluvium and the confined aquifer where erosion can occur due to the existence of local hydraulic gradients in the vicinity of the cavity. The location of the collapse of the karst rock may be uncertain, therefore, 9 cases were analyzed in which the cavity was supposed to be located at 0 m, 2.5 m, 5 m, 8 m, 11 m, 14 m, 17 m, 20 m and 23 m from the left boundary, respectively. To simplify, the influence of the size of the cavity was not considered, the cavity was assumed to be localized at a single point of the model. Considering the position of the cavity, only the right part of the typical cross section of the dike-on-foundation was simulated.
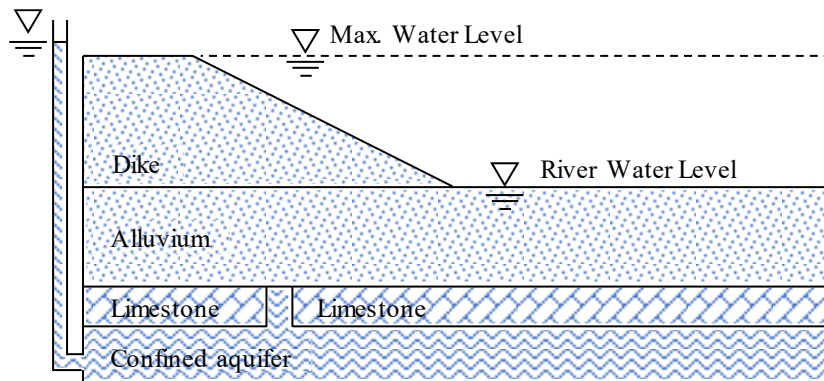

Figure 6.11 Scheme of the dike-on-foundation near Orléans (France)
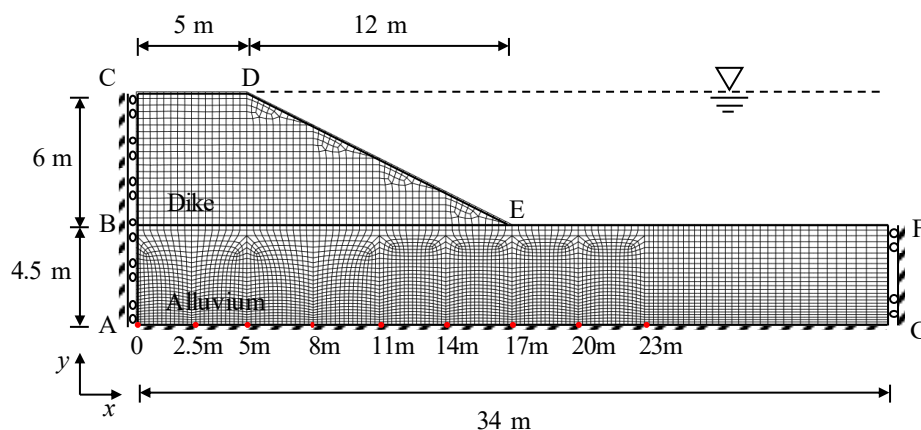

Figure 6.12 Schematic configuration of the dike and mesh of numerical model.

The boundary conditions were given as vertical rollers on the left and right boundaries AC and FG, and fully fixed at the base AG. The boundaries CD, DE and EF were fully permeable; AC, AG and

106

FG were assumed to be impervious. Gravity loads were applied to the model to generate the initial stresses and the initial water pressure. Then, the water head at the cavity was set to 11 m in order to initiate the water flow in and out the cavity. The alluvium and the dike were considered to be made of the same mixture of sand and silt. The physical properties and the material parameters, summarized in Table 6.3 and

Table 5.2, correspond to the Ottawa 50/200 sand-silt characteristics [52] with $e_0 = 0.6$, $c_0 = 0.01$ and $f_{c0} = 0.4$.

<div align="center">Table 6.3 Physical properties of soils</div>

Density of fluid	ρ_f	1.0 g/cm^3	Kinematic viscosity of fluid	η_k	5.0E-6 m^{2}s^{-1}
Density of solids	ρ_s	2.65	Intrinsic permeability	k_0	2.1E-10 m^2

<div align="center">Table 6.4 Material constants of soils</div>

Elastic parameters			Plastic parameters			CSL-related parameters				Fines parameters			Erosion parameters		
$G_0/$ MPa	ν	n	k_p	A_d	ϕ_u	$e_{hc,cr0}$	$e_{fc,cr0}$	ξ	λ	a	m	f_{th}	λ_e	k_1	k_2
150	0.2	0.5	0.0017	1	32	0.805	1.03	0.196	0.081	0	0.7	0.3	0.005	3	2

Insofar as a simple erosion law was adopted in this simulation, the end of the erosion process could take place only after all the fine particles were eroded due to the local water pressure gradient. However, one may assume that, with an increasing concentration of eroded particles in suspension, the probability for the existence of a plugging phenomenon in the pore network would also increase. In experiments under a given hydraulic gradient, a residual proportion of fines content could be observed [5, 23]. Therefore, in this analysis, a residual fines content was artificially given for the sake of simplicity. In this example, the residual fines content $f_{c,r}$ was fixed equal to 0.3.

6.7.2. Hydro-mechanical responses induced by internal erosion

Figure 6.13 shows the evolution with time of the void ratio inside the dike and the underlying soil foundation. As internal erosion takes place, the void ratio, which is initially spatially uniform throughout the whole model, begins to increase with time. The void ratio increase starts at the vicinity of the cavity where a highly eroded zone appears and develops towards the dike, following the direction of the maximum hydraulic gradient. At places where the fines content reaches the residual fines content, it is assumed that the erosion process is balanced by the filtration process and, as a consequence, the void ratio will no longer change, but the size of the eroded area will continue to develop.

Figure 6.14 and Figure 6.15 show the displacement and the deviatoric plastic strain fields within the dike at the corresponding times of Figure 6.13. The displacements were reset after the initiation of the stresses by gravity. The increase of the void ratio accompanied by a downward shift of the CSL in the *e-p'* plane induced by the decrease of the fines content makes the soil looser. Consequently, the soil resistance decreases. Two stages can be distinguished from the results. Plastic deformation

initiates in the vicinity of the cavity. The deformation of the dike develops at a slow pace at the early stage of the erosion when the eroded zone is concentrated in the foundation. At this stage, the soil moves downwards to the cavity, as the eroded zone around the cavity is weaker. The rate of the deformation keeps increasing with the development of the eroded zone, confirmed by the time variation of the displacement magnitude, as shown in Figure 6.16. 316 days after the beginning of erosion, a measurable deformation of the dike appears, accompanied by the initiation of a shear sliding surface in the eroded zone near the toe of the slope. At this stage, the plastic deformation develops drastically with time until the dike is destroyed by a sliding rupture of the slope. It should be noted that this simulation is an example under extreme conditions, where the soil cohesion has not been considered, and the dike is immersed. The decrease of the fines content, in this case, leads to the decrease of e_{cr0}, according to Eq.(6.52). Furthermore, the hydro-mechanical responses also depend on the location of the cavity, the rate of erosion, the initial and the residual fines content, to be discussed in the following section.
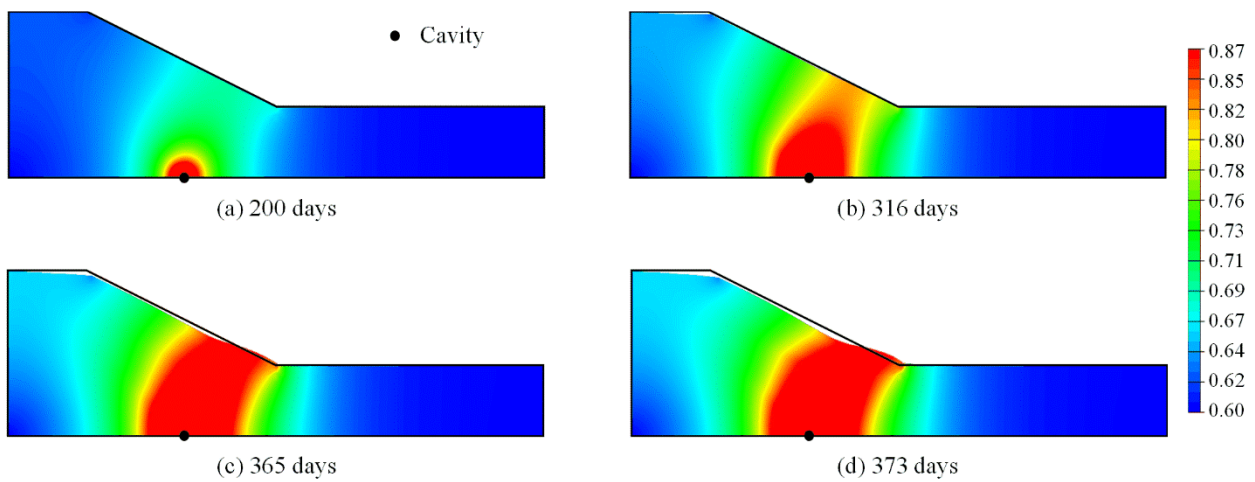
Figure 6.13 Spatial distribution of void ratio at different times, in which the cavity is located at x=11m (Deformation scale = 200)

108
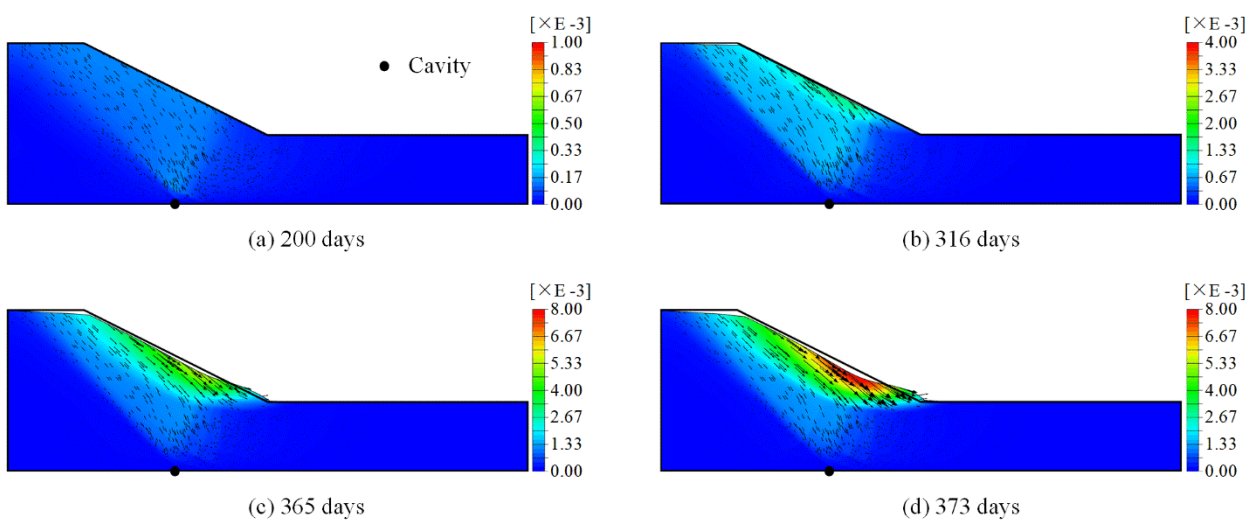
Figure 6.14 Displacement magnitude field and vector field at different times, in which the cavity is located at x=11m. (Deformation scale = 200)

(a) 200 days

(b) 316 days

(c) 365 days

(d) 373 days
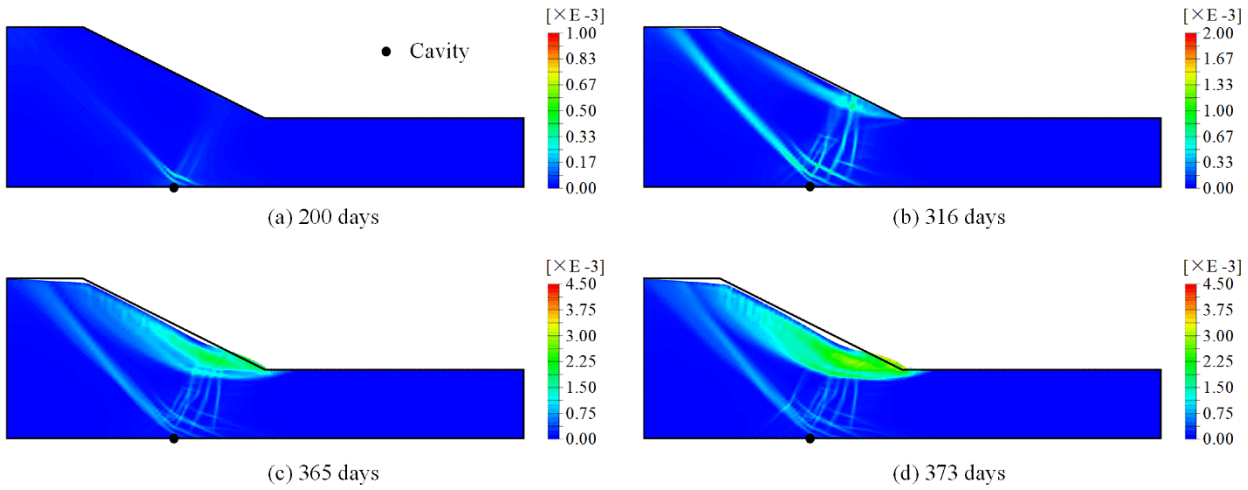
Figure 6.15 Deviatoric plastic strain field at different times, in which the cavity is located at x=11m. (Deformation scale = 200)
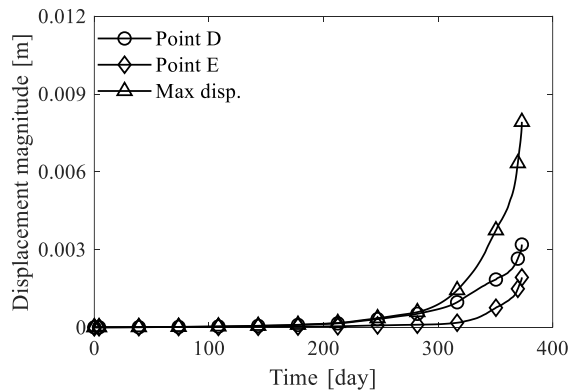
Figure 6.16 Time variation of displacement magnitude at point D, point E and maximum displacement

6.8. Discussion

6.8.1. Effect of cavity location

The effects of the cavity location on the degradation of the dike are illustrated in Figure 6.17 and Figure 6.18, showing the variation of the maximum displacement magnitude with time and the dike deformation at the end of erosion for different cavity locations. Figure 6.17 shows that the dike fails earlier and in a sudden way when the cavity is located below the surface of the slope ($x = 8$, 11 and 14 m). The failure time is delayed when the cavity is moved away from the surface of the slope and the mode of failure changes from sudden to progressive. Figure 6.18 shows different profiles of the dike at the end of erosion. A significant settlement of the dike is observed when the cavity is located below the top of the dike. As the cavity moves toward the surface of the slope, the sliding of the slope begins to appear. The simulation is terminated with a sliding rupture. As the cavity continues to move away from the toe of the slope, the influence of erosion on the stability of the dike is

109

rapidly reduced. It can be seen that the most dangerous location of the cavity is at the vertical of the slope toe.
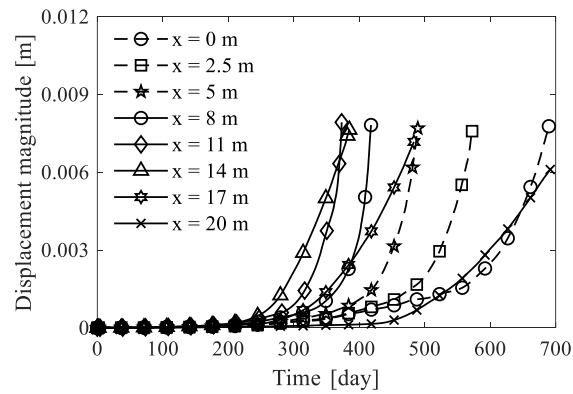
Figure 6.17 Variation of max. displacement magnitude with time for different cavity locations

(a) x = 0 m

(b) x = 2.5 m

(c) x = 5 m

(d) x = 8 m
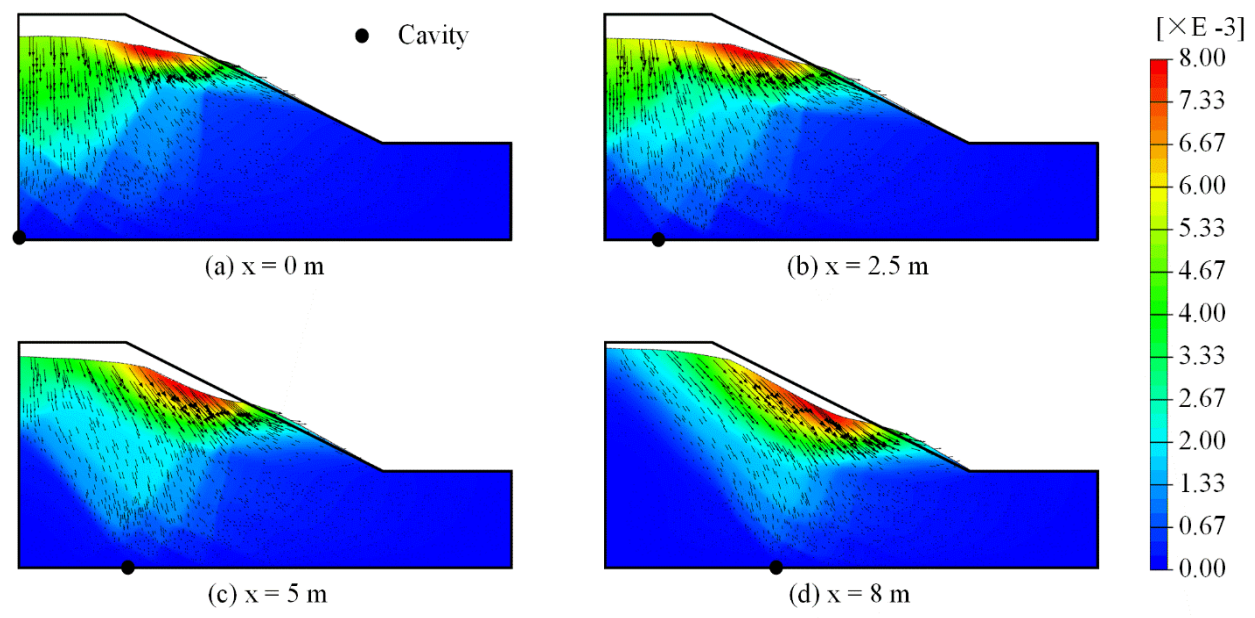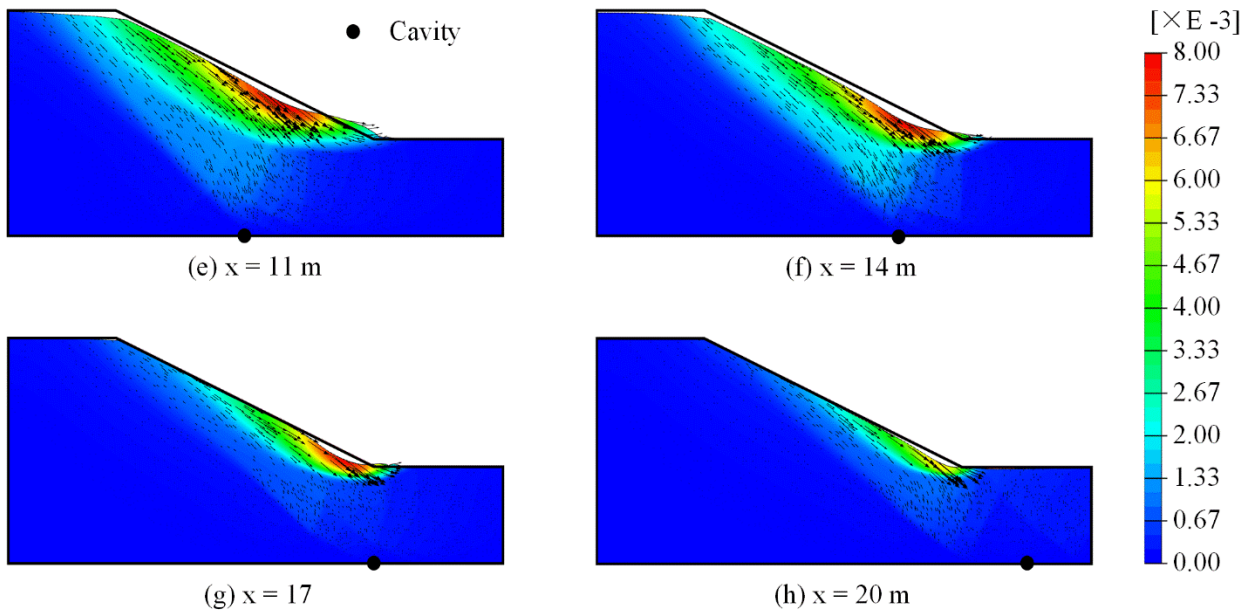
Figure 6.18 Displacement magnitude field and vector field at the end of erosion for different cavity locations (Deformation scale = 200)

6.8.2. Effect of erosion rate

The effect of the erosion rate on the stability of the dike is illustrated in Figure 6.19, showing the variation of the maximum displacement magnitude with time. The erosion rate is controlled by the coefficient β in Eq. (6.12). Here, β is an intrinsic property reflecting the nature of the soil and the method of construction of the dike, so that the higher its value, the higher the erosion rate will be. Figure 6.19 shows that an increase in the erosion rate will lead to a decrease in the time of failure. For a higher erosion rate the displacement evolution is more abrupt when it nears the failure state.
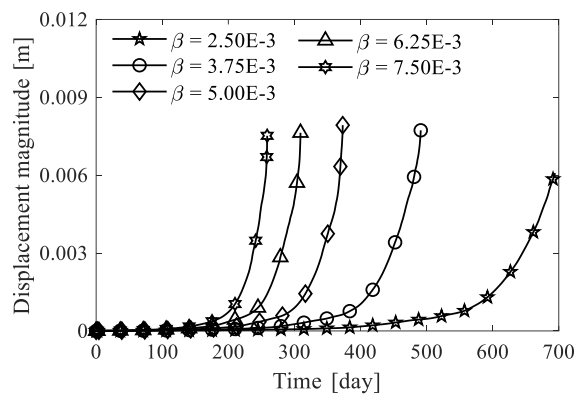
Figure 6.19 Variation of max. displacement magnitude with time for different erosion rate

6.8.3. Effect of fines content

As mentioned previously, the location of the critical state line, determined by the reference critical void ratio e_{cr0}, depends dynamically on the fines content f_c, i.e., e_{cr0} increases with f_c when $f_c > f_{th}$, or decreases with f_c when $f_c < f_{th}$. It is, therefore, necessary to discuss the influence of the initial fines content on the behavior of the dike subjected to internal erosion. The influence of the erodible

range of f_c is not considered here, as an increase of the eroded fines content will precede the formation of piping channels. Beyond this, internal erosion will lead to the creation of pipes of fluid flow, local collapses and discontinuities within the soil mass. At the piping stage, the current model would not be applicable, and further simulation must revert to an approach which takes into consideration the discontinuous soil and fluid interfaces. Therefore, the erodible range of fines content is fixed at 0.1 as in the previous simulations, *i.e.*, the residual fines content $f_{c,r} = f_{c0} - 0.1$. The initial fines content f_{c0} is set to 0.5, 0.45, 0.4, 0.35, 0.3, 0.25 and 0.2, respectively.

Figure 6.20 shows the variation of the maximum displacement magnitude with time for different initial fines contents. It shows that the dike failed suddenly during the erosion process for the cases $f_{c0} = 0.5$, 0.45, 0.4 and 0.35, whereas for the case $f_{c0} = 0.3$, the deformation of the dike developed progressively. For the cases $f_{c0} = 0.25$ and 0.2, the deformation of the dike subjected to erosion is very small. This can be understood from the relationship $f_c - e_{cr0}$. The reference critical void ratios e_{cr0} corresponding to the analyzed initial fines contents f_{c0} are shown in Figure 6.21. It can be seen that for the cases of $f_{c0} > 0.3$, e_{cr0} decreases with the decrease of the fines content, which reduces the resistance of the soil as a result of the downward shift of the critical state line in the $e - p'$ plane. For cases where $f_{c0} < 0.3$, e_{cr0} increases with the decrease of the fines content, offsetting the degradation of the resistance induced by the increase of the void ratio. Although more experimental studies are needed to justify these observations, it appears reasonable to consider the existence of a minimum f_{c0}, beyond which the degradation caused by internal erosion is crucial.
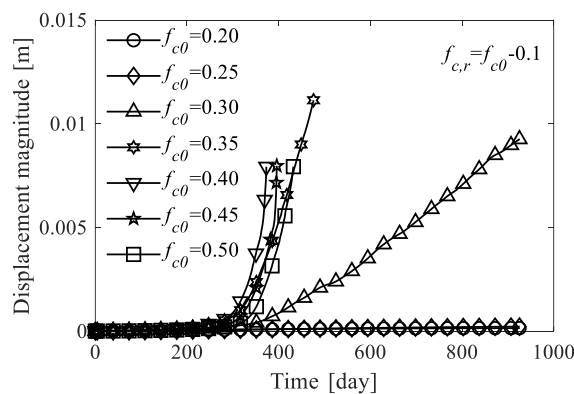
Figure 6.20 Variation of max. displacement magnitude with time for different initial fine content
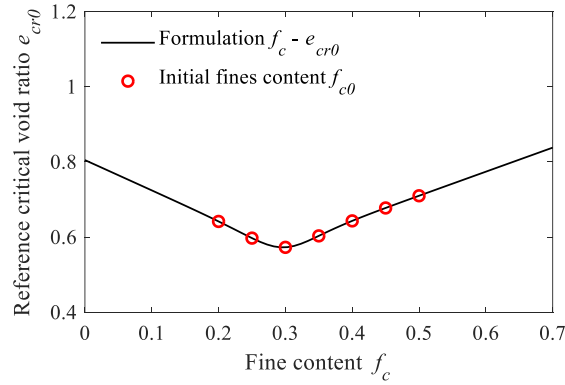
Figure 6.21 Variation of reference critical void ratio with fine content

6.9. Conclusion

This study has been an attempt to provide a novel contribution to the numerical approach for quantifying the impact of internal erosion on geotechnical infrastructures. The work consisted of modeling the internal erosion of the soil and the transport of fine particles by the fluid through the mass exchange between the solid and the fluid phases. The governing differential equations were formulated based on the mass balance of four assumed constituents: the stable fabric of the solid skeleton, the erodible fines, the fluidized particles, and the pure fluid, which were then implemented into a finite element code. An elasto-plastic constitutive model for a sand-silt mixture considering the fines content influence was used to consider the hydro-mechanical coupling induced by internal erosion.

The example of a dike-on-foundation demonstrated the applicability of the model to simulate the evolution of internal erosion with time for a real scale problem. The effects of the internal erosion led to an increase of the void ratio of the soil and a decrease of the fines content, which in turn resulted in the decrease of the shear strength of the eroded zone, evaluated by the sand-silt mixture constitutive model. In this case, the numerical results showed that the deformation of the dike developed rather slowly when the eroded zone was concentrated within the foundation. A measurable deformation within the dike appeared when the eroded zone developed towards the slope area. It increased dramatically until the dike failed suddenly due to a sliding rupture of the slope. The effects of the cavity location, the erosion rate and the fines content have been discussed.

Let us emphasize that this study is a 2-dimensional analysis. It was observed that an initially localized internal erosion resulted in the global instability or collapse of the geo-structure. However, under 3-dimensional condition, the constraint of the surrounding soil may limit or delay the development of the strains of the soil, which may then introduce a more 'local' failure-collapse mode, *i.e.*, a sinkhole, instead of a global landslide type instability. This point will be fully addressed in the next chapter.

Chapter 7   Three-dimensional finite element analysis of the internal erosion in dike-on-foundation

7.1. Introduction

In the previous chapter, the four-constituent model coupled with an elasto-plastic sand-silt mixture constitutive model has been implemented into the commercial finite element code ABAQUS in order to perform analyses at the scale of engineering structures. The model was used to analyze the internal erosion within a fully saturated dike under plain strain condition. It was found that the deformation of the dike developed rather slowly when the eroded zone was concentrated within the dike foundation. When the eroded zone developed towards the slope, a major sliding failure occurred. Furthermore, the discussion of the effect of the cavity location showed that when the cavity was located below the top of the dike, only a significant settlement of the dike was obtained. However, in a 3-dimensional condition, the constraint of the surrounding soil may limit or delay the development of the strains of the soil, which may in turn introduce a more 'local' failure-collapse mode, *i.e.*, a sinkhole, instead of a global landslide type instability.

Three-dimensional condition has long been thought to be a significant factor in the internal erosion process. Some attempts have been made to model the three-dimensional internal erosion by using discrete approaches [49, 81, 83, 85, 86]. But, unfortunately, sufficient computer modeling tools were not widely available to allow for a deeper examination of these 3-D effects at the scale of engineering structures. This chapter aims to simulate the 3-D effects of internal erosion within a linear dike on a foundation under more general and realistic conditions. Firstly, the unsaturated flow condition has been implemented into the hydro-mechanical model of internal erosion in order to describe more accurately the seepage within the dike and the foundation due to the difference in water pressure at the upstream and the downstream sides of the dike-on-foundation. Afterwards, the enhanced model has been applied to simulate the effect of internal erosion induced by the seepage within the dike and the leakage at the bottom of the foundation. The influence of the size of the leakage cavity and the elevation of the water level at the upstream and downstream sides of the dike-on-foundation will be discussed.

7.2. Unsaturated flow in dike-on-foundation

For isotropic partially saturated porous continua, a general expression for the Cauchy effective stress tensor $\boldsymbol{\sigma}'$ consistent with continuum principles of thermodynamics can be expressed as follows [152]:

$$\boldsymbol{\sigma}' = \boldsymbol{\sigma} + B\bar{p}\mathbf{I} \quad\text{..}(7.1)$$

where $\boldsymbol{\sigma}$ is the total Cauchy stress tensor, B is the Biot coefficient, $\mathbf{I}$ is the second-order identity tensor (Kronecker delta function), and $\bar{p}$ is the mean pore pressure given by the expression:

$$\bar{p} = s_w p_w + s_a p_a \quad\text{..}(7.2)$$

where p_w and p_a are the pore water and pore air pressures, respectively; s_w and s_a are the degree of water saturation and degree of air saturation, respectively, defined as:

$$s_w = \frac{dV_w}{dV_V}, \; s_a = \frac{dV_a}{dV_V}$$ ....(7.3)

where dV_V is the volume of the voids in the elementary volume dV, dV_w and dV_a are the volumes of the water and the air in the voids, respectively. It is assumed that tensile stresses are positive, p_w and p_a are pressure stress values. This explains the sign in Eq. (7.1). For soils, the Biot coefficient B may be taken as equal to one [129], and so, an equivalent effective stress equation may be written in the form:

$$\boldsymbol{\sigma}' = \boldsymbol{\sigma} + p_a \mathbf{I} - s_w p_c \mathbf{I}$$ ....(7.4)

where $p_c = p_a - p_w$ is the suction stress or capillary pressure.

In a transient quasi-static analysis, we can simplify the model by assuming that the air pressure is constant throughout the modeled domain and is small enough so that its value can be neglected. This assumption allows p_a to be removed from the equation, provided that the atmospheric pressure on the boundary of the medium is also omitted from the equilibrium equations and that p_a is small enough so that its effect on the deformation of the medium can be neglected. This simplification reduces the effective stress expression to:

$$\boldsymbol{\sigma}' = \boldsymbol{\sigma} - s_w p_c \mathbf{I},$$
$$p_c = -p_w$$ ....(7.5)

Therefore, the medium is fully saturated for $p_w > 0$; negative values of p_w represent the capillary effects within the medium. For $p_w < 0$, it is known that, at a given value of the capillary pressure, $p_c (= -p_w)$, the saturation condition lies within certain limits [168, 169]. In this study, the empirical soil-water characteristic curve (SWCC) model proposed by van Genuchten [168], which has been proved to be suitable for silt sand [168], has been adopted to determine explicitly the degree of water saturation at a given capillary pressure.

In the van Genuchten model, the SWCC is assumed as [168]:

$$s_w = \left(s_{w,s} - s_{w,r}\right)s_{w,e} + s_{w,r}$$
$$s_{w,e} = \left[1 + \left(\alpha_{vg} p_c\right)^{n_{vg}}\right]^{-m_{vg}}$$ ....(7.6)

where $s_{w,e}$ is the effective degree of water saturation, $s_{w,r}$ is the residual (minimum) degree of water saturation, $s_{w,s}$ is the maximum degree of water saturation ($s_{w,s} = 1.0$), and α_{vg}, n_{vg} and m_{vg} are the material parameters of the van Genuchten model. For $p_c < 0$ (saturated medium), the effective degree of saturation $s_{w,e}$ is set to be 1.0. The permeability coefficients of water within the van Genuchten model are assumed to be dependent on the effective water saturation as:

$$k = k_s \left(s_{w,e} \right)^{\xi_{vg}} \left[1 - \left\{ 1 - \left(s_{w,e} \right)^{1/m_{vg}} \right\}^{m_{vg}} \right]^2 \quad ....(7.7)$$

where k_s is the saturated (maximum) coefficient of water permeability, ξ_{vg} is a material parameter.

Therefore, the unsaturated flow can be introduced into the hydro-mechanical model for internal erosion by combining Eqs. (7.5)-(7.7) with Eqs. (6.15)-(6.19). It can be solved numerically by using the finite element method described in detail in section 6.3.

7.3. Three-dimensional modeling of internal erosion within a dike

7.3.1. Description of the problem

The characteristics of the studied configuration are presented in Figure 6.11 according to the dike of Val d'Orléans [167]. The dike was built on sandy-silt alluvium formation over limestones. The upstream face of the dike-on-foundation (surface s_1 in Figure 6.11) is exposed to the water in the river behind the dike. Likewise, the downstream face of the dike-on-foundation (surface s_4 in Figure 6.11) is exposed to the atmosphere. If the soil is partially saturated, the phreatic surface in the dike and foundation (surface s_2 in Figure 6.11) corresponds to the locus of the points at which the pore fluid pressure, p_w, is zero. Above this surface the pore fluid pressure is negative, representing the capillary tension which causes the fluid to rise against the gravitational force, creating a capillary zone. The saturation associated to specific values of the capillary pressure for the absorption of the fluid by the porous medium is a physical property of the material and is defined by the van Genuchten model. The bottom of the alluvium layer (surface s_3 in Figure 6.11) is assumed to rest on an impermeable limestone layer. The seepage due to the water pressure gradient at the upstream and downstream faces of the dike-on-foundation can lead to the detachment of fine particles which will move from the upstream to the downstream side and eventually lead to the degradation of the dike. Furthermore, for the dike of Val d'Orléans, it has been reported that karst collapses underneath the foundation can lead to a leakage cavity through which the underground water and the fine particles could flow out. Internal erosion can take place due to local hydraulic gradients in the vicinity of the cavity. The computations aim to show how the internal erosion may weaken the foundation and the dike under different boundary conditions.
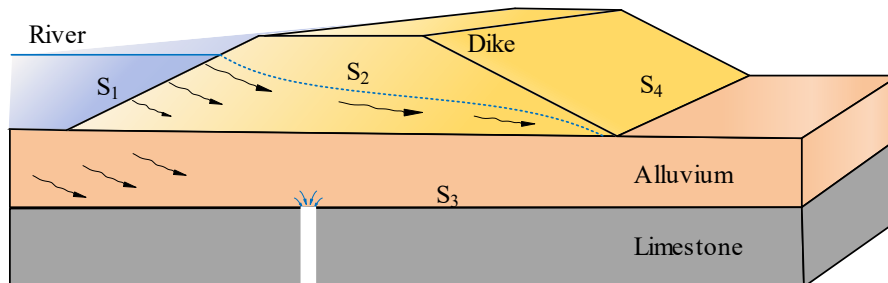
Figure 7.1 Scheme of the dike-on-foundation near Orléans (France)
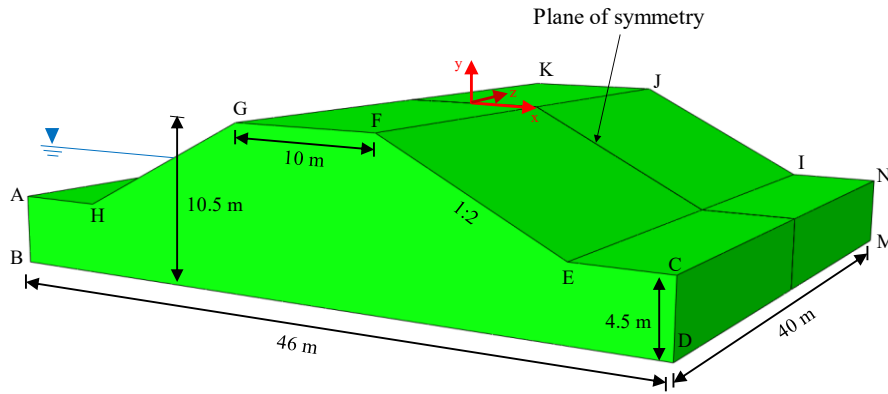
Figure 7.2 Schematic configuration of the dike and mesh of the numerical model.

The dimensions of the numerical model are shown in Figure 6.12. The dike is assumed to be initially stable under the gravity load. Firstly, 2 cases with different hydraulic boundary conditions have been simulated. In both cases, the water level at the upstream face was located at the top of the dike, *i.e.,* 10.5 m, representing the extreme configuration of a flooding condition. The water level at the downstream face is supposed to be located at the bottom of the alluvium layer, below the toe of the dike, as shown in Figure 7.3. The phreatic surface is calculated accordingly. Furthermore, in case 2, a leakage cavity of a 0.2 m diameter created by the karst collapse underneath the alluvium layer is assumed at the bottom of the symmetry plane of the model, where the water pressure is assumed to be zero.

(a)

D=0.2m

(b)
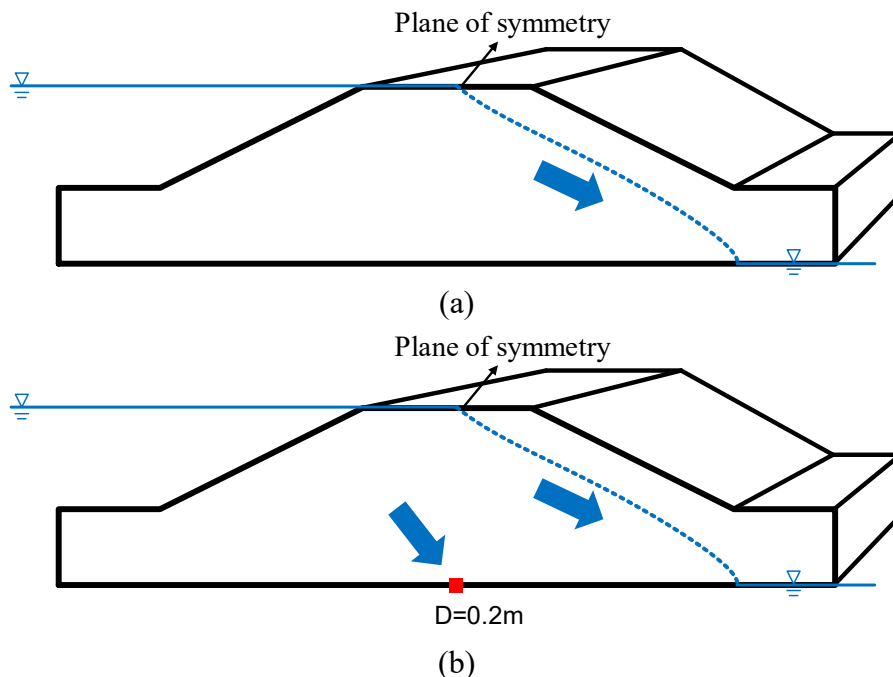
Figure 7.3 hydraulic boundary conditions: (a) Case1, without the cavity; (b) Case 2, with the cavity (diameter=0.2 m)

The boundary conditions were taken as vertical rollers on the left and right boundary surfaces of the foundation and fully fixed at the base of the foundation. The gravity load was initially applied to generate the initial stresses and the initial water pressure fields. Then, the water head at the cavity

was set to 11m in order to initiate the water flow in and out the cavity. The alluvium and the dike were considered to be made of the same soil, a mixture of sand and silt. The physical properties and the material parameters, summarized in Table 6.3 and

Table 5.2, correspond to the Ottawa 50/200 sand-silt characteristics [52] with $e_0=0.6$, $c_0=0.01$ and $f_{c0}=0.4$. Similar to the previous 2D analysis, a residual fines content was artificially fixed equal to 0.05 for the sake of simplicity in the 3D analysis.

Due to the lack of experimental data, the set of van Genuchten model parameters used by Uzuoka et al. [95] was adopted, as shown in Table 7.3. Figure 7.4 shows the SWCC and the relationship between the relative permeability of water and the degree of water saturation given by the van Genuchten model with the parameters in Table 7.3.

Table 7.1 Physical properties of soils

Density of fluid	ρ_f	1.0 g/cm³	Kinematic viscosity of fluid	η_k	5.0E-6 m²s⁻¹
Density of solids	ρ_s	2.65	Intrinsic permeability	k_0	2.5E-9 m²

Table 7.2 Material constants of soils

Elastic parameters			Plastic parameters			CSL-related parameters				Fines parameters			Erosion parameters		
G_0/MPa	ν	n	k_p	A_d	ϕ_u	$e_{hc,cr0}$	$e_{fc,cr0}$	ξ	λ	a	m	f_{th}	λ_e	k_1	k_2
150	0.2	0.5	0.0017	1	32	0.805	1.03	0.196	0.081	0	0.7	0.3	0.02	3	2

Table 7.3 Material parameters in van Genuchten model

$s_{w,s}$	1.0
$s_{w,r}$	0.1
α_{vg}	0.02
m_{vg}	0.667
n_{vg}	3.0
ξ_{vg}	3.5

(a)

(b)

7.3.2. Hydro-mechanical responses in 3D condition

Due to the symmetry of the domain and the mechanical and hydraulic boundary conditions, only half the domain has been modeled. Figure 7.5 shows the initial space distribution of the pore pressure in the dike and foundation under the gravity load. The phreatic surface corresponds to the locus of the points at which the pore water pressure is zero. Figure 7.6 shows the space distribution of the fines content after erosion for Case 1. As internal erosion takes place, the fines content, which is initially spatially uniform throughout the whole soil volume, begins to decrease with time. The decrease of the fines content starts at the two ends of the phreatic surface, which correspond to the locations of the maximum flow rate. A highly eroded zone appears and develops, following the direction of the maximum hydraulic gradient.

Figure 7.7 and Figure 7.8 show the displacement and the deviatoric plastic strain fields within the dike at the end of the erosion for Case 1. The increase of the void ratio accompanied by a downward shift of the CSL in the *e-p'* plane induced by the decrease of the fines content makes the soil looser. Consequently, the soil strength decreases. It leads to the onset of a shear sliding surface in the most eroded area near the phreatic surface at the downstream side. The plastic deformation keeps developing with time until the dike collapses by a sliding failure of the slope.
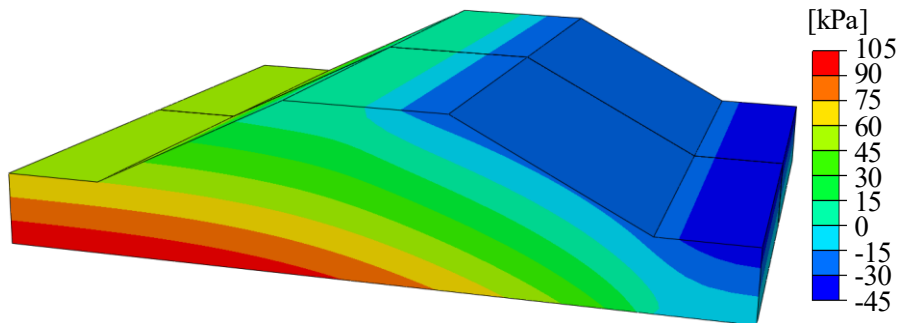
Figure 7.5 Spatial distribution of initial pore pressure in the dike and foundation under gravity load.
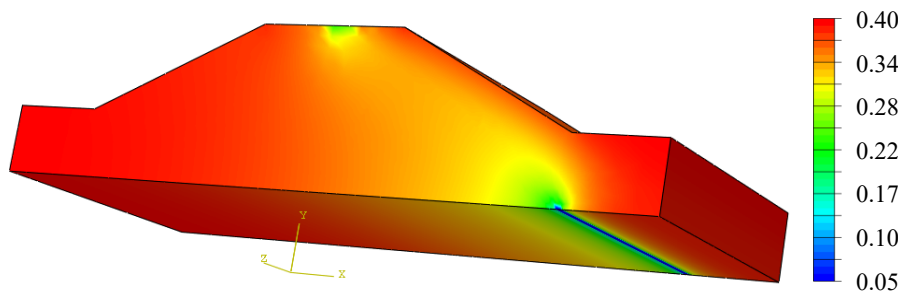
Figure 7.6 Spatial distribution of fines content after erosion for Case 1 (without the leakage cavity) (1/2 model).

119
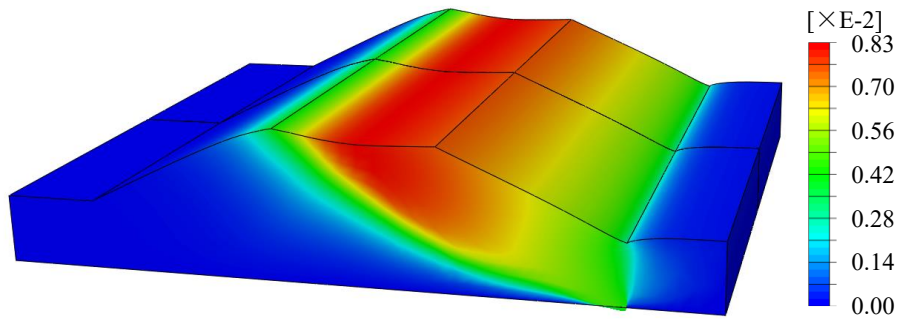
Figure 7.7 Displacement magnitude field after erosion for Case 1 (without the leakage cavity).
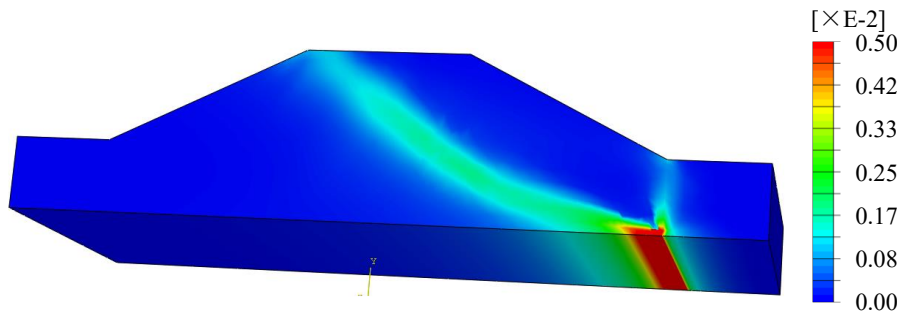
Figure 7.8 Deviatoric plastic strain field after erosion for Case 1 (without the leakage cavity) (1/2 model).

Figure 7.9 and Figure 7.10 show the displacement and the deviatoric plastic strain fields within the dike at the end of erosion for Case 2 with a leakage cavity of 0.2 m in diameter at the bottom of the symmetry plane. Figure 7.11 shows the distribution of fines content at the end of erosion for Case 2. An area with significant settlement is found at the top of the dike, which indicates the inception of a sinkhole as a result of internal erosion. The fine particles close to the leakage cavity were washed out due to high local hydraulic gradients. The sinkhole was formed due to the "rigid" movement of the soil above the eroded area. It is noted that an eroded zone developed also near the phreatic surface at the downstream side due to the difference in water pressure at the upstream and downstream faces of the dike; this eroded zone led to a global sliding failure of the dike at the end of the simulation.
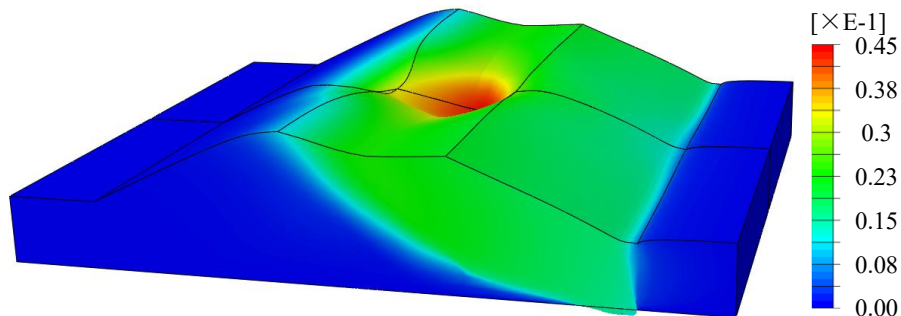
Figure 7.9 Displacement magnitude field after erosion for Case 2 (with the leakage cavity)
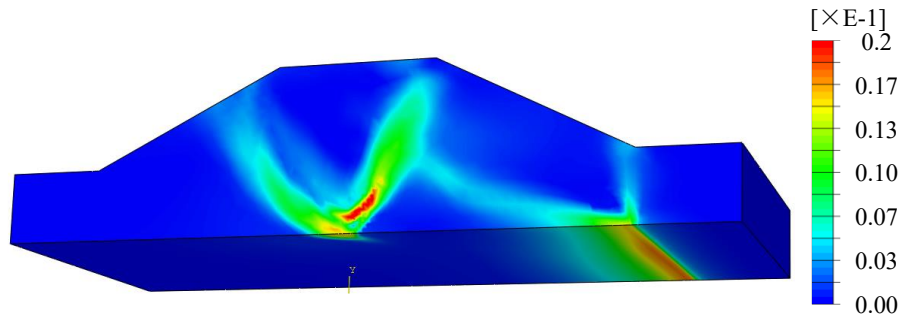
Figure 7.10 Deviatoric plastic strain field after erosion for Case 2 (with the leakage cavity) (1/2 model).
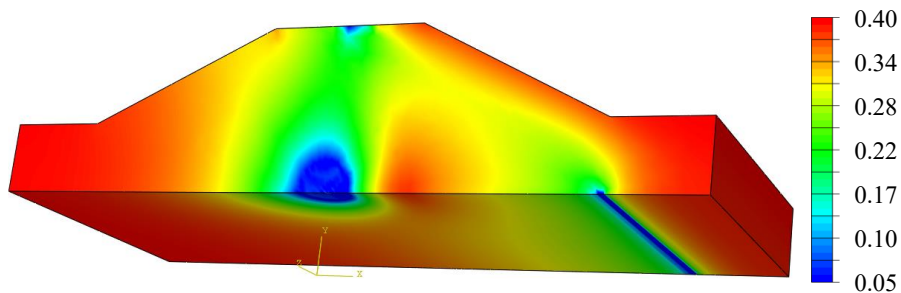
Figure 7.11 Spatial distribution of fines content after erosion for Case 2 (with the leakage cavity) (1/2 model).

In the previous chapter, similar simulations in 2D condition have been carried out. Figure 6.18 showed the dike deformation at the end of erosion for different cavity locations. A significant settlement of the dike was observed when the cavity was located below the top of the dike, whereas the results of simulations in 3D condition show that the constraint of the surrounding soil limits the development of the deformation, which in turn introduces a local failure, i.e., a sinkhole shown in Figure 7.9-Figure 7.11, before the global sliding failure occurred. Furthermore, by introducing the unsaturated condition into the physical problem of the seepage in the dike and the foundation, it was found that the location of the phreatic surface and the size of the leakage cavity play an important role in the initiation and development of the eroded zone. Therefore, the influence of the size of the leakage cavity and the water levels at the upstream and downstream surface needs to be discussed.

7.4. Discussion

7.4.1. Effect of the size of the leakage cavity

In Case 3, a larger leakage cavity of a 1.0 m in diameter was assumed at the bottom of the symmetry plane of the model, as shown in Figure 7.12, in order to investigate the influence of the size of the leakage cavity on the development of internal erosion within the dike and foundation.
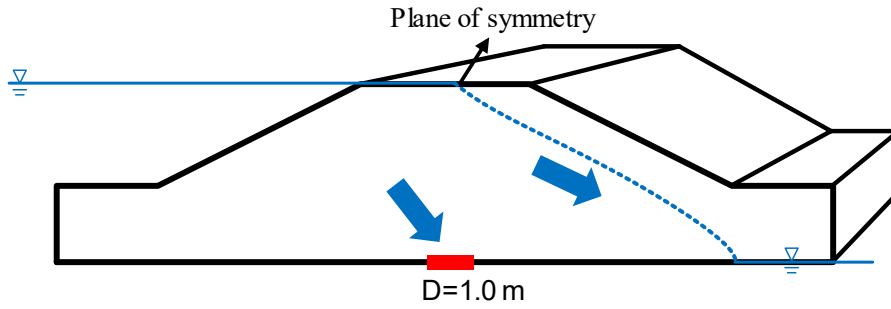
Figure 7.12 hydraulic boundary conditions for Case 3 with the cavity of leakage (Diameter=1.0 m)
Figure 7.13 shows the displacement of the dike-on-foundation at the end of erosion for Case 3. Similar to Case 2, the initiation of a sinkhole as a result of internal erosion is found at the top of the dike. By comparing the time variation of the maximum settlement of Case 2 and Case 3, shown in Figure 7.14, it is obvious that the enlargement of the cavity accelerates the formation of the sinkhole. Figure 7.15 compares the spatial distribution of the fines content at the end of erosion for Case 2 and Case 3. For a larger leakage cavity, the internal erosion within the dike and foundation develops faster, leading to the earlier appearance of the sinkhole at the top of the dike.
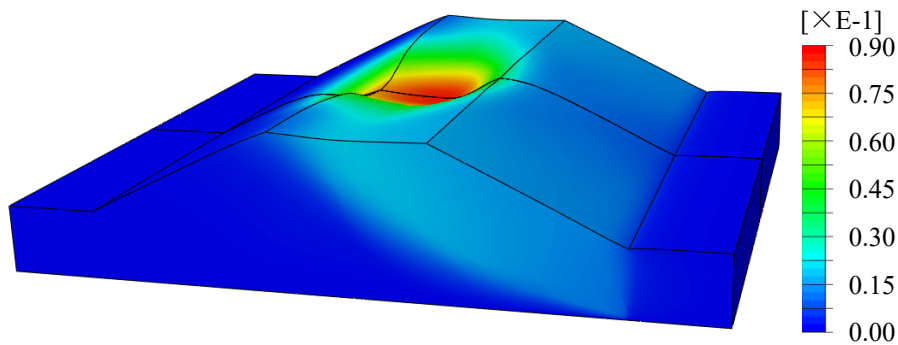
Figure 7.13 Displacement magnitude field after erosion for Case 3.
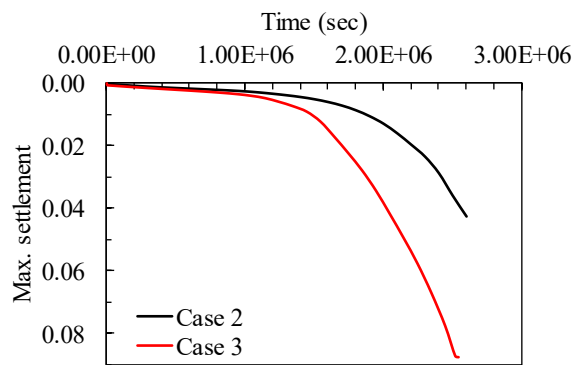
Figure 7.14 Time variations of the maximum settlement during erosion for Case 2 and Case 3.

<center>(a)   (b)</center>
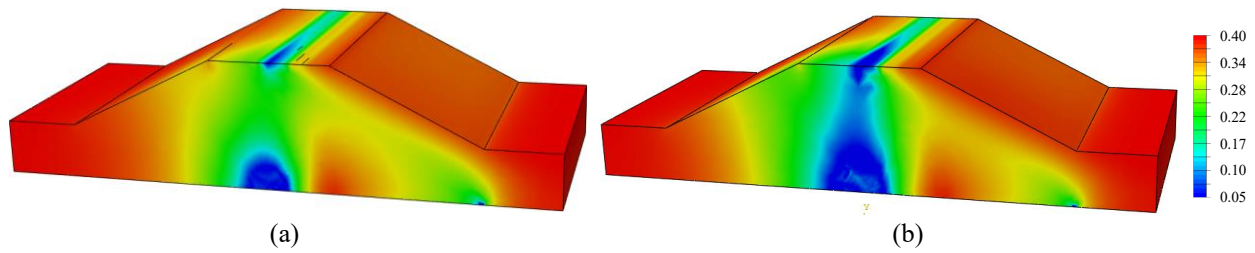
Figure 7.15 Spatial distribution of fines content after erosion for Case 2 and Case 3 (1/2 model).

7.4.2. Effect of water head

As observed previously, the decrease of the fines content starts in the vicinity of the phreatic surface due to the seepage flow induced by the difference in water pressure at the upstream and downstream faces of the dike-on-foundation. 2 additional cases were analyzed to investigate the influence of the elevation of the water surface at the upstream and downstream surface on the development of internal erosion. In Case 4, the water level at the upstream side is located at the top of the dike, the water level at the downstream side is supposed to be at the top of the foundation. The dike and the foundation are therefore supposed to be saturated as shown in Figure 7.16(a). In Case 5, the water level at the upstream side is reduced to the middle of the dike height as shown in Figure 7.16(b).

Figure 7.17-Figure 7.19 compare the displacement fields, the deviatoric plastic strain fields and the spatial distributions of the fines content at the end of erosion for Case 2 and Case 4. It can be seen that, when the water level at the downstream side is raised to the top of the foundation, a global sliding failure occurs at an early stage of erosion. In Case 4, a decrease of the fines content at the toe of the dike is observed at the end of erosion, indicating that a loss of fines at the toe of the dike can induce the global sliding failure of the dike. It may be reasonable to assert that the elevation of the water surface within the foundation at the downstream side will increase the risk of global sliding failure of the dike.

<center>(a)</center>

Plane of symmetry

D=0.2 m
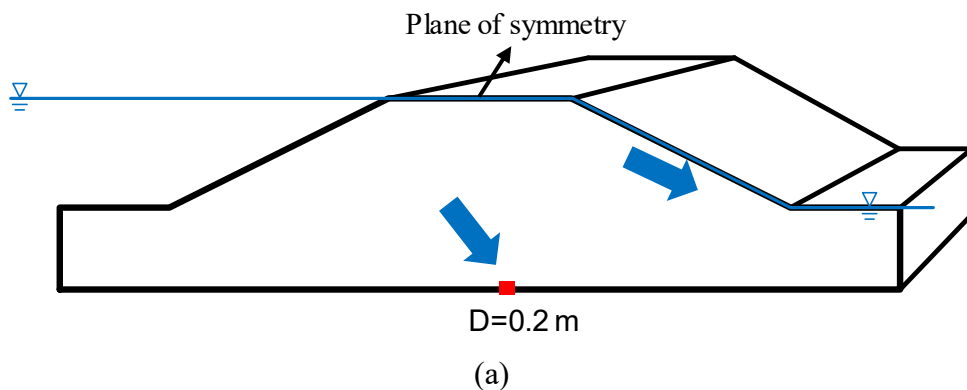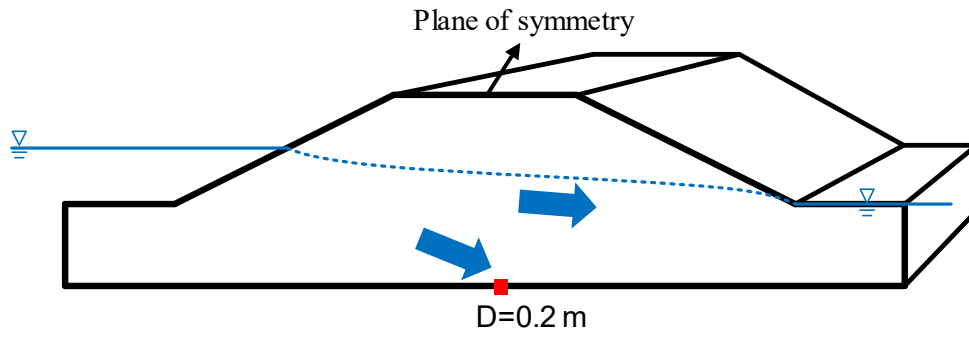
(b)

Figure 7.16 hydraulic boundary conditions for Case 4 and Case 5 with different water levels at the downstream and upstream faces
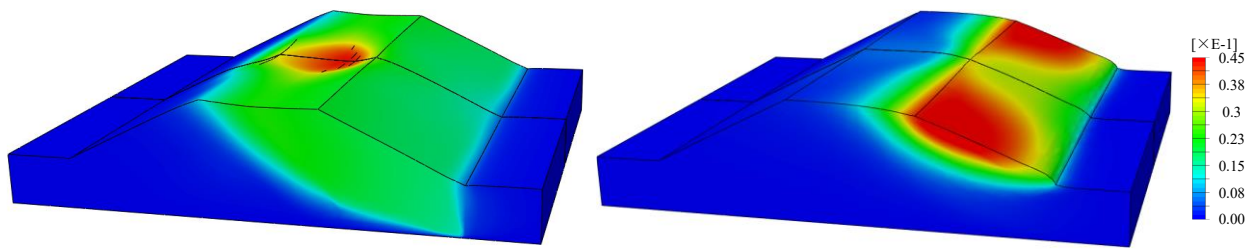
(a)

(b)

Figure 7.17 Displacement magnitude field after erosion for Case 2 and Case 4.
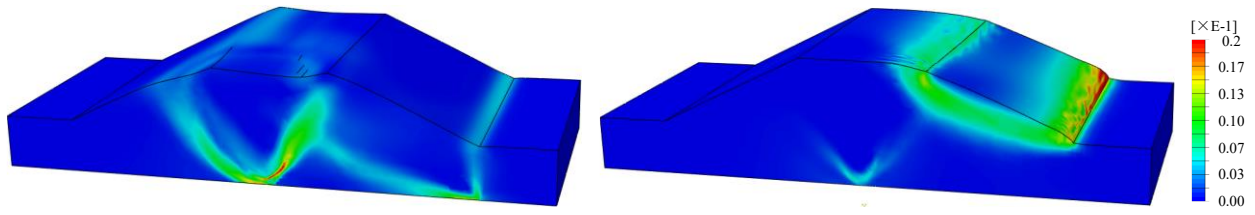
(a)

(b)

Figure 7.18 Deviatoric plastic strain field after erosion for Case 2 and Case 4 (1/2 model).
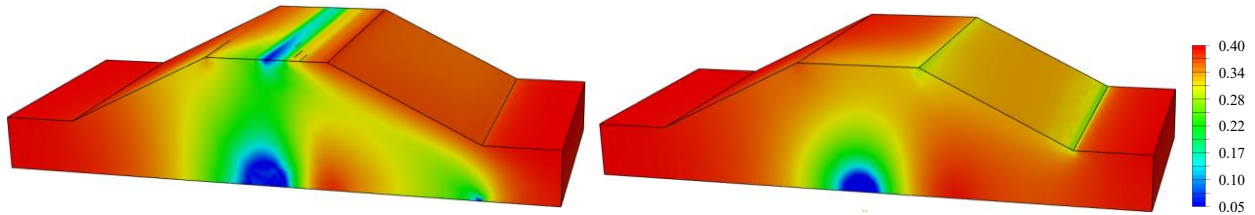
(a)

(b)

Figure 7.19 Spatial distribution of fines content after erosion for Case 2 and Case 4 (1/2 model).

Figure 7.20-Figure 7.22 compare the displacement fields, the deviatoric plastic strain fields and the spatial distributions of the fines content at the end of erosion for Case 2 and Case 5. It can be concluded that the decrease of the water level at the upstream side of the dike decreases the loss of fines at the toe of the dike. The eroded zone develops following the direction of the maximum hydraulic gradient. The initiation of a sinkhole is, therefore, found at the upstream side of the phreatic surface. It should be noted that these analyses were carried out with constant water level. However, in the reality, the water level may vary, slowly or rapidly, as a result of rainfall or human

activities. More experimental and numerical analyses are still needed in the future to study this aspect.

(a)   (b)
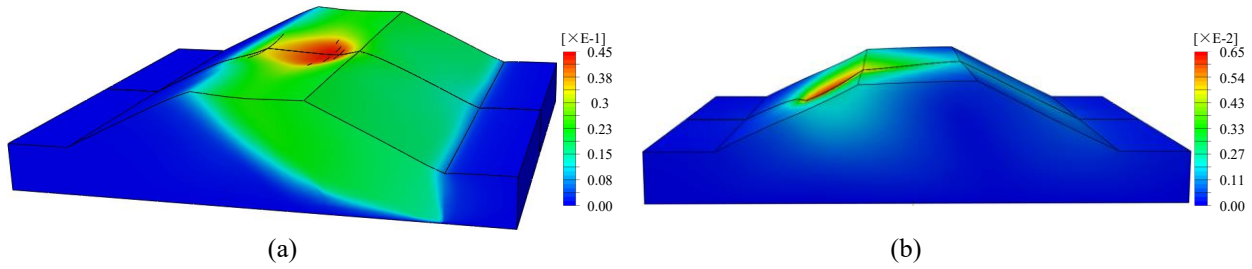
Figure 7.20 Displacement magnitude field after erosion for Case 2 and Case 5.

(a)   (b)
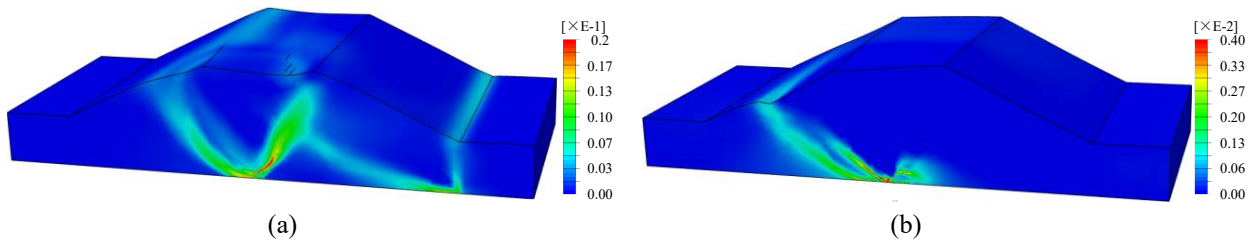
Figure 7.21 Deviatoric plastic strain field after erosion for Case 2 and Case 5 (1/2 model).

(a)   (b)
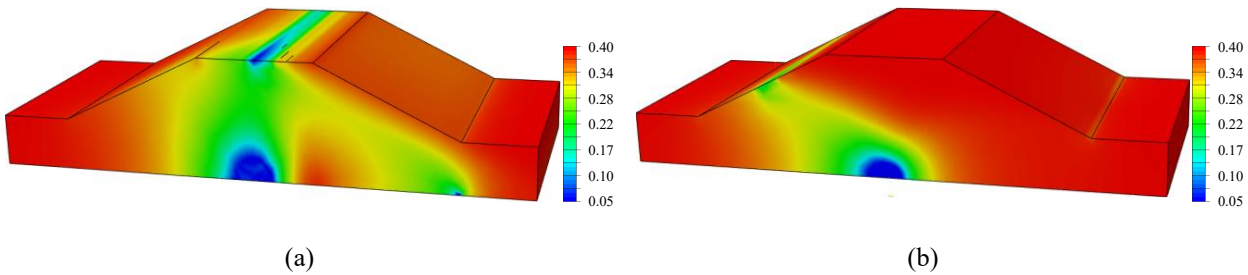
Figure 7.22 Spatial distribution of fines content after erosion for Case 2 and Case 5 (1/2 model).

7.5. Conclusion

Even if the studied cases are mainly theoretical, they are very close to real case problems. This chapter is an attempt to provide a novel method to identify the potential consequences of internal erosion developed within a dike under different boundary conditions. The developed hydro-mechanical model for internal erosion has been enhanced by introducing the unsaturated flow in order to describe the seepage in the dike and the foundation due to the difference in water pressure at the upstream and downstream sides of the dike-on-foundation. Then, a series of 3D simulations of the development of internal erosion within the dike and the foundation were carried out. The results indicate that the continuous loss of fines at the downstream side of the dike and foundation will eventually lead to the sliding failure of the slope. It is observed that, in this case, the decrease of the fines content close to the toe of the dike can stimulate the global sliding failure of the system. The elevation of the water surface within the foundation at the downstream side will increase the risk of global sliding failure of the system. Furthermore, the presence of a leakage cavity could lead to the initiation of a sinkhole which is formed due to the rigid movement of the soils above the eroded area in the vicinity of the cavity. The location of the sinkhole is found to be related to the location of the phreatic surface.

However, it should be noted that these analyses were carried out with constant water head, and the materials of the dike and the foundation are assumed to be initially homogeneous. In nature, the water head may vary, slowly or rapidly, as a result of rainfall or human activities. The seepage path and the location of the phreatic surface may become more complicated and could evolve with time in a heterogeneous medium, which will eventually increase the uncertainty of the location of the sinkhole. These aspects should be analyzed in future works.

Chapter 8   Conclusions and perspectives

Geo-structures such as dams, levees, or dikes are subjected to seepage flows varying in time and space. The water flowing through these porous media can lead to the detachment and transport of part of the soil particles within these structures or their foundations. This problem is usually called internal erosion. The term suffusion, one type of internal erosion, refers to the detachment and transport of finer particles through a coarser porous soil matrix due to seepage flow. Suffusion can modify with time the hydraulic and mechanical properties of the soils and may trigger significant damage on such structures and lead eventually to their collapse.

Experimental and computational studies on internal erosion were reviewed thoroughly at the beginning of this research. The laboratory tests and numerical analyses at the scale of the sample play undoubtedly an important role in engineering practice by determining the material susceptibility to internal erosion and in the knowledge of the physical mechanism behind the internal erosion phenomena. However, it fails to determine where and when the action of the seepage flow can trigger the internal instability in the granular soil and the subsequent mechanical responses at the scale of an entire geo-engineering structure. Few model tests or numerical studies at the scale of an entire geo-engineering structure are available in the literature.

Therefore, this research attempted to contribute to the design and sustainability of geotechnical and hydraulic engineering structures, with a particular focus on embankment dams, levees, and dikes. It aimed to develop a numerical model of suffusion by introducing, on the one hand, the coupling of the hydraulic and mechanical phenomena and, on the other hand, the coupling of erosion and filtration. This was achieved thanks to the development a four-phase erosion model built in the framework of the porous continuous medium theory. In conjunction with efficient finite element implementation and simulations, it was important to improve the predictive capability of soil suffusion and to facilitate reliable detection and early warning of the eventual dysfunction of hydraulic structures, urban infrastructures, the slope failures, and landslides.

To reach these objectives, this research was divided into two main parts:

- At the laboratory scale :

- To formulate a new numerical model considering both erosion and filtration in suffusion in the framework of the porous and continuous medium theory. This model aimed to reproduce the mains features observed in the laboratory erosion tests.

- To study the influence of the soil spatial variability on the initial porosity and fines content on filtration during suffusion under one-dimensional (1D) and two-dimensional (2D) conditions.

- To propose a simulation platform for the triaxial erosion tests under mechanical loadings based on the proposed four-constituent model, in order to analyze the coupled hydro-

mechanical behavior of soils subjected to internal erosion.

- At the geo-structure scale :

- To implement the developed hydro-mechanical model into a finite element code.

- To validate this code by simulating some numerical examples issued from the literature.

- To apply the numerical model to perform 2D and 3D computations at the geo-engineering structure scale to assess how internal erosion could impact the stability of earthen structures.

The major contributions and conclusions obtained from this study are summarized below. Perspectives and recommendations for future research work are also presented.

8.1. General conclusions

The main achievements and results of this thesis can be summarized as follows.

Numerical model considering both erosion and filtration in suffusion in the framework of the porous continuous medium theory

Based on the porous medium theory, the saturated porous medium was considered as a system composed of 4 constituents: the stable fabric of the solid skeleton, the erodible fines, the fluidized particles and the fluid phase. The fines could behave either as a fluid-like (described as fluidized particles) or as a solid-like (described as erodible fines) material. The approach consisted of modeling the erosion of the soil skeleton, the transport by the water flow and the filtration of the fine particles through the mass exchange between the solid and fluid phases. The terms of mass exchange were introduced into the mass balance equations complemented by a filtration term to simulate the filling of the initial voids due to the filtration of transported fines from the suspension to the solid fraction.

A 1-D numerical problem was solved with the finite difference method in order to compare the numerical results with the experimental measurements of two series of erosion tests performed on cohesionless soils. It was found that the numerical results were in agreement with the experimental data and that the model could capture the main features of both erosion and filtration during the suffusion process.

Influence of the soil spatial variability on filtration during suffusion

One and two-dimensional random finite difference analyses were performed by implementing the random field theory to the finite difference code. Monte Carlo simulations of suffusion were conducted to investigate the influence of the variability, the spatial correlation length, and the cross correlation of the initial porosity (ϕ_0) and the initial fines content (f_{c0}) on the rate of the eroded mass and the minimum hydraulic conductivity during the test.

It was found that, in 1D Monte Carlo analyses, an increase of the variability in ϕ_0 and f_{c0}, or a decrease of the spatial correlation length of the variables generally decreased the mean rate of the eroded mass and the mean minimum hydraulic conductivity. A greater variability led to more

significant changes in soil porosity at the interface of different layers; the lower the spatial correlation length, more uneven became the layers, producing more interfaces between loose and dense layers, both of them in turn facilitating the capture of the fine particles transported by the water flow. Furthermore, even if the sample behavior was more strongly affected by the soil variability and spatial correlation and somewhat less so by the cross-correlation between ϕ_0 and f_{c0}, negatively correlated ϕ_0 and f_{c0} were more likely to cause blockage leading to the potential increase of excess pore pressure and, thus, to strength degradation.

The results obtained in 2D analyses confirmed that the influx could bypass local blockages. The mean rates of the eroded mass in 2D condition were generally smaller than in 1D condition. Interestingly, the greatest probability of blockage in 2D isotropic random fields occurred when the spatial correlation length was about half of the specimen length.

Numerical model for triaxial erosion tests under mechanical loading

The four-constituent model was enhanced by including a non-linear incremental constitutive model to account for the effects of the evolution of the fines content on the behavior of the soil. A numerical model was then developed to simulate the downward erosion tests under triaxial mechanical loading with a special emphasis on the evolution of the eroded mass, the hydraulic conductivity and the deformation of the specimen during and after erosion.

The numerical platform was validated by simulating the behavior of HK-CDG (Hong Kong - completely decomposed granite) mixtures before, during, and after erosion during triaxial tests. After a significant amount of fine particle loss, the stress-strain behavior of the soil changed from dilative to contractive with a decrease of the shear strength. The comparison between experimental results and numerical computations showed that the model could reproduce quite well the initiation of internal erosion, the sudden increases in the erosion rate, the changes in the hydraulic conductivity and the deformations of the soil sample. The results confirmed that the deformations were linked to the stress ratio under which the erosion process was activated.

The simulation platform was then applied to analyze the influence of the stress state and the soil initial state (relative density and fines content) from a numerical standpoint. Interestingly, besides the stress ratio, the amount of loss of fines indicating the yielding from a stable to an unstable mechanical response appeared to be linked to the initial density as well as to the initial fines content of the soil mixture. These results should provide some inspiration for the design of future experiments in order to better understand the physics of internal erosion and its impact on the soil behavior.

Impact of suffusion on the dike stability (2D)

In order to perform analyses at the scale of an entire engineering structure, a more general elasto-plastic sand-silt mixture model has been introduced within the four-constituent model of suffusion. The hydro-mechanical model was first implemented into the commercial finite element code ABAQUS and used to assess how internal erosion could impact the stability of earthen structures.

After having simulated for validation some numerical examples from the literature, the developed model was applied to compute the suffusion within a dike-on-foundation under plane-strain assumption. In this example, the dike was built on a sandy-silt alluvium formation over karstic limestones. A confined aquifer under pressure was located underneath the limestone layer. It could rise inside the karstic caves and even reach the alluvium layer. Internal erosion due to seepage flow could take place when the water level was different in the alluvium and in the confined aquifer. The main results are:

- The effects of the internal erosion led to an increase of the void ratio of the soil and a decrease of the fines content, which in turn resulted in the decrease of the shear strength of the eroded zone, calculated by the sand-silt mixture constitutive model.

- In this case, the numerical results showed that the deformation of the dike developed rather slowly when the eroded zone was concentrated within the foundation. A measurable strain within the dike appeared when the eroded zone developed towards the slope area. It increased dramatically until the dike collapsed suddenly due to a sliding of the slope.

- Effect of cavity location: a significant settlement of the dike was observed when the cavity was located below the top of the dike. As the cavity moved toward the slope, a sliding of the slope began to appear. The simulation was terminated with a sliding failure. As the cavity moved away from the toe of the slope, the influence of erosion on the stability of the dike decreased quickly.

- Effect of erosion rate: an increase of the erosion rate led to a decrease of the time of the failure onset. For a higher erosion rate, the evolution of the slope displacement was more abrupt near the failure state.

- Effect of fines content: from the results of a series of simulation with different initial fines content f_{c0}, it appeared reasonable to consider the existence of a minimum f_{c0}, beyond which the degradation caused by internal erosion would be crucial. In this example, the dike failed suddenly during the erosion process for the cases $f_{c0} = 0.5$, 0.45, 0.4 and 0.35, whereas for the case $f_{c0} = 0.3$, the deformation of the dike developed more progressively. For the cases $f_{c0} = 0.25$ and 0.2, the deformation of the dike was very small.

Mechanical consequences of internal erosion within the dike due to different boundary conditions in 3D

Three-dimensional condition has long been thought to be a significant factor in the internal erosion process. But unfortunately, computer modeling tools are not widely available to allow for a deeper analysis of these 3-D effects at the geo-engineering structure scale. Therefore, a modeling approach was developed to simulate the 3-D effects of internal erosion within a linear dike on a foundation that retains the water under more general and realistic initial and boundary conditions. Firstly, a unsaturated flow condition was considered and implemented into the hydro-mechanical model of

internal erosion in order to describe more accurately the seepage in the dike and the foundation due to the difference in water pressure at the upstream and downstream sides of the dike-on-foundation. Afterwards, the enhanced model was applied to simulate the effect of internal erosion induced by the seepage within the dike and the leakage at the bottom of the foundation. The influence of the size of the leakage cavity and of the elevation of the water surface at the upstream and downstream sides of the dike-on-foundation have been analyzed. It was found that:

- The continuous loss of fines in the downstream side of the dike and foundation could lead to the failure of the dike. In this case, the decrease of the fines content near the toe of the dike could stimulate the global sliding of the dike.

- The increase of the water head in the foundation on the downstream side increased the risk of global sliding failure of the dike.

- The presence of a leakage cavity below the dike could lead to the onset of a sinkhole which was formed due to the deformation of the soils above the eroded area in the vicinity of the cavity.

- The location of the sinkhole was found to be closely related with the location of the phreatic surface.

8.2. Perspectives

This research attempted to develop a model of suffusion at the scale of entire geo-engineering structures to facilitate the determinations of how, where, and when, the action of a seepage flow could trigger the internal instability of the granular soil and the subsequent mechanical response of the geo-engineering structures. It could be applied to analyze the influence of suffusion within the hydraulic structures (dams, dikes, etc.), the urban infrastructures (pipelines, tunnels, etc.), the slope failures, and landslides.

The analyses of the suffusion within a dike were chosen as an example in this research. However, it should be noted that these analyses were carried out with constant water head. The materials of the dike and the foundation were assumed to be initially homogeneous. In reality, the water head may vary, slowly or rapidly, as a result of rainfall or human activities. The seepage path and the location of the phreatic surface may be more complex and evolve with time within an heterogeneous domain, which will eventually increase the uncertainty of the sinkhole location. These aspects should be considered in future works for real case studies.

In what follows, recommendations for future research work are presented concerning both experimental and numerical aspects.

- More advanced laboratory testing is required to identify the influencing factors of suffusion and to capture the impact of internal erosion on the mechanical behavior of the soils. Ideally, the design of the erosion test apparatus should accommodate measurements of the specimen deformation, the mass loss from the specimen, and the evolution of the hydraulic

conductivity along the specimen in order to improve the modelling.

- The physics behind the suffusion phenomena remains unclear since the experimental results in the literature present contradictions. On the one hand, the specimen preparation could introduce significant perturbations to the specimen; on the other hand, the real-time updating microscopic observations of the eroded soil fabric are necessary to better understand the hydro-mechanical behavior of eroded soils.

- Taking advantage of the discrete approach (DEM) which allows for a better consideration and understanding of the material behavior at the grain scale, an alternative to experimental studies is to improve the existing hydro-mechanical coupled numerical approaches based on a discrete formulation (DEM-CFD, DEM-LBM, DEM-PFV, etc.). It would provide a visualization of the particle migration at grain scale and the possibility of parametric studies at relatively low cost.

- Develop a multi-scale and multi-physics modelling approach under the framework of the continuous medium theory in which multi-scale denotes a micromechanics-based model.

References

[1] Bonelli S, Marot D. On the modelling of internal soil erosion. The 12th International Conference of International Association for Computer Methods and Advances in Geomechanics (IACMAG)2008. p. 7.

[2] Fell R, Wan CF, Cyganiewicz J, Foster M. Time for development of internal erosion and piping in embankment dams. Journal of geotechnical and geoenvironmental engineering. 2003;129(4):307-14.

[3] Wan CF, Fell R. Investigation of rate of erosion of soils in embankment dams. Journal of geotechnical and geoenvironmental engineering. 2004;130(4):373-80.

[4] Kenney T, Lau D. Internal stability of granular filters. Canadian geotechnical journal. 1985;22(2):215-25.

[5] Chang D, Zhang L. A stress-controlled erosion apparatus for studying internal erosion in soils. Geotechnical Testing Journal. 2011;34(6):579-89.

[6] Xu Y, Zhang L. Breaching parameters for earth and rockfill dams. Journal of Geotechnical and Geoenvironmental Engineering. 2009;135(12):1957-70.

[7] Zhang L, Chen Q. Seepage failure mechanism of the Gouhou rockfill dam during reservoir water infiltration. Soils and Foundations. 2006;46(5):557-68.

[8] Zhang L, Xu Y, Jia J. Analysis of earth dam failures: A database approach. Georisk. 2009;3(3):184-9.

[9] Rönnqvist H, Fannin J, Viklander P. On the use of empirical methods for assessment of filters in embankment dams. Géotechnique Letters. 2014;4(4):272-82.

[10] Foster M, Fell R, Spannagle M. The statistics of embankment dam failures and accidents. Canadian Geotechnical Journal. 2000;37(5):1000-24.

[11] Muir Wood D. The magic of sands—the 20th Bjerrum Lecture presented in Oslo, 25 November 2005. Canadian Geotechnical Journal. 2007;44(11):1329-50.

[12] Sterpi D. Effects of the erosion and transport of fine particles due to seepage flow. international journal of Geomechanics. 2003;3(1):111-22.

[13] Crosta G, Prisco Cd. On slope instability induced by seepage erosion. Canadian Geotechnical Journal. 1999;36(6):1056-73.

[14] Hu W, Hicher P-Y, Scaringi G, Xu Q, Van Asch T, Wang G. Seismic precursor to instability induced by internal erosion in loose granular slopes. Géotechnique. 2018:1-13.

[15] Burenkova V. Assessment of suffusion in non-cohesive and graded soils. Filters in geotechnical and hydraulic engineering Balkema, Rotterdam. 1993:357-60.

[16] Foster M, Fell R. Assessing embankment dam filters that do not satisfy design criteria. Journal of Geotechnical and Geoenvironmental Engineering. 2001;127(5):398-407.

[17] Kenney T, Lau D. Internal stability of granular filters: Reply. Canadian Geotechnical Journal. 1986;23(3):420-3.

[18] Kézdi A. SOIL PHYSICS-SELECTED TOPICS-DEVELOPMENTS IN GEOTECHNICAL ENGINEERING-25. 1979.

[19] Li M, Fannin RJ. Comparison of two criteria for internal stability of granular soil. Canadian Geotechnical Journal. 2008;45(9):1303-9.

[20] Sherard J. Sinkholes in dams of coarse, broadly graded soils. 13th Int. Congress on Large Dams, New Delhi Q1979. p. R2.

[21] Wan CF, Fell R. Assessing the potential of internal instability and suffusion in embankment dams and their foundations. Journal of Geotechnical and Geoenvironmental Engineering. 2008;134(3):401-7.

[22] Skempton A, Brogan J. Experiments on piping in sandy gravels. Geotechnique. 1994;44(3):449-60.

[23] Sibille L, Marot D, Sail Y. A description of internal erosion by suffusion and induced settlements on cohesionless granular matter. Acta Geotechnica. 2015;10(6):735-48.

[24] Rochim A, Marot D, Sibille L, Thao Le V. Effects of Hydraulic Loading History on Suffusion Susceptibility of Cohesionless Soils. Journal of Geotechnical and Geoenvironmental Engineering. 2017;143(7):04017025.

[25] Zhang L, Du J. Effects of abutment slopes on the performance of high rockfill dams. Canadian Geotechnical Journal. 1997;34(4):489-97.

[26] Moffat RA, Fannin RJ. A large permeameter for study of internal stability in cohesionless soils. Geotechnical Testing Journal. 2006;29(4):273-9.

[27] Moffat R, Fannin RJ, Garner SJ. Spatial and temporal progression of internal erosion in cohesionless soil. Canadian Geotechnical Journal. 2011;48(3):399-412.

[28] Bendahmane F, Marot D, Alexis A. Experimental parametric study of suffusion and backward erosion. Journal of Geotechnical and Geoenvironmental Engineering. 2008;134(1):57-67.

[29] Marot D, Rochim A, Nguyen H-H, Bendahmane F, Sibille L. Assessing the susceptibility of gap-graded soils to internal erosion: proposition of a new experimental methodology. Natural Hazards. 2016;83(1):365-88.

[30] Ke L, Takahashi A. Experimental investigations on suffusion characteristics and its mechanical consequences on saturated cohesionless soil. Soils and Foundations. 2014;54(4):713-30.

[31] Slangen P, Fannin R. A Flexible Wall Permeameter for Investigating Suffusion and Suffosion. Geotechnical Testing Journal. 2016;40(1):1-14.

[32] Mehdizadeh A, Disfani MM, Evans R, Arulrajah A. Progressive Internal Erosion in a Gap-Graded Internally Unstable Soil: Mechanical and Geometrical Effects. International Journal of Geomechanics. 2017;18(3):04017160.

[33] Ke L, Takahashi A. Triaxial erosion test for evaluation of mechanical consequences of internal erosion. Geotechnical Testing Journal. 2014;37(2):347-64.

[34] Ke L, Takahashi A. Drained monotonic responses of suffusional cohesionless soils. Journal of Geotechnical and Geoenvironmental Engineering. 2015;141(8):04015033.

[35] Ke L, Ouyang M, Horikoshi K, Takahashi A. Soil deformation due to suffusion and its consequences on undrained behavior under various confining pressures. Japanese Geotechnical Society Special Publication. 2016;2(8):368-73.

[36] Cividini A, Gioda G. Finite-element approach to the erosion and transport of fine particles in granular soils. International Journal of Geomechanics. 2004;4(3):191-8.

[37] Papamichos E, Vardoulakis I, Tronvoll J, Skjaerstein A. Volumetric sand production model and experiment. International journal for numerical and analytical methods in geomechanics. 2001;25(8):789-808.

[38] Stavropoulou M, Papanastasiou P, Vardoulakis I. Coupled wellbore erosion and stability analysis. International journal for numerical and analytical methods in geomechanics. 1998;22(9):749-69.

[39] Vardoulakis I, Stavropoulou M, Papanastasiou P. Hydro-mechanical aspects of the sand production problem. Transport in porous media. 1996;22(2):225-44.

[40] Zhang X, Wong H, Leo C, Bui T, Wang J, Sun W, et al. A thermodynamics-based model on the internal erosion of earth structures. Geotechnical and Geological Engineering. 2013;31(2):479-92.

[41] Lominé F, Scholtès L, Sibille L, Poullain P. Modeling of fluid–solid interaction in granular media with coupled lattice Boltzmann/discrete element methods: application to piping erosion. International Journal for Numerical and Analytical Methods in Geomechanics. 2013;37(6):577-96.

[42] Mansouri M, El Youssoufi MS, Nicot F. Numerical simulation of the quicksand phenomenon by a 3D coupled Discrete Element‐Lattice Boltzmann hydromechanical model. International Journal for Numerical and Analytical Methods in Geomechanics. 2017;41(3):338-58.

[43] Reboul N, Vincens E, Cambou B. A statistical analysis of void size distribution in a simulated narrowly graded packing of spheres. Granular Matter. 2008;10(6):457-68.

[44] Sari H, Chareyre B, Catalano E, Philippe P, Vincens E. Investigation of internal erosion processes using a coupled dem-fluid method. Particles 2011 II International Conference on Particle-Based Methods, E Oate and DRJ Owen (Eds), Barcelona2011. p. 1-11.

[45] Sibille L, Lominé F, Poullain P, Sail Y, Marot D. Internal erosion in granular media: direct numerical simulations and energy interpretation. Hydrological Processes. 2015;29(9):2149-63.

[46] Zhang F, Li M, Peng M, Chen C, Zhang L. Three-dimensional DEM modeling of the stress–strain behavior for the gap-graded soils subjected to internal erosion. Acta Geotechnica. 2018:1-17.

[47] Zhao J, Shan T. Coupled CFD–DEM simulation of fluid–particle interaction in geomechanics. Powder technology. 2013;239(248-58.

[48] Muir Wood D, Maeda K, Nukudani E. Modelling mechanical consequences of erosion. Géotechnique. 2010;60(6):447-57.

[49] Scholtès L, Hicher P-Y, Sibille L. Multiscale approaches to describe mechanical responses induced by particle removal in granular materials. Comptes Rendus Mécanique. 2010;338(10-11):627-38.

[50] Hosn RA, Sibille L, Benahmed N, Chareyre B. A discrete numerical model involving partial fluid-solid coupling to describe suffusion effects in soils. Computers and Geotechnics. 2018;95(30-9.

[51] Hicher P-Y. Modelling the impact of particle removal on granular material behaviour. Géotechnique. 2013;63(2):118.

[52] Yin Z-Y, Huang H-W, Hicher P-Y. Elastoplastic modeling of sand–silt mixtures. Soils and Foundations. 2016;56(3):520-32.

[53] Yin Z-Y, Wu Z-X, Hicher P-Y. Modeling Monotonic and Cyclic Behavior of Granular Materials by Exponential Constitutive Function. Journal of Engineering Mechanics. 2018;144(4):04018014.

[54] USACE. Best Practices in Dam and Levee Safety Risk Analysis. https://, 2015.

[55] Fell R, Fry J-J. The state of the art of assessing the likelihood of internal erosion of embankment dams, water retaining structures and their foundations. Internal Erosion of Dams and their Foundations, Robin Fell & Jean-Jacques Fry–editors, Taylor & Francis. 2007.

[56] ICOLD. Internal erosion of existing dams, levees and dikes, and their foundations. ICOLD Paris, France, 2015.

[57] Molenkamp F, Calle E, Heusdens J, Koenders M. Cyclic filter tests in a triaxial cell. Proceedings, 7th European Conference on Soil Mechanics and Foundation Engineering1979. p. 97-101.

[58] Chapuis RP, Contant A, Baass KA. Migration of fines in 0 20 mm crushed base during placement, compaction, and seepage under laboratory conditions. Canadian Geotechnical Journal. 1996;33(1):168-76.

[59] Fannin R, Slangen P. On the distinct phenomena of suffusion and suffosion. Géotechnique Letters. 2014;4(4):289-94.

[60] van Beek VM, Knoeff H, Sellmeijer H. Observations on the process of backward erosion piping in small-, medium-and full-scale experiments. European Journal of Environmental and Civil Engineering. 2011;15(8):1115-37.

[61] Sharp M, Wallis M, Deniaud F, Hersch-Burdick R, Tourment R, Matheu E, et al. The international levee handbook. CIRIA, London. 2013:497-8.

[62] Ziems J. Beitrag zur Kontakterosion nichtbindiger Erdstoffe: Verlag nicht ermittelbar, 1969.

[63] Fannin J, Slangen P, Ataii S, McClelland V, Hartford D. Erosion of Zoned Earthfill Dams by Internal Instability: Laboratory Testing for Model Development. European Working Group on Internal Erosion: Springer, 2018. p. 34-49.

[64] Sherman W. Filter Experiments and Design Criteria. ARMY ENGINEER WATERWAYS EXPERIMENT STATION VICKSBURG MISS, 1953.

[65] Kenney T, Chahal R, Chiu E, Ofoegbu G, Omange G, Ume C. Controlling constriction sizes of granular filters. Canadian Geotechnical Journal. 1985;22(1):32-43.

[66] Lafleur J, Mlynarek J, Rollin AL. Filtration of broadly graded cohesionless soils. Journal of Geotechnical Engineering. 1989;115(12):1747-68.

[67] Cividini A, Bonomi S, Vignati GC, Gioda G. Seepage-induced erosion in granular soil and consequent settlements. International Journal of Geomechanics. 2009;9(4):187-94.

[68] Ke L, Takahashi A. Strength reduction of cohesionless soil due to internal erosion induced by one-dimensional upward seepage flow. Soils and Foundations. 2012;52(4):698-711.

[69] Moffat R, Fannin RJ. A hydromechanical relation governing internal stability of cohesionless soil. Canadian Geotechnical Journal. 2011;48(3):413-24.

[70] Sail Y, Marot D, Sibille L, Alexis A. Suffusion tests on cohesionless granular matter: Experimental study. European Journal of Environmental and Civil Engineering. 2011;15(5):799-817.

[71] Bendahmane F, Marot D, Rosquoët F, Alexis A. Characterization of internal erosion in sand kaolin soils: Experimental study. Revue européenne de génie civil. 2006;10(4):505-20.

[72] Marot D, Bendahmane F, Rosquoet F, Alexis A. Internal flow effects on isotropic confined sand-clay mixtures. Soil & sediment contamination. 2009;18(3):294-306.

[73] Nguyen HH, Marot D, Bendahmane F. Erodibility characterisation for suffusion process in cohesive soil by two types of hydraulic loading. La Houille Blanche. 20126):54-60.

[74] Chang DS, Zhang LM. Critical Hydraulic Gradients of Internal Erosion under Complex Stress States. Journal of Geotechnical and Geoenvironmental Engineering. 2013;139(9):1454-67.

[75] Nguyen CD, Benahmed N, Andò E, Sibille L, Philippe P. Experimental investigation of microstructural changes in soils eroded by suffusion using X-ray tomography. Acta Geotechnica. 2019:1-17.

[76] Horikoshi K, Takahashi A. Suffusion-induced change in spatial distribution of fine fractions in embankment subjected to seepage flow. Soils and Foundations. 2015;55(5):1293-304.

[77] van Beek VM, Knoeff H, Sellmeijer H. Observations on the process of backward erosion piping in small-, medium- and full-scale experiments. European Journal of Environmental and Civil Engineering. 2011;15(8):1115-37.

[78] Cundall PA, Strack ODL. A discrete numerical model for granular assemblies. Géotechnique. 1979;29(1):47-65.

[79] Tsuji Y, Tanaka T, Ishida T. Lagrangian numerical simulation of plug flow of cohesionless particles in a horizontal pipe. Powder Technology. 1992;71(3):239-50.

[80] Tsuji Y, Kawaguchi T, Tanaka T. Discrete particle simulation of two-dimensional fluidized bed. Powder Technology. 1993;77(1):79-87.

[81] Shamy UE, Zeghal M. Coupled Continuum-Discrete Model for Saturated Granular Soils. Journal of Engineering Mechanics. 2005;131(4):413-26.

[82] Chen F, Drumm EC, Guiochon G. Coupled discrete element and finite volume solution of two classical soil mechanics problems. Computers and Geotechnics. 2011;38(5):638-47.

[83] Tao H, Tao J. Quantitative analysis of piping erosion micro-mechanisms with coupled CFD and DEM method. Acta Geotechnica. 2017;12(3):573-92.

[84] Li X, Zhao J. Dam-break of mixtures consisting of non-Newtonian liquids and granular particles. Powder Technology. 2018;338(493-505.

[85] Zhang D-M, Gao C-P, Yin Z-Y. CFD-DEM modeling of seepage erosion around shield tunnels. Tunnelling and Underground Space Technology. 2019;83(60-72.

[86] Wautier A, Bonelli S, Nicot F. DEM investigations of internal erosion: Grain transport in the light of micromechanics. International Journal for Numerical and Analytical Methods in Geomechanics. 2019;43(1):339-52.

[87] Cook BK, Noble DR, Williams JR. A direct simulation method for particle‐fluid systems. Engineering Computations. 2004;21(2/3/4):151-68.

[88] Feng YT, Han K, Owen DRJ. Coupled lattice Boltzmann method and discrete element modelling of particle transport in turbulent fluid flows: Computational issues. International Journal for Numerical Methods in Engineering. 2007;72(9):1111-34.

[89] Cui X, Li J, Chan A, Chapman D. Coupled DEM–LBM simulation of internal fluidisation induced by a leaking pipe. Powder Technology. 2014;254(299-306.

[90] Wang M, Feng YT, Pande GN, Chan AHC, Zuo WX. Numerical modelling of fluid-induced soil erosion in granular filters using a coupled bonded particle lattice Boltzmann method. Computers and Geotechnics. 2017;82(134-43.

[91] Wautier A, Bonelli S, Nicot F. Flow impact on granular force chains and induced instability. Physical Review E. 2018;98(4):042909.

[92] Chareyre B, Cortis A, Catalano E, Barthélemy E. Pore-Scale Modeling of Viscous Flow and Induced Forces in Dense Sphere Packings. Transport in Porous Media. 2012;92(2):473-93.

[93] Aboul Hosn R, Sibille L, Benahmed N, Chareyre B. A discrete numerical model involving partial fluid-solid coupling to describe suffusion effects in soils. Computers and Geotechnics. 2018;95(30-9.

[94] Steeb H, Diebels S, Vardoulakis I. Modeling internal erosion in porous media. Computer Applications In Geotechnical Engineering2007. p. 1-10.

[95] Uzuoka R, Ichiyama T, Mori T, Kazama M. Hydro-mechanical analysis of internal erosion with mass exchange between solid and water. 6th International Conference on Scour and Erosion2012. p. 655-62.

[96] Istomina VS. Filtration Stability of Soils. Gostroizdat, Moscow, Leningrad1957.

[97] Terzaghi K. Soil mechanics: a new chapter in engineering science: Harvard University, 1939.

[98] Abdoulaye Hama N, Ouahbi T, Taibi S, Souli H, Fleureau JM, Pantet A. Analysis of mechanical behaviour and internal stability of granular materials using discrete element method. International Journal for Numerical and Analytical Methods in Geomechanics. 2016;40(12):1712-29.

[99] Chang DS, Zhang LM. Extended internal stability criteria for soils under seepage. Soils and Foundations. 2013;53(4):569-83.

[100] Reboul N, Vincens E, Cambou B. A computational procedure to assess the distribution of constriction sizes for an assembly of spheres. Computers and Geotechnics. 2010;37(1):195-206.

[101] Vincens E, Witt KJ, Homberg U. Approaches to determine the constriction size distribution for understanding filtration phenomena in granular materials. Acta Geotechnica. 2015;10(3):291-303.

[102] Indraratna B, Nguyen VT, Rujikiatkamjorn C. Assessing the potential of internal erosion and suffusion of granular soils. Journal of Geotechnical and Geoenvironmental Engineering. 2011;137(5):550-4.

[103] Marot D, Bendahmane F, Nguyen HH. Influence of angularity of coarse fraction grains on internal erosion process. La Houille Blanche - Revue internationale de l'eau. 20126, 2012, pp.):47-53.

[104] Chang D. Internal erosion and overtopping erosion of earth dams and landslide dams: The Hong Kong University of Science and Technology, 2012.

[105] Li M. Seepage induced instability in widely graded soils: University of British Columbia, 2008.

[106] LI M, FANNIN RJ. A theoretical envelope for internal instability of cohesionless soil. Géotechnique. 2012;62(1):77-80.

[107] Moffat R, Herrera P. Hydromechanical model for internal erosion and its relationship with the stress transmitted by the finer soil fraction. Acta Geotechnica. 2015;10(5):643-50.

[108] Luo Y-l, Qiao L, Liu X-x, Zhan M-l, Sheng J-c. Hydro-mechanical experiments on suffusion under long-term large hydraulic heads. Natural hazards. 2013;65(3):1361-77.

[109] Bonelli S, Marot D. Micromechanical modeling of internal erosion. European Journal of Environmental and Civil Engineering. 2011;15(8):1207-24.

[110] Reddi LN, Lee I-M, Bonala MV. Comparison of internal and surface erosion using flow pump tests on a sand-kaolinite mixture. Geotechnical Testing Journal. 2000;23(1):116-22.

[111] Sakthivadivel R, Irmay S. A review of filtration theories: University of California, Hydraulic Engineering Laboratory, College of …, 1966.

[112] Sakthivadivel R, Irmay S. A review of filtration theories, HEL 15-4. University of California, Berkeley, USA. 1966.

[113] Yang SL, Sandven R, Grande L. Instability of sand–silt mixtures. Soil Dynamics and Earthquake Engineering. 2006;26(2):183-90.

[114] Lade PV, Yamamuro JA. Effects of nonplastic fines on static liquefaction of sands. Canadian Geotechnical Journal. 1997;34(6):918-28.

[115] Pitman TD, Robertson PK, Sego DC. Influence of fines on the collapse of loose sands. Canadian Geotechnical Journal. 1994;31(5):728-39.

[116] Lade PV, Liggio C, Yamamuro JA. Effects of non-plastic fines on minimum and maximum void ratios of sand. Geotechnical testing journal. 1998;21(336-47.

[117] Thevanayagam S, Mohan S. Intergranular state variables and stress–strain behaviour of silty sands. Géotechnique. 2000;50(1):1-23.

[118] Thevanayagam S, Shenthan T, Mohan S, Liang J. Undrained Fragility of Clean Sands, Silty Sands, and Sandy Silts. Journal of Geotechnical and Geoenvironmental Engineering. 2002;128(10):849-59.

[119] Micro and Macro Modeling of Ground Depression Due to Internal Erosion. Soil Behavior and Geomechanics. p. 445-55.

[120] Fujisawa K, Murakami A, Nishimura S-i. Numerical analysis of the erosion and the transport of fine particles within soils leading to the piping phenomenon. Soils and foundations. 2010;50(4):471-82.

[121] Bear J, Bachmat Y. Introduction to modeling of transport phenomena in porous media: Springer Science & Business Media, 2012.

[122] Wong H, Zhang X, Leo C, Bui T. Internal Erosion of earth structures as a coupled hydromechanical process. Applied Mechanics and Materials: Trans Tech Publ, 2013. p. 1084-9.

[123] Schaufler A, Becker C, Steeb H. Infiltration processes in cohesionless soils. ZAMM‐Journal of Applied Mathematics and Mechanics/Zeitschrift für Angewandte Mathematik und Mechanik. 2013;93(2‐3):138-46.

[124] Muhlhaus H, Gross L, Scheuermann A. Sand erosion as an internal boundary value problem. Acta Geotechnica. 2015;10(3):333-42.

[125] Sato M, Kuwano R. Suffusion and clogging by one-dimensional seepage tests on cohesive soil. Soils and Foundations. 2015;55(6):1427-40.

[126] Reboul N, Vincens E, Cambou B. A computational procedure to assess the distribution of constriction sizes for an assembly of spheres. Computers and Geotechnics. 2010;37(1-2):195-206.

[127] de Boer R. Contemporary progress in porous media theory. Applied Mechanics Reviews. 2000;53(12):323-70.

[128] Steeb H, Diebels S. A thermodynamic-consistent model describing growth and remodeling phenomena. Computational materials science. 2003;28(3):597-607.

[129] Uzuoka R, Borja RI. Dynamics of unsaturated poroelastic solids at finite strain. International Journal for Numerical and Analytical Methods in Geomechanics. 2012;36(13):1535-73.

[130] Revil A, Cathles L. Permeability of shaly sands. Water Resources Research. 1999;35(3):651-62.

[131] Guide MUs. The mathworks. Inc, Natick, MA. 1998;5(333.

[132] Aboul Hosn R. Suffusion and its effects on the mechanical behavior of granular soils: numerical and experimental investigations: Grenoble Alpes, 2017.

[133] Jin YF, Yin ZY, Shen SL, Hicher PY. Selection of sand models and identification of parameters using an enhanced genetic algorithm. International Journal for Numerical and Analytical Methods in Geomechanics. 2016;40(8):1219-40.

[134] Yin ZY, Jin YF, Shen JS, Hicher PY. Optimization techniques for identifying soil parameters in geotechnical engineering: Comparative study and enhancement. International Journal for Numerical and Analytical Methods in Geomechanics. 2018;42(1):70-94.

[135] Vanmarcke EH. Probabilistic modeling of soil profiles. Journal of the geotechnical engineering division. 1977;103(11):1227-46.

[136] DeGroot DJ, Baecher GB. Estimating autocovariance of in-situ soil properties. Journal of Geotechnical Engineering. 1993;119(1):147-66.

[137] Dasaka S, Zhang L. Spatial variability of in situ weathered soil. Géotechnique. 2012;62(5):375.

[138] Freeze RA. Probabilistic one-dimensional consolidation. Journal of Geotechnical and Geoenvironmental Engineering. 1977;103(ASCE 13067).

[139] Badaoui Mh, Nour A, Slimani A, Berrah MK. Consolidation statistics investigation via thin layer method analysis. Transport in porous media. 2007;67(1):69-91.

[140] Huang J, Griffiths DV, Fenton GA. Probabilistic analysis of coupled soil consolidation. Journal of Geotechnical and Geoenvironmental Engineering. 2009;136(3):417-30.

[141] Schrefler B. Mechanics and thermodynamics of saturated/unsaturated porous materials and quantitative solutions. Applied Mechanics Reviews. 2002;55(4):351-88.

[142] Griffiths DV, Fenton GA. Probabilistic slope stability analysis by finite elements. Journal of Geotechnical and Geoenvironmental Engineering. 2004;130(5):507-18.

[143] Griffiths DV, Huang J, Fenton GA. Probabilistic infinite slope analysis. Computers and Geotechnics. 2011;38(4):577-84.

[144] Fenton GA, Griffiths DV. Bearing-capacity prediction of spatially random c φ soils. Canadian geotechnical journal. 2003;40(1):54-65.

[145] WANG Y. Reliability-based design of spread foundations by Monte Carlo simulations. Géotechnique. 2011;61(8):677-85.

[146] Zhong C. Study of Soil Behavior Subjected to An Internal Erosion Process Universié de Nantes, 2018.

[147] Fenton GA, Vanmarcke EH. Simulation of random fields via local average subdivision. Journal of Engineering Mechanics. 1990;116(8):1733-49.

[148] Fenton GA. Error evaluation of three random-field generators. Journal of Engineering Mechanics. 1994;120(12):2478-97.

[149] Farias M, Naylor D. Safety analysis using finite elements. Computers and Geotechnics. 1998;22(2):165-81.

[150] Suri A. Cleanup of internal filter cake during flowback 2005.

[151] Al-Abduwani FAH. Internal filtration and external filter cake build-up in sandstones: TU Delft, Delft University of Technology, 2005.

[152] Borja RI. On the mechanical energy and effective stress in saturated and unsaturated porous continua. International Journal of Solids and Structures. 2006;43(6):1764-86.

[153] Jin Y-F, Wu Z-X, Yin Z-Y, Shen JS. Estimation of critical state-related formula in advanced constitutive modeling of granular material. Acta Geotechnica. 2017;12(6):1329-51.

[154] Jin Y-F, Yin Z-Y. ErosLab: A modelling tool for soil tests. Advances in Engineering Software. 2018;121(84-97.

[155] Yin Z-Y, Zhao J, Hicher P-Y. A micromechanics-based model for sand-silt mixtures. International journal of solids and structures. 2014;51(6):1350-63.

[156] Jin Y-F, Yin Z-Y, Wu Z-X, Zhou W-H. Identifying parameters of easily crushable sand and application to offshore pile driving. Ocean Engineering. 2018;154(416-29.

[157] Yin Z-Y, Jin Y-F, Shen S-L, Huang H-W. An efficient optimization method for identifying parameters of soft structured clay by an enhanced genetic algorithm and elastic–viscoplastic model. Acta Geotechnica. 2017;12(4):849-67.

[158] Wood D, Maeda K, NUKUDANI E. Discrete element modelling of soil erosion. Fourth International Conference on Scour and Erosion2008. p. 491-6.

[159] Wood DM, Maeda K. Changing grading of soil: effect on critical states. Acta Geotechnica. 2008;3(1):3-14.

[160] Hibbitt, Karlsson, Sorensen. ABAQUS/standard User's Manual: Hibbitt, Karlsson & Sorensen, 2001.

[161] Ladyzhenskaya OA. The mathematical theory of viscous incompressible flow: Gordon & Breach New York, 1969.

[162] Babuška I. The finite element method with Lagrangian multipliers. Numerische Mathematik. 1973;20(3):179-92.

[163] Brezzi F. On the existence, uniqueness and approximation of saddle-point problems arising from Lagrangian multipliers. Revue française d'automatique, informatique, recherche opérationnelle Analyse numérique. 1974;8(R2):129-51.

[164] Jin Y-F, Yin Z-Y, Shen S-L, Hicher P-Y. Investigation into MOGA for identifying parameters of a critical-state-based sand model and parameters correlation by factor analysis. Acta Geotechnica. 2016;11(5):1131-45.

[165] Wu Z-X, Yin Z-Y, Jin Y-F, Geng X-Y. A straightforward procedure of parameters determination for sand: a bridge from critical state based constitutive modelling to finite element analysis. European Journal of Environmental and Civil Engineering. 2017:1-23.

[166] Chang CS, Yin Z-Y. Micromechanical modeling for behavior of silty sand with influence of fine content. International Journal of Solids and Structures. 2011;48(19):2655-67.

[167] Alboresha R. Evaluation of the impact of a cavity upon an earth dike (analytical and numerical approaches): Application to the Val d'Orléans area (France): Université de Lorraine, 2016.

[168] Van Genuchten MT. A closed-form equation for predicting the hydraulic conductivity of unsaturated soils. Soil science society of America journal. 1980;44(5):892-8.

[169] McKee C, Bumb A. Flow-testing coalbed methane production wells in the presence of water and gas. SPE formation Evaluation. 1987;2(04):599-608.

List of publications

Articles:

1. Yang J, Yin Z-Y, Laouafa F, Hicher P-Y. Internal erosion in dike-on-foundation modeled by a coupled hydro-mechanical approach. International Journal for Numerical and Analytical Methods in Geomechanics 2019; 43(3): 663-683
2. Yang J, Yin Z-Y, Laouafa F, Hicher P-Y. Modeling coupled erosion and filtration of fine particles in granular media. Acta Geotechnica (DOI: 10.1007/s11440-019-00808-8)
3. Yang J, Yin Z-Y, Laouafa F, Hicher P-Y. Analysis of suffusion in cohesionless soils with randomly distributed porosity and fine content. Computers and Geotechnics 2019; 111: 157-171.
4. Yang J, Yin Z-Y, Laouafa F, Hicher P-Y. Hydro-mechanical modeling of granular soils considering internal erosion. Canadian Geotechnical Journal (DOI: 10.1139/cgj-2018-0653).
5. Yang J, Yin Z-Y, Hicher P-Y, Laouafa F. A Finite Element Modeling of the Impact of Internal Erosion on the Stability of a Dike. Poromechanics VI2017. p. 354-361.
6. Yang J, Yin Z-Y, Hicher P-Y, Laouafa F. How Spatial Variability of Initial Porosity and Fines Content Affects Internal Erosion in Soils. Proceedings of China-Europe Conference on Geotechnical Engineering: Springer, 2018. p. 439-443.
7. Yang J, Yin Z-Y, Zhang D-M, Hicher P-Y, Laouafa F. A Coupled Hydro-Mechanical Modeling of Tunnel Leakage in Sand Layer. GeoShanghai International Conference: Springer, 2018. p. 506-514.
8. Yang J, Laouafa F, Yin Z-Y, Hicher P-Y. Hydro-mechanical modeling of internal erosion in dike. ARMA 2019.

International conferences:

1. Oral presentation, EMI (Engineering Mechanic Institute), 2016, Metz, France
2. Oral presentation, MSGG (Symposium on Multi-Scale Geomechanics and Geo-engineering) - Tongji 2016, Shanghai, China
3. Oral presentation, GDRI 2016, Nantes, France
4. Oral presentation, 6th Biot conference, 2017, Paris, France
5. Oral presentation, GDRI 2018, Lyon, France
6. Oral presentation, China-Europe Conference on Geotechnical Engineering, 2018, Vienne, Austria
7. Oral presentation, COGGUS2, 2019, Nancy, France
8. Oral presentation, ARMA 2019, New-York.

Titre : Analyses numériques de la problématique multi-physique des fontis au voisinage d'une digue ou d'un ouvrage linéaire

Mots clés : érosion interne, suffusion, méthode des éléments finis, teneur en particules fines, couplage hydromécanique, couplage érosion-filtration

Résumé : Les géo-structures telles que les barrages et les digues sont soumises à des écoulements hydrauliques variant dans le temps et dans l'espace. L'eau qui traverse ces milieux poreux peut entraîner le détachement et le transport de certaines particules des sols constituant les structures et leurs fondations. Ce problème est généralement appelé "érosion interne". Le terme suffusion, un type d'érosion interne, se réfère au détachement et au transport de particules les plus fines à travers une matrice de sol poreuse plus grossière en raison d'un écoulement hydraulique. L'évolution temporelle de la suffusion peut modifier les propriétés hydrauliques et mécaniques des sols et peut entraîner des changements importants dans le comportement de telles structures pouvant aller jusqu'à leur effondrement. Ce travail de thèse tente de contribuer à la conception et à la durabilité des ouvrages en ingénierie géotechnique et hydraulique en mettant un accent particulier sur les barrages, les levées et les digues. Il a été consacré à développer un modèle numérique de suffusion en introduisant d'une part le couplage des phénomènes hydrauliques et mécaniques et d'autre part le couplage des phénomènes d'érosion et de filtration.

Title : Numerical analyses of the multi-physics problem of sinkholes in the vicinity of a dike or a linear geo-structure

Keywords : internal erosion, suffusion, finite element method, fines content, hydro-mechanical coupling, erosion-filtration coupling

Abstract : Geo-structures such as dams and levees or dikes are subjected to seepage varying in time and space. The water flowing through these porous media can lead to the detachment and transport of part of the soil particles within the structures or their foundations. This problem is usually called internal erosion. The term suffusion, one type of internal erosion, refers to the detachment and transport of finer particles through a coarser porous soil matrix due to seepage flow. Suffusion can modify with time the hydraulic and mechanical properties of the soils and may trigger significant damage on such structures and lead eventually to their collapse. This research attempts to contribute to the design and sustainability of geotechnical and hydraulic engineering structures, with a particular focus on embankment dams, levees, and dikes. It aims to develop a numerical model of suffusion by introducing, on the one hand, the coupling of the hydraulic and mechanical phenomena and, on the other hand, the coupling of erosion and filtration.